Unravelling the magneto-ionic fabric of the Milky Way Galaxy

By

Alec James McInnes Thomson

A thesis submitted for the degree of Doctor of Philosophy
of The Australian National University
Research School of Astronomy and Astrophysics
March 2020

Australian National University

Declaration

I hereby declare that the work in this thesis is that of the candidate alone, except where indicated below or in the text of the thesis. The work was undertaken between the 15$^{\text{th}}$ of February, 2016 and the 26$^{\text{th}}$ of August, 2019 at the Australian National University (ANU), Canberra. It has not been submitted in whole or in part for any other degree at this or any other university.

Statement of Contribution

This thesis is submitted as a Thesis by Compilation in accordance with https://policies.anu.edu.au/ppl/document/ANUP_003405.

I declare that the research presented in this thesis represents original work that I carried out during my candidature at the Australian National University, except for contributions to multi-author papers incorporated in the thesis where my contributions are specified in this Statement of Contribution.

Title and authors: *The Global Magneto-Ionic Medium Survey: Polarimetry of the Southern Sky from 300 to 480 MHz.* Wolleben, M.; Landecker, T. L.; Carretti, E.; Dickey, J. M.; Fletcher, A.; McClure-Griffiths, N. M.; McConnell, D.; **Thomson, A. J. M.**; Hill, A. S.; Gaensler, B. M.; Han, J. -L.; Haverkorn, M.; Leahy, J. P.; Reich, W.; Taylor, A. R.

Current status of paper: Published.

Contribution to paper: I made two primary contributions to this paper; namely, validating the total intensity spectrum and performing Faraday tomography. As presented within the paper, these comprise sections 6.1 and 5.9, respectively. Within this thesis I present a summary of this work.

Senior author or collaborating authors endorsement:

Tom L. Landecker	T. Landecker	22nd August 2019
Senior author	Signature	Date

Title and authors: *Ghost of a shell: magnetic fields of Galactic supershell GSH 006 - 15 + 7.* **Thomson, Alec J. M.**; McClure-Griffiths, N. M.; Federrath, Christoph; Dickey, John M.; Carretti, Ettore; Gaensler, B. M.; Haverkorn, Marijke; Kesteven, M. J.; Staveley-Smith, Lister

Current status of paper: Published.

Contribution to paper: I was the primary author of this paper. As such, I was responsible for the vast majority of the text. My coauthors contributed through providing data, giving comments and feedback on the text, in-person discussions, and some small passages of text.

Title and authors: *Through thick or thin: multiple components of the magneto-ionic medium towards the nearby H II region Sharpless 2-27 revealed by Faraday tomography.* **Thomson, Alec J. M.**; Landecker, T. L.; Dickey, John M.; McClure-Griffiths, N. M.; Wolleben, M.; Carretti, E.; Fletcher, A.; Federrath, Christoph; Hill, A. S.; Mao, S. A.; Gaensler, B. M.; Haverkorn, M.; Clark, S. E.; Van Eck, C. L.; West, J. L.

Current status of paper: Published.

Contribution to paper: I was the primary author of this paper. As such, I was responsible for the vast majority of the text. My coauthors contributed through providing data, giving comments and feedback on the text, in-person discussions, and some small passages of text.

Title and authors: *The brightest polarized region in the Southern sky at 400MHz.* **Thomson, Alec J. M.**; GMIMS consortium.

Current status of paper: Not Yet Submitted.

Contribution to paper: I was the primary author of this paper. As such, I was responsible for the vast majority of the text. My coauthors contributed through providing data, giving comments and feedback on the text, in-person discussions, and some small passages of text.

Alec James McInnes Thomson		26/08/2019
Candidate	Signature	Date

Endorsed

Naomi McClure-Griffiths		25/08/2019
Chair of Supervisory Panel	Signature	Date
Delegated Authority	Signature	Date

...BUT, when the contrary magnetic poles were on the same side, there was an effect produced on the polarized ray, and thus magnetic force and light were proved to have relation to each other.

– MICHAEL FARADAY

Acknowledgements

The completion of my PhD would not have possible without the support of all the fantastic people in my life. To all my friends, family, peers, and colleagues, I cannot thank you enough. I will try here, to name a few of the people who contributed not only to this work but also my well-being and, on occasion, my sanity.

I am incredibly privileged to have been guided by three amazing supervisors. Together, their mentorship has made me the scientist I am today. I must deeply thank Naomi McClure-Griffiths as my primary supervisor. I could not have asked for a better mentor over the past three and half years. Naomi trusted me to take on the projects and questions I found the most interesting. She struck the perfect balance of leaving me to find my own way and guiding me, as I needed it. John Dickey has been teaching me since 2011, and I do not see that stopping any time soon. John was also the person who first introduced me to the field of radio polarization, and that clearly left an impression on me. Nearly all my conversations with John end with me feeling far more illuminated than before. Finally, working with Christoph Federrath has shown me that bridging observer-theorist divide yields fantastic results. Without Christoph, I could not have achieved much of the technical work of this thesis. Christoph also holds the title of 'fastest paper commenter in the West'.

It has been a highlight of my PhD to have worked with so many amazing collaborators and coauthors. In particular, I need to thank Tom Landecker. He has been guiding me in the ways of polarization for five years. The Global Magneto-Ionic Medium Survey is the backbone of this thesis, and it simply would not exist without Tom. Further, I have a long list of collaborators I would like to thank, including Ettore Carretti, Alex Hill, Bryan Gaensler, Marijke Haverkorn, Ann Mao,

Susan Clark, Cameron Van Eck, Jennifer West, Jane Kaczmarek, and Paddy Leahy. I very much look forward to working with everyone again in the future.

My amazing and loving parents, Rachel and Douglas Thomson, have given me the best support through my PhD, as they have throughout my life. They have always encouraged me to take on whatever pursuit I had my heart set on, and provided me with the platform of love and assistance whenever I needed it. I will always be indebted to my parents for all the things they have done for me. Whether it was helping me move interstate, flying over 4 hours to cook me a homemade meal, or letting me FaceTime with my cat Kenji. Here I just want to say thank you, and I love you both.

Perched on top of Mount Stromlo, the people of the ANU Research School of Astronomy & Astrophysics have become part of my daily life. Ryan Ridden-Harper, as my long-suffering officemate, has kept me smiling for three and half years. Thanks also to the 12 o'clock lunchtime crew for all the banter and the excuse to escape the Woolley basement. I am also very fortunate to have worked with two amazing research groups, along with a huge roster of fellow students and post-docs. As part of these groups, I always found that I was able to reach out for help when I needed it.

Thank you to the members of the Boobialla Street family, Emily Look, Andrew 'Ando' Cavenagh, Pat Atkinson, and honorary members Manik Mahajan and Nathan Attrill. Also, thank you to the gym crew, the OCI quiz team, and ANU cycling club. You have all helped to make Canberra my home.

Finally, and most importantly, I need to thank my incredible partner Georgia Avent. When we met four years ago, I was unsure where to undertake my PhD, if at all. Georgia encouraged me to move from Hobart to Canberra, knowing that it would be the best place for me to study. Although, this meant living apart for nearly three years. In that time, Georgia became the most important person in my life. I can safely say that I have found my life partner, and I simply could not have completed a PhD without her. I am overjoyed to be finally living together with her, and her grumpy 17 year-old cat Pepsi. I can't wait to see what the future brings for us.

Abstract

Magnetic fields pervade the interstellar medium (ISM) of the Milky Way. These fields interact with various components within the ISM, locking in to the ionized phases of the ISM, forming the magneto-ionic medium. This medium is responsible for a significant input of energy into the ISM. The study of magnetic fields in the ISM of the Milky Way is therefore critical to understanding the energetics and evolution of the Galaxy. This thesis investigates magnetic fields in the Galaxy, and how they interact with a variety of ISM structures. Much remains unknown about the magneto-ionic medium of the Milky Way. This is due, in part, to the difficulty in measuring the strength and structure of magnetic fields. Overall, this limits our understanding of how gas in the Milky Way interacts with magnetic fields, and how those interactions influence Galactic dynamics. Additionally, our location within the Galaxy results in structures on the sky that are large in angular scale and diffuse in nature. The studies presented within this thesis make use of diffuse radio polarimetry made with the Parkes 64 m Telescope. Considerable effort has recently been made in the observation of diffuse polarized emission across the entire sky. Polarized radio emission carries a wealth of information on the magneto-ionic medium. Linearly polarized waves experience Faraday rotation as they propagate through the magneto-ionic medium of the Milky Way. Further, the Galaxy itself is a significant source of polarized emission via synchrotron radiation. In combination with measurements of additional ISM tracers, observations of polarization from the Galaxy can unravel the magneto-ionic properties of the Galactic ISM.

I present results from four research papers. I am the primary author of three

of these papers. I first describe my technical contribution to the Southern, low-frequency component of the Global Magneto-Ionic Medium Survey (GMIMS-LBS). This spectro-polarimetric survey measures diffuse, linearly polarized emission from 300 to 480 MHz across the entire Southern sky. The second research component of this thesis utilizes the S-band Polarization All Sky Survey (S-PASS), which maps linear polarization at 2.3 GHz. Using these data we map the magnetic structure of the Galactic supershell GSH 006−15+7. In the third research chapter I describe the results of the GMIMS-LBS towards the nearby H II region Sharpless 2-27 (Sh2-27). In this work we expand on the use of depolarizing regions, such as H II regions, as powerful distance constraints in the analysis of diffuse polarized emission. Finally, I present analysis of the brightest region in the 408 MHz polarized sky, G150−50. This region exhibits remarkably high fractional polarization, without a corresponding bright region in total intensity. Further, the polarized spectra, as measured by GMIMS-LBS, show remarkable structure. Considering both the morphology and spectral structure of this region, we find that G150−50 is explained by a Faraday caustic. Each of the works presented here highlights both the power and complexity of radio polarimetry. Using diffuse polarized emission we are able to unravel the magneto-ionic medium of the Galaxy. Surveys such as GMIMS provide us with broad-band polarimetry which enables techniques such as Faraday tomography. The features that arise from these observations are often unique to this tracer of the ISM. As we enter the SKA era, understanding how to best utilize and understand these data will be key to solving the mysteries of cosmic magnetism.

Contents

1

Introduction

The discovery of interstellar magnetic fields is tied with the birth of radio astronomy. The pioneering work of Karl Jansky and Grote Reber showed that the sky emitted at radio frequencies and that this emission came from the Milky Way itself (Jansky, 1933; Reber, 1944). It was soon found that this radio emission could not arise from a blackbody (e.g. Reber & Greenstein, 1947), instead this non-thermal emission is produced by synchrotron radiation (e.g. Burbidge, 1956). This emission is caused by cosmic-ray electrons or positrons gyrating at relativistic speeds around a magnetic field. Therefore, the discovery of synchrotron radiation confirmed unequivocally that magnetic fields exist in the Milky Way. This emission is found across the entire sky, further showing that magnetic fields must also extend throughout the Galaxy. The 2D structure of Galactic synchrotron emission is classically traced by the 408 MHz total intensity survey of Haslam et al. (1982), which I show in Figure 1.1. This image highlights the sheer ubiquity of this emission, and the magnetic fields which generate them, throughout both the Galaxy and extragalactic sources.

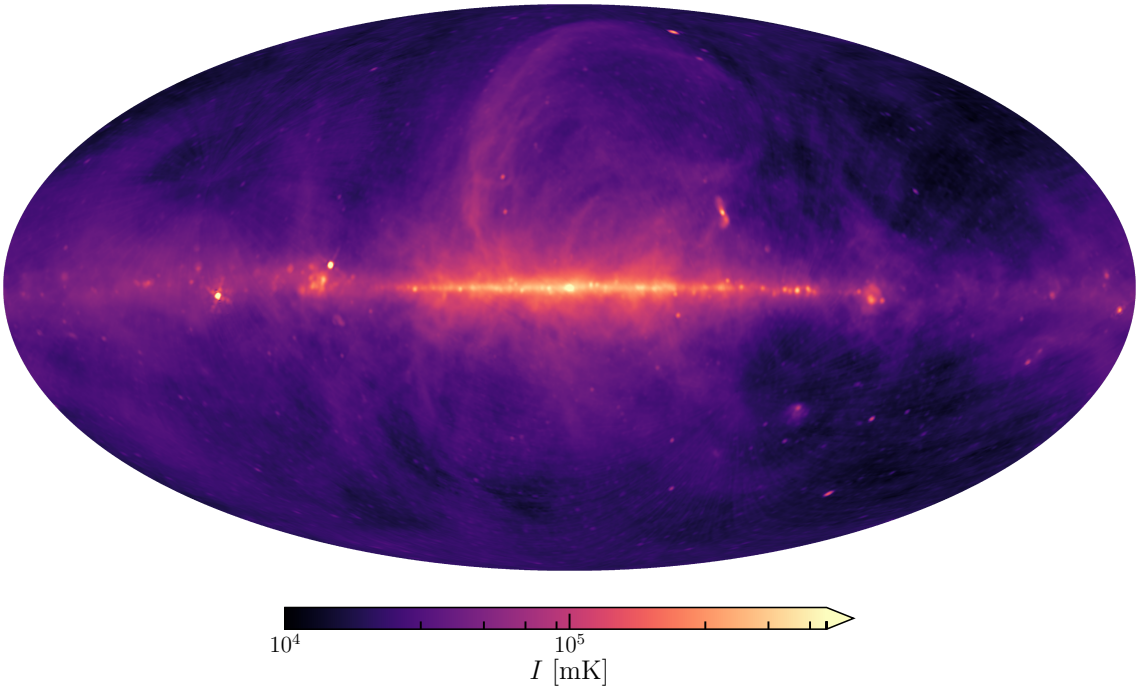

Figure 1.1: The Haslam et al. (1982) survey of synchrotron emission across the whole sky. Here, I show the image in Mollweide projection, centred on $l, b = [0°, 0°]$.

Along with magnetic fields, the Galactic interstellar medium (ISM) is comprised of various components, with the bulk of the interstellar volume containing ionized gas. Fundamentally, as charged components of the ISM move throughout the Galaxy, the magnetic fields influence these components through the Lorentz force. The magnetic fields which thread through the ISM can become 'frozen-in' with the ionized components. These mechanisms have a two-way impact: kinetic motions can be transferred to magnetic energy through the dynamo mechanism (Brandenburg & Subramanian, 2005; Federrath, 2016), and the flow of material and subsequent structure formation is governed by magnetic pressure. These fields must therefore play a tremendously important role in the dynamics of the Galaxy. If we wish to obtain complete knowledge of the evolution and dynamics of the Milky Way, we must also understand its magnetic fields. This understanding includes the strength and structure of Galactic magnetic fields, and the nature of how they interact with the ISM.

Many mysteries still remain, however, regarding Galactic magnetic fields. This is despite considerable effort on both observational and theoretical fronts. A fundamental issue with which we must grapple is that magnetic fields are not directly observable. Instead we must infer their properties from their interactions with other

observable phenomena. This observational challenge has proved to be difficult to overcome. As highlighted by Gaensler et al. (2004), we still lack a detailed understanding of cosmic magnetic fields and their interactions. Without solving the observational challenges in observing magnetic fields, the complete picture of the Milky Way's ISM will remain obscured to us.

1.1 The Galactic interstellar medium

The vast and tenuous material of the Milky Way's ISM is described by Ferrière (2001) as being composed of 4 primary constituents: dust, gas, magnetic fields, and cosmic rays. The ISM is the lifeblood of the Milky Way and is responsible for the transport of energy and matter throughout the Galaxy. The conditions that drive Galactic evolution and star formation are therefore governed by the ISM.

Interstellar dust makes up only a small fraction of the overall ISM, $\lesssim 1\%$ by mass. Despite this, dust plays a critical role in the chemistry and radiative processes of the ISM. Dust also correlates with cool components of the gaseous ISM. Observationally, the two-dimensional structure of dust is traced on the sky from its far-infrared emission. Three-dimensional structure can be obtained, however, using optical photometry towards stars whose distances are known. With the advent of the *Gaia* mission data release (Gaia Collaboration et al., 2016, 2018) projects, such as `Bayestar` (Green et al., 2015, 2018, 2019) and the STructuring by Inversion the Local Interstellar Medium (STILISM Lallement et al., 2014; Capitanio et al., 2017; Lallement et al., 2018), have been able to produce 3D maps of dust in the ISM within $\lesssim 1\,\mathrm{kpc}$ of the Sun.

The bulk of the ISM is gaseous, $\sim 13\%$ of the total Galactic baryonic mass (Kalberla et al., 2007), with the majority ($\sim 70\%$ by mass, 91% by number) being made of hydrogen. Classically, the gaseous ISM is further decomposed into phases. Adopting the nomenclature of Heiles & Haverkorn (2012), these phases are molecular clouds, the cold neutral medium (CNM), the warm neutral medium (WNM), the warm ionized medium (WIM), the hot ionized medium, and the warm partially ionized medium (WPIM). This polychotomy is derived from both an observational perspective and from theory (particularly McKee & Ostriker, 1977; Wolfire et al., 2003). I

summarize the properties of these phases in Table 1.1, adopting values from Ferrière (2001) and Heiles & Haverkorn (2012). It is important to bear in mind that these phases do not exist in isolation from one another. The Galactic ISM is constantly stirred through injections of energy, such as stellar winds and supernova, driving large-scale structures, shocks, and turbulent processes. As I will discuss later, magnetic fields are also a key driver, linking many of these processes together.

Table 1.1: Typical properties of the gaseous phases of the interstellar medium. Col. (1): Name of each phase. Col. (2): Temperature of each phase. Col. (3): The number density ($n_{\rm H}$) of hydrogen nuclei. Col. (4): The ionization fraction ($x = n_e/n_{\rm H}$) of each phase.

Phase	T [K]	$n_{\rm H}$ [cm^{-3}]	x
Molecular	10 – 20	10^2 – 10^6	10^{-8} – 10^{-6}
CNM	50 – 10^2	20 – 80	2×10^{-4} – 10^{-3}
WNM	6000	0.2 – 0.7	10^{-3} – 5×10^{-2}
WPIM	7000	0.2	0.5
WIM	8000	0.25	1
HIM	$\sim 10^6$	0.0034	1

Molecular gas, in the form of the H_2 molecule, is the primary fuel for star formation. Most of this cold, dense gas is contained within large, gravitationally bound 'giant molecular complexes' (Heyer & Dame, 2015), which are themselves comprised of clouds and dense cores. In the Milky Way's ISM H_2 makes up a total mass of $\sim 10^9 M_\odot$. The H_2 molecule, unfortunately, requires a temperature higher than the typical neutral cloud in order to produce radiation. Therefore molecular gas is traced using proxy observations such as millimetre emission from the carbon monoxide (CO) molecule. As CO emission is a spectral line, its spatial and velocity structure can be derived. Surveys of such emission show that molecular clouds are typically found within a 90 pc layer around the Galactic disc and inside of the Galactic spiral arms.

The gas of the CNM and WNM exist in thermal equilibrium in the ISM (McKee & Ostriker, 1977; Wolfire et al., 1995, 2003). Observationally, however, there is also evidence for the existence of thermally unstable gas in a 'lukewarm neutral

medium' (Heiles & Troland, 2003; Kalberla & Haud, 2018). Despite the name 'neutral', this gas has a non-negligible ionization fraction (see Table 1.1). Atomic gas, H I, is traced using the 21 cm line in both emission and absorption. Galactic H I emission is found all across the sky, and this emission is now mapped in exquisite detail (Kalberla & Kerp, 2009). The 21 cm line provides the total column density of H I along the line of sight, and the line-of-sight structure can be extracted in combination with the Galactic rotation curve. H I forms structures on a huge variety of scales. For a detailed discussion of the Galactic atomic gas, I refer the reader to the reviews of Dickey & Lockman (1990), Ferrière (2001), and Kalberla & Kerp (2009). The current state-of-the-art all-sky survey of H I is the HI4PI survey (HI4PI Collaboration et al., 2016a), which combines the Effelsberg-Bonn H I Survey (EBHIS Kerp et al., 2011) and the Galactic All-Sky Survey (GASS, McClure-Griffiths et al., 2009; Kalberla et al., 2010; Kalberla & Haud, 2015). The Galactic Arecibo L-Band Feed Array H I survey (GALFA-H I, Peek et al., 2011, 2018) offers improved velocity and angular resolution over HI4PI, but is limited to declinations of $-1° \lesssim \delta \lesssim 38°$. The Galactic plane has also been mapped in arcminute resolution using combined single-dish and interferometric observations in the Canadian, Southern, and VLA Galactic Plane Surveys (Taylor et al., 2003; McClure-Griffiths et al., 2005; Stil et al., 2006).

The WIM, as per its name, is highly ionized, with a typical temperature of $\sim 8000\,\mathrm{K}$. This gas is found throughout the Galaxy in two broadly distinct regions: in H II regions surrounding O and B type stars, and in a diffuse layer around the Galactic disc. The former is typically traced using observations of H α emission, for which diffuse all-sky surveys are available. The Wisconsin H-Alpha Mapper Sky Survey (WHAM-SS, Haffner et al., 2003, 2010) provides velocity separated data at 1° resolution, and Finkbeiner (2003) provides a velocity integrated image at higher (but varied) spatial resolution. By assuming a thermal electron temperature, and correcting for dust reddening, the H α intensity can provide the emission measure (EM):

$$\mathrm{EM} = \int n_e^2 \mathrm{d}r, \tag{1.1}$$

where n_e is the thermal electron density, integrated along the LOS r. H α can therefore be used to infer the thermal electron density in the ISM. The diffuse

component of the WIM can be traced through a mixture of observations, including pulsar dispersion measures (DM) and free-free absorption of synchrotron emission. Dispersion measure is a defined similarly to EM:

$$\mathrm{DM} = \int n_e \mathrm{d}r. \tag{1.2}$$

DM can therefore also trace the thermal electron density in the ISM, but with a lower weighting factor compared to the EM (n_e vs. n_e^2). Gaensler et al. (2008) compiled a mixture of diffuse WIM observations and found an exponential distribution of gas, with a scale-height of $\sim 1.8\,\mathrm{kpc}$.

The HIM, also known as 'coronal gas', is totally ionized and very tenuous, with temperatures on the order of $10^6\,\mathrm{K}$. The Galactic distribution of this phase is not totally understood, but it has been found in the evacuated regions of Galactic (super)shells and bubbles and in the Galactic Halo (Savage & Wakker, 2009). This gas is found through observations of ultra-violet absorption spectra and diffuse x-ray emissions. I note that the ISM surrounding the Sun, known as the Local Bubble, is itself comprised of the HIM (Cordes & Lazio, 2002; Shelton, 2009).

It has been argued by Heiles & Haverkorn (2012) that an additional gas phase, the WPIM, exists between the WNM and WIM. This phase, envisioned to have an ionization fraction of $x \sim 50\%$ and a temperature of $\sim 7000\,\mathrm{K}$, does not correspond to a typical ISM tracer. It is too ionized to be strongly associated with H I, but too cool to appear in observations of H α. As such, the definitive existence of this phase, and therefore its properties, is not well understood. Heiles & Haverkorn (2012) instead argue that this phase may be revealed through its relationship to magnetic fields. I note additionally that the most ubiquitous phases by volume, the WIM and WNM, straddle the WPIM in pressure-temperature space. The WIM and WNM alone also correlate with a high population of ions (see Table 1.1, Col. 4), which in turn interact with magnetic fields in the ISM.

The magnetic fields of the Milky Way are threaded through the gas of the ISM. These fields mix with the phases of the ISM and form the magneto-ionic medium (MIM). This occurs not only in the purely ionized phases of the ISM, but also in the 'neutral phases'. In the CNM and WNM the ionization fraction is high enough to interact significantly with these magnetic fields. The interactions with

the ionized components of the ISM allows significant amounts of energy to be stored in magnetic fields, as shown in Figure 1.2 (also see Figure 5 of Beck, 2007). In

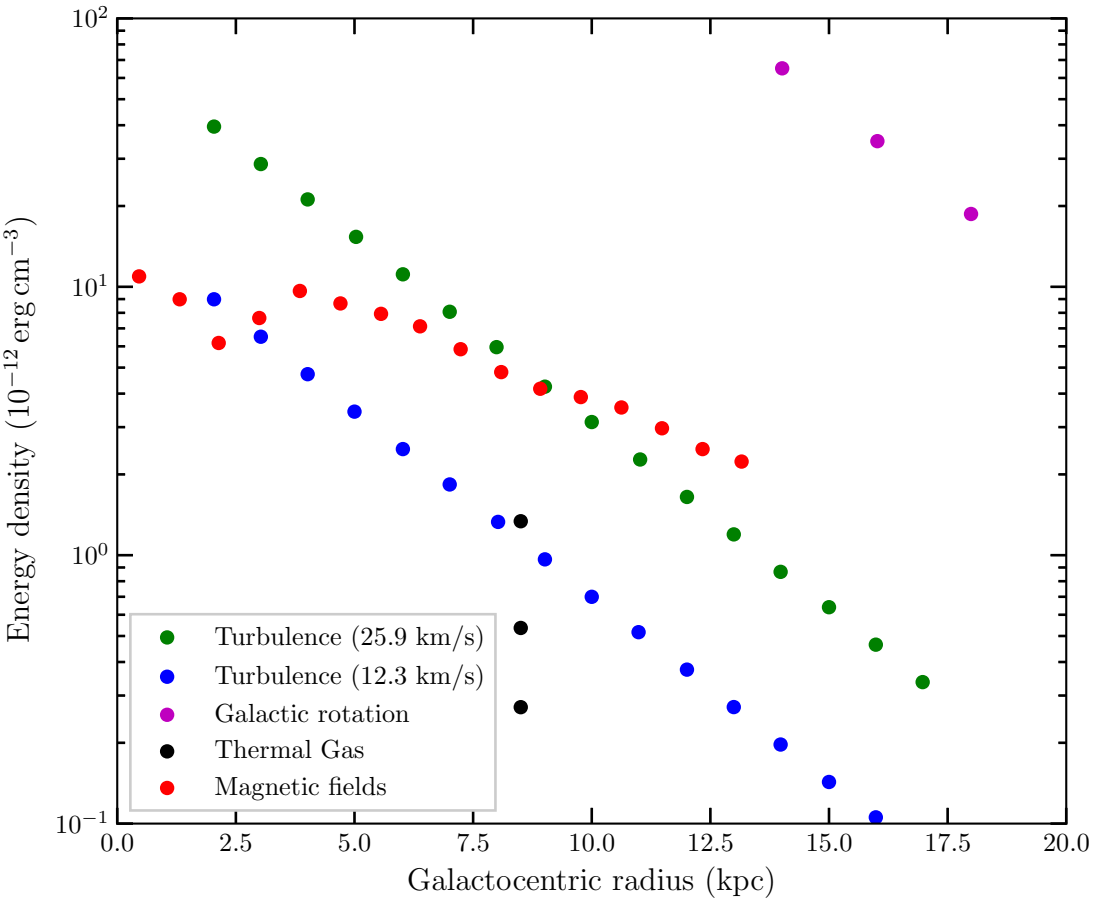

Figure 1.2: Figure 1 from Heiles & Haverkorn (2012): Estimated energy densities from ISM components in the Milky Way as a function of Galacto-centric radius. Here the velocities associated 'turbulence' components are velocity dispersion measurements of the gas. Also note that the 'magnetic field' measurements are approximate only.

molecular clouds the effect of self-gravitation is also very important. As shown by Crutcher et al. (2010), in such regimes the magnetic field strength couples to the number density of the ISM. I show this in Figure 1.3, where $B \propto \nu^{0.65}$ for number densities $n_{\rm H} > 300\,{\rm cm}^{-3}$.

Galactic Magnetic fields, and the associated MIM, are a significant dynamic driver within the ISM and are crucial to various astrophysical phenomena. On the largest scales, magnetic fields supply pressure that balances against the overall gravitational potential of the Galaxy (Ferrière, 2001), and have a significant influence

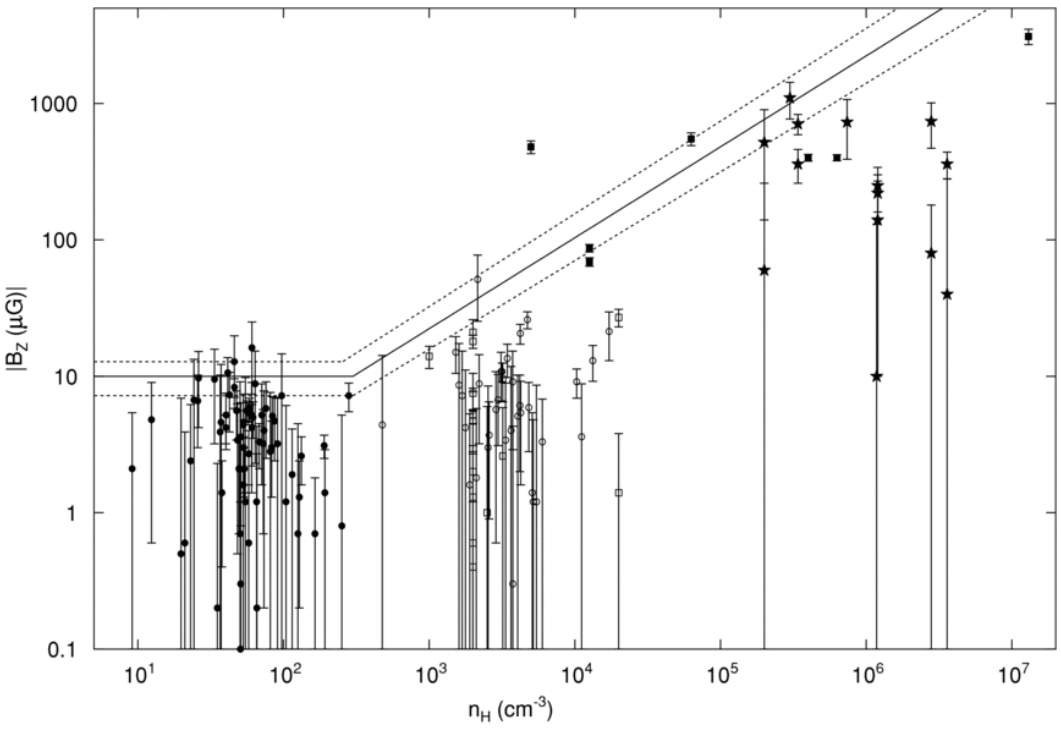

Figure 1.3: Figure 1 from Crutcher et al. (2010): Line-of-sight magnetic field strengths against number density in diffuse H I and molecular clouds. Here the magnetic field strengths were derived from Zeeman splitting observations.

on the distribution of cosmic rays (Beck, 2015). The combination of these large-scale effects means that the strength of the magnetic fields are of great importance in the overall hydrostatic balance in the Milky Way. These findings are relevant to overall Galactic evolution; de Avillez & Breitschwerdt (2005) found that, in magneto-hydrodynamic simulations of Galactic evolution, magnetic fields slow the transport of material out of the disk and into the Galactic halo. On smaller size-scales, magnetic fields play roles in star formation and turbulent gas flows. Star formation processes are slowed by a factor of 2-3 by the presence of magnetic fields (Padoan & Nordlund, 2011; Federrath & Klessen, 2012; Federrath, 2015). Magnetic fields have profound consequences for the initial mass function of stars (Offner et al., 2014). Turbulence in the ISM is itself affected by magnetic fields, which has flow on effects to many astrophysical phenomena including accretion disks, proto-stellar disks, the

diffuse ISM, and molecular cloud formation (Federrath, 2016). Simulations of the Galactic ISM require measurements of magnetic fields in order to produce accurate results.

1.2 Observing magnetic fields

As observers, we have at our disposal a number of methods for measuring Galactic magnetic fields. As summarised by Beck & Wielebinski (2013) (and references therein), each of these methods is capable of probing different components of the Galactic magnetic field, and each has its own observational limitations.

Elongated dust grains in the ISM can become aligned to the ambient magnetic field, such that their major axis is perpendicular to the magnetic field direction (Davis & Greenstein, 1951). These dust grains then act as a polarizing filter to the background unpolarized optical starlight. The measured polarized electric field vector is therefore aligned to the direction of the magnetic field projected on the plane of the sky (POS). In regions of the ISM where rotational modes of these dust grains are excited, the grains produce sub-millimetre and far infrared emission that is intrinsically polarized. Again, the polarization angle of this emission traces the POS component of the magnetic field. Together, these methods trace the POS Galactic magnetic fields at the location of interstellar dust. Recently, the *Planck* mission (Planck Collaboration et al., 2018b,c,a,d) has provided surveys of the entire sky of dust polarization at 353 GHz. These images, whilst rich in information, trace only the POS component of magnetic fields in the nearby ISM.

The Zeeman effect has been utilized in both optical and radio astronomy to measure magnetic fields. In the presence of magnetic fields at the site of spectral line emission, the line will be split. In the case of a line-of-sight (LOS) magnetic field, an emission line will be split into two circularly polarized components of opposite chirality. Thus, measuring the frequency separation of these components yields the LOS magnetic field strength at the site of emission. In the Galactic ISM, this technique has been applied to observations of hydroxyl and water masers, as well as the H I line (see e.g. Crutcher et al., 2010, for a compilation of such observations).

Structures within the ISM itself can also trace magnetic fields. Specifically, in

the CNM and molecular clouds, the gas forms magnetically aligned features known as 'fibres' or 'striations' (McClure-Griffiths et al., 2006b; Clark et al., 2014). The principle of deriving magnetic field strengths from ISM structure was outlined by Chandrasekhar & Fermi (1953), now known as the Chandrasekhar-Fermi method, and assumes that these structures arise from Alfvén waves and yields an estimate of the mean magnetic field in a given region. Since this formulation, many 'improved' methods have been suggested in the literature. Of particular note, is the Rolling Hough Transform technique of Clark et al. (2014) and the 'temporal evolution' method of Tritsis et al. (2019). Both of these techniques can produce the POS magnetic field strength and orientation. These observations, however, can only produce magnetic field information where magnetically-aligned structures are observed in the ISM.

Finally, synchrotron emission is perhaps the most powerful probe of Galactic magnetic fields. Synchrotron emission is observed from the Galaxy itself as well as extra-galactic sources. Synchrotron emission, produced by charged cosmic rays gyrating around magnetic fields, dominates the radio sky. The density of cosmic rays follows a power-law distribution as a function of their energy, such that:

$$N(E) = N_0 E^{\gamma}, \tag{1.3}$$

where γ is between ~ -2.5 to ~ -3 in the Milky Way, depending on the frequency band and Galactic latitude. The synchrotron emissivity (ε) of such emission can be quantified by considering a volume with density N_0 of cosmic rays, a POS magnetic filed of $B_{\perp}$, at a frequency ν:

$$\varepsilon \propto N_0 \nu^{(\gamma+1)/2} B_{\perp}^{(1-\gamma)/2}. \tag{1.4}$$

Integrating along the LOS yields the observed intensity (I) of synchrotron emission:

$$I \propto I^{\alpha}, \tag{1.5}$$

where $\alpha = (\gamma + 1)/2$. Thus, by characterising both the synchrotron spectrum and cosmic ray density, the POS magnetic field can be determined at the site of emission.

In a remarkable cosmic coincidence, however, synchrotron radiation can also provide information of the LOS component of the Galactic magnetic field. Further, we can even obtain the three-dimensional structure and strength of the LOS field. We gain this information by utilising the polarized component of synchrotron emission.

1.2.1 Radio polarimetry

Synchrotron emission has a high degree of linear polarization. Rybicki & Lightman (1986) show that a single synchrotron emitting electron will be elliptically polarized. For an emitting ensemble of electrons following the distribution of Equation 1.3, the circular components cancel, producing a linearly polarized wave. The intrinsic polarization angle χ of this wave, measured as the position angle of the waves E-field, is aligned with the POS B-field. The intrinsic polarization fraction p_0 of:

$$p_0 \equiv \frac{L}{I} = \frac{3 - 3\alpha}{5 - 3\alpha}, \tag{1.6}$$

where L is the polarized intensity of the wave. For typical Milky Way spectra, the intrinsic synchrotron polarization fraction is therefore ~ 70–75%.

The aforementioned cosmic coincidence is that, not only is the radio sky full of polarized emission, the polarized emission is perturbed by the magneto-ionic medium of the Galaxy. This perturbation, known as the Faraday rotation effect, embeds information of the LOS B-field into the polarized wave and is strongest at radio frequencies.

1.2.1.1 Faraday rotation

As any linearly polarized electromagnetic wave propagates through a magneto-ionic medium, the polarization angle of the wave will rotate through the process of Faraday rotation. First observed by Michael Faraday, the theoretical formulation for this effect was provided by James Clerk Maxwell. Derivations of Faraday rotation in an astrophysical context are given in Kraus (1966) and Harwit (2006).

We can gain a qualitative sense of these derivations through considering the propagation of a linearly polarized wave. A purely linearly polarized wave can be decomposed into right- and left-handed circularly polarized waves. Consider

now if these waves propagate into a volume that contains a magnetic field with a component along the direction of propagation and some free electron density. Under these conditions, the phase velocity of the two circular components will be different, leading to a phase lag between them. Superposing these circular components back together yields a linearly polarized wave whose polarization angle χ changes as a function of distance. Integrating through the magneto-ionic medium yields a change in angle of:

$$\Delta\chi = \frac{e^3\lambda^2}{4\pi^2c^4m_e^2}\int_0^d n_e(\boldsymbol{r})\boldsymbol{B}(\boldsymbol{r})\cdot \mathrm{d}\boldsymbol{r}, \tag{1.7}$$

where e is the charge on the electron, λ is the wavelength, c is the speed of light, m_e is the mass of the electron, d is the total distance through the medium, n_e is the electron density, $\boldsymbol{B}$ is the total magnetic field strength, and $\boldsymbol{r}$ is the infinitesimal distance vector through the medium along the direction of propagation.

Therefore, if we can determine the amount of Faraday rotation, we can measure the strength of the LOS magnetic field. This is readily done through observations of the polarization state of synchrotron emission. Using a radio polarimeter, we can measure the complex polarization ($\mathcal{P}$) of a linearly polarized wave:

$$\mathcal{P} = p_0 I = Q + iU, \tag{1.8}$$

as defined in terms of the Stokes parameters I, Q, and U. Or equivalently, in terms of the polarized intensity (L) and χ:

$$\mathcal{P} = Le^{2i\chi}, \tag{1.9}$$

$$L = ||\mathcal{P}|| = ||p_0||I = \sqrt{Q^2 + U^2}, \tag{1.10}$$

and

$$\chi = \arg(\mathcal{P}) = \frac{1}{2}\ \arctan\left(\frac{U}{Q}\right). \tag{1.11}$$

Observationally, the direction of propagation of the synchrotron emission will always be along the LOS. If emission from a background polarized source propagates through a non-emitting magneto-ionic medium, the amount of Faraday rotation from the point of emission to an observer is given by the rotation measure (RM). This

quantity is defined as the change in polarization angle per wavelength-squared (λ^2):

$$\mathrm{RM} \equiv \frac{\mathrm{d}\chi}{\mathrm{d}\lambda^2} \left[\mathrm{rad\,m^{-2}}\right]. \tag{1.12}$$

Physically, the value of RM is given by Equation 1.7:

$$\mathrm{RM} = 0.812 \int_d^0 n_e B_\parallel \mathrm{d}r, \tag{1.13}$$

where $B_\parallel$ is the LOS component of $\boldsymbol{B}$ in μG, n_e is in $\mathrm{cm^{-3}}$, and d is the distance to the polarized source in pc. Note that the amount of Faraday rotation is proportional to λ^2, and therefore it is radio frequencies that are the most affected by this phenomenon.

Astrophysical Faraday rotation was first detected by Cooper & Price (1962) using the Parkes 64 m radio telescope towards the radio galaxy Centaurus A. I give their measurement of χ vs. λ^2 for a single pointing towards this source in Figure 1.4. These data are well-fit by a linear model, the slope of which provides the RM of $-65\,\mathrm{rad\,m^{-2}}$, indicating that the LOS B-field is aligned away from the observer.

I note here that to determine RM unambiguously, one requires at least three measurements of χ with sufficient spacing in λ^2. In the absence of such data, there are an infinite set of possible RMs that would fit the data, each separated by $n\pi$ radians ($n \in \mathbb{Z}$) in angle. This effect is referred to as the '$n\pi$-ambiguity'.

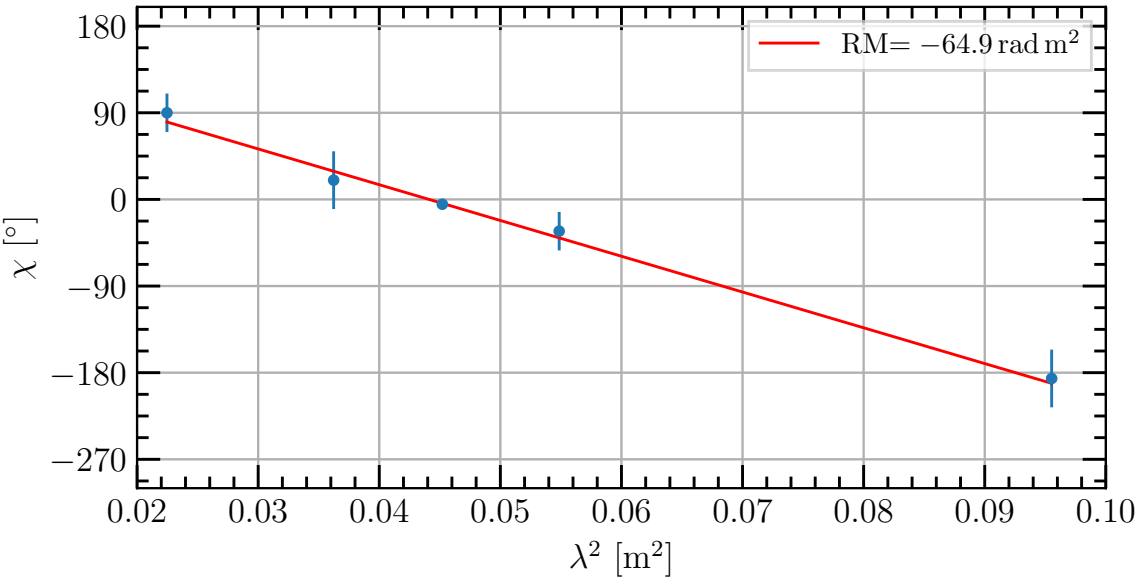

Figure 1.4: Polarization angle χ against wavelength-squared (λ^2) from Cooper & Price (1962), demonstrating the first detection of astrophysical Faraday rotation.

1.2.1.2 Rotation measure synthesis

The simplifying assumption, that emission and rotation occur in separate volumes, will not hold in many cases. This is particularly likely in observations of the Milky Way itself. In the case of mixed emission and rotation in the same volume along the LOS the RM can no longer be used to describe the Faraday rotation. Burn (1966) define the more general counterpart to RM, the Faraday depth (ϕ), as:

$$\chi(d, \lambda) = \chi_0(d) + \phi(d)\lambda^2, \tag{1.14}$$

where $\chi(d, \lambda)$ is the polarization angle from a source at distance d, with initial angle χ_0, and

$$\phi(d) \equiv 0.812 \int_d^0 n_e(r) B_\parallel(r) \mathrm{d}r \left[\mathrm{rad\,m^{-2}}\right]. \tag{1.15}$$

Burn (1966) and Brentjens & de Bruyn (2005) provide the method of measuring ϕ, known as 'RM synthesis'. In this process, we can define the 'Faraday dispersion function' ($F(\phi)$), which describes the complex polarization $\mathcal{P}$ as a function of Faraday depth, and is defined by:

$$\mathcal{P}(\lambda^2) = \int_{-\infty}^{+\infty} F(\phi) e^{2i\phi\lambda^2} \mathrm{d}\phi. \tag{1.16}$$

Taking this relationship naively, we can see that this equation describes a Fourier transform, and that $\mathcal{P}(\lambda^2)$ and $F(\phi)$ are Fourier conjugates. Note that the former is an observable quantity, and the latter would provide us with complete information of the Faraday depth along the LOS, weighted by the polarized emissivity. As such, we want to invert this transform in order to obtain $F(\phi)$ and the information it contains about the magneto-ionic medium:

$$F(\phi) = \frac{1}{\pi} \int_{-\infty}^{+\infty} \mathcal{P}(\lambda^2) e^{-2i\phi\lambda^2} \mathrm{d}(\lambda^2). \tag{1.17}$$

This function is spectral in nature because of the λ^2 term, with peaks in the amplitude of $F(\phi)$ corresponding to Faraday depths along the LOS. Here I will refer to $F(\phi)$ as the 'Faraday spectrum'. As originally noted by Burn (1966), it is non-physical to consider 'negative wavelengths'. At the time, they also lamented that

"unfortunately, this procedure cannot yet be usefully applied to the present data because of the large errors and the small number of wavelengths covered".

Brentjens & de Bruyn (2005) revisited this technique in the light of new radio telescope instrumentation providing many frequency channels over broad bandwidths. They provide a series of equations that allow for the inversion of Equation 1.16 under observational constraints:

$$\tilde{F}(\phi) \approx K \sum_{i=1}^{N} \tilde{\mathcal{P}}_i e^{-2i\phi\left(\lambda_i^2 - \lambda_0^2\right)}, \tag{1.18}$$

$$R(\phi) \approx K \sum_{i=1}^{N} w_i e^{-2i\phi\left(\lambda_i^2 - \lambda_0^2\right)}, \tag{1.19}$$

$$K = \left(\sum_{i=1}^{N} w_i\right)^{-1}. \tag{1.20}$$

Note that the integral terms of Burn (1966) are replaced by sums, specifically discrete Fourier transforms, since we can only observe wavelengths discretely, over N channels. Here $\tilde{F}(\phi) = F(\phi) * R(\phi)$ is the observed Faraday spectrum, and is equal to the true $F(\phi)$ convolved with $R(\phi)$, the 'RM spread function' (RMSF). This terminology is used in analogy to a point spread function in optics. Since we can only measure a discrete and finite set of wavelengths, some information is lost. The RMSF describes the transformation of a δ-function in $F(\phi)$ to the observed $\tilde{F}(\phi)$. Both $\tilde{F}(\phi)$ and the RMSF are weighted by the factor K, which is the sum of the weight (w_i) on each wavelength-squared channel. These weights can be set in a number of ways, but in the simplest case one would set w_i to 1 for all wavelengths that were observed and 0 for all other wavelengths. Finally, the value of λ_0 affects the behaviour of the RMSF. These transforms are, in effect, de-rotating each polarization vector to λ_0^2, where $\lambda_0^2 = 0$ corresponds to the initial polarization angle. Brentjens & de Bruyn (2005) show, however, that setting $\lambda_0^2 = 0$ results in rapid beating of the real and imaginary components of the RMSF, resulting in a rapidly changing phase. This makes it difficult to determine polarization angles as a function of ϕ. Instead, Brentjens & de Bruyn (2005) show that putting λ_0^2 to be the weighted average observed λ^2:

$$\lambda_0^2 = \frac{\sum_{i=1}^{N} w_i \lambda_i^2}{\sum_{i=1}^{N} w_i}, \tag{1.21}$$

results in a more stable phase in the RMSF.

The results of RM synthesis are set by the behaviour of the RMSF. This process is highly analogous to radio aperture synthesis, but reduced to one dimension. The effective resolution of the Faraday spectra ($\delta\phi$) is set by the width of the RMSF at full-width of half maximum (FWHM):

$$\delta\phi \approx \frac{2\sqrt{3}}{\Delta\lambda^2} \tag{1.22}$$

where $\Delta\lambda^2 = \lambda^2_{\text{max}} - \lambda^2_{\text{min}}$ is the bandwidth in λ^2-space, with λ^2_{max} and λ^2_{min} being the maximum and minimum observed wavelengths-squared, respectively. This is equivalent to the resolution of an aperture synthesis telescope being set by its largest baseline. The largest observable value of Faraday depth (ϕ_{max}) is set by the width of the observed λ^2 channels ($\delta\lambda^2$):

$$\phi_{\text{max}} \approx \frac{\sqrt{3}}{\delta\lambda^2} \tag{1.23}$$

This quantity is analogous to the field-of-view being set by the size of the individual telescopes in an aperture synthesis array. Finally, similar to how the smallest baselines of an aperture synthesis telescope set the largest observable angular scale; the smallest observed wavelength-squared sets the maximum scale observable in Faraday depth space:

$$\phi_{\text{max-scale}} \approx \frac{\pi}{\lambda^2_{\text{min}}} \tag{1.24}$$

Note that observing $\lambda^2 = \lambda = 0$, or equivalently an infinite frequency (f), is not possible. As such the 'zero-spacing' Faraday component can never be measured. Observationally, this is not much of a concern, as such a feature would have to be produced by an infinite column of emission. What this does highlight, however, is that observations that cover different frequency bands will have very different strengths and shortcomings. Long wavelength observations provide high precision in Faraday depth, whereas high wavelength observations can resolve broad features in the Faraday spectrum. Ideally, one would want a survey that covers as many wavelengths as possible, from high to low radio frequencies.

1.2.1.3 Features of the Faraday spectrum

Sources that produce a broad feature Faraday spectrum are referred to as 'Faraday thick'. Quantitatively, this is when the extent of a feature ($\Delta\phi$) in the Faraday spectrum is large enough such that $\lambda_0^2\Delta\phi \gg 1$. Such features can be modelled as a mixture of a coherent and turbulent magnetic fields that produces both synchrotron emission and Faraday rotation of background polarized emission (Burn, 1966; Sokoloff et al., 1999). Conversely, a source is 'Faraday thin' if $\lambda_0^2\Delta\phi \ll 1$. Thin sources are well-modelled by a δ-function in ϕ. Sources with a thickness greater than $\phi_{\text{max-scale}}$ will suffer from being resolved out. Whereby, the broad feature is hollowed out, leaving only the front and back edges present in Faraday depth space.

We can attempt to mitigate the observational effects in Faraday tomography using deconvolution techniques. Currently, the most popular algorithm is `RM-CLEAN` (Heald et al., 2009), which acts similarly to the Högbom `CLEAN` algorithm (Högbom, 1974) in aperture synthesis. `RM-CLEAN` replaces $R(\phi)$ with a smooth Gaussian restoring function, thus reducing the effect of side-lobes that are present in the 'dirty' Faraday spectra.

I demonstrate both RM synthesis and `RM-CLEAN`, again using the data of Cooper & Price (1962). Here I use routines provided in RM-tools[1] (Purcell et al., in prep.). In Figure 1.5(a) I show the RMSF of those data. Here we can see that by only having polarization measurements at 5 values of λ^2 leads to strong side-lobes in the RMSF. This is akin to having missing baselines in an aperture synthesis array. The effect of setting λ_0^2 to the weighted mean is also clear, with the real component of the RMSF dominating near the peak and the imaginary component remaining close to 0. Finally, I overlay the `CLEAN` RMSF, which is a simply a Gaussian fit to the primary lobe of the RMSF.

In Figure 1.5(b) I show the results of RM synthesis on the Cooper & Price (1962) data before and after the application of `RM-CLEAN`. The dirty spectrum highlights the need for deconvolution, as many peaks appear which could be mistaken for real features. After deconvolving we can see that a strong peak remains at $\phi = -65 \pm 2\,\text{rad}\,\text{m}^{-2}$, satisfyingly close to the result from fitting χ against λ^2. The second feature at $\phi \sim 120\,\text{rad}\,\text{m}^{-2}$ appears to correspond to a side-lobe in the

[1] https://github.com/CIRADA-Tools/RM

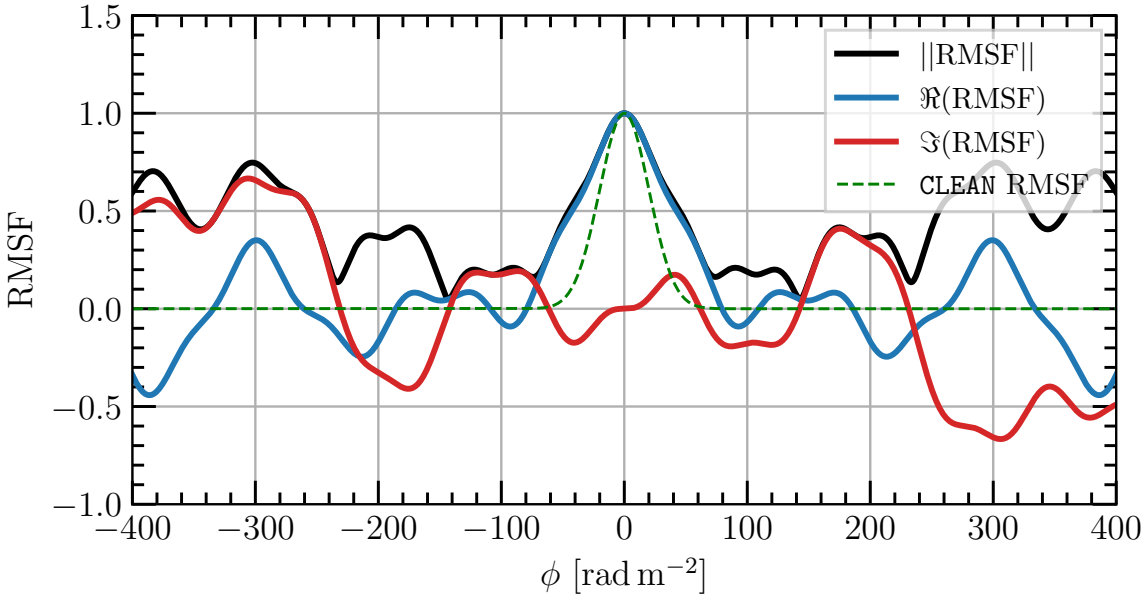

(a)

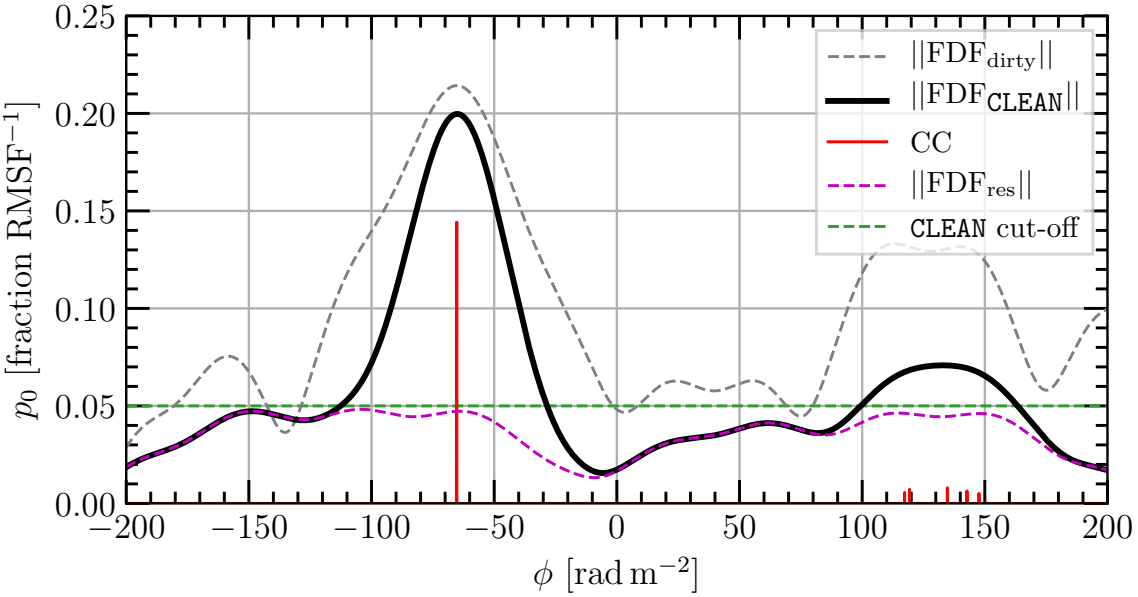

(b)

Figure 1.5: The results applying RM-synthesis to the data of Cooper & Price (1962). ((a)): The rotation measure spread function (RMSF) of the data. Since only 5 data points were used to construct the RMSF, notice that the 'side-lobe' structure is very strong. Also, note that the units of the RMSF are normalized to the peak value. Here I show the absolute value in black, the real ($\Re$) part in blue, and the imaginary ($\Im$) part in red. The fitted `CLEAN` Gaussian RMSF is shown in the green-dashed line. ((b)): The Faraday spectra of the data. The scale of Faraday spectrum is in polarization fraction per RMSF. The 'dirty' (non-deconvolved) spectrum is shown in grey-dashed, the `CLEAN` (deconvolved) spectrum is shown in black, the `CLEAN` components (CC) are in red, the residual spectrum is in purple-dashed, and the `CLEAN` cut-off is shown with a green-dashed line.

RMSF structure, and is reduced significantly after deconvolution. Some tuning of the `RM-CLEAN` may even result in the eradication of this feature. Much like deconvolution in aperture synthesis, `RM-CLEAN` is a sensitive process. Over-`CLEAN`ing can result in false features appearing in the data. As such care must always be taken, particularly with low signal-to-noise data.

1.2.1.4 Observations of radio polarization

Measurements of Galactic Faraday rotation fall into two categories: diffuse images and point-source catalogues. Radio jets and cores from very distance extra-galactic sources appear as point-sources on the radio sky. As a significant source of polarized emission, this radiation propagates through the entire Galactic MIM. Each individual source may have its own intrinsic and inter-galactic Faraday rotation component, but collections of sources can be used together to trace the Galactic foreground (e.g. Oppermann et al., 2012, 2015). Currently, there are two primary all-sky surveys that provide Faraday rotation measurements: the Taylor et al. (2009) catalogue from the NRAO VLA Sky Survey (NVSS) and S-PASS/ATCA from Schnitzeler et al. (2019). The former survey is by far the largest catalogue of RMs, with 37543 sources, but is derived from only 2 closely-spaced frequency measurements and is therefore susceptible to $n\pi$-ambiguities in polarization angle (Ma et al., 2019). Additionally, these sources probe the entire LOS through the Galaxy, which is useful for measuring global, large scale magnetic field properties. Interactions between magnetic fields and the ISM, however, are better traced using diffuse polarimetry.

Diffuse polarized emission has two primary advantages over observations of point-sources. First, where point-source observations sparsely sample the MIM, diffuse observations recover detail at the resolution of the observing telescope. Second, as diffuse polarized emission originates from throughout the Galaxy, three-dimensional detail of the MIM can be revealed if the distance to the emission can be constrained. As reviewed by Landecker (2012), all-sky surveys of the diffuse polarized sky have been produced for some time, from Brouw & Spoelstra (1976) to Wolleben et al. (2006); Testori et al. (2008) (shown in Figure 1.7) and Carretti et al. (2019). The earliest of these surveys, however, sampled the sky sparsely and all sample only a single frequency. The Global Magneto-Ionic Medium Survey (GMIMS, Wolleben

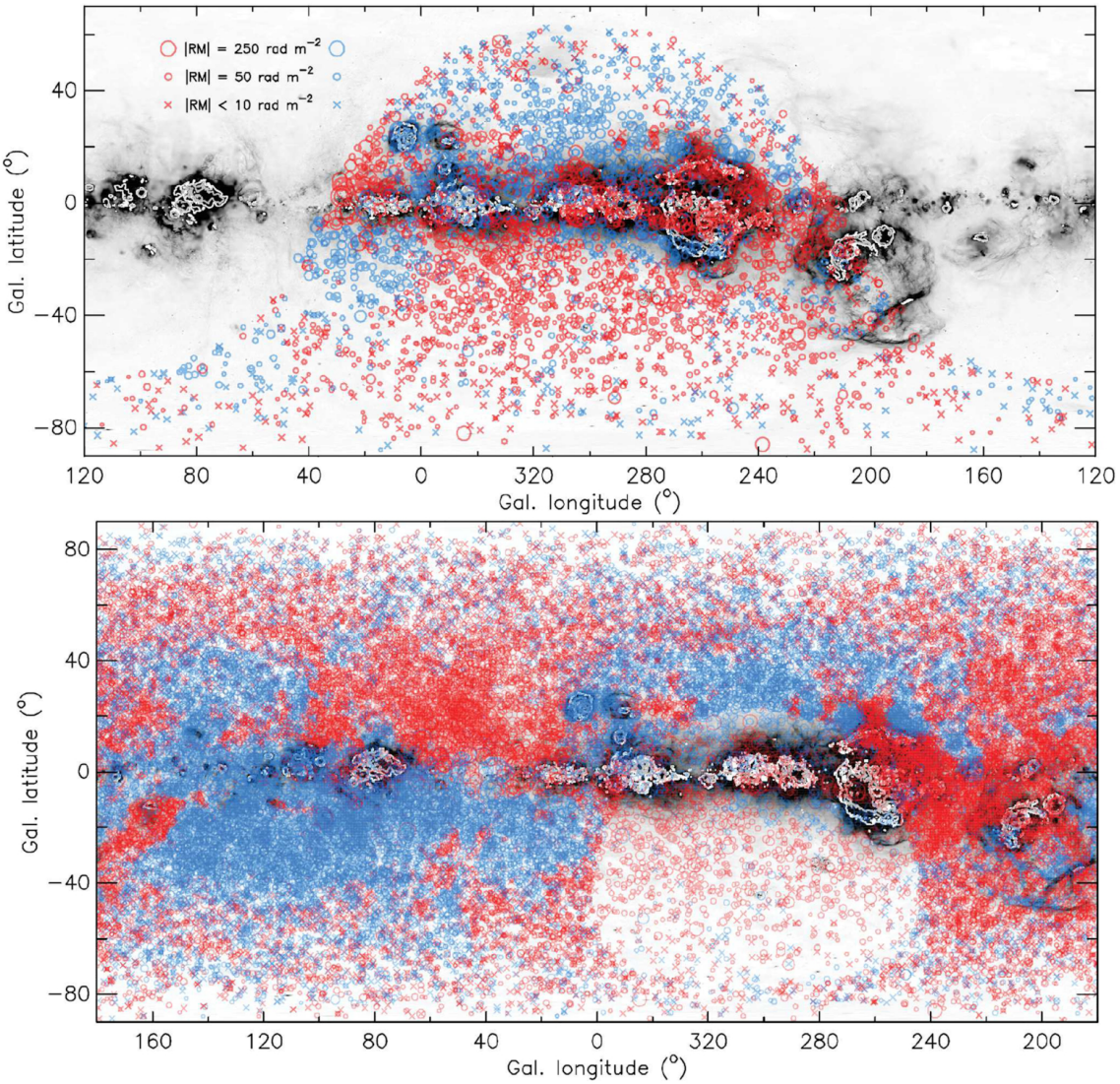

Figure 1.6: Figure 10 from Schnitzeler et al. (2019): Rotation measures (RM) of point-sources across the entire sky in Galactic coordinates. Upper panel: RMs from S-PASS/ATCA. Lower panel: RMs from S-PASS/ATCA and NVSS (Taylor et al., 2009). In both panels the Finkbeiner (2003) H α survey is shown in greyscale.

et al., 2009) seeks to solve these deficiencies and enable 'Faraday tomography', which is RM synthesis mapped across the sky. GMIMS is an ambitious project to map polarized emission across the entire sky from 300 to 1800 MHz. The overall survey has been broken into 6 components in three frequency bands and the Northern and Southern hemispheres. Currently, the high-band Northern (Wolleben et al., 2010a, Wolleben et al. in prep.) and low-band Southern Wolleben et al. (2019) components have been completed. The high-band Southern component (a.k.a. the Southern Twenty-centimeter All-sky Polarization Survey, STAPS, Haverkorn, 2015) has been observed and is currently in the data-reduction phase.

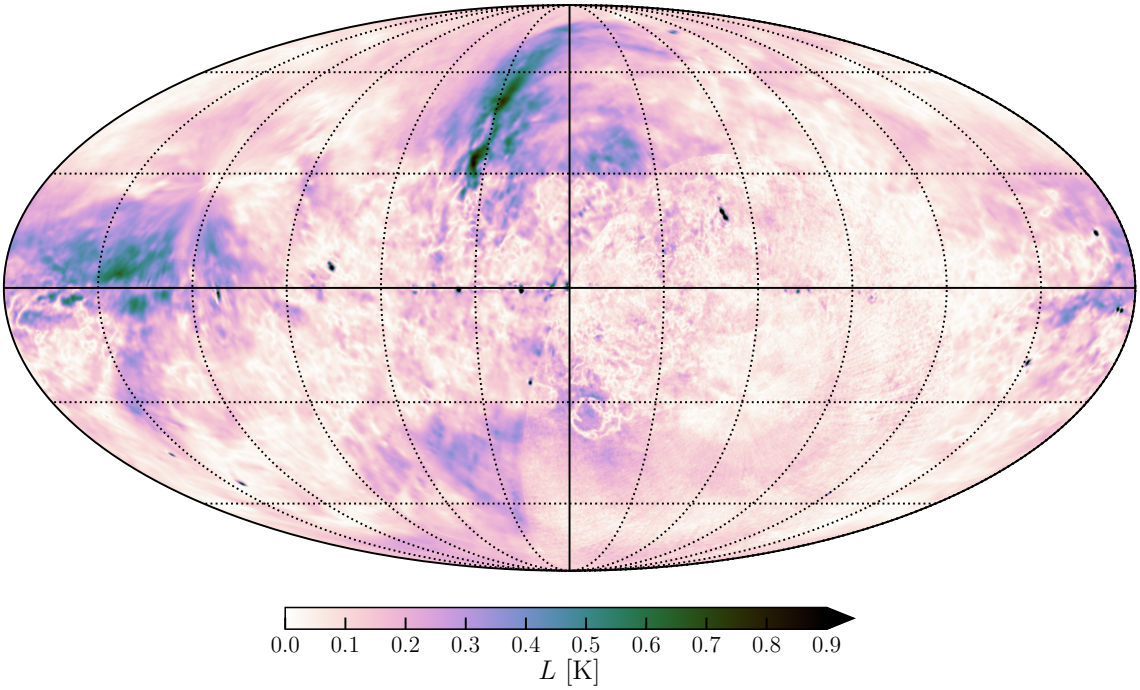

Figure 1.7: Surveys of polarized intensity (L) across the entire sky at 21 cm. This image combines the Northern Wolleben et al. (2009) survey and Testori et al. (2008) in the South for declinations $\delta < -29°$. I show this image in Mollweide projection, centred on $l, b = [0°, 0°]$, with graticules overlaid every 30° in longitude and latitude.

The power of Faraday tomography has most recently been demonstrated, somewhat surprisingly, by low-frequency interferometers such as the Murchison Widefield Array (MWA) and the Low-Frequency Array (LOFAR). One may naively expect diffuse Galactic emission to be depolarised at low radio frequencies; rather, works including Lenc et al. (2016); Jelić et al. (2015); Van Eck et al. (2017, 2019) have revealed diffuse Galactic polarised emission, and its Faraday rotation, in exquisite detail. These diffuse polarized images sometimes showed remarkable correspondence to tracers of the CNM, such as cool H I and three-dimensional dust maps. Conversely, many of the observed features were unique to the polarized observations alone. Such results highlight both the entanglement of the magneto-ionic medium with other components of the Galactic ISM, and the unique information that can be gleaned from polarimetric surveys. These interferometric surveys, however, are currently limited in two ways: First, none have yet imaged the entire diffuse, polarized sky. Second, the frequency coverage of these surveys has limited their sensitivity to broad Faraday depth structures.

The techniques of radio polarimetry are hungry for band-width, perhaps more

so than any other astronomical technique. This hunger has proved to be an observational limitation for some time, both in terms of existing radio astronomy instrumentation and radio-frequency interference. As the power of this technique has been realized, however, considerable effort has been made in the development of receivers and back-end systems that are capable of utilizing radio polarimetry to map the Galactic magnetic field.

1.3 Aim of this thesis

In this thesis I use spectro-polarimetric observations from the Parkes 64 m radio telescope to study the diffuse magneto-ionic medium of the Milky Way Galaxy. The structures of the Milky Way are large on the sky and diffuse in nature, making single-dish observations the only practical way of studying them. Magnetic fields weave their way throughout many parts of the Galactic ISM producing a complex, and sometimes tangled, tapestry. Here I seek to unravel this magneto-ionic fabric into its constituent parts, so that we may better understand our home Galaxy.

1.3.1 Overview of chapters

1.3.1.1 Chapter 2: The low-band Southern Global Magneto-Ionic Medium Survey

The low-band Southern GMIMS component (GMIMS-LBS) was observed over 1800 hours using the Parkes 64 m telescope from 2009 to 2012. Following the calibration and map making process, I became involved in the production of this survey. In this chapter, I describe our work validating the total intensity measurements against existing data, as well as performing self-consistency checks. Following this, I describe how we applied RM synthesis to the all-sky data cubes of GMIMS-LBS. My work presented here is now incorporated into Wolleben et al. (2019), published in the Astronomical Journal.

1.3.1.2 Chapter 3: Magnetic fields of a Galactic supershell

Whilst the data reduction and validation work was underway on GMIMS-LBS, I utilized a sister-survey of GMIMS, the S-band Polarization All Sky Survey (S-PASS,

Carretti et al., 2019). Centred on 2.3 GHz, the diffuse polarization images from this survey reveal remarkable two-dimensional structure in the Galactic magneto-ionic medium on the plane of the sky. In this chapter I present the work from Thomson et al. (2018), published in MNRAS. We identified the signature of a nearby H I supershell, GSH 006−15+7. In order to extract the magnetic field structure we modelled this shell as a foreground screen, utilizing additional data from Wilkinson Microwave Anisotropy Probe (WMAP) and Wisconsin H α Mapper Sky Survey (WHAM-SS). From the line-of-sight magnetic field structure we find the the supershell expended into an ambient field perpendicular to the line of sight. The magnetic field strength we find, $\sim 2\,\mu$G, is dynamically weak, similar to other large, diffuse objects in the ISM. Despite this, these fields still produce a significant signature in the polarization images, highlighting the power of diffuse polarization surveys in investigating the diffuse magneto-ionic medium. In this work there were two major threads I had to untangle. First, I had to measure the amount of Faraday rotation through the shell, which I accomplished using S-PASS and WMAP polarization together. Second, I had to separate the magnetic and ionic components in GSH 006−15+7. Together, this untangling process revealed the magneto-ionic structure of this nearly kiloparsec-scale object.

1.3.1.3 Chapter 4: Faraday tomography in 3D towards an H II region

In this chapter I bring together my work in Chapters 2 and 3, where I use GMIMS-LBS to study the diffuse MIM. In Thomson et al. (2019), published in MNRAS, we found the signature of the large, diffuse H II region Sharpless 2-27 (Sh2-27) in GMIMS-LBS. In this work, we provided a method of determining distance information in polarization observations. This is a common problem in analyzing polarization spectra. We determined that the highly ionized and turbulent medium of Sh2-27 prevents any diffuse polarized emission in the GMIMS-LBS band from propagating through it. Therefore the emission detected in GMIMS-LBS towards this region must arise in the foreground medium. Using the low-frequency, broadband capability of GMIMS-LBS we found a triple-peak Faraday spectrum. Combining this observation with 3D dust maps from the STILISM (Lallement et al., 2014;

Capitanio et al., 2017; Lallement et al., 2018) project, we found that this polarization structure is tied to two foreground neutral clouds and the Local Bubble. Our modelling showed that we have to consider diffuse emission from the entire line of sight, with reduced synchrotron emissivity in the Local Bubble. From this, we determined the line-of-sight structure and strength of the magnetic field in these regions. Here I encountered a surprising entanglement of cold neutral clouds with magnetic structures. Typically, we expect to find the ionized medium causing Faraday rotation. Our results here highlight that magnetic fields permeate throughout the entire ISM, and Faraday tomography is a powerful tool of uncovering them.

1.3.1.4 Chapter 5: The first observational detection of a Faraday caustic

After studying a region of depolarization in Chapter 4, in this chapter we investigated the brightest polarized region in GMIMS-LBS. Here I present the paper, in preparation for submission, describing our analysis of this unusually polarized area of the sky. This region, G150−50, covers nearly 20 square degrees in the Southern Galactic hemisphere. We compared the GMIMS-LBS images to L-band polarization observations from Wolleben et al. (2006) and total intensity surveys from Reich (1982); Reich & Reich (1986); Reich et al. (2001) and Haslam et al. (1982); Remazeilles et al. (2015), and found that G150−50 only appears in polarization and at low frequencies. To explain the appearance of this region, we apply both RM synthesis and model-fitting techniques. Both of these analyses indicated that this region corresponds to a 'Faraday caustic' (Bell et al., 2011). These features arise from along the line-of-sight in the Galactic magnetic field, and correspond to where the line-of-sight field reaches 0 μG. This work is the first observational confirmation of such a feature. The magneto-ionic medium can contain many unique features, and observations of diffuse polarization is often the only way of finding them in the Galactic ISM. My work here highlights how we can bring multiple analysis tools to bear on broad-band polarization data to discover what kind of property is tied up inside of our observations.

1.3.1.5 Chapter 6: Conclusions and future work

Finally, I draw together the works presented in this thesis. Each chapter represents a different way of analysing the magneto-ionic medium, and together they demonstrate the power of diffuse radio polarimetry. I conclude by discussing future work in this field. The techniques I have outlined in this thesis can be employed in future surveys, such as the complete GMIMS, and in observations of diffuse polarization using the Square Kilometre Array and its precursors.

2

The low-band Southern Global Magneto-Ionic Medium Survey

This chapter is published in The Astronomical Journal as part of: Wolleben, M.; Landecker, T. L.; Carretti, E.; Dickey, J. M.; Fletcher, A.; McClure-Griffiths, N. M.; McConnell, D.; **Thomson, A. J. M.**; Hill, A. S.; Gaensler, B. M.; Han, J. -L.; Haverkorn, M.; Leahy, J. P.; Reich, W.; Taylor, A. R., *"The Global Magneto-Ionic Medium Survey: Polarimetry of the Southern Sky from 300 to 480 MHz"*, 2019, ApJ, 158, 44.

As part of the data-processing and validation of this survey, I carried out the work which is now described in this chapter and in Wolleben et al. (2019). I prepared this text, as presented here, for both internal survey reports and for the survey paper itself. Those passages were re-written for the survey paper to match the style and flow of the overall text. In Wolleben et al. (2019), my work here is now incorporated in Sections 5.9 and 6.1.

2.1 Introduction

We used the Parkes 64 m Telescope to observe the entire Southern sky (up to declination +20°). These data were taken as a contribution to the Global Magneto-Ionic Medium Survey (GMIMS), with the aim to cover the Southern, low-frequency component of the survey (GMIMS-LBS). We observed over 1800 hours, in 12 sessions from 2009.8 to 2012.5. Our observations were carried out at night using a wideband feed and receiver, and covered a frequency range of 300 to 900 MHz. Radio-frequency interference (RFI) was severe, and only data in the range 300 – 480 MHz is usable. We made azimuth scans, between 110° and 250° in length, with the telescope moving at a rate of 15° per minute. The survey is absolutely calibrated in intensity, based on an assumed flux density ($S = 1450$ Jy) and spectral index ($\alpha = -0.299$, where $S \propto \nu^{\alpha}$), for Taurus A (Cohen et al., 2007). We consider the amplitude scale to be correct within 7%. The calibration of polarization angle is tied to earlier surveys of the Southern (Mathewson & Milne, 1965) and Northern (Brouw & Spoelstra, 1976) skies. We estimate that the probable error in polarization angle is 15°.

Our initial steps in data reduction were excision of RFI, removal of gain drifts and instrumental bandpass, removal of instrumental polarization, and correction for Faraday rotation in the ionosphere. The numerous (~ 3000) survey scans were reconciled by a 'basketweaving' algorithm (Haslam et al., 1970; Haslam et al., 1981) which iteratively adjusted the baselevel of scans taking into account the 2×10^6 scan crossings.

2.2 Quality of the total intensity spectrum

We compare our data with comparable existing surveys in order to assess the quality of our independent calibration, and to estimate the errors in our own survey. We first examine the total intensity scale of our observations, measured as Stokes I.

We compare our data against Haslam et al. (1982) survey, an absolutely calibrated and fully sampled image of the whole sky at 408 MHz, observed with the Parkes 64 m Telescope and Lovell Telescope. Conveniently, the frequency of the Haslam et al. (1982) survey sits in the middle of our observed band and, since it

was observed with the same telescope as GMIMS-LBS, matches our $51'$ resolution at 408 MHz. To compare these surveys we employ the 'T-T plot' technique (Costain, 1960), plotting the brightness temperature (T) from one survey against the other for each direction on the sky. Using this technique, one fits a linear model to the data. The intercept of this model provides any absolute offsets between the two datasets. The slope of the model will give either the ratio between the datasets if they are at the same frequency (ν), or, if the frequencies are different, the brightness temperature spectral index β, where $T \propto \nu^{\beta}$.

In Figure 2.1 we show the T-T plot of GMIMS-LBS against the Haslam et al. (1982) survey. Here we have averaged 7 GMIMS-LBS channels to match the 3.5 MHz bandwidth from Haslam. From fitting a linear model to the T-T plot we find a slope 1.09 and an intercept of -19 K. The latter result is expected from our basketweaving process, which subtracts the minimum value from the data at each frequency, whereas the minimum value in the Haslam survey is $\sim 13 \pm 3$ K. The slope of the T-T plot indicates that GMIMS-LBS is $\sim 9\%$ higher than Haslam, on average. This difference is small enough for us to conclude that our independent calibration method was successful. It is difficult to account for this difference, however, given that the calibration methods of Haslam are entirely different from ours.

We now turn our attention to the rest of the GMIMS-LBS band. We apply the T-T plot technique across the GMIMS-LBS band, sampling seven 30 MHz frequency intervals from 290.25 to 470.25 MHz (which we show in Figure 2.2). The slope of the T-T plots between these intervals should correspond to the spectral index of the Galactic, extended, non-thermal emission with relatively little thermal contamination.

At each of these intervals we take the mean of 5 channels, centred on the frequency interval, giving a bandwidth of 2.5 MHz. This boosts the signal-to-noise ratio of each sub-band and helps to minimize RFI flagging a single channel might contain. GMIMS-LBS was observed through heavy RFI contamination, and we show the fraction of flagged pixels in Figure 2.2. In Figure 2.3 we show the T-T plot results for each frequency pair. Excluding the higher and lower intervals, all the T-T plots show tight correlations, with correlation coefficients of > 0.994. The bands sampled at 290.25 and 470.25 MHz demonstrate weaker correlation, but also

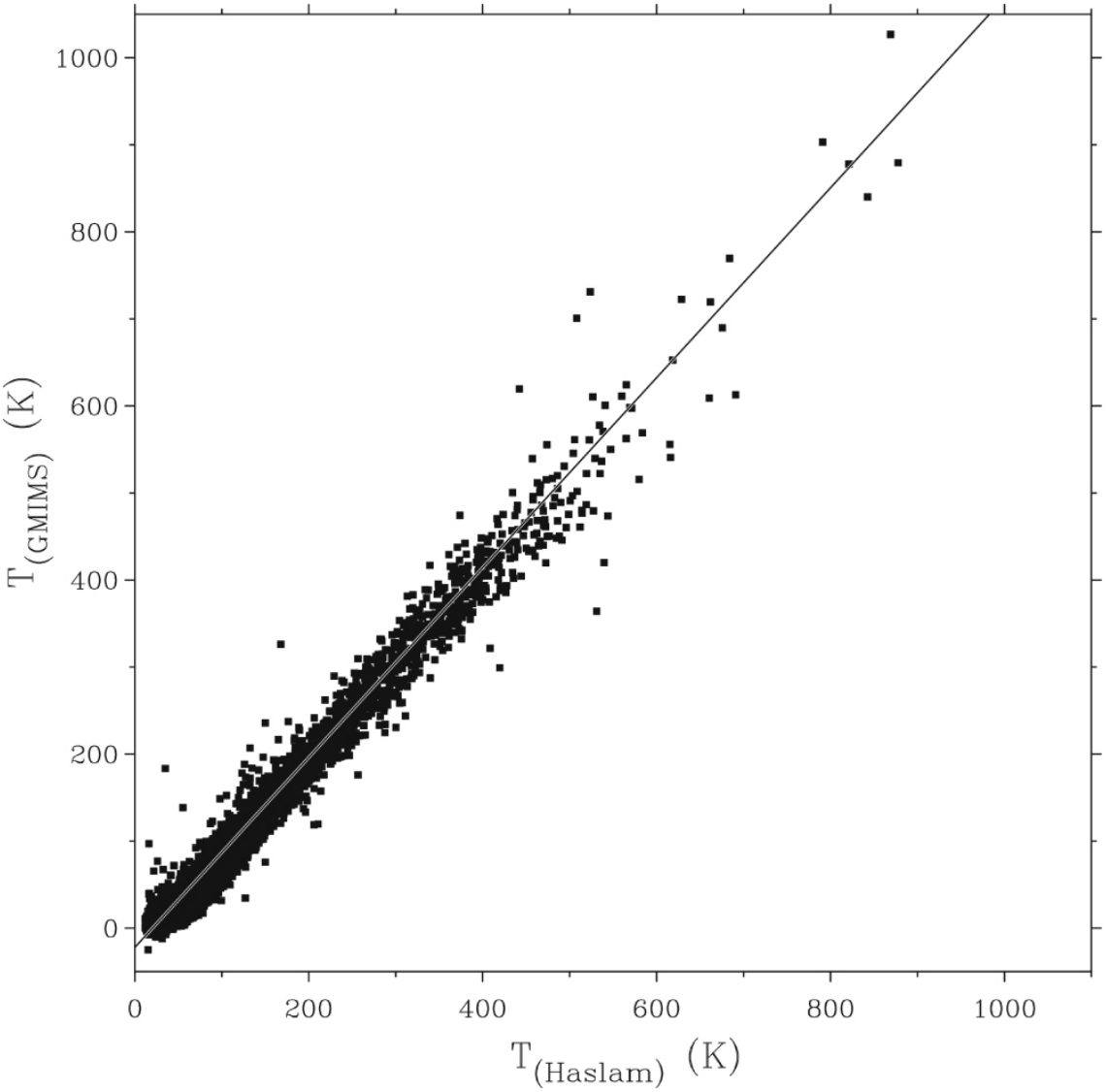

Figure 2.1: The 'T-T plot', comparing the Stokes I brightness temperature from Haslam et al. (1982) against GMIMS-LBS over the entire GMIMS-LBS area. We show the measured Stokes I brightness temperature (T) from each survey in black points. We show the fitted linear model as the black line, which has a slope of 1.09 and an intercept of -19 K.

suffer from stronger RFI contamination with 86% and 60% of the pixels flagged in these bands, respectively.

We can now compare the slopes from each T-T plot to known values obtained from other surveys. Our data indicate spectral indices of ~ -0.9 to -3.7. In the Northern sky, Sironi (1974) found $\beta \approx -2.5$ for data from 151 to 408 MHz, and (Webster, 1974) gives $\beta \approx -2.8$ in data between 408 and 1407 MHz. Additionally, Landecker (1969) found $\beta \approx -2.8$ in the Southern sky in the range 408 to 720 MHz. We note that the spectral index derived from a T-T plot in a narrow frequency range

is very sensitive to small changes in the slope. We find that we can correct all our T-T plots to obtain a spectral index $\beta \approx -2.8$ through multiplying by a factor in the range 0.994 to 1.178, even at the heavily-flagged start and end of the band. It is important to note that we could choose many correction factors in the range 0.9 to 1.1 and obtain spectral indices of -2.4 to -3.2.

All together, we consider that these results show our data are absolutely calibrated in the band 300 to 480 MHz. Our data are accurate within a factor 10%. The polarization intensity data, which was processed identically to the total intensity spectrum, is therefore also correct within the same factor.

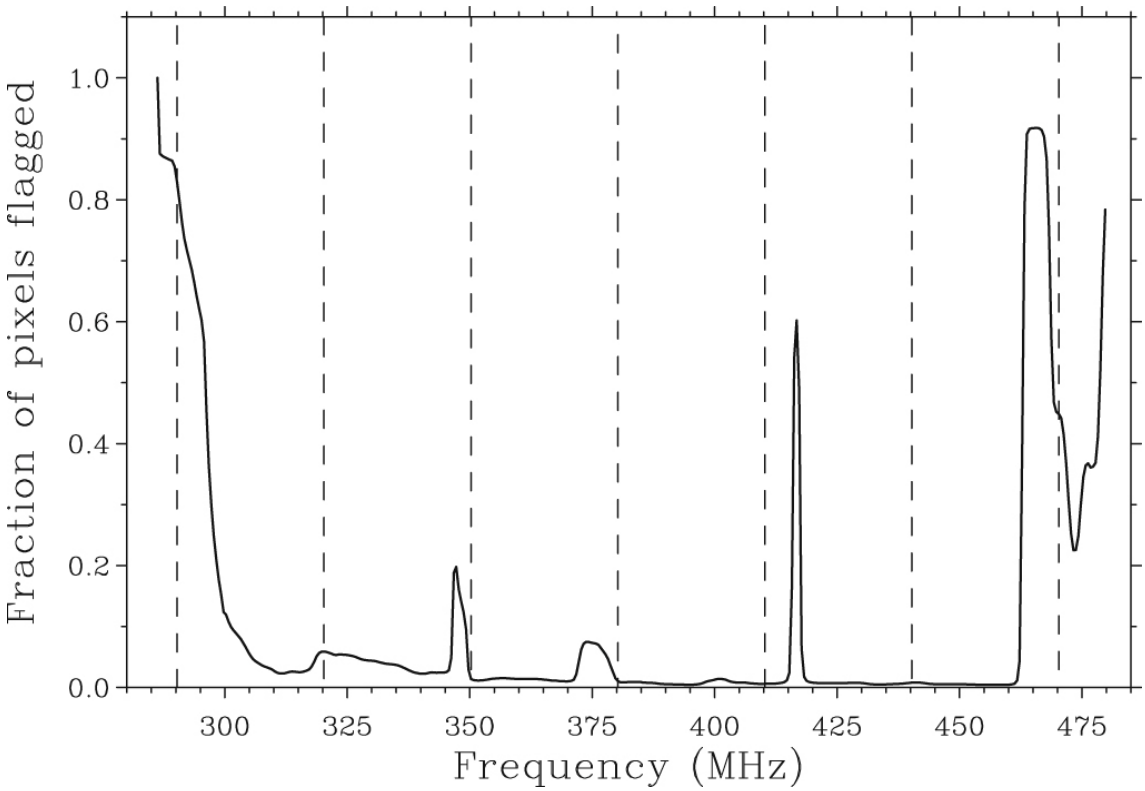

Figure 2.2: Solid: The fraction of pixels across the entire sky, as seen by GMIMS-LBS, flagged due to RFI across the GMIMS-LBS band. Dashed: The frequencies selected for the T-T plot comparison shown in Figure 2.3.

2.3 Application of Faraday Tomography

Faraday tomography is the rotation measure (RM) synthesis process (Burn, 1966; Brentjens & de Bruyn, 2005) applied across the sky. Before performing Faraday tomography on GMIMS-LBS we spatially smooth the spectral cubes to 1.35°, which is

the beamwidth of the telescope at 300 MHz. This is critical, as the Fourier transform-like RM synthesis process adds together channels at multiple frequencies. We also excise data below 300.25 MHz, as data in the frequency range of the GMIMS-LBS suffer from significant RFI flagging.

We use the RM-TOOLS[1] software package to perform both Faraday tomography and `RM-CLEAN` (Heald et al., 2009) deconvolution. The inputs to Faraday tomography are the datacubes of the Stokes Q and U brightness temperature, observed in each of the frequency channels. RM-TOOLS then returns the Stokes Q and U cubes as a function of Faraday depth (ϕ), as well as a cube of the complex RM spread function (RMSF) per pixel in the map. We specify an output channel-spacing in Faraday depth of $0.5\,\mathrm{rad\,m^{-2}}$ and a range in Faraday depth of $|\phi| \leq 100\,\mathrm{rad\,m^{-2}}$. We choose $0.5\,\mathrm{rad\,m^{-2}}$ as the spacing because it is a simple divisor and is about 8% of the full-width-at-half-maximum (FWHM) of the primary RMSF lobe. Additionally, emission with Faraday depths much higher than $\pm 100\,\mathrm{rad\,m^{-2}}$ is likely to be depth-depolarized at these frequencies.

The output of the RMSF per pixel is crucial for use with GMIMS-LBS. RM-TOOLS has the option to compute the RMSF per pixel numerically, taking into account if any spectral flagging has occurred. The nature of our survey method, in combination with strong RFI, results in varying amounts of flagging occurring in different areas of the sky. In other words, we do not uniformly sample the observed bandwidth across the entire sky. This results in an RMSF that will vary in width spatially. We also perform a Gaussian fit to the primary lobe of the RMSF per pixel to measure the width of the RMSF for each pixel in the map. This has consequences for both the deconvolution process (specifically in restoration) and the interpretation of the intensity value in the Faraday spectra. In Figure 2.4 we show examples of the RMSF for our observations. We compare the average RMSF across the map, as well as the widest and narrowest RMSFs from the map, with the RMSF that would occur if the entire bandwidth from 300-480 MHz were sampled with 500 kHz channels. The primary effect of the missing channels in frequency space on the RMSF is to create a secondary ripple. This ripple generates side-lobes in the RMSF, with a first peak around $\pm 90\,\mathrm{rad\,m^{-2}}$, at a height of $\sim 4\%$ of the primary beam. We also note that

[1] https://github.com/crpurcell/RM-tools

the width of the median RMSF is matched more closely to the narrowest RMSF, rather than the widest; showing that, across the majority of the sky, the width of the RMSF is mostly consistent.

We input the 'dirty' Q and U Faraday cubes, along with the fitted RMSF cube, into the `RM-CLEAN` component of RM-TOOLS. We `CLEAN` to a noise threshold of 60 mK, the RMS noise level in the survey, with a loop gain of 0.1, and an iteration cut-off of 1000. Figure 2.5 shows the peak polarized intensity (PI) for each Faraday spectrum in an all-sky map. The structure shown in this map is unlike that of any other tracer. We note, however, that the bright structure along the Galactic plane is likely due to leakage from Stokes I.

In Figure 2.6 we show both the `CLEAN` and dirty spectra for three lines of sight (indicated on Figure 2.5). Each LOS shown demonstrates a different behaviour of the sidelobes of the RMSF. The first panel shows what we might expect from a Faraday thin component, with symmetric sidelobes in the dirty spectrum. This feature is fit well by a single primary `CLEAN` component which removes nearly all of the sidelobe structure. In the second panel the feature is clearly broad, with the dirty spectrum showing a long tail towards positive ϕ. This asymmetric structure is likely due to interference between the sidelobes of the dirty spectrum. Strikingly, the `CLEAN` spectrum shows a tail towards negative ϕ, with the sidelobe structure almost entirely removed. Finally, the third panel shows a complex spectrum with a weaker signal. Most notably, the relative heights of the three primary peaks in the spectrum change after `RM-CLEAN`. Each of these examples shows the necessity of performing deconvolution before attempting to analyze the Faraday spectra from GMIMS-LBS.

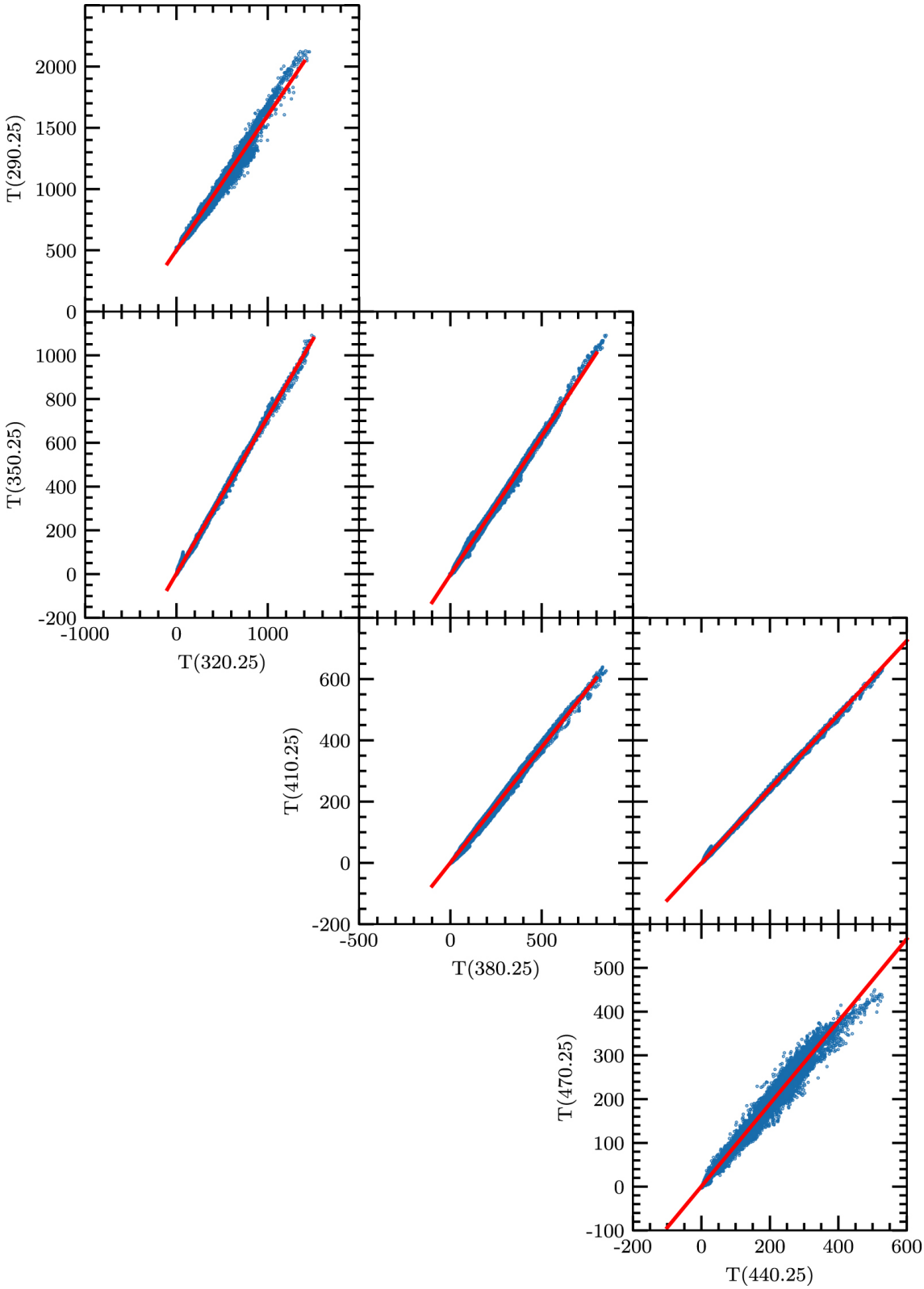

Figure 2.3: T-T plots derived from sub-bands of the GMIMS-LBS total intensity spectrum. Here we select 7 frequency intervals from 290.25 to 470.25 MHz (shown in Figure 2.2), each with a 2.5 MHz bandwidth. In blue we show the Stokes I brightness temperature (T) on the sky for each pixel between at each frequency interval. In red we show the linear model fitted to the data, the slope of which provides the brightness temperature spectral index β.

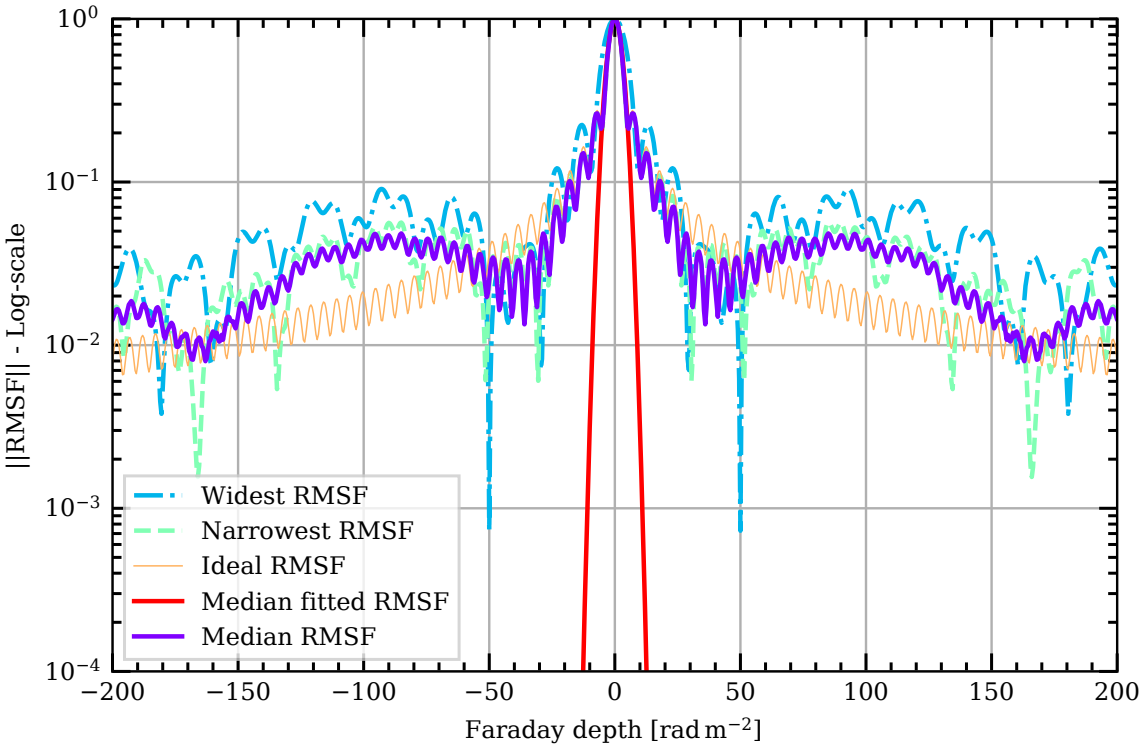

Figure 2.4: The RMSF for GMIMS-LBS. The range in Faraday depth is twice the selected range for the purpose of deconvolution. Purple, thick solid – The median RMSF across the map. Orange, thin solid – The ideal RMSF if the full band-width were sampled from 300-480 MHz in 500 kHz channels. Green, dashed – The RMSF for the pixel with the narrowest FWHM. Blue, dash-dot – The RMSF for the pixel with the widest FWHM. Red, solid – The median Gaussian RMSF fitted to the RMSF in each pixel.

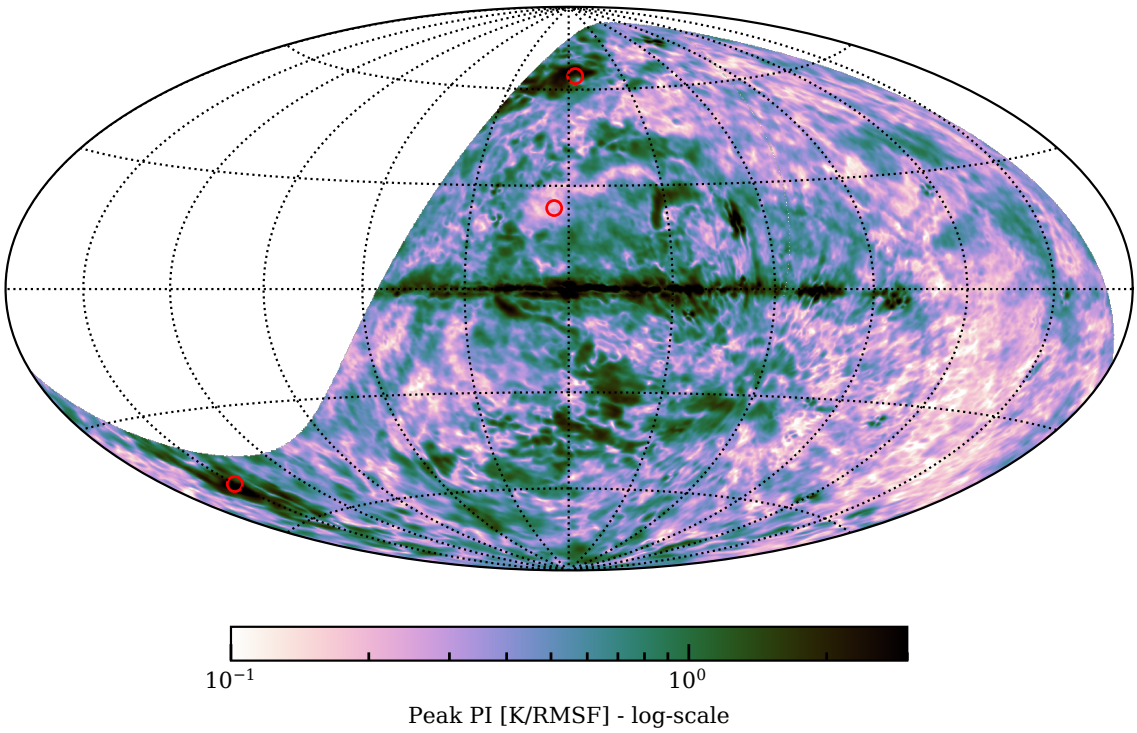

Figure 2.5: Polarized intensity at the peak in the Faraday spectra across the entire sky in Aitoff projection, centred on $l, b = [0, 0]^\circ$. Red circles – Lines of sight as shown in Figure 2.6. White, dashed area – region to be shown in subsequent maps. We overlay graticules every 30° in longitude and latitude.

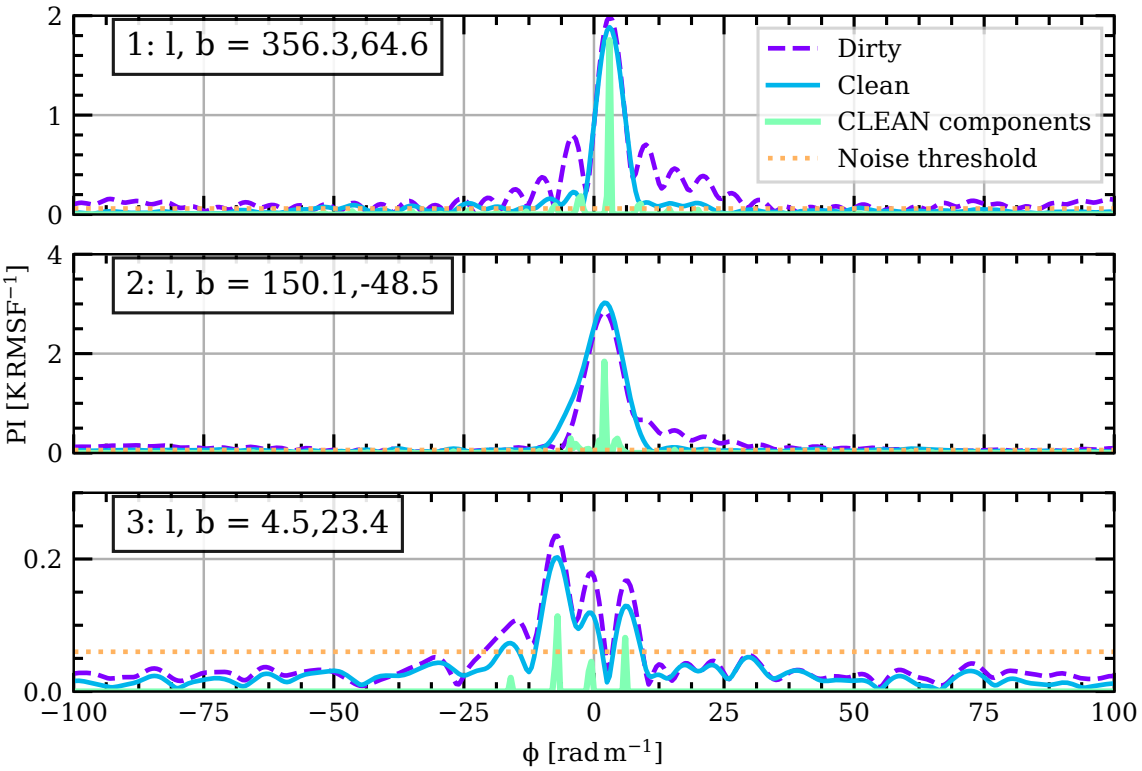

Figure 2.6: Faraday spectra for three lines-of-sight in the map. Purple, dashed – Dirty spectrum. Blue, thin solid – `CLEAN`ed spectrum. Green, thick solid – `CLEAN` components. Red, dotted – CLEAN noise threshold of 60 mK.

3

Magnetic fields of a Galactic supershell

This chapter is published in Monthly Notices of the Royal Astronomical Society: **Thomson, A. J. M.**, McClure-Griffiths, N. M., Federrath, C., Dickey, J. M., Carretti, E., Gaensler, B. M., Haverkorn, M., Kesteven, M. J., & Staveley-Smith, L., *"Ghost of a shell: magnetic fields of Galactic supershell GSH 006 - 15 + 7"*, 2018, MNRAS, 479, 5620.

3.1 Abstract

We identify a counterpart to a Galactic supershell in diffuse radio polarisation, and use this to determine the magnetic fields associated with this object. GSH 006−15+7 has perturbed the polarised emission at 2.3 GHz, as observed in the S-band Polarisation All Sky Survey (S-PASS), acting as a Faraday screen. We model the Faraday rotation over the shell, and produce a map of Faraday depth over the area across it. Such models require information about the polarised emission behind the screen, which we obtain from the Wilkinson Microwave Anisotropy Probe

(WMAP), scaled from 23 GHz to 2.3 GHz, to estimate the synchrotron background behind GSH 006−15+7. Using the modelled Faraday thickness we determine the magnitude and the plane-of-the-sky structure of the line-of-sight magnetic field in the shell. We find a peak line-of-sight field strength of $|B_{\parallel}|_{\rm peak} = 2.0^{+0.01}_{-0.7}\,\mu$G. Our measurement probes weak magnetic fields in a low-density regime (number densities of $\sim 0.4\,{\rm cm}^{-3}$) of the ISM, thus providing crucial information about the magnetic fields in the partially-ionised phase.

3.2 Introduction

H I shells, bubbles, supershells, and superbubbles are large structures in the interstellar medium (ISM) blown out by hot OB star clusters and supernovae. Both a supernova and the winds from a massive star in its main sequence lifetime will each inject around 10^{51}-10^{53} ergs into the ISM. These winds and shocks ionise what will become the cavity of the shell, and sweep out the neutral material (McClure-Griffiths et al., 2002). It is now understood that these objects are strongly influenced by magnetic fields in their formation (Tomisaka, 1990, 1998; Ferriere et al., 1991; Slavin & Cox, 1992; Ntormousi et al., 2017; Gao et al., 2015; Stil et al., 2009). Magnetic fields both oppose the expansion of the shell from the exterior, and prevent the collapse of the swept up shell walls (Ferrière, 2001). H I shells have been discovered throughout our Galaxy (Hu, 1981; Koo et al., 1992; Maciejewski et al., 1996; Uyaniker et al., 1999; McClure-Griffiths et al., 2000, 2002, 2006a; Pidopryhora et al., 2007; Heiles, 1979), as well as external galaxies. These objects play a large role in determining the dynamics, evolution, and overall structure of the ISM (McClure-Griffiths et al., 2002).

Supershells and superbubbles are the largest classification of H I shells, with radii between 10^2 and 10^3 pc (Heiles, 1979). Such objects occupy an intermediate size-scale within the ISM; a scale at which the role of magnetic fields in the magneto-ionic medium (MIM) is not well understood. Supershells are most commonly found in H I surveys, and appear as cavities in the neutral hydrogen (e.g. McClure-Griffiths et al., 2002); but they can also have multi-wavelength properties. Supershells can have associated emission in H α, soft X-rays, far ultra-violet, polarised radio continuum,

and 100 μm (Heiles, 1979; Moss et al., 2012; Heiles et al., 1999; McClure-Griffiths et al., 2001; Heiles, 1984; McClure-Griffiths et al., 2002; Ehlerová & Palouš, 2005, 2013; Suad et al., 2014; Jo et al., 2011; Reynolds et al., 1998; Boumis et al., 2001; Jo et al., 2015). It is thought that once bubbles expand far enough to break out of the gas of the Galactic plane, the shell breaks open into a Galactic chimney, allowing the flow of hot gas into the halo (Norman & Ikeuchi, 1989). This transition from bubble to chimney is slowed by the presence of magnetic fields, which tend to confine the expanding shell in the disc (Tomisaka, 1998).

A powerful method for probing the magnetic fields of the ISM is the study of Faraday rotation. This phenomenon describes how the polarisation angle (PA) of a linearly polarised wave will rotate as the wave propagates through a MIM. Faraday rotation is measured from the linear Stokes parameters, Q and U. Following Burn (1966) and Brentjens & de Bruyn (2005), these can be parametrised as the complex polarisation, $\mathcal{P}$:

$$\mathcal{P} = Q + iU = \mathrm{PI}e^{2i\mathrm{PA}} \tag{3.1}$$

From this, the polarised intensity (PI) and the polarisation angle can therefore be defined as:

$$\begin{aligned} \mathrm{PI} &= \sqrt{Q^2 + U^2} \\ \mathrm{PA} &= \frac{1}{2}\arctan\left(\frac{U}{Q}\right) \end{aligned} \tag{3.2}$$

The amount of Faraday rotation at a wavelength λ is described by the Faraday depth (ϕ) times λ^2:

$$\phi(L) \equiv 0.812 \int_0^L n_e B_\parallel dr \,\mathrm{rad\,m^{-2}}, \tag{3.3}$$

where $B_\parallel$ is the line-of-sight magnetic field in μG, n_e is the electron density in cm^{-3}, and r is the distance along the line of sight integrated through the Faraday rotating medium with length L in pc. The sign of $B_\parallel$ is taken to be positive when the field is aligned towards the observer and vice-versa. In the simplest Faraday rotation case, where all the emission is in the background and all the Faraday rotation occurs in the foreground, the Faraday depth is given by the rotation measure (RM):

$$\mathrm{RM} = \frac{\Delta\mathrm{PA}}{\Delta(\lambda^2)} \tag{3.4}$$

This also assumes no depolarisation occurs along the line of sight. A method of obtaining Faraday depth in more complex scenarios is described in Brentjens & de Bruyn (2005).

Despite the important role magnetic fields play in the Galactic ISM, several mysteries remain unresolved. Firstly, as summarised by Han (2017), the magnetic fields of a number of extended diffuse objects have been studied. However, obtaining the complete scale and structure of the magnetic fields associated with these objects is difficult. This arises as a result of both the methods used to measure these fields, and line-of-sight confusion from other magneto-ionic objects. Studies of RMs from both extragalactic point sources and pulsars can suffer from line-of-sight field reversals and confusion, and intrinsic Faraday rotation. These line-of-sight effects are a particular concern towards the Galactic plane. In this sense, diffuse polarisation studies have a particular advantage in revealing large-scale, extended structures.

GSH 006−15+7 is a recently discovered Galactic supershell located near the Galactic plane (Moss et al., 2012). This supershell was discovered in H I observations with a central velocity around $v_{\rm LSR} \approx 7\,{\rm km\,s^{-1}}$, and subtends about 25 deg on the sky. Moss et al. (2012) constrain the age and distance to this object at $15 \pm 5\,{\rm Myr}$ and $1.5 \pm 0.5\,{\rm kpc}$, respectively; this gives the shell an approximate diameter of $670 \pm 220\,{\rm pc}$, making it one of the largest discovered H I shells near the Sun. From their analysis, Moss et al. (2012) find that GSH 006−15+7 is likely in a break-out phase between a supershell and a chimney structure.

In this paper we present the counterpart to GSH 006−15+7 in diffuse polarised radio emission data at 2.3 GHz. The shell appears as a 'shadow' in polarised emission, and shows evidence of Faraday rotation of background synchrotron radiation. The data we use in this analysis are described in Section 3.3. In Section 3.4 we discuss this morphological association found in diffuse polarisation at 2.3 GHz. We continue to use these polarisation data to model the Faraday rotation through GSH 006−15+7 as a Faraday screen, following Sun et al. (2007) and Gao et al. (2015). From this, in Section 3.5 we constrain both the magnitude and the plane-of-sky structure of the line-of-sight magnetic fields associated with GSH 006−15+7. We use this information to estimate the thermal and magnetic pressures within the Galactic supershell. This dynamical information, as well as the magnetic field

strengths themselves, will aid in the future modelling of supershells and the ISM, as well as in our overall understanding of ISM magnetohydrodynamics. Our conclusions are given in Section 3.6.

3.3 Data

3.3.1 Diffuse H I Emission

3.3.1.1 Galactic All-Sky Survey

We make use of H I data from the third release of the Parkes Galactic All-Sky Survey (GASS, McClure-Griffiths et al., 2009; Kalberla et al., 2009), now incorporated in HI4PI (HI4PI Collaboration et al., 2016b). GASS is a fully-sampled survey of H I emission over the entire sky south of declination zero with an angular resolution of 14.4 arcmin. The survey was conducted with the Parkes radio telescope using the 13-beam multibeam receiver. The data cover the velocity range $-468 \leq v_{LSR} \leq 468$ km s^{-1} with a velocity resolution of 1 km s^{-1}and a typical RMS noise of 57 mK. In the third data release of GASS used here, the calibration and stray radiation correction were refined by Kalberla & Haud (2015). We use the GASS data to extract velocity separated H I emission of GSH 006−15+7.

3.3.2 Radio Continuum Polarisation

3.3.2.1 S-band Polarisation All Sky Survey

The S-band Polarisation All Sky Survey (S-PASS, Carretti et al. 2013, Carretti et al. in preparation) was completed in 2010, and provides a highly sensitive polarisation (Stokes Q and U) map of the Southern sky at 2.3 GHz. The survey was conducted using the Parkes 64 m Telescope with its 'Galileo' receiver and covers the Southern sky at declinations $\delta < -1$ deg. This receiver operates in S-Band (13 cm) and is sensitive to circularly polarised radiation; allowing for the linear Stokes parameters, Q and U, to be measured. Table 3.1 lists the observational parameters for S-PASS. Initial morphological analysis was conducted by Carretti et al. (2013), and here we provide additional morphological descriptions; specifically we find a morphological

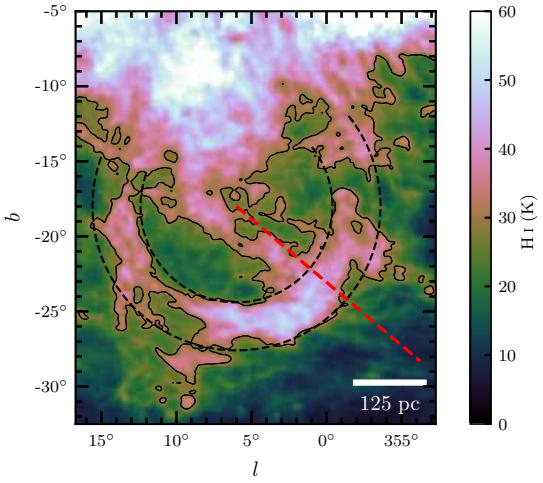

Figure 3.1: GASS – Brightness temperature of the H I 21 cm line in the region of the GSH 006−15+7 shell at $v_{LSR} = 6.6\,\mathrm{km\,s^{-1}}$. All maps are given in Galactic longitude and latitude (l, b). Contour given at 30 K, which well outlines the H I emission associated with the shell. The black dashed lines give the approximate inner and outer bounds of the shell; approximately matching the 30 K contour. The scalebar gives the approximate size scale assuming a distance of 1.5 kpc. The red dashed line in corresponds to the profile given in Figure 3.3. This profile was chosen to match the one given in Figure 3.2(a).

correlation between the structure of GSH 006−15+7 in H I and the structure found in Stokes Q and U from S-PASS.

S-PASS supplies a number of significant improvements over previous polarisation surveys. Observations of polarised emission at 2.3 GHz are inherently less prone to depolarisation effects (Burn, 1966; Sokoloff et al., 1999) with respect to lower frequencies. This higher observing frequency allows for greater angular resolution, with S-PASS presenting a gridded angular resolution (full width at half maximum FWHM) of 10.75'. The original data resolution was 8.9', these were then smoothed with a Gaussian window of FWHM = 6' producing a map with a final resolution of 10.75'. Additionally, a much lower system temperature was achieved with respect to previous surveys in the same band. For example, S-PASS achieves a factor of two improvement over the Parkes 2.4 GHz polarisation survey by Duncan et al. (1997), and they observed only a belt across the Galactic Plane ($|b| < 5°$) not covering the area subject of this work. We use the S-PASS Stokes Q and U maps for computation of the RM associated with GSH 006−15+7.

Table 3.1: Observational parameters of S-PASS (e.g. Carretti et al., 2013) and WMAP K-band (Bennett et al., 2013). * – Map noise is per observation.

Property	Symbol	S-PASS	WMAP
Reference frequency	ν	2307 MHz	22.69 GHz
Bandwidth	$\delta\nu$	184 MHz	4 GHz
Telescope beamwidth	$\mathrm{FWHM_{tel}}$	8.9′	0.88 deg
Map beamwidth	$\mathrm{FWHM_{map}}$	10.75’	–
Map RMS noise (Stokes Q/U)	σ	$\lesssim$1 mJy beam^{-1}	1.435 mK* (Q/U) – 6.00 mK* (I)
Gain (Jy/K) at ν	A	1 mJy = 0.58 mK	–
System temperature	T_{sys}	$\approx$ 20 K	29 K

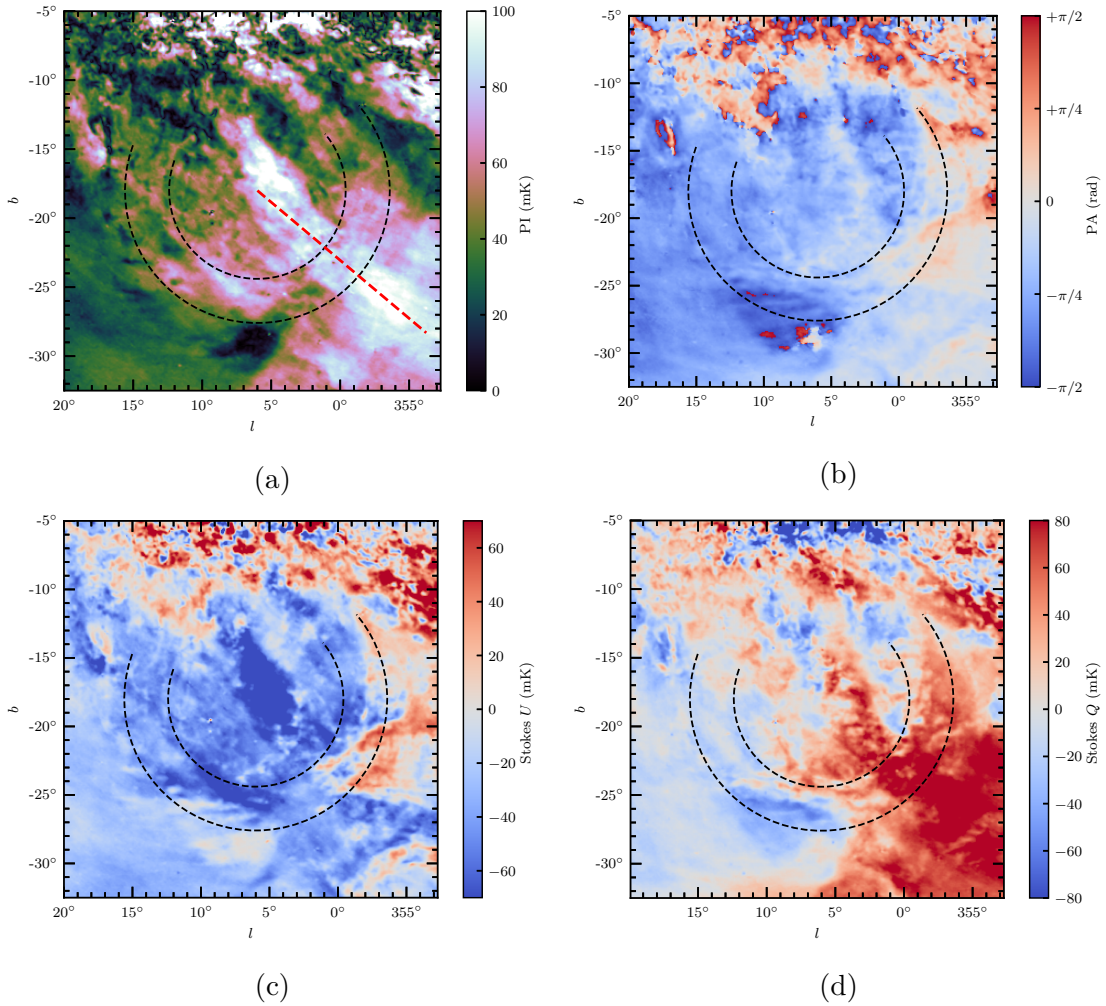

Figure 3.2: Maps of S-PASS polarisation in the region of GSH 006−15+7. (a) S-PASS - polarised intensity. The red dashed line corresponds to the profile given in Figure 3.3. This profile runs along the ridge of the polarised emission of the Fermi bubble from the centre of the shell region. (b) S-PASS - polarisation angle in radians. (c) S-PASS - Stokes U. (d) S-PASS - Stokes Q. In each panel, the black dashed lines give the approximate inner and outer bounds of the lower part of the shell.

3.3.2.2 Wilkinson Microwave Anisotropy Probe

The Wilkinson Microwave Anisotropy Probe (WMAP) survey released its final, 9-year data in 2013 (Bennett et al., 2013). The observational properties of WMAP are also summarised in Table 3.1. The project was focused on measuring cosmological parameters and the cosmic microwave background (CMB), however, the foreground data provides invaluable Galactic information. In particular, WMAP K-band, centred on 23 GHz, gives a calibrated, whole-sky map of polarised synchrotron emission at high frequency. Discussion of the structure present in the WMAP K-band images was also conducted by Carretti et al. (2013), with a particular focus on comparison with the structure present in the S-PASS data. Specifically, the Northern and Southern Fermi bubbles feature prominently in the polarised emission of WMAP K-band. We make use of the high-frequency polarisation information provided by WMAP and compare these results with S-PASS data in the region of GSH 006−15+7.

3.3.3 Radio Continuum

3.3.3.1 Continuum HI Parkes All-Sky Survey

The Continuum HI Parkes All-Sky Survey (CHIPASS) is a map of the radio continuum at 1.4 GHz across the whole sky below declination of $\delta = 25$ deg (Calabretta et al., 2014). CHIPASS is a combination and reprocessing of the HI Parkes All-Sky Survey (HIPASS) and the HI Zone of Avoidance (HIZOA) survey, the result of which is a highly sensitive (sensitivity = 40 mK), all-sky, total intensity survey at a resolution of 14.4', with very well treated artefacts. We use these data to derive information on the synchrotron spectrum in the region of GSH 006−15+7.

3.4 Results and Analysis

3.4.1 Polarisation Morphology

The most prominent feature in the diffuse polarisation in the region of GSH 006−15+7 is the Southern lobe of the Fermi bubbles (Ackermann et al., 2014; Su et al.,

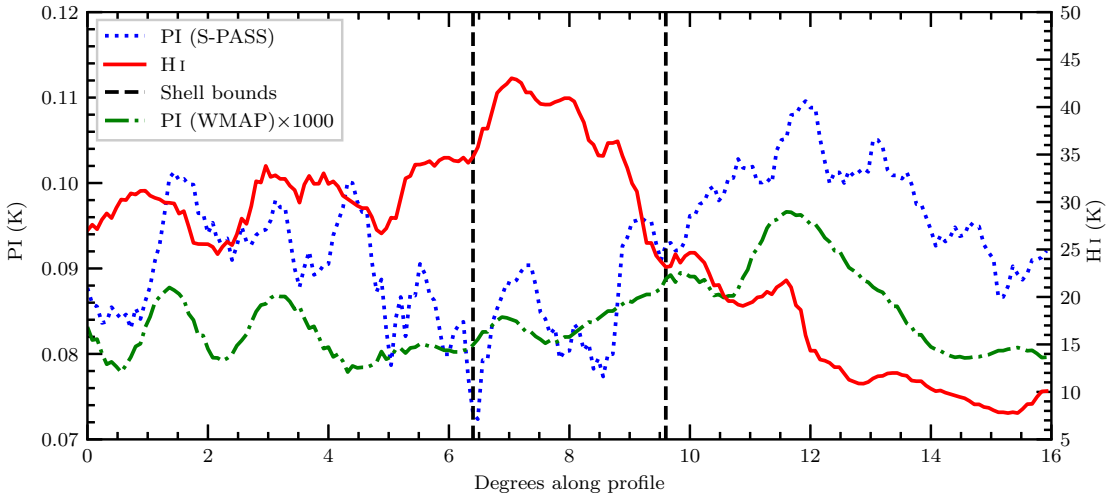

Figure 3.3: Brightness temperature profiles of polarised intensity (PI) at 2.3 GHz (blue, dotted), 23 GHz (green, dash-dotted), and GASS H I at $v_{LSR} = 6.6\,\mathrm{km\,s^{-1}}$(red, solid). The region from which the profiles are taken is shown in Figures 3.1 and 3.2 as the red dashed line. The profile runs from the centre of the shell region to well past the outer boundary, along the bright polarised emission from the Fermi bubble. The black dashed lines correspond to the inner and outer shell boundaries and also shown in Figures 3.1 and 3.2.

2010; Carretti et al., 2013), as seen in Figure 3.2. There are number of structures, however, that show significant morphological correlation with the supershell GSH 006−15+7. We claim that these features are perturbations caused by the MIM of GSH 006−15+7 to the polarised emission from behind it. This supershell has a distance estimate of $\sim 1.5 \pm 0.5\,\mathrm{kpc}$ (Moss et al., 2012), and therefore is situated in the foreground relative to the Fermi bubbles (distance of the front surface from Sun $> 2.5\,\mathrm{kpc}$ (Carretti et al., 2013)).

The spatial correlation between S-PASS polarisation and GSH 006−15+7, as it appears in H I (see Figure 3.1), is most apparent in Stokes parameters Q and U. The Stokes U image (see Figure 3.2(c)) shows the strongest morphological correlation with GSH 006−15+7, although the structure seen in Stokes U is also similar to the structure seen in PA (see Figure 3.2(b)). Along the upper and right-hand outer edge of the shell there is a significant shift in the values of Stokes U, from $U \approx +0.05\,\mathrm{K}$ to $U \approx -0.05\,\mathrm{K}$. A circular edge can be seen following the right-hand boundary of the shell, where predominately positive U switches to negative inside the boundary. On the left side of the image, where U appears negative, the magnitude of U increases on the shell. There is a bright, polarised region in the centre of the image, which

corresponds to the tip of the Fermi bubble.

The Stokes Q image at 2.3 GHz (Figure 3.2(d)) is dominated by emission from the Fermi bubble. Similar to Stokes U, there is a change of sign in Q along the right-hand, inner boundary of the shell as defined by H I. This region in Stokes Q, however, is not as clearly defined as Stokes U. Additionally the change of sign occurs along the inner boundary of the shell in Q, rather than the outer boundary. A similar feature can be found along the bottom-left, inner boundary of the shell. Here Q again appears to change sign across the inner boundary of the shell. Along the left inner and outer boundaries of the shell we find a weak change in sign of Stokes Q.

Inspecting the total linear polarisation intensity (PI) at 2.3 GHz (Figure 3.2(a)) the brightest polarised feature is the Southern ridge of the Fermi bubble (Carretti et al., 2013). This feature runs from the centre of the image to the bottom-right corner. Where the Fermi bubble appears to intersect the shell, however, the polarised intensity is reduced 10-15% relative to the rest of the lobe. This is indicative that near the boundary of the shell, polarised emission is being perturbed and depolarised. Carretti et al. (2013) presented the first morphological description of S-PASS, focusing particularly on the polarised emission from the Fermi bubbles. They also noted the perturbation feature and suggested that this feature could be due to a line-of-sight reversal of the magnetic field, associated with the Fermi bubbles. We argue however, that due to the high degree of spatial correlation, this feature is explained by the presence of GSH 006−15+7 in the foreground. This spatial correlation is exemplified in the profiles shown in Figure 3.3. Here we can see the anticorrelation of S-PASS PI with H I brightness temperature, especially across the thickness of the shell from ~ 5 deg to ~ 10 deg along the profile. This demonstrates that the shell is weakly depolarising the background polarised emission from the Fermi bubble. In addition, as depolarisation is a Faraday rotation effect, we also note a change in the polarisation angle across the same boundary in Figure 3.2(b). Depolarisation towards the Galactic plane is also apparent in the PI image, as noted by Carretti et al. (2013), as well as in Stokes Q and U. Significant depolarisation is visible in the region near GSH 006−15+7 down to a latitude of $b \approx -5$ deg. This

region is associated with large H II regions in the Galactic plane, as seen in H α emission. Additional depolarisation can be seen at latitudes as low as $b \approx -10$ deg. The modulation from this effect makes structure difficult to interpret in the polarisation images near the Galactic plane.

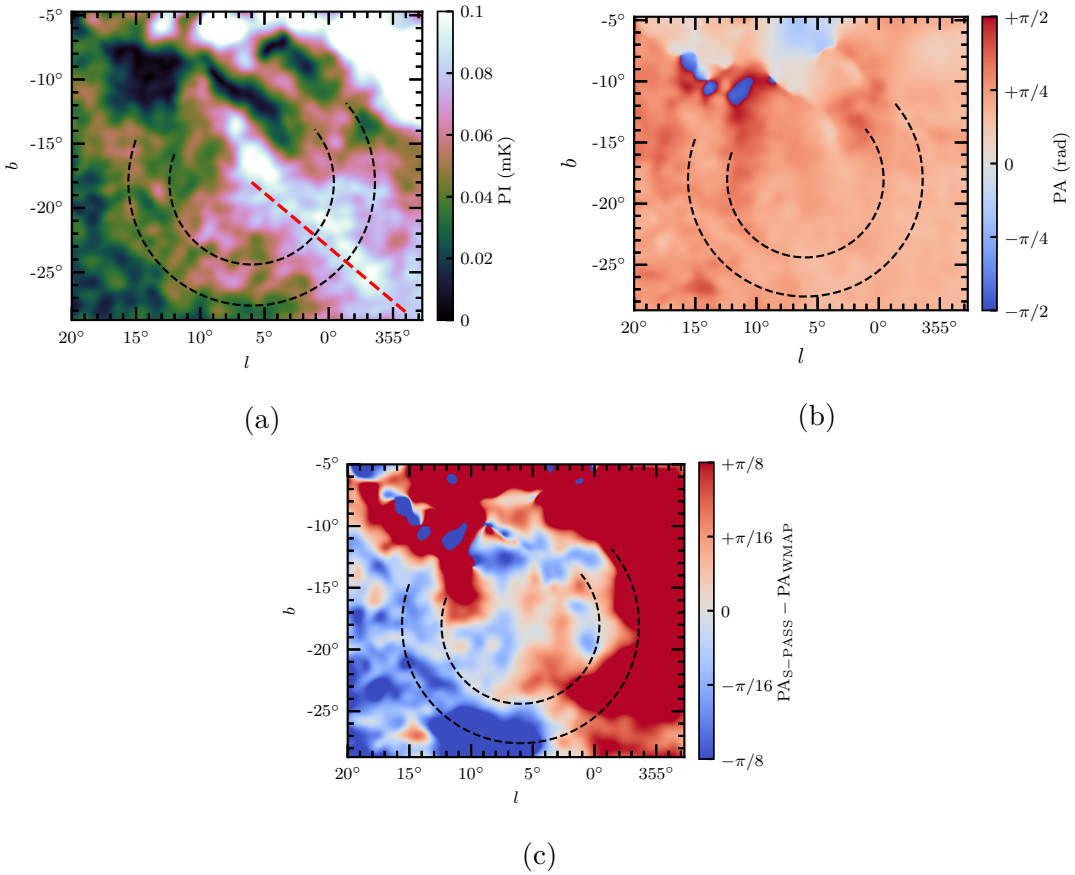

Figure 3.4: Panels (a) and (b): Maps of polarisation in the region of GSH 006−15+7 at 23 GHz from WMAP K-band observations. Here we have applied a Gaussian smoothing to the data with a FWHM of 1 deg. We applied this filter to increase the signal-to-noise ratio in the WMAP data, which originally had a very high noise level. (a) WMAP - polarised intensity. Again, the red dashed line corresponds to the profile given in Figure 3.3. (b) WMAP - polarisation angle in radians. (c) Polarisation angle difference between S-PASS and WMAP in radians. Here the S-PASS data were smoothed to common spatial resolution of the smoothed WMAP data. As in Figure 3.2, the dashed lines give the approximate bounds of GSH 006−15+7.

Unlike the S-PASS polarisation, we see no correlation with GSH 006−15+7 in any of the WMAP polarisation maps. As seen in Figure 3.4 the polarised emission at 23 GHz from the Southern Fermi bubble is the dominant source of polarised emission in the region of GSH 006−15+7. Carretti et al. (2013) also provide a detailed description of the polarised emission from WMAP in this region, again in regards to emission from the Fermi bubbles. We note that there is no noticeable depolarisation

across the thickness of the shell, unlike the S-PASS observations. This is particularly clear in Figure 3.3 where, unlike the S-PASS profile, there is no appreciable drop in the WMAP PI profile as it intersects the shell. The lack of depolarisation is to be expected, as high frequency observations are far less affected by Faraday rotation. We find that the polarisation angle is relatively uniform across the region of GSH 006−15+7 (see Figure 3.4(b)), with a median value of $\sim 37\,\mathrm{deg}$ and a standard deviation of $\sim 9\,\mathrm{deg}$. We also note the significant lack of polarised emission in both WMAP and S-PASS in a few regions above the shell along $b \approx -10\,\mathrm{deg}$. The signal-to-noise in these regions is therefore very low, particularly in WMAP, and also corresponds to large changes in the polarisation angle which are probably spurious. These regions will likely propagate large errors through this analysis.

The strongest morphological indication appears when the polarisation information from S-PASS and WMAP are combined. Inspecting the map of the polarisation angle difference ($\mathrm{PA_{S\text{-}PASS}} - \mathrm{PA_{WMAP}}$) in Figure 3.4(c) reveals the circular structure we expect to be associated with GSH 006−15+7. Again, here the right-hand portion of the shell is most prominent, but the entire region is visible in Figure 3.4(c) where the angle difference is of relatively low magnitude. This change in polarisation angle is indicative that the shell is Faraday rotating the background polarised emission. The motivation for using this polarisation angle difference is expanded upon in Section 3.4.3. In short, as the WMAP data was at high frequency, the polarisation as measured should have encountered very little Faraday rotation, in contrast to the S-PASS polarisation. Thus, the difference in polarisation angle contains information on how much Faraday rotation has occurred along the line of sight. As this difference bears a great deal of morphological similarity to GSH 006−15+7, we therefore assume that, within this region, it is the supershell alone that is causing the observed rotation effect.

3.4.2 Total Intensity Morphology

We also carefully inspect the total intensity data from S-PASS, CHIPASS, and WMAP for any morphological indication of GSH 006−15+7. The presence of such emission, especially in the S-PASS data, would mean that the interpretation that the shell was acting as a pure Faraday screen would be false. Faraday screens,

by definition, do not produce any emission of their own. We find, however, no such emission in any of these data. The only structure of note is emission from the Corona Australis molecular cloud, visible in WMAP K-band total intensity. This comet-shaped reflection nebula is a common feature in infra-red observations (Schlegel et al., 1998; Neuhäuser & Forbrich, 2008), and appears to lie along the bottom edge of GSH 006−15+7. However, its overall morphology is very distinct from GSH 006−15+7, and sits far closer to us at a distance of $\sim 130\,\mathrm{pc}$ (Neuhäuser & Forbrich, 2008).

3.4.3 Faraday Screen Model

3.4.3.1 General concept of the Faraday screen model

As discussed above, GSH 006−15+7 does present a clear polarisation signature at 2.3 GHz. This signature however is not directly evident as polarised emission, nor is there a clear correlation in H α emission (Moss et al., 2012). This is indicative of a relatively low free electron density (compared to an H II region). This type of interaction is dubbed a 'Faraday screen' effect (Wolleben & Reich, 2004; Sun et al., 2007). Faraday screens are simple Faraday rotating regions that affect the synchrotron emission that is produced from behind them (along the line of sight). Faraday screens do not produce polarised emission themselves, instead they rotate the background polarisation angle, and/or reduce the polarised intensity through depolarisation effects. Sun et al. (2007) provide a model for determining the Faraday rotation that occurs due to the presence of a Faraday screen. This Faraday screen model is visualised in Figure 3.5. In this scenario, an observer can measure polarisation ($\mathcal{P}$) either 'on' or 'off' the screen. The terms 'on' and 'off' refer to whether the polarised emission has been affected by the Faraday screen or not, respectively. In either case the model assumes that the observer will measure the superposition of the polarised emission from the 'background' and 'foreground', relative to the screen. When observing 'on' the screen the background polarised emission will be perturbed. Specifically, the polarised intensity will be multiplied by the depolarisation factor 'f' (where $f < 1$), and the polarisation angle will be rotated by an amount 'ψ'. As such, the Stokes parameters 'on' the screen are given by (from Sun

et al., 2007):

$$\begin{aligned} U_{\rm on} &= {\rm PI}_{\rm fg} \sin\left(2\psi_0\right) + f{\rm PI}_{\rm bg} \sin\left[2\left(\psi_0 + \psi\right)\right] \\ Q_{\rm on} &= {\rm PI}_{\rm fg} \cos\left(2\psi_0\right) + f{\rm PI}_{\rm bg} \cos\left[2\left(\psi_0 + \psi\right)\right] \end{aligned} \tag{3.5}$$

These equations assume that the intrinsic polarisation angles in the background and foreground are related by ${\rm PA}_{\rm bg} = {\rm PA}_{\rm fg} = \psi_0$. This assumption is in contrast to Sun et al. (2007) who assumed that $\psi_0 \approx 0\,{\rm deg}$. We are unable to make this same assumption, as it implies that ${\rm PA}_{\rm off} \approx 0\,{\rm deg}$. If we take the WMAP polarisation angle information as an estimate of ${\rm PA}_{\rm off}$, it is clear from Figure 3.4(b) that this is not the case. Our assumption is reasonable in the case of either: 1) a random field, or 2) a dominant coherent field in a single direction. From this, we derive the same model of a Faraday screen as Sun et al. (2007), using observations of polarised intensity (PI) and polarisation angle (PA), 'on' and 'off' the screen:

$$\begin{aligned} \frac{{\rm PI}_{\rm on}}{{\rm PI}_{\rm off}} &= \sqrt{f^2(1-c)^2 + c^2 + 2fc(1-c)\cos 2\psi} \\ {\rm PA}_{\rm on} - {\rm PA}_{\rm off} &= \frac{1}{2}\arctan\left(\frac{f(1-c)\sin 2\psi}{c + f(1-c)\cos 2\psi}\right) \end{aligned} \tag{3.6}$$

This model describes the change in polarised intensity and polarisation angle between observations 'on' and 'off' the screen. Here the four observables are ${\rm PI}_{\rm on}$, ${\rm PI}_{\rm off}$, ${\rm PA}_{\rm on}$, and ${\rm PA}_{\rm off}$. The model parameters are f, c, and ψ. The parameters f and ψ are as described above, where f is the factor of depolarisation that has occurred at the observed frequency, with $f \in [0, 1]$, while ψ is the amount of Faraday rotation through the screen, with $\psi \in [-\pi/2, +\pi/2]$. The parameter c is the fraction of foreground polarised intensity given by:

$$c = \frac{{\rm PI}_{\rm fg}}{({\rm PI}_{\rm fg} + {\rm PI}_{\rm bg})} \tag{3.7}$$

The range of this parameter is therefore $c \in [0, 1]$. The Faraday thickness (ϕ) of the screen can be estimated from this model by:

$$\phi = \frac{\psi}{\lambda^2} \tag{3.8}$$

Here 'Faraday thickness' refers to the Faraday depth of the shell alone. This equation applies in the case of a rotating-only Faraday screen, as the RM of the

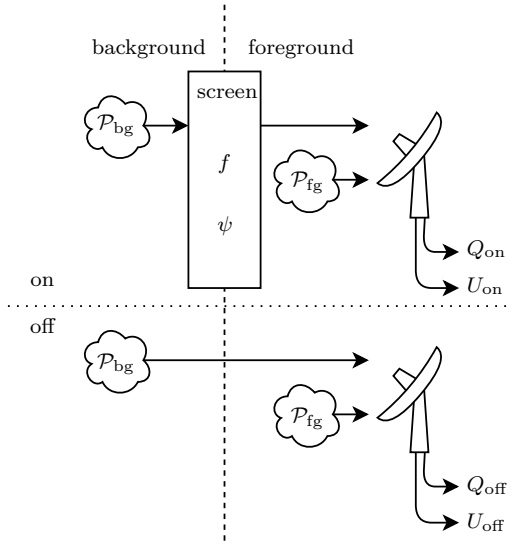

Figure 3.5: Cartoon of the Faraday screen model. The 'foreground'/'background' divide refers to the line-of-sight region where the polarised emission is produced, relative to the screen. The 'on'/'off' divide refers to whether the line-of-sight observes through the screen or not. In both the 'on' and 'off' case the measured polarisation ($\mathcal{P}$) is the superposition of the 'background' and 'foreground' emission. In the 'on' case, however, the background emission is perturbed by the screen.

screen is equal to the Faraday depth. This model has an advantage over the model presented in Wolleben & Reich (2004), as it only requires observations at a single frequency.

In previous uses of this model the 'on' and 'off' components were taken from a common set of radio polarisation observations at the same frequency, but were spatially offset to sample 'on' and 'off' the proposed location of the Faraday screen (Sun et al., 2007, 2011; Gao et al., 2010, 2015). There are two primary assumptions made by this technique: (1) that the polarised emission located beside ('off') the screen region accurately represents the superposition of synchrotron emission from the foreground and background; and, (2) that all Faraday rotation along the line of sight occurs at the Faraday screen. In our analysis, the Faraday screen region of GSH 006−15+7 appears in the direction of the Galactic plane. As the line of sight approaches the plane, the amount of Faraday rotating structure increases; further, the angular extent of GSH 006−15+7 is enormous. As such, assumption (1) is not easily satisfied here.

3.4.3.2 Using WMAP to obtain 'off' polarisation

In contrast to previous uses of the Sun et al. (2007) Faraday screen model, we use S-band-scaled, high frequency (23 GHz), polarisation data as the 'off' measurements to the S-PASS 'on' measurements. By utilising polarisation data from a high frequency survey we bypass the need for assumption (1) to be satisfied. That is, rather than using a spatially-offset pointing at the same frequency for the 'off' measurement, we use pointings towards the screen, but at a different frequency that is negligibly affected by the screen, thus serving as the 'off' measurement. Additionally, this allows for the computation of a Faraday depth for each line of sight through the Faraday screen.

With this consideration, we obtain high frequency polarisation data from the WMAP survey. As Faraday rotation increases as λ^2, only strong Faraday depth sources ($\phi > 100\,\mathrm{rad\,m^{-2}}$) can produce non-negligible Faraday rotation at 23 GHz. Since GSH 006−15+7 is an object in the diffuse ISM, likely occupying some combination of the warm neutral and warm ionised medium (Heiles & Haverkorn, 2012), we do not expect significant Faraday thickness to be produced by this object.

A limitation of a Faraday screen model is that this technique is only sensitive to Faraday rotation values of $-90\,\mathrm{deg} < \psi < +90\,\mathrm{deg}$, due to assumption (2). Any rotations greater than this through the screen would create '$n\pi$' ambiguities in the measured polarisation angle. As such, we are only able to obtain Faraday depths between $\phi = \pm(\pi/2\lambda^2) \approx \pm 92\,\mathrm{rad\,m^{-2}}$. We can exclude the possibility of '$n\pi$' ambiguities by inspecting the morphology of the polarisation angle image from S-PASS (see Figure 3.2(b)). Regions that strongly Faraday rotate appear to have 'onion skin' structure in polarisation angle. That is, across these regions the polarisation angle changes sign multiple times towards the centre of the object. This corresponds to multiple revolutions of the polarisation vector as the physical and Faraday depth of the object increases towards the centre. The GSH 006−15+7 region does not exhibit this morphology, rather it has an approximately uniform polarisation angle structure within the boundaries of the shell. This is therefore consistent with the assumption that the amount of rotation through the shell is $< |90\,\mathrm{deg}\,|$.

WMAP K-band does suffer low signal-to-noise ratio as it measures synchrotron

radiation at the far end of the spectrum. The low signal-to-noise of the WMAP data must be addressed in order to be used in analysis of the Galactic synchrotron emission. We do this by applying Gaussian smoothing to these images. We convolve a Gaussian smoothing function with a FWHM = 1 deg with both the Stokes Q and U maps.

3.4.3.3 Frequency scaling of WMAP to S-Band

In order to estimate the synchrotron background at S-Band, we need to scale WMAP data to 2.3GHz. To do this we require the synchrotron spectral index (β) between these frequencies. Between any two frequencies (ν) with total intensity (T), the spectral index is given by:

$$\beta = \frac{\log\left(T_1/T_2\right)}{\log\left(\nu_1/\nu_2\right)} \tag{3.9}$$

As the zero–offset calibration total intensity map of S-PASS is not yet finalised, we instead obtain the synchrotron spectral index between 1.4 GHz and 23 GHz. This assumes a spectrally constant β between these frequencies. We then use this value of β to scale the WMAP K-band data to S-band. To find the spectral index we use the total intensity data at 1.4 GHz from the CHIPASS survey (Calabretta et al., 2014). The synchrotron spectral index can usually be obtained from the slope (m) of the T-T plot of the total intensity (Stokes I) between two frequencies using (Turtle et al., 1962):

$$\beta \approx \frac{\log m}{\log\left(\nu_{\mathrm{W}}/\nu_{\mathrm{C}}\right)} \tag{3.10}$$

where 'W' stands for WMAP, 'C' for CHIPASS. We find, however, that the slope of the T-T plot is not constant in the region of GSH 006−15+7, indicating thermal emission processes (see Section 3.7.1).

Rather than using this result, we compute the spectral index for each point in the region of GSH 006−15+7 using Equation 3.9. We then analyse the indices as a function of latitude, as shown in Figure 3.6. The spectral index remains relatively constant for $b < -10$ deg; after which β starts to increase to values greater than -3, as also indicated in the T-T plot. Following this, we bin the obtained indices, and compute the error from this binning (shown as the solid line with the 1σ uncertainty band in Figure 3.6). Based on Figure 3.6, we use the binned spectral index as a

function of Galactic latitude and assume that it is constant in Galactic longitude. We use this to scale WMAP Q and U to S-Band, and carry the associated errors forward. The presence of thermal contamination in the spectral index with $b \gtrsim -10\,\mathrm{deg}$ is irrelevant for the following analyses, because the region of GSH 006−15+7 that is depolarised in S-band is also at $b \gtrsim -10\,\mathrm{deg}$ and is thus excluded. We note that using this technique requires that the CMB emission must be subtracted from CHIPASS, as it is not present in the WMAP K-band data. A T-T plot technique usually side-steps this requirement, but since we are unable to use such a technique in this case we subtract 2.7 K uniformly from the CHIPASS total intensity data.

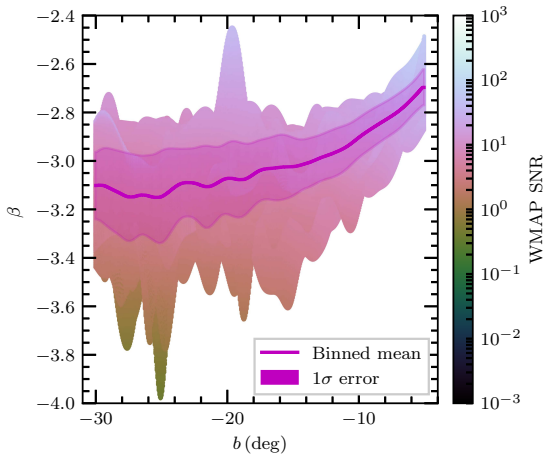

Figure 3.6: Spectral index for each point in the region of GSH 006−15+7 as a function of Galactic latitude. The longitude range used is $45\,\mathrm{deg} < l < 315\,\mathrm{deg}$. The points are coloured by the signal-to-noise ratio (SNR) of WMAP Stokes I. Despite the smoothing applied to the data, the effects of point sources and regions of low intensity are still present. These effects cause a large variance in the derived spectral index. However, after we apply a box-car smooth to the data, we recover a consistent spectral index of $\beta \sim -3.1$ in the region of the shell. Additionally, we also find a clear trend of the spectral index flattening towards the Galactic plane.

3.4.3.4 Summary of our Faraday screen observables

Finally, we obtain the four observables, as required for the Faraday screen model, as follows:

$$\begin{aligned} \mathrm{PI}_{\mathrm{on}} &= \sqrt{Q_{\mathrm{S}}^2 + U_{\mathrm{S}}^2} \\ \mathrm{PI}_{\mathrm{off}} &= \left(\frac{\nu_{\mathrm{S}}}{\nu_{\mathrm{W}}}\right)^{\beta} \sqrt{\left(Q_{\mathrm{W}}\right)^2 + \left(U_{\mathrm{W}}\right)^2} \\ \mathrm{PA}_{\mathrm{on}} &= \frac{1}{2} \arctan\left(\frac{U_{\mathrm{S}}}{Q_{\mathrm{S}}}\right) \\ \mathrm{PA}_{\mathrm{off}} &= \frac{1}{2} \arctan\left(\frac{U_{\mathrm{W}}}{Q_{\mathrm{W}}}\right) \end{aligned} \tag{3.11}$$

here Q and U refer to the Stokes Q and U maps from S-PASS ('S') and WMAP ('W'), β is the spectral index binned as a function of latitude (see Figure 3.6 above), and ν refers to the frequency of each survey. We note there are some regions that have $\mathrm{PI}_{\mathrm{on}} > \mathrm{PI}_{\mathrm{off}}$, which cannot be accommodated by the model. These regions will be excluded from later analysis.

3.4.4 Best Fit Procedure

From the Faraday screen model (Equation 3.6), we have four observables and three model parameters. We obtain the observables from the data using Equation 3.11. To obtain the model parameters we need to fit the Faraday screen model to the data. In order to determine the 'best fit' of the Faraday screen model, we have developed a 'brute-force' method that determines which values of the parameters f, c, and ψ produce the closest fit to the input data. To this end, we implement a grid search technique of the model hyperspace. Specifically, we sample the model for a large number of possible parameter values and find the combination of the parameter values that provide the closest fit to the data. For the purposes of our analysis, each parameter is allowed to take values in the ranges $f \in [0, 1]$, $c \in [0, 1]$, and $\psi \in [-\frac{\pi}{2}, +\frac{\pi}{2}]$. We refer to the number of samples of parameters f, c, and ψ as N_f, N_c, and N_ψ, respectively. For simplicity we use the same number of samples for each parameter; namely $N_f = N_c = N_\psi = N_{\mathrm{samp}}$. This is possible because the final results are insensitive to the number of samples per parameter, provided a large enough value is used. We then evaluate the Faraday screen model (Equation 3.6) for all of these parameter values. This results in two hypersurface cubes of size N_{samp}^3;

one containing all the possible model (mod) PI ratio ($\mathrm{PIR} = \mathrm{PI_{on}}/\mathrm{PI_{off}}$) values and the other the model PA difference ($\mathrm{PAD} = \mathrm{PA_{on}} - \mathrm{PA_{off}}$) values. For a given set of observed (obs) PIR and PAD we find the following 'ξ^2' quantity:

$$\xi^2 = [\mathrm{PIR_{obs}} - \mathrm{PIR_{mod}}]^2 \times [\mathrm{PAD_{obs}} - \mathrm{PAD_{mod}}]^2 \tag{3.12}$$

This quantity is constructed similarly to χ^2, but with a few key differences. Each component in ξ^2 is not weighted by the variance from an underlying distribution. This is because the observed values are themselves sampled from a probability distribution function (PDF) which we produce. In principle we could compute the variance from this distribution and then find and minimise the χ^2. In doing so, however, we would lose the ability to propagate a PDF through the modelling process. As the components of ξ^2 are not weighted by the variance, each factor still has the dimensions of the observable. That is, we have the dimensionless PIR quantity and the PAD quantity in radians. Thus, unlike χ^2, we take the product of the two factors. Like χ^2 the smallest value within our ξ^2 cube corresponds to the values of f, c, and ψ which provide the best fit to the data. This minimum value should also correspond to $\xi^2 = 0$, provided a solution exists, within numerical precision. We check for multiple solutions of (f, c, ψ) that could produce $\xi^2 = 0$, but we only ever find a unique solution for (f, c, ψ) for which $\xi^2 = 0$. Additionally, we check for the existence of an exact solution for each input pixel, and exclude pixels for which no solution exists from further analysis. We provide an example of where we find a minimum in the ξ^2 cube for a randomly sampled line-of-sight input in Figure 3.7. This example is typical of how the hypersurface appears; with the location of the minimum in the cube occurring at the intersection of two 'troughs' of local minima, and being numerically very close to 0.

Our method does not rely on choosing reasonable initial conditions, nor does it require iteration for convergence. Instead, once the grid is built, the best fit is immediately obtained in the (f, c, ψ) parameter grid as the location of the global minimum within the ξ^2 cube.

To obtain the error in the fit of this model we apply a Monte-Carlo approach. First, we obtain the PDF of each input parameter, assuming that the starting input data (S-PASS Stokes Q and U, WMAP Stokes Q and U, and β) have Gaussian

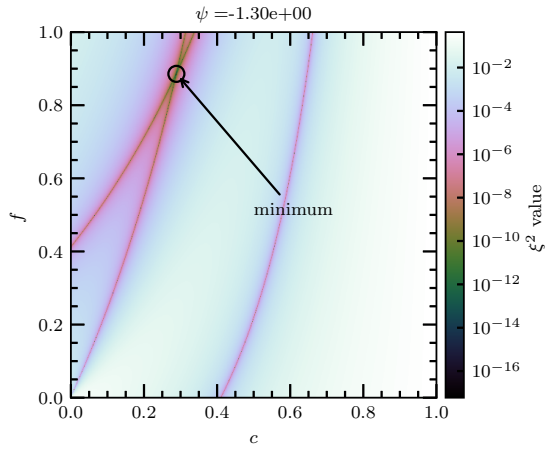

Figure 3.7: Slice through ξ^2 cube for a random line-of-sight $(l, b = [0.0\,\text{deg}, -24.96\,\text{deg}])$ at mean input value. The cube shown is a 500^3 grid, whose $[x, y, z]$ coordinates correspond to the parameters $[f, c, \psi]$. The cube is sliced through the ψ coordinate at the minimum value of ξ^2. Note that in our final analysis, we use a 50^3 grid, which still provides robust results.

distributed errors. For each pixel in each of the input data maps we produce a Gaussian PDF. To compute the PDFs of the observables, as required for the Faraday screen model, we apply the arithmetic described in Equation 3.11 to each value in each PDF. These PDFs become the priors, which we input into the best-fit algorithm; where we find a best-fit for the entire prior PDF for every pixel in the region around GSH 006−15+7. We sample the PDFs as a histogram with N_{PDF} bins.

By propagating the entire prior PDF through the best-fit process we are able to obtain the full posterior PDF of the model parameters f, c, and ψ. Thus, we can gain an estimation of the uncertainty in each parameter. Examples of these posterior PDFs are given in Figure 3.10. We obtain the number of samples, N_{PDF} and N_{samp}, from a convergence test on the first moment values of random pixels in the region of GSH 006−15+7. We tested values of N_{PDF} between 100 and 10^6, and N_{samp} between 1 and 200. We found $N_{\text{PDF}} = 3000$ and $N_{\text{samp}} = 50$ to be the minimum values that still provide robust posterior results. For the entirety of our analysis we use these two sample values across the entire region.

This process is repeated for each pixel available in the S-PASS map in the vicinity of GSH 006−15+7; the result of which is a PDF for each model parameter (f, c, and ψ) for each pixel on the map. Additionally, we also produce the best-fit values from a χ^2 minimisation for comparison with the ξ^2 results. We find that the model values

from this χ^2 minimisation are consistent with centroid values from the distributions of the model parameters. We present here a map of the first moment of the model parameters f and c (Figure 3.8). We also present a map of the first moment of Faraday thickness, as given by Equation 3.8, and its 1σ error map (Figure 3.9).

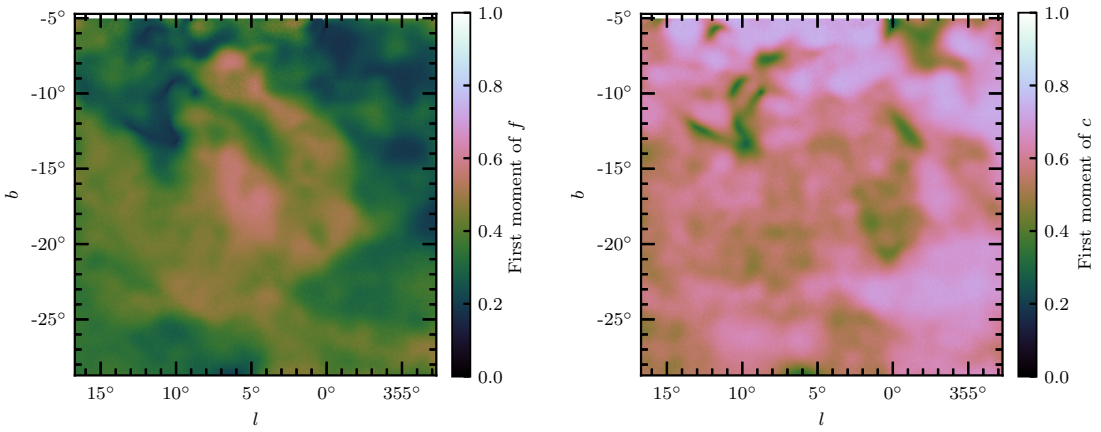

Figure 3.8: First moment map of model parameters in the region of GSH 006−15+7: the depolarisation factor, f (left panel), and the fraction of foreground polarisation, c (right panel).

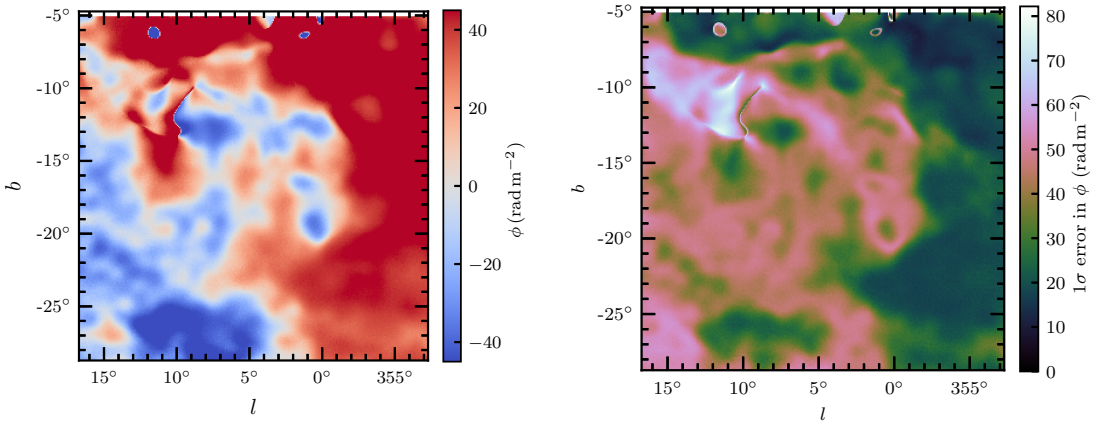

Figure 3.9: First moment map of Faraday depth in the region of GSH 006−15+7 (left panel) and 1σ error associated with this Faraday depth from the model fit (right panel).

We exclude regions in the output data where the Faraday screen model does not apply i.e. where $\mathrm{PIR_{obs}} > 1$, and regions outside the outer boundary of GSH 006−15+7 or inside of the inner boundary, as defined by its H I emission. The resulting map is given in Figure 3.11. We also apply the same mask to the

maps of f and c. Within this masked region both f and c have a roughly uniform value, with spatial standard deviations of 0.08 and 0.06, respectively. We therefore compute the mean values of f and c and their associated errors. From this we find the average depolarisation factor $f_{\rm av} = 0.4 \pm 0.3$ and fraction of foreground polarisation $c_{\rm av} = 0.6 \pm 0.3$. The errors given here are derived from the uncertainties in the mean, and not from the spatial variation. These values imply that on average roughly half of the background emission is depolarised by GSH 006−15+7, and that the background and foreground polarised emission are approximately on parity, with the foreground being slightly dominant.

3.4.5 Error Propagation of Best-Fit Parameters

We use a Monte Carlo error propagation method to carry the errors forward through our best-fit procedure. As such, we are able to constrain regions within the output data where the fit is poor. Figure 3.10 shows the PDFs of f, c, and ψ for two pixels sampled at $l, b = [4.96\,\mathrm{deg}, -18.0\,\mathrm{deg}]$ (blue area) and $l, b = [0.0\,\mathrm{deg}, -24.96\,\mathrm{deg}]$ (orange area). Recall f is the depolarisation factor, where a value of 0 refers to total depolarisation, and a value of 1 to no depolarisation. The parameter c is the fraction of foreground polarisation, where values of 0 implies that all the emission is from the background, and 1 implies that all the emission originated in the foreground. These two pixels provide typical examples of the results we see across the region of the shell. Here we see the pixel sampled at $l, b = [0.0\,\mathrm{deg}, -24.96\,\mathrm{deg}]$ has a well constrained value of ψ, whereas the pixel at $l, b = [4.96\,\mathrm{deg}, -18.0\,\mathrm{deg}]$ does not. The pixel at $l, b = [4.96\,\mathrm{deg}, -18.0\,\mathrm{deg}]$ has an input PA difference very close to 0 deg. In general we find that the value of ψ is poorly constrained in regions where the input PA difference ($\mathrm{PA_{on}} - \mathrm{PA_{off}}$) is very close to 0 deg, and in regions away from the bright background polarised emission of the Fermi bubbles. The former case is a resultant behaviour of the Faraday screen model, which is better able to constrain values of ψ which are significantly greater or smaller than 0 deg. Additionally, in the lower panel of Figure 3.10, the blue distribution of the pixel at $l, b = [0.0\,\mathrm{deg}, -24.96\,\mathrm{deg}]$ has a dip around $\psi \approx 0$. We find similar distributions for all pixels where the input PA difference is 0 deg. This can be seen in the lower panel of Figure 3.9 as high values of the 1σ error. In this Figure we note that

the outline of the shell region is visible due to the increased error inside the inner boundary of the shell, where $\mathrm{PA_{on}} - \mathrm{PA_{off}} \approx 0\,\mathrm{deg}$. The uncertainties in f and c do follow similar trends to ψ, but overall the errors are much more uniform. Of note, the region around $l, b \approx [11\,\mathrm{deg}, -11\,\mathrm{deg}]$ corresponds to the highest error in ψ and unusual values in all the output parameters. The region is also associated with very low polarised intensity from the WMAP and S-PASS observations, resulting in high uncertainty in that region.

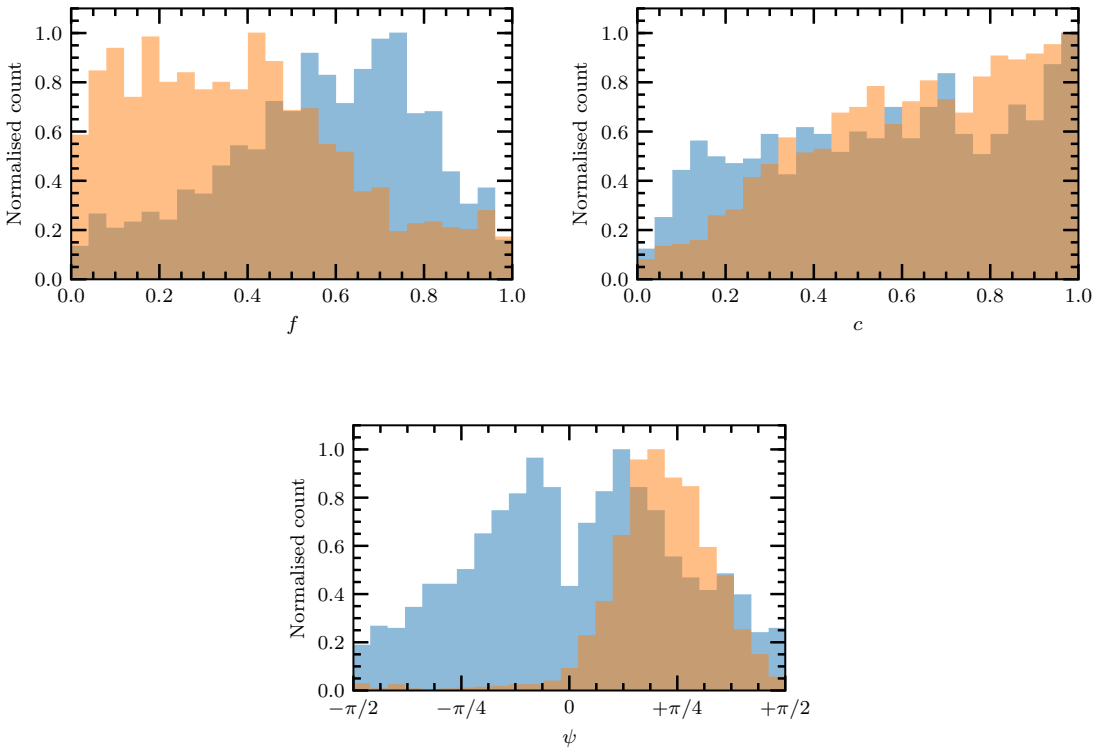

Figure 3.10: Posterior PDFs for two lines-of-sight in the f, c, and ψ data. Blue: $l, b = [4.96\,\mathrm{deg}, -18.0\,\mathrm{deg}]$, Orange: $l, b = [0.0\,\mathrm{deg}, -24.96\,\mathrm{deg}]$. Recall that f is the depolarisation factor, c is the fraction of foreground polarisation, and ψ is the amount of Faraday rotation through the screen.

3.5 Discussion

3.5.1 Line of Sight Magnetic Field

The magnetic fields associated with GSH 006−15+7 can be determined from its Faraday thickness. To compute this magnetic field strength we evaluate Equation 3.3

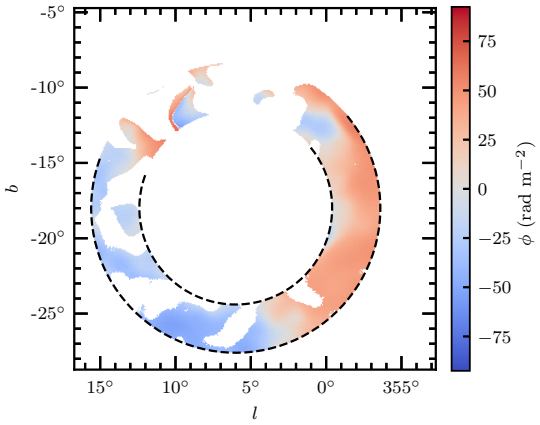

Figure 3.11: First moment map of Faraday thickness of GSH 006−15+7. A mask was applied to remove regions where the Faraday screen model does not apply.

along the line of sight:

$$B_{\parallel} = \frac{\phi}{0.812\langle n_e \rangle L} \tag{3.13}$$

where $B_{\parallel}$ and $\langle n_e \rangle$ are the line-of-sight of averages of the magnetic field and the electron density, respectively.

The problem that Equation 3.13 presents is an ambiguity between ϕ, $\langle n_e \rangle$, and L when trying to determine $B_{\parallel}$. We have already determined ϕ using the Faraday screen model, which also sets the sign of the magnetic field along the line of sight; as $\langle n_e \rangle$, and L are positive definite.

To constrain the path-length through the shell (L) we assume a simple spherical model. This model takes the path-length through the shell to be the chord between two concentric spheres. These spheres are co-centred and have an inner and outer radius such that they align with the centre, and the inner and outer bound of GSH 006−15+7, as observed in H I. This path length is also a function of the distance to the centre of the shell. We provide a derivation for this path-length in Appendix 3.7.2.

To obtain the electron density information various different methods can be employed, each with its own advantages and disadvantages. We use the emission measure (EM) as determined by H α emission, following the procedure set out by Harvey-Smith et al. (2011) and Gao et al. (2015). Emission from H α can be observed in a diffuse manner over the entire sky; providing finely sampled spatial information on electron density. GSH 006−15+7 is not clear in H α however, which means

associating emission with the shell is difficult. Additionally, as a thermal process, the H α line is very broad. This makes constraining the emission to a particular velocity challenging; especially to velocities near the local standard of rest. If instead we use velocity integrated H α observations, we would of course be including emission from both in front of and behind our region of interest. In either case, making use of H α emission will at least provide an upper limit on the electron density. Computing an emission measure also requires information in addition to H α intensity. As such, the uncertainty associated with the electron density that is derived from an emission measure will be high.

As an alternative, we did consider the electron density measured from the dispersion measure (DM) of pulsars behind GSH 006−15+7. To obtain the required DM data, we consult the ATNF Pulsar Catalogue (Manchester et al., 2005), and find thirteen pulsars within a 10 deg radius of the centre of the spherical region of GSH 006−15+7[1]. Only three of these pulsars have distance estimates independent of the dispersion measure. Of these three, one sits on the other side of the Galactic centre, meaning that most of its dispersion measure likely comes from the Galactic central region. This makes any simplifying assumptions, such as a roughly constant n_e unusable. The other two pulsars sit in front of the shell region. This means no usable electron density information was available from pulsar dispersion measures in the region of the shell. We also considered electron density information from other tracers such as S II, S III, and O II. However, we find from Shull et al. (2009) that intermediate velocity observations of ionised tracers, from both the *Hubble Space Telescope* and *Far Ultraviolet Spectroscopic Explorer*, do not probe near to the Galactic plane, and thus exclude the region around GSH 006−15+7. As each of these alternatives cannot provide us with with a value of n_e in the region of GSH 006−15+7, we continue to use the EM to estimate this value.

3.5.1.1 Emission Measure

The emission measure is defined as the path integral of n_e^2 along the line of sight:

$$\mathrm{EM} \equiv \int_0^L n_e^2 dr \tag{3.14}$$

[1]Catalogue version: 1.57, Accessed 23rd of August 2017.

By constraining the limits of integration to within the path-length of the shell (L), we limit the EM obtained to be from the shell only. EM can be determined from observations of H α emission as follows (Haffner et al., 1998; Valls-Gabaud, 1998; Finkbeiner, 2003):

$$\mathrm{EM} = 2.75 T_4^{0.9} I_{\mathrm{H}\,\alpha} \exp\left[2.44 E(B-V)\right] \mathrm{pc\,cm^{-6}} \tag{3.15}$$

Again, if we constrain the measured H αemission to within the shell, the resulting EM will be similarly constrained. Where T_4 is the thermal electron temperature in 10^4 K, $I_{\mathrm{H}\,\alpha}$ is the H α intensity in Rayleighs, and $E(B-V)$ is the colour excess (Finkbeiner, 2003). Note that to use this method, we require both an estimate of the electron temperature in the warm ionised medium (WIM) and measurements of the extinction from dust reddening. Here we assume a typical WIM temperature of $T_4 \approx 0.8 \times 10^4$ K, following Gao et al. (2015) and Haffner et al. (1998). We obtain the colour excess from infrared dust measurements by Schlegel et al. (1998) and find a mean value within the region of the shell of ~ 0.17.

To find the electron density associated with the supershell we adopt the same formalism as Harvey-Smith et al. (2011). We allow the thermal electrons to be 'clumped' along the line of sight. Outside of a clump we take $n_e = 0$ and within a clump $n_e = n_{e,c}$. Using this information, Equation 3.14 can be solved for the electron density inside a clump:

$$n_{e,c} = \sqrt{\frac{\mathrm{EM}}{f_e L}} \tag{3.16}$$

Note the addition of the thermal electron filling factor f_e. This term quantifies the line-of-sight distribution of thermal electrons. If the electrons are uniformly distributed then $f_e = 1$; however, if the electrons are 'clumped', or if the shell has an ionised layer, then $f_e < 1$. That is, the electron clumps inhabit a column of $f_e L$ along the line of sight. From this, the average line-of-sight electron density is given by:

$$\langle n_e \rangle = f_e n_{e,c} \tag{3.17}$$

Combining Equations 3.13, 3.16, and 3.17 yields the line-of-sight magnetic field as:

$$B_{\parallel} = \frac{\phi}{0.812\sqrt{\mathrm{EM} f_e L}} \tag{3.18}$$

We use the EM as obtained from velocity separated H α data, as it provides a more accurate estimate of the electron density within GSH 006−15+7. We obtain the kinematic data from the Wisconsin H-Alpha Mapper (WHAM) survey (Haffner et al., 2003, 2010). The H α data from the WHAM kinematic survey will produce an upper limit on the electron density due to its broad line-width. We provide a map of EM in the Appendix in Figure 3.19. In the shell we find a mean EM of 12.6 pc cm^{-6}.

We now compute the line-of-sight magnetic field magnitude ($B_{\parallel}$) using Equation 3.18, taking a distance to the shell of 1.5 kpc to evaluate the line-of-sight distance L (see Section 3.7.2). We note here that the $B_{\parallel}$ we obtain is a lower limit, as the electron density derived from EM is an upper limit. In addition f_e is not constrained, we therefore present $B_{\parallel}$ as a function of this factor. The spatial distribution of $B_{\parallel}$ over the shell for each value of f_e is given in Figure 3.12. We also indicate in this Figure that the mean 1σ error in $B_{\parallel}$ is $\sim 1.2\,\mu$G when $f_e = 0.5$. As expected from Equation 3.18, the magnitude of $B_{\parallel}$ remains relatively constant as a function of f_e, until the filling factor becomes very small.

The value of f_e is not well constrained, and as such a value is often assumed in the literature. A value of $f_e = 1$, implying a uniform distribution of electrons, is unlikely; as are small values of f_e, since they imply large magnetic fields for a given Faraday depth measurement. We summarise some recent values of f_e from the literature in Table 3.2. Purcell et al. (2015) determined f_e from an MCMC model fit to their data; as such, they constrain lower limit of $f_e = 0.24$ and a mean value of $f_e = 0.3$. They note, however, that a value of around 0.5 provided a better match to dispersion measure data from pulsars. Kaczmarek et al. (2017) adopted their value of 0.5 following McClure-Griffiths et al. (2010). We note that some of these values are not directly derived, but rather chosen based on previous studies. Considering these values, and the range over which our derived field strength remains relatively constant, we will now adopt a value of $f_e = 0.5$ for further analysis.

Table 3.2: A summary of recent literature values of f_e. Recall f_e is the filling factor of thermal electrons. (HVC - High velocity cloud.)

f_e	Phenomena	Work
0.04 ± 0.01	Mid-plane WIM	Gaensler et al. (2008)
~ 0.3	Off-plane WIM	Gaensler et al. (2008)
0.5	HVC	McClure-Griffiths et al. (2010)
0.1	H II regions	Harvey-Smith et al. (2011)
0.4 - 1	W4 Superbubble	Gao et al. (2015)
≥ 0.24	Gum nebula	Purcell et al. (2015)
0.5	Magellanic Bridge	Kaczmarek et al. (2017)

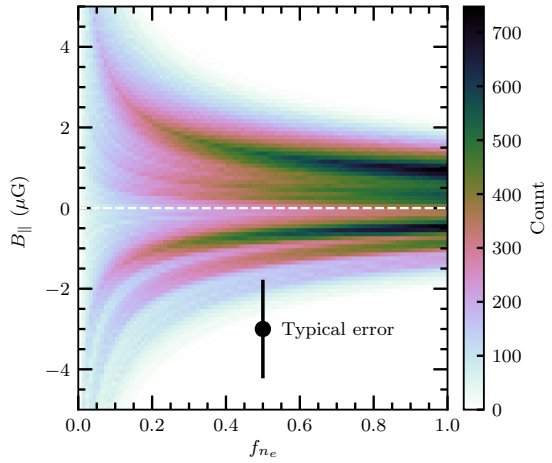

Figure 3.12: Distribution of the line-of-sight magnetic field ($B_\parallel$) as determined by the velocity separated H α, using Equation 3.18. We find distribution from the histogram of $B_\parallel$ between $\pm 5\,\mu$G, with a bin-width of $0.1\,\mu$G, across the region of the shell, for each value of f_{n_e}. Note that the spread of values here does not necessarily correspond to error in $B_\parallel$, rather it shows the range of values found in the region in GSH 006−15+7. The 'typical error' shown is the mean error in $B_\parallel$ when $f_{n_e} = 0.5$.

3.5.2 Line of Sight Magnetic Field Structure

We provide a map of the line-of-sight magnetic field structure in Figure 3.13(a) taking $f_e = 0.5$ and a distance of 1.5 kpc. The uncertainty of the values in this map is provided in Figure 3.13(b). The structure presented in the map of the line-of-sight B-field appears to follow the general trend of away from the observer (negative) in the bottom-left of the shell; transitioning to toward the observer in the top-right of the shell. This structure is, upon simple consideration, consistent with a field that is azimuthally wrapped around the surface of the shell.

Stil et al. (2009) analysed the role of magnetic fields in expanding superbubbles through MHD simulations. Their work also provided simulations of RM signatures

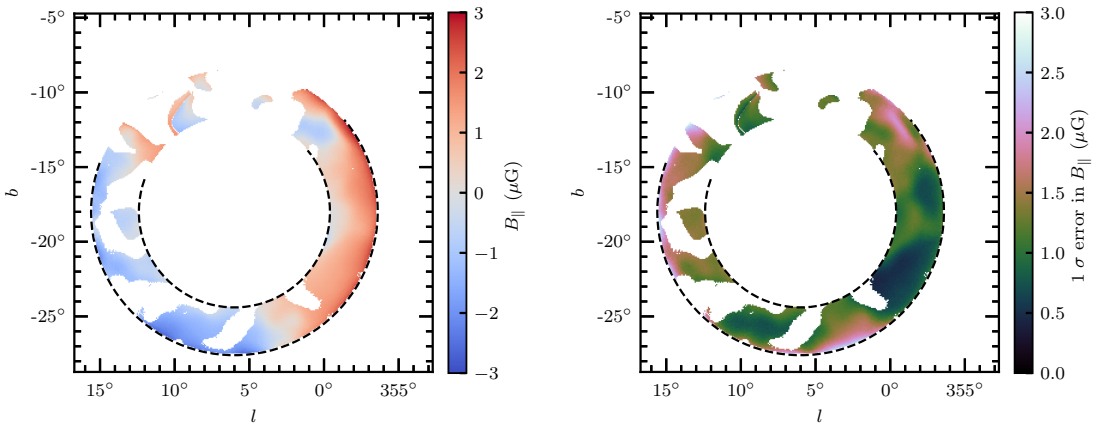

(a) (b)

Figure 3.13: (a) The line-of-sight magnetic field map through GSH 006−15+7. Here $B_{\parallel}$ is determined from Equation 3.18 using EM from velocity separated H α, taking $f_e = 0.5$ and a distance to the shell of 1.5 kpc. We provide a map of EM in Figure 3.19. Note that some extreme values of the magnetic field occur towards the outer boundary of the shell, and arise due to the path-length L becoming very small at the limb. (b) The map of uncertainty in the line-of-sight magnetic field.

from superbubbles expanding from the Galactic plane with a magnetic field parallel to the plane. This provides two examples to compare with our Faraday depth map (Figure 3.11): an observation looking perpendicular to the Galactic magnetic field, and an observation looking parallel. In the former case, the strongest RM values are found in lines of sight through the cavity of the simulated bubble. Most notably, the sign of the RM in the shell of the bubble reverses along the line that goes through the centre of the bubble, parallel to the external field direction. In the case of observing parallel to the Galactic magnetic field the RM values are greatly amplified overall, and the wall of the bubble exhibits the strongest RM signature. Between these two scenarios, our Faraday thickness map is in better agreement with a shell which has expanded into a field perpendicular to the line of sight as we see a very clear sign change in the shell from lower left to upper right. It is likely, however, that we observe this shell at some angle between the two cases described by Stil et al. (2009). This is an area that could be further probed by simulation work. If the geometry and orientation of the shell can be well determined, and therefore the total magnetic field structure, this information could provide insight into the Galactic field into which the shell expanded.

3.5.3 Implications

3.5.3.1 Dynamical Role of B-fields in GSH 006−15+7

The dynamical importance of magnetic fields in an ionised medium can be quantified by the plasma beta ($\beta_{\rm th}$):

$$\beta_{\rm th} = \frac{P_{\rm th}}{P_{\rm mag}} \tag{3.19}$$

which is the ratio of the thermal pressure ($P_{\rm th}$) to the magnetic pressure ($P_{\rm mag}$). In this analysis the plasma beta quantifies the dynamical role of the magnetic fields in the shell itself.

We will assume that the shell contains a mixture of a warm neutral medium (WNM) and WIM as described by Heiles & Haverkorn (2012) and that the value of $B_\parallel$ remains the same in both phases. This is motivated by the observations of H I and H α in this region. We are therefore also assuming that the measured H I emission, H α emission, and Faraday depth, all arise from the same location. The thermal pressure is therefore the sum of the partial pressures of the ionised ($P_{{\rm th},i}$) and neutral media ($P_{{\rm th},n}$):

$$P_{\rm th} = \langle P_{{\rm th},i} \rangle + \langle P_{{\rm th},n} \rangle \tag{3.20}$$

where the terms in angular parentheses refer to the line-of-sight averages of those values. The partial pressures are given by:

$$\begin{aligned} \langle P_{{\rm th},i} \rangle &= 2 \langle n_e \rangle k T_i = 2 f_e n_e k T_i \\ \langle P_{{\rm th},n} \rangle &= \langle n_H \rangle k T_n \end{aligned} \tag{3.21}$$

where n_e is the electron number density derived from EM, n_H is the neutral hydrogen number density, k is Boltzmann's constant, and T_i and T_n are the temperatures of the ionised and neutral phase, respectively. We take values of $T_i = 8000\,{\rm K}$ for the ionised medium and $T_n = 6000\,{\rm K}$ for the neutral medium. We obtain the number density of neutral hydrogen from the column density derived by Moss et al. (2012) from GASS H I. They find a mean column density of $N_{H,{\rm av}} \sim 2 \times 10^{20}\,{\rm cm}^{-2}$ in the shell of GSH 006−15+7. From this, we find the line-of-sight averaged number

density of H I in the shell from:

$$\langle n_H \rangle = \frac{N_{H,\mathrm{av}}}{L} \tag{3.22}$$

where L is the path-length through the shell (see Appendix 3.7.2). Note that L varies across the projected area of the shell, therefore we also obtain a spatially varying value of n_H. In this region we find mean values of $\langle n_e \rangle$ and $\langle n_H \rangle$ of $0.15\,\mathrm{cm}^{-3}$ and $0.28\,\mathrm{cm}^{-3}$, respectively. Recall, however, that our value of $\langle n_e \rangle$, as derived from EM, is an upper limit.

The magnetic pressure in the shell in given by:

$$P_{\mathrm{mag}} = \frac{B_{\mathrm{tot}}^2}{8\pi} \tag{3.23}$$

where B_{tot} is the total local magnetic field. Our observations have provided us with the line-of-sight field, however. If we consider the case of an azimuthally wrapped magnetic field within the shell, we expect the line-of-sight field to have a distribution across the shell. That is, maximum when the total field is aligned with the line of sight, and null when the field is perpendicular. Additionally, as our model for the path length through the shell has a hard boundary, the values of this length become very small towards the edge of the shell and thus resulting in large $|B_\parallel|$. Overall what we expect from the distribution of $|B_\parallel|$ over the shell is a smooth peak near small values of $|B_\parallel|$, a peak at the value which corresponds to the field being aligned with the line of sight, and a tail of more extreme values of $|B_\parallel|$. We find a similar distribution to this across GSH 006−15+7, as shown in the left panel of Figure 3.14. This distribution is bi-modal; we interpret the first peak to correspond to regions where the total field is close to perpendicular to the line of sight and the second peak to where the total field is close to parallel. To find the locations of these peaks we fit a double Gaussian (i.e. the sum of two Gaussians) to the distribution. To obtain the uncertainty of the peak value we perform the same analysis of the distribution of $|B_\parallel + \sigma_{B_\parallel}|$ and $|B_\parallel - \sigma_{B_\parallel}|$, as shown in the middle and right-hand panels of Figure 3.14. From this we obtain a value of the second peak of $|B_\parallel|_{\mathrm{peak}} = 2.0^{+0.01}_{-0.7}\,\mu\mathrm{G}$. The error range given here includes uncertainties arising from our best-fit ϕ value, $\langle n_e \rangle$ estimate, and our model L. We now assume that

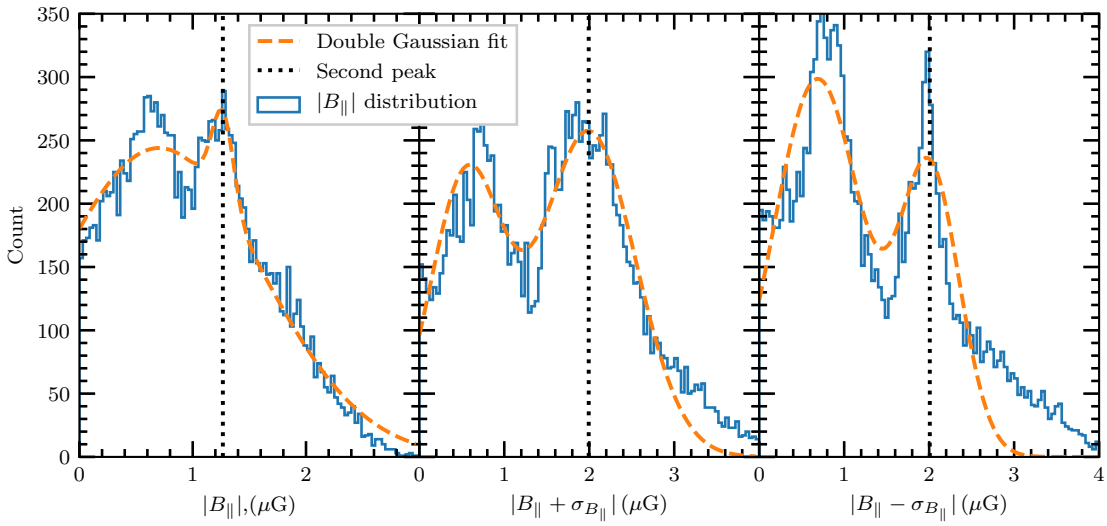

Figure 3.14: The distribution of the absolute value line-of-sight magnetic field ($|B_\parallel|$) across GSH 006−15+7. The left panel shows the distribution of $|B_\parallel|$ taking $f_e = 0.5$ and a distance to the shell of 1.5 kpc (i.e. the distribution of values from Figure 3.13(a)). The middle and right-hand panels show the distribution of $|B_\parallel|$ plus and minus the error in $B_\parallel$ (as shown in Figure 3.13(b)), respectively. Each distribution has been fit with a double Gaussian (i.e. the sum of two Gaussians), shown in orange. The centre of the second fitted peak is shown by the black dashed line. The locations of the second peak for the left, middle, and right panels are 1.27 μG, 1.99 μG, and 2.00 μG, respectively.

$B_{\rm tot} = |B_\parallel|_{\rm peak}$, since this value is likely associated with the total field being aligned with the line of sight in the case of a coherent total field. Recall that as $B_\parallel$ depends on the value we found for EM, which is an upper limit, the value of $B_\parallel$ and our approximation of $B_{\rm tot}$ are therefore lower limits. We note it would be possible for a stronger magnetic field to be obtained from our modelled Faraday depth if the electron density or f_e were demonstrated to be smaller than our current estimates. Additional data would be required, however, to motivate a different estimation.

We compute the mean plasma beta across GSH 006−15+7 using both the ionised and neutral partial pressures as described above. From this we obtain a plasma beta of $\beta_{\rm th} = 4^{+11}_{-2}$. We note that this value has a high variance, which is due to the sensitivity of $\beta_{\rm th}$ to small values of $B_{\rm tot}$. Additionally, the value of $\beta_{\rm th}$ is an upper limit only, as $B_{\rm tot}$ was a lower limit and $\langle n_e \rangle$ was an upper limit. The errors given here include uncertainties in $\langle n_e \rangle$, $\langle n_H \rangle$, and $B_{\rm tot}$. This value of $\beta_{\rm th}$ implies that magnetic field pressures in GSH 006−15+7 are dominated by thermal pressures in the region of the shell. Due to the large uncertainties involved it is

hard to draw further conclusions regarding the dynamical role of magnetic fields in GSH 006−15+7. Such analysis would also require additional information about thermal pressures in the cavity of the shell (Ferriere et al., 1991), which is beyond the scope of this work. What is of note, however, is that despite how relatively weak the magnetic fields in GSH 006−15+7 are, this technique has allowed their detection.

3.5.3.2 Comparison to other results

Two structures of similar origin to GSH 006−15+7 have recently had measurements of their associated B-fields. Gao et al. (2015) analyse the magnetic fields associated with the W4 superbubble, and Purcell et al. (2015) study the Gum Nebula. Gao et al. (2015) find strong magnetic fields in association with the W4 superbubble ($B_{\parallel} = -5.0\,\mu\mathrm{G}/\sqrt{f_e} \pm 10\%$, $B_{\mathrm{tot}} > 12\,\mu\mathrm{G}$), which generally dominate the thermal pressures in the Western wall of the shell. They also find that towards the high-latitude region of W4 the magnetic fields weaken; making the magnetic and thermal pressures comparable. In the Gum Nebula, Purcell et al. (2015) find a total magnetic field strength of $B_{\mathrm{tot}} = 3.9^{+4.9}_{-2.2}\,\mu\mathrm{G}$. From this they compute a plasma beta $\beta_{\mathrm{th}} = 4.8$, which is relatively high, meaning that the thermal pressures dominate the region, similar to our findings for GSH 006−15+7.

To place these values in a broader context, we compare these results to magnetic fields found in molecular and H I clouds by Crutcher et al. (2010) and in H II regions by Harvey-Smith et al. (2011). In Figure 3.15 we add this work on GSH 006−15+7, as well as the W4 and Gum Nebula results, to the comparison of density against magnetic field strength. We find the H-nuclei number density ($n_{\mathrm{H\text{-}nuclei}}$) in GSH 006−15+7 using $n_{\mathrm{H\text{-}nuclei}} = \langle n_H \rangle + \langle n_p \rangle = \langle n_H \rangle + f_e n_e$, where n_p is the number density of protons in the ionised phase. We note that the largest objects appear in a cluster together in the lowest density region of this Figure. The H II region that appears along with GSH 006−15+7, W4, and the Gum Nebula, is Sivian 3; which is the largest H II region analysed by Harvey-Smith et al. (2011). We find that GSH 006−15+7 has comparable magnetic fields amongst these objects, but is slightly weaker and occupies a lower density regime. The resulting plasma beta for this object is therefore indicative that thermal pressures dominate the shell.

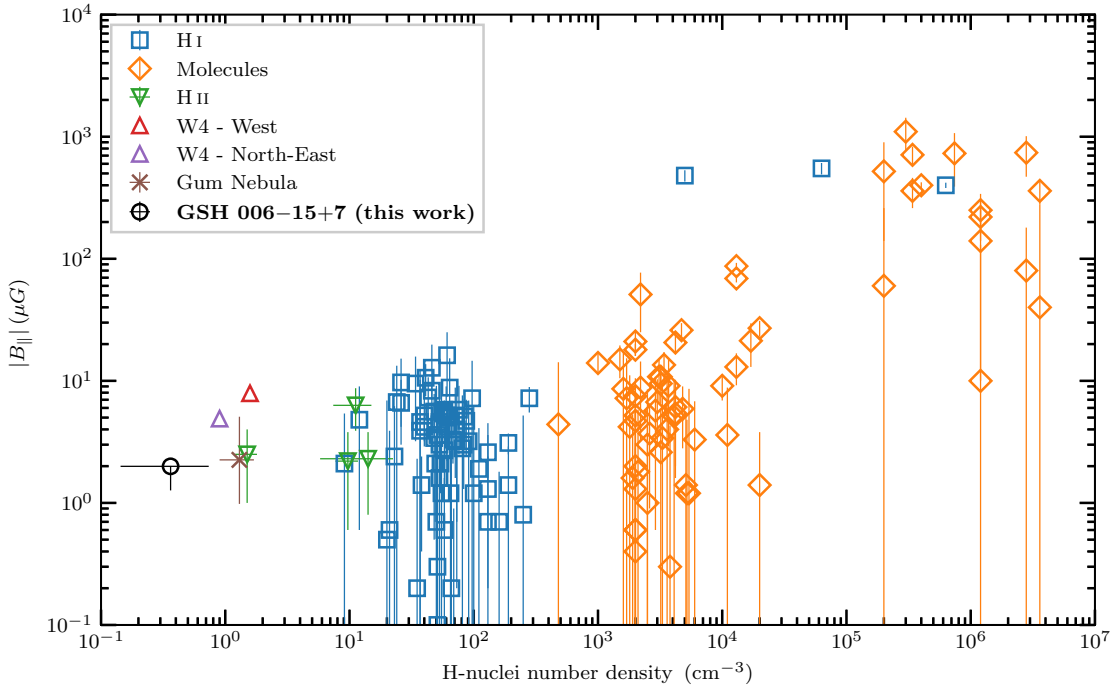

Figure 3.15: Line-of-sight magnetic field amplitude against number density in the associated ISM. The H I and molecular data were originally compared by Crutcher et al. (2010), and the H II data were added by Harvey-Smith et al. (2011). We make the addition of GSH 006−15+7 (this work) using the RMS value of the field, as well as the W4 superbubble (Gao et al., 2015) and the Gum Nebula (Purcell et al., 2015). Note that we have computed the line-of-sight B-field strength in the Gum Nebula from the total field strength by $B_\parallel \sim B_{\rm tot}/\sqrt{3}$.

Finally, we compare the Faraday thickness derived from the Faraday screen model with RMs from extragalactic sources. If GSH 006−15+7 is the dominant Faraday component along the line-of-sight, we expect to see evidence of it in these data. We obtain the all-sky map of extragalactic RMs from Oppermann et al. (2015). We find a correlation between these extragalactic RMs and the Faraday thicknesses from the screen model, as shown in Figure 3.16. There is significant scatter present in this correlation; which is as expected as extragalactic RMs probe the entire line-of-sight through the Galaxy, and thus multiple Faraday components. We fit a linear model to these data, and find that RM $\sim 0.6\phi - 15.5$, with a coefficient of determination $R^2 = 0.4$. The physical reason for the slope correlation is not obvious, as a factor of 1/2 is usually expected for regions of mixed emission and rotation (e.g. Sokoloff et al., 1999).

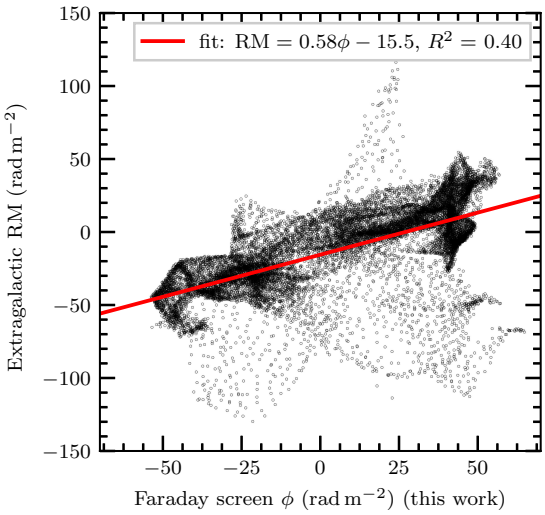

Figure 3.16: The comparison of extragalactic RMs from Oppermann et al. (2012) with the Faraday depth found from the Faraday screen model in the region of GSH 006−15+7. The solid red line corresponds to a least-squares linear fit to the data.

3.6 Summary and Conclusions

We found the polarised signature at 2.3 GHz of Galactic supershell GSH 006−15+7 in S-PASS. The morphological correlation indicates a direct detection of the MIM in association with this Galactic supershell. The 'shadow' of GSH 006−15+7 is most obvious in the Stokes U images. While there are signatures of the shell in polarised intensity and in Stokes Q, they are not as obvious. This highlights the importance of investigating multiple polarisation modes when searching for polarised features.

We have provided a method of obtaining a Faraday depth map from two single-frequency observations; modifying the approach for modelling a Faraday screen. To estimate the background synchrotron emission of this object we used high-frequency polarisation observations from WMAP K-band scaled to S-band. This has allowed us to obtain Faraday rotation information with fewer assumptions than just using single-frequency observations. This method can be applied wherever a bright polarised background source illuminates purely Faraday-rotating foreground object. The source itself can be extended and complex in structure; so long as the Faraday rotation in the screen remains between $-90\,\mathrm{deg} < \psi < +90\,\mathrm{deg}$, the Faraday depth can be successfully recovered. This condition can be verified through inspection of a single-frequency polarisation-angle map. In Section 3.4.4 we describe our best-fit

procedure, which we find to be robust and parallelisable on multi-core computers.

From this Faraday depth map we determine the line-of-sight magnetic field and structure in association with the Galactic supershell GSH 006−15+7. We derive the line-of-sight field in Section 3.5.1, and discuss the structure in Section 3.5.2. We find a peak line-of-sight field strength of $|B_{\parallel}|_{\rm peak} = 2.0^{+0.01}_{-0.7}\,\mu$G. From these results we have gained insight into the dynamical role of the magnetic fields associated with GSH 006−15+7. In the region of the shell we find that the magnetic pressures are likely dominated by thermal pressures. The line-of-sight magnetic field structure indicates that the Galactic magnetic field has a significant component perpendicular to the line of sight in the region of GSH 006−15+7.

We find that the line-of-sight field strength is comparable to similarly sized objects with similar densities. This indicates that by using diffuse polarisation observations we are able to probe the magnetic fields in low-density regimes of the ISM. The method we have developed has a number of advantages in comparison to observations of point-source RMs. Most relevant to this work is that our method allows the Faraday thickness of a single, extended object to be constrained, even though it lies close to the Galactic plane.

As this object was illuminated by an extended, bright polarised source in the background, we are still able to detect Faraday rotation and assume a Faraday screen interaction. Point-source RMs probe all Faraday depths along the line of sight, which becomes very complex near the Galactic plane. Secondly, the magnetic fields detected here are weak relative to most of the previous measurements from other ISM sources reported in the literature. As such, we have shown this method to be useful in the detection of weak magnetic fields in large and diffuse areas.

Acknowledgements

The authors would like to acknowledge the significant contributions of the reviewer, Katia Ferriere, whose comments have made a substantial improvement to this work.

A.T. acknowledges the support of the Australian Government Research Training Program (RTP) Scholarship. N. M. M.-G. acknowledges the support of the

Australian Research Council through grant FT150100024. C.F. gratefully acknowledges funding provided by the Australian Research Council's Discovery Projects (grants DP150104329 and DP170100603) and the ANU Futures Scheme. The Dunlap Institute is funded through an endowment established by the David Dunlap family and the University of Toronto. B.M.G. acknowledges the support of the Natural Sciences and Engineering Research Council of Canada (NSERC) through grant RGPIN-2015-05948, and of the Canada Research Chairs program. The parallel data analysis presented in this work used high performance computing resources provided by the Australian National Computational Infrastructure (grant ek9), and the Pawsey Supercomputing Centre with funding from the Australian Government and the Government of Western Australia, in the framework of the National Computational Merit Allocation Scheme and the ANU Allocation Scheme. The Parkes Radio Telescope is part of the Australia Telescope National Facility, which is funded by the Commonwealth of Australia for operation as a National Facility managed by CSIRO. This work has been carried out in the framework of the S-band Polarisation All Sky Survey (S-PASS) collaboration.

The authors acknowledge the use of the following archival data:

- The Legacy Archive for Microwave Background Data Analysis (LAMBDA), part of the High Energy Astrophysics Science Archive Centre (HEASARC). HEASARC/LAMBDA is a service of the Astrophysics Science Division at the NASA Goddard Space Flight Centre.

- The Southern H-Alpha Sky Survey Atlas (SHASSA), which is supported by the National Science Foundation.

- The Wisconsin H α Mapper and its H α Sky Survey, funded primarily by the National Science Foundation. The facility was designed and built with the help of the University of Wisconsin Graduate School, Physical Sciences Lab, and Space Astronomy Lab. NOAO staff at Kitt Peak and Cerro Tololo provided on-site support for its remote operation.

3.7 Appendix

3.7.1 T-T Plot

There is an increase in the slope of the T-T plot above $b \approx -10\,\mathrm{deg}$, as shown in Figure 3.17, which occurs above $T_{\mathrm{CHIPASS}} \approx 5\,\mathrm{K}$. Additionally, there are multiple 'bifurcations' present in the scatter, As such, the slope, as fitted to this T-T plot, does not correspond to the synchrotron emission alone. Additionally, there is significant noise present below $b \approx -10\,\mathrm{deg}$ in the WMAP data; resulting in a poor fit with a coefficient of determination $R^2 = 0.5$.

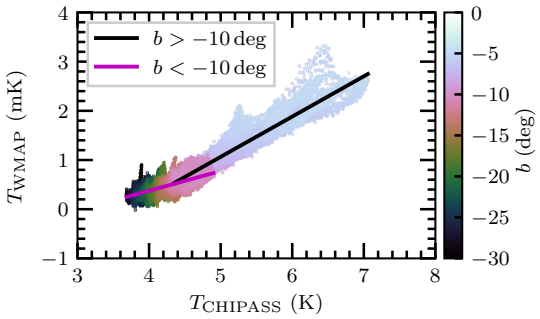

Figure 3.17: T-T plot: 1.4 GHz (CHIPASS) against 23 GHz (WMAP) total intensity (Stokes I) in the region of GSH 006−15+7. Linear fit to $b > -10\,\mathrm{deg}$ (black): $m = 8.2 \times 10^{-4}$, $\beta = -2.6$, $R^2 = 0.9$. Linear fit to $b < -10\,\mathrm{deg}$ (magenta): $m = 4.0 \times 10^{-4}$, $\beta = -2.8$, $R^2 = 0.5$. Note: point source at $l, b \approx [9\,\mathrm{deg}, -19\,\mathrm{deg}]$ is excluded. Here R^2 is the statistical coefficient of determination. Here we find that the slope of the T-T plot steepens towards the Galactic plane; which is due to non-thermal emission from warm gas in the disc. This emission, as well as emission from point sources, also causes 'filaments' in the T-T plot and increases the overall scatter.

3.7.2 Derivation of path length through shell

To obtain the path length L through GSH 006−15+7 we consider a spherical shell with an inner radius of R_i, a thickness of R_s, and therefore an outer radius of $R_o = R_i + R_s$. We consider both the near and far side of the shell. We also consider the centre of the shell to be at a distance of d_c from the Sun and at a Galactic latitude of $b = b_c$ and longitude $l = l_c$. Initially, we calculate L through the line through the centre of shell at $l = l_c$, and then use axisymmetry to find L over the entire shell. Taking $l = l_c$ we obtain the following equation:

$$R^2 = (r\cos b - d_c \cos b_c)^2 + (r \sin b - d_c \sin b_c)^2 \tag{3.24}$$

Where $R = R_o = R_i + R_s$ for the outer boundary, and $R = R_i$ for the inner boundary. This simplifies to:

$$R^2 = r^2 - 2d_c r[\cos(b - b_c)] + d_c^2 \tag{3.25}$$

Now, solving for r

$$r = d_c \cos(b - b_c) \pm \sqrt{(R^2 - d_c^2 \sin^2(b - b_c))} \tag{3.26}$$

The two exact solutions to this equation correspond to the near (r_-) and far (r_+) intersections with the line of sight. Such solutions only exist within the considered boundary (outer boundary if $R = R_o$ and inner boundary if $R = R_i$). So, the path-length through the shell (L) is the chord between these two boundaries and is given by:

$$L(l_c, b) = (r_+(R_o) - r_+(R_i)) + (r_-(R_i) - r_-(R_o)) \tag{3.27}$$

when the line of sight intersects both boundaries. When the line of sight intersects only the outer boundary the path length is:

$$L(l_c, b) = r_+(R_o) - r_-(R_o) \tag{3.28}$$

To obtain the path-length as a function of l and b ($L(l, b)$), we assume spherical symmetry. Meaning we simply apply our solution for L on the line $l = l_c$ axisymmetrically across the entire region.

3.7.3 Emission Measure map

Figure 3.19 shows the map of EM as obtained using Equation 3.15. This map has been smoothed to the spatial resolution of WMAP and then further smoothed with a 1 deg Gaussian to match the other data used.

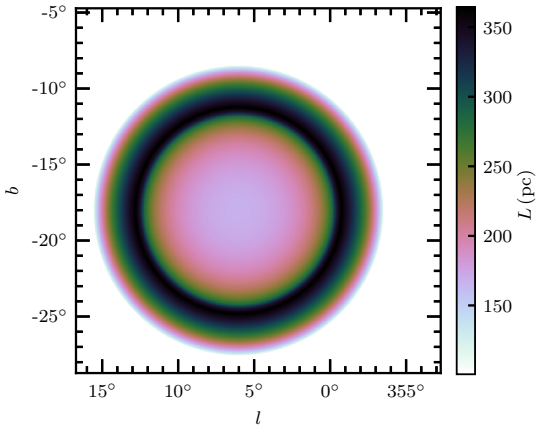

Figure 3.18: A map of the path-length (L) through GSH 006−15+7, as modelled by Equation 3.27 and 3.28. Here we adopt a distance to the shell of $d_c = 1.5\,\mathrm{kpc}$. The inner and outer radii (R_i, R_o) were chosen to match the inner outer bounds of the shell as projected on the sky. These have radii of 6.4 deg and 9.6 deg, respectively.

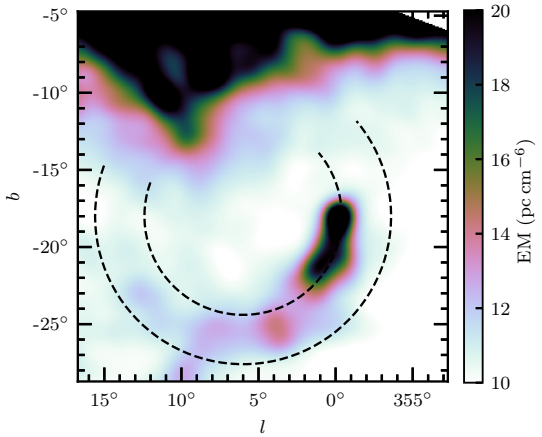

Figure 3.19: Map of emission measure (EM) in the region of GSH 006−15+7. The black dashed lines give the inner and outer bounds of the shell.

4

Faraday tomography in 3D towards an H II region

This chapter is published in Monthly Notices of the Royal Astronomical Society: **Thomson, Alec. J. M.**, Landecker, T. L., Dickey, John M., McClure-Griffiths, N. M., Wolleben, M., Carretti, E., Fletcher, A., Federrath, Christoph, Hill, A. S., Mao, S. A., Gaensler, B. M., Haverkorn, M., Clark, S. E., Van Eck, C. L., and West, J. L., *"Through thick or thin: multiple components of the magneto-ionic medium towards the nearby H II region Sharpless 2-27 revealed by Faraday tomography"*, 2019, MNRAS, 487, 4751.

4.1 Abstract

Sharpless 2-27 (Sh2-27) is a nearby H II region excited by ζOph. We present observations of polarized radio emission from 300 to 480 MHz towards Sh2-27, made

with the Parkes 64 m Radio Telescope as part of the Global Magneto-Ionic Medium Survey. These observations have an angular resolution of 1.35°, and the data are uniquely sensitive to magneto-ionic structure on large angular scales. We demonstrate that background polarized emission towards Sh2-27 is totally depolarized in our observations, allowing us to investigate the foreground. We analyse the results of Faraday tomography, mapping the magnetised interstellar medium along the 165 pc path to Sh2-27. The Faraday dispersion function in this direction has peaks at three Faraday depths. We consider both Faraday thick and thin models for this observation, finding that the thin model is preferred. We further model this as Faraday rotation of diffuse synchrotron emission in the Local Bubble and in two foreground neutral clouds. The Local Bubble extends for 80 pc in this direction, and we find a Faraday depth of -0.8 ± 0.4 rad m^{-2}. This indicates a field directed away from the Sun with a strength of $-2.5 \pm 1.2\,\mu$G. The near and far neutral clouds are each about 30 pc thick, and we find Faraday depths of -6.6 ± 0.6 rad m^{-2} and $+13.7 \pm 0.8$ rad m^{-2}, respectively. We estimate that the line-of-sight magnetic strengths in the near and far cloud are $B_{\parallel,\mathrm{near}} \approx -15\,\mu$G and $B_{\parallel,\mathrm{far}} \approx +30\,\mu$G. Our results demonstrate that Faraday tomography can be used to investigate the magneto-ionic properties of foreground features in front of nearby H II regions.

4.2 Introduction

Magnetic fields are crucial dynamical drivers in the Galactic interstellar medium (ISM). They are responsible for injecting significant energy into the ISM (Heiles & Haverkorn, 2012; Beck & Wielebinski, 2013; Beck, 2015). Magnetic fields play roles in star formation and turbulent gas flows (Padoan & Nordlund, 2011; Federrath & Klessen, 2012; Federrath, 2015), and also have profound consequences for the initial mass function of stars (Offner et al., 2014; Federrath et al., 2014). Despite their importance, much remains unknown regarding both the magnitude and structure of these magnetic fields. This has arisen from the general difficulty in measuring the strength of structure of magnetic fields in the ISM.

Radio spectro-polarimetry is one of the most effective ways to study interstellar magnetic fields (Han, 2017). Linearly polarized emission is produced within the

Milky Way by relativistic electrons emitting synchrotron radiation as they orbit around magnetic fields. At radio frequencies this emission suffers Faraday rotation as it propagates towards the observer through the magneto-ionic medium (MIM). Thus, observations of Galactic polarized radio emission contain a wealth of information on the Milky Way's magneto-ionic structure.

Faraday rotation causes the polarization angle (χ) of an electromagnetic wave to rotate from an initial angle (χ_0) at wavelength λ:

$$\chi(\lambda^2) = \chi_0 + \lambda^2\phi, \tag{4.1}$$

where ϕ is the Faraday depth (Burn, 1966; Brentjens & de Bruyn, 2005):

$$\phi(d) \equiv 0.812 \int_d^0 n_e(r) B_\parallel(r) dr \left[\mathrm{rad\,m^{-2}}\right], \tag{4.2}$$

and n_e is the thermal electron density in $\mathrm{cm^{-3}}$, $B_\parallel$ is the line-of-sight (LOS) component of the magnetic field in μG, and dr is the incremental distance along the LOS in pc to a source at distance d. In the case of a single rotating region in front of a polarized source, referred to as a 'Faraday screen', the Faraday depth is equivalent to the rotation measure (RM):

$$\mathrm{RM} \equiv \frac{d\chi}{d(\lambda^2)} \left[\mathrm{rad\,m^{-2}}\right]. \tag{4.3}$$

We follow the definitions of Brentjens & de Bruyn (2005) throughout, we quantify Faraday rotation using Faraday depth, and we refer to RMs from extragalactic sources. Due to the strong wavelength dependence, low-frequency radio observations of polarized emission are very sensitive for measuring Faraday rotation in the magneto-ionic medium (MIM). The determination of the Faraday depth from Galactic synchrotron emission is non-trivial, however, due both to the complexity of the Galactic MIM and the mixing of emission and Faraday rotation in the same volume. This can be overcome by mapping polarization across many frequency channels in a technique called 'Faraday tomography'. We outline this technique in Section 4.3.

The large angular scales of diffuse Galactic polarized emission calls for global radio spectro-polarimetric survey. The Global Magneto-Ionic Medium Survey (GMIMS,

Wolleben et al., 2009) was devised specifically to probe the MIM of the Milky Way. This survey will ultimately measure diffuse polarized emission across the entire sky from 300 MHz to 1.8 GHz using single-dish telescopes, giving excellent sensitivity to a wide range of Faraday structures. Results from the GMIMS high-band North (GMIMS-HBN, Wolleben et al., 2010a), taken with the DRAO 26 m telescope, have been used directly to investigate the magneto-ionic properties of a nearby H I shell (Wolleben et al., 2010b), the North Polar Spur (Sun et al., 2015), and the Fan Region (Hill et al., 2017), and they are incorporated into other work analysing all-sky emission (e.g. Dickey et al., 2019; Zheng et al., 2017).

The nearby H II region Sharpless 2-27 (Sh2-27) appears in various radio polarization observations. Sh2-27 surrounds the star ζOph which is located at $[l, b] \sim [6.3°, +23.6°]$ (van Leeuwen, 2007). The region subtends about 10° on the sky and is readily identifiable in H α images. H II regions are highly ionized regions of the ISM, and thus have a greater thermal electron density over the typical Galactic warm neutral medium Ferrière (2001). In the presence of magnetic fields H II regions have a strong effect on observations of radio polarization (e.g. Gaensler et al., 2001). At 2.3 GHz in the S-band Polarization All Sky Survey (S-PASS, Carretti et al., 2019) Sh2-27 has been identified as a Faraday screen, modulating the polarization angle but not producing polarized emission itself (Robitaille et al., 2017, 2018; Iacobelli et al., 2014). In polarization observations at 1.4 GHz, such as GMIMS-HBN, Sh2-27 can be identified as a depolarizing region. Wolleben et al. (2010b) used the depolarization of Sh2-27 to constrain the distance of polarized emission through a nearby H I shell. The magneto-ionic properties of Sh2-27 were directly investigated by Harvey-Smith et al. (2011) using the NVSS catalogue of point-source RMs (Taylor et al., 2009). This region stands out in the Taylor et al. (2009) catalogue, and derivative maps such as Oppermann et al. (2012, 2015), due to high values of RM from extragalactic sources seen through it.

In this paper we present results from the low-band Southern Global Magneto-Ionic Medium Survey (GMIMS-LBS) towards Sh2-27. Using these data we are able to isolate a column of foreground MIM for analysis with Faraday tomography. The distance to Sh2-27 is known to be ~ 180 pc (Gaia Collaboration et al., 2016, 2018), which means we are able to map results from polarization observations within that

distance. We provide additional background and definitions we use that are specific to radio polarimetry in Section 4.3. We describe the GMIMS-LBS observations in Section 4.4, including the application of Faraday tomography. In Section 4.5 we present the results of these observations towards Sh2-27 and show that it is depolarizing the background emission in the GMIMS-LBS band. We conclude that Sh2-27 is acting as a 'depolarization wall' for extended structures, and can therefore be used to constrain distances in Faraday tomography. We describe the structure in the GMIMS-LBS Faraday depth cubes towards Sh2-27 in Section 4.5.2. We analyse how this structure maps to distance along the LOS in Section 4.6. In Section 4.6.1 we consider a Faraday thin interpretation in combination with data on the local ISM to both reconstruct the magnetic field structure and estimate the magnetic strength along the LOS. In Section 4.6.2 we consider an alternate model using Faraday thick structures. We discuss our results in Section 4.7, and provide a summary and conclusion in Section 4.8.

4.3 Background

4.3.1 Faraday Tomography

It is highly unlikely that any given LOS in the Galaxy would be as simple as a Faraday screen. With this in mind, the technique of Faraday tomography (also known as RM synthesis) (Burn, 1966; Brentjens & de Bruyn, 2005; Heald et al., 2009) was developed. This method applies a discrete Fourier transform to the complex polarization as a function of λ^2. The primary result of this technique is the Faraday dispersion function ($F(\phi)$), the polarized flux as a function of Faraday depth. This function is spectral in nature, and we refer to it as the Faraday spectrum. The output parameters of Faraday tomography are set by the behaviour of the 'RM spread function' (RMSF). The effective resolution of the Faraday spectra ($\delta\phi$) is given by the width of the RMSF at full-width of half maximum (FWHM) (Brentjens & de Bruyn, 2005):

$$\delta\phi \approx \frac{2\sqrt{3}}{\Delta\lambda^2} \tag{4.4}$$

where $\Delta\lambda^2 = \lambda^2_{\rm max} - \lambda^2_{\rm min}$ is the bandwidth in λ^2-space, and $\lambda^2_{\rm max}$ and $\lambda^2_{\rm min}$ are the maximum and minimum observed λ^2, respectively. The largest observable value of Faraday depth ($\phi_{\rm max}$) is set by the width of the observed λ^2 channels ($\delta\lambda^2$):

$$\phi_{\rm max} \approx \frac{\sqrt{3}}{\delta\lambda^2} \tag{4.5}$$

Finally, the smallest observed λ^2 sets the maximum scale observable in Faraday depth space:

$$\phi_{\text{max-scale}} \approx \frac{\pi}{\lambda^2_{\rm min}} \tag{4.6}$$

Sources that produce a broad feature in the Faraday spectrum are referred to as 'Faraday thick'. Specifically, a source is 'thick' if $\lambda^2\Delta\phi \gg 1$, where $\Delta\phi$ is the extent of the source in $F(\phi)$ observed at λ^2 (Brentjens & de Bruyn, 2005). Such features can be modelled as a mixture of a coherent and turbulent magnetic field that produces both synchrotron emission and Faraday rotation of background polarized emission (Burn, 1966; Sokoloff et al., 1999). Conversely, a feature is Faraday thin if $\lambda^2\Delta\phi \ll 1$. Faraday thin features can be modelled as a δ function in the Faraday spectrum.

Observational restrictions on wavelength coverage have a strong effect on Faraday tomography. These effects can be mitigated using deconvolution techniques. Currently, the most popular algorithm is `RM-CLEAN` (Heald et al., 2009), which replaces the 'dirty' RMSF with a smooth Gaussian restoring beam. This reduces the effect of sidelobes that are present in the 'dirty' Faraday spectra.

4.3.2 Depolarization

Depolarization is a common feature of almost all radio polarization observations, with the exception of polarized emissions from pulsars. This effect can occur through three primary mechanisms (Burn, 1966; Tribble, 1991; Sokoloff et al., 1999): depth, beam, and bandwidth depolarization. Depth depolarization refers to the effect of Faraday thick sources in λ^2 space. Such sources lose polarized flux as a function of λ^2. Beam and bandwidth depolarization arise from observational parameters. In the former case, the variation of Faraday depth occurs spatially within the beam of the telescope. Bandwidth depolarization occurs when significant Faraday rotation

occurs within one frequency channel.

In low-frequency observations depolarization features become far more common and are often associated with ionised regions of the ISM, such as H II regions. As these features depolarize emission from behind them, they can be used as distance indicators in radio polarization observations.

Despite their higher Faraday resolution, low-frequency observations can face an issue by not observing polarized flux at short λ^2. The result of missing this emission is that sources with a Faraday thickness greater than $\phi_{\text{max-scale}}$ are 'resolved out', whereby broad features are lost leaving only narrow features present in Faraday depth space. In practice this can give rise to an ambiguity between a Faraday thick feature or a number of Faraday thin features.

A 'depolarization wall' (Hill, 2018) is a form of spatially discrete depolarization. Whilst conceptually similar to the 'polarization horizon' (Uyaniker et al., 2003), a depolarization wall arises when a specific and discrete depolarising object (such as an H II region) lies along the LOS. When a LOS passes through a wall the background polarized emission is totally depolarized. Whether or not an object acts as a wall in a given observation will depend on both the observed λ^2 and the angular resolution. Polarization walls have a great utility for analysing results of Faraday tomography. Despite the large amount of information contained within Faraday spectra, mapping that structure to physical space is challenging. If the distance to a depolarization wall can be determined, however, that places a constraint on the distance along which the observed Faraday structure occurs. This is highly analogous to the use of H II regions as free-free absorbers of Galactic synchrotron emission (e.g. Nord et al., 2006; Su et al., 2018).

4.4 Observations

4.4.1 GMIMS Low-Band South

Recently we completed GMIMS-LBS with the Parkes 64 m telescope. A complete description of these observations is provided in Wolleben et al. (submitted). These observations measure diffuse polarized emission (Stokes I, Q, and U) across the entire Southern sky from 300 MHz to 480 MHz with a spectral resolution of 0.5 MHz.

Here we analyse the Faraday spectral cubes from this survey. These spectra have been deconvolved using `RM-CLEAN` (Heald et al., 2009). We summarise the properties of these data, including the parameters resulting from Faraday tomography, in Table 4.1. The long wavelengths and high spectral resolution result in a unique property for this survey: a very fine Faraday resolution of $\delta\phi = 6.2\,\mathrm{rad\,m^{-2}}$, smaller than the Faraday max-scale of the survey. This is the first large-scale sky survey with $\phi_{\text{max-scale}} > \delta\phi$ at frequencies above 250 MHz. This property means that *only* features that are broader than $\phi_{\text{max-scale}}$ will be resolved out. Without this property, the observed spectra become more complex (Dickey et al., 2019) and their interpretation more difficult.

It is also important to consider the behaviour of noise in Faraday spectra. The RMS noise in the Stokes Q and U spectra is $\sigma_{QU} = 60\,\mathrm{mK}$. We primarily consider the absolute value of the Faraday dispersion function, which represents the polarized intensity. When analysing the polarized intensity the variance (σ_{PI}) is given by a Rayleigh distribution (Wardle & Sramek, 1974; Heald et al., 2009):

$$\sigma_{\mathrm{PI}} = \sqrt{\frac{4-\pi}{2}}\sigma_{QU} \approx 0.66\sigma_{QU}, \tag{4.7}$$

in the low signal-to-noise limit. For increasing signal-to-noise the variance approaches a Gaussian distribution and $\sigma_{\mathrm{PI}} = \sigma_{QU}$.

4.4.2 Complementary data

We use a number of other datasets to complement our GMIMS-LBS observation. Finkbeiner (2003) combines data from the Virginia Tech Spectral Line Survey (VTSS, Dennison et al., 1998), the Southern H-Alpha Sky Survey (SHASSA, Gaustad et al., 2001) and the Wisconsin H-alpha mapper (WHAM, Haffner et al., 2003) to produce an all-sky H α intensity image with a resolution of 6′. We use these data to identify Sh2-27 and other H II regions around it.

The Taylor et al. (2009) catalogue provides measurements of RM towards extragalactic point sources as measured by the Very Large Array (VLA). These data are derived from NRAO VLA Sky Survey (NVSS, Condon et al., 1998), and provide a source density of $\sim 1\,\mathrm{deg^{-2}}$. Since these data were taken at L-band, and

Table 4.1: Summary of the observational parameters of the GMIMS-LBS (Wolleben et al. submitted, Dickey et al., 2019). [a] – This range is determined by the high and low signal-to-noise limits. [b] – We select these values during Faraday tomography.

Survey parameter	Symbol	min.	max.
Declination [°]	δ	-90	$+20$
Beamwidth [′]		79.4	83.6
Frequency [MHz]	f	300.25	479.75
Frequency resolution [MHz]	δf	0.5	
Wavelength-squared [m^2]	λ^2	0.391	0.999
λ^2 bandwidth [m^2]	$\Delta\lambda^2$	0.608	
λ^2 resolution [m^2]	$\delta\lambda^2$	3.32×10^{-3}	
Stokes Q and U RMS noise [mK]	σ_{QU}	60	
PI RMS noise[a] [mk]	σ_{PI}	39	60
Faraday resolution [rad m^{-2}]	$\delta\phi$	6.2	
Max. Faraday depth [rad m^{-2}]	ϕ_{max}	1.3×10^3	
Faraday max. scale [rad m^{-2}]	$\phi_{\mathrm{max\text{-}scale}}$	8.0	
ϕ range[b] [rad m^{-2}]		-100	$+100$
ϕ sampling[b] [rad m^{-2}]		0.5	

with 45″resolution, they are far less susceptible to depolarization effects. We are therefore able to investigate the Faraday rotation through Sh2-27 with these data.

The STructuring by Inversion the Local Interstellar Medium project[1] (STILISM, Lallement et al., 2014; Capitanio et al., 2017; Lallement et al., 2018) provides information on the three-dimensional structure of the nearby ISM. These data are produced using dust reddening of starlight (e.g. Vergely et al., 2010; Lallement et al., 2014; Green, 2014; Capitanio et al., 2017; Green et al., 2018; Lallement et al., 2018), with stellar parallax distances from *Gaia*, to map dust features in the nearby ISM. We use the data cube from this project, which covers a 4 kpc by 4 kpc by 600 pc grid around the Sun.

4.5 Results

4.5.1 Depolarization from Sh2-27

Polarized intensity is very low in GMIMS-LBS towards Sh2-27. The depolarizing effect of Sh2-27 in our data can be seen in Figure 4.1, which shows the peak polarized intensity from the `CLEAN` Faraday spectra in the region towards Sh2-27. We also

[1] https://stilism.obspm.fr/, version 4.1, accessed October 2018

show the combined SHASSA and WHAM H α intensity from Finkbeiner (2003) as white contours. We identify two important features from this map. First, while the area towards Sh2-27 is clearly reduced in polarized intensity with respect to the surrounding emission, the polarized intensity is well above the noise (60 mK). Second, a strong but narrow depolarization feature extends out to the right from the edge of the Sh2-27's depolarization region. We will address these features in turn with respect to several depolarization mechanisms.

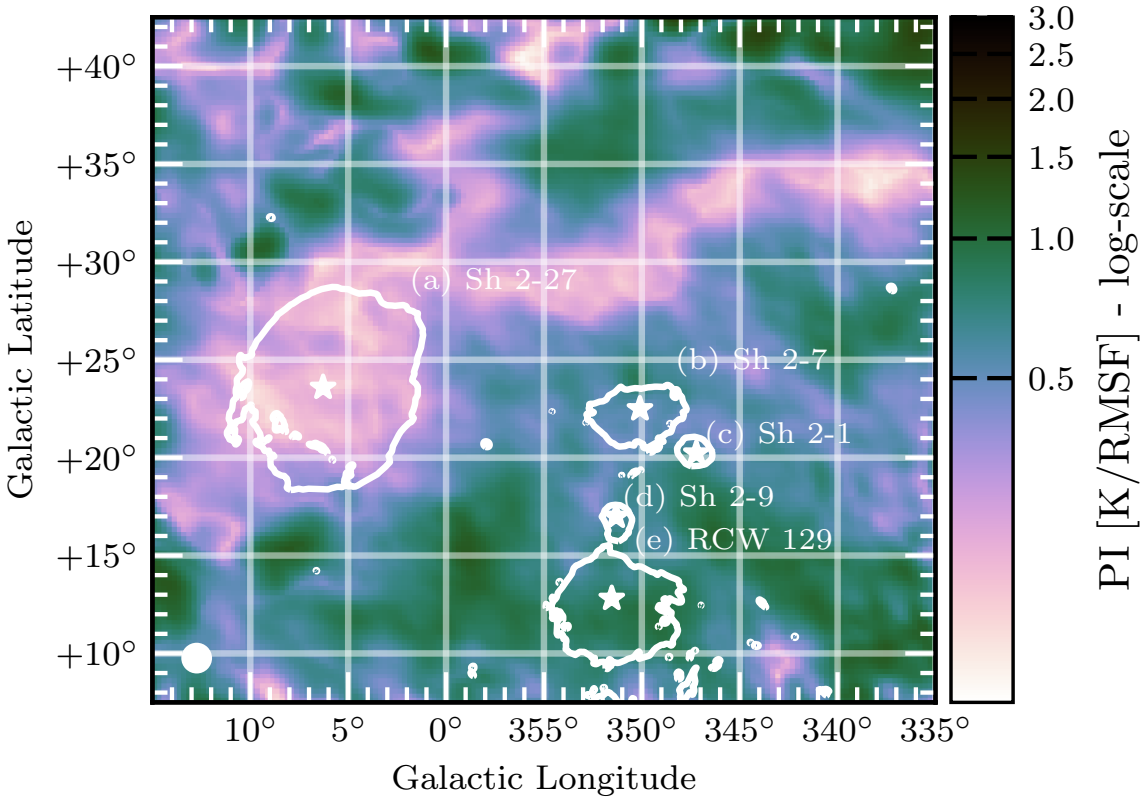

Figure 4.1: The peak PI in the Faraday cube towards Sh2-27. Contours are H α intensity from Finkbeiner (2003) at 30 R. We label the five visible H II regions, and their corresponding central stars (white stars), in this region as: (a) – Sh2-27 / ζOph, (b) – Sh2-7 / δSco, (c) – Sh2-1 / πSco, (d) – Sh2-9 / σSco, (e) – RCW 129 / τSco. We show the beam as a white circle in the lower-left corner. We note that in H α there are four other nearby H II regions that appear close on the sky to Sh2-27. In contrast to Sh2-27, these H II regions have no discernible effect on the polarization data. We identify a depolarization wall that occurs approximately within the H α contour of Sh2-27. We further find that the depolarized feature extending horizontally across this map is a depolarization canal.

GMIMS-LBS is able to probe magneto-ionic effects in great detail due to the long wavelengths observed. Consequently, these observations are also more sensitive to depolarization features. A Faraday depth of about $\pm 940\,\mathrm{rad\,m^{-2}}$ would be required

to completely depolarize our lowest frequency observation through bandwidth depolarization. Such extreme values are rarely observed away from the Galactic plane. We therefore do not expect bandwidth depolarization to affect our observations.

Given the large beam of GMIMS-LBS (81 arcmin at 300 MHz), beam depolarization is likely to be a significant effect. We quantify the beam depolarization towards Sh2-27 using point-source RMs. These values probe Faraday rotation along the entire LOS out to the edge of the Galaxy, thus allowing the investigation of the intervening ISM.

Here we apply a similar analysis to Harvey-Smith et al. (2011), but instead we will obtain the variation in Faraday depth across Sh2-27, and thus estimate the beam depolarization in GMIMS-LBS using the Taylor et al. (2009) catalogue. We adopt the same boundary conditions and background RM correction as Harvey-Smith et al. (2011), given in their Table 2. This results in 65 background-corrected RMs through Sh2-27, which we show in Figure 4.2(a). We also show the distribution of these RMs in Figure 4.2(b). From these RMs we find a median value of $-166\,\mathrm{rad\,m^{-2}}$ and a standard deviation of $\sigma_{\mathrm{RM}} = 78\,\mathrm{rad\,m^{-2}}$. To analyse how σ_{RM} changes across angular scales we compute the second-order structure function ($\mathrm{SF_{RM}}$) of the RMs on Sh2-27, as defined by Haverkorn et al. (2004):

$$\mathrm{SF_{RM}}(\Delta\theta) = \langle[\mathrm{RM}(\theta) - \mathrm{RM}(\theta + \Delta\theta)]^2\rangle, \tag{4.8}$$

where $\Delta\theta$ is the angular distance on the sky between two LOS, and $\langle \ldots \rangle$ represents the average on all pairs of separation $\Delta\theta$. We estimate the errors in the structure function by utilising Monte-Carlo error propagation. Assuming that the errors in the Taylor et al. (2009) RMs are Gaussian distributed, we take 1000 samples of a Gaussian distribution for each RM on Sh2-27 and propagate the entire distribution through the $\mathrm{SF_{RM}}$ computation. We find that the function remains flat from the angular scale of Sh2-27 ($\sim 10^\circ$) to scales smaller than the beamwidth of our observations. We can therefore expect that the variation in RM as computed across the entire Sh2-27 region will be about the same as the variation within the GMIMS-LBS beam.

We estimate that the variance in Faraday depth due to Sh2-27 can be related to

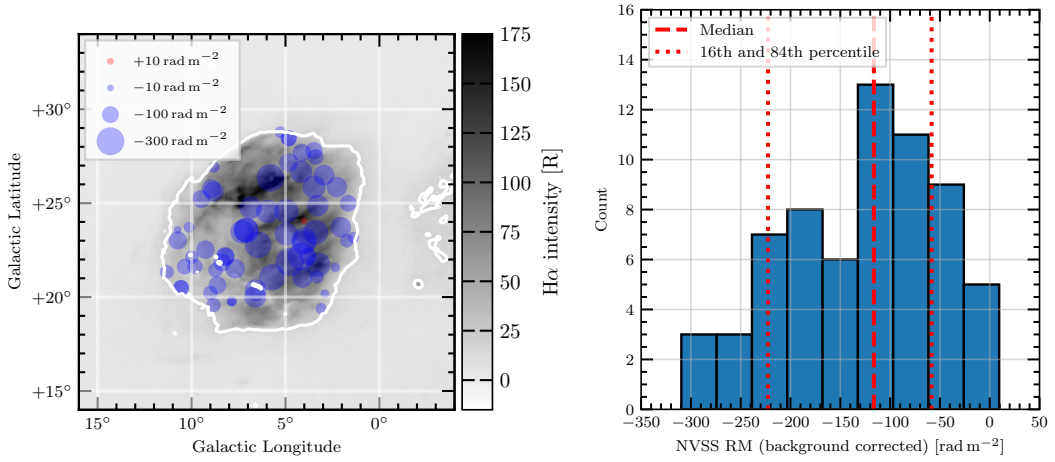

(a) (b)

Figure 4.2: The Taylor et al. (2009) RMs towards Sh2-27. Here, we apply the selection criteria and background correction of Harvey-Smith et al. (2011). (a) The spatial distribution of RMs on Sh2-27. (b) The histogram of the RM distribution towards Sh2-27. We also show the median RM (dashed line), and 16th and 84th percentiles (dotted lines). We use these data to demonstrate that Sh2-27 is a depolarization wall to the diffuse emission measured by GMIMS-LBS. The high RM values shown here are not detected in our Faraday spectra as polarized emission from behind the H II region is totally depolarized.

the variation in RM by:

$$\sigma^2_{\rm RM} = \sigma^2_{\rm H\,II} + \sigma^2_{\rm gal} + \sigma^2_{\rm exgal} + \sigma^2_{\rm err} \tag{4.9}$$

where $\sigma_{\rm H\,II}$ is the variation in Faraday depth caused by turbulent structures in the H II region, $\sigma_{\rm gal} \approx 8/\sin(b) \approx 20\,{\rm rad\,m^{-2}}$ (Schnitzeler, 2010) is the variation along the rest of the LOS through the Galaxy, $\sigma_{\rm exgal} \approx 6\,{\rm rad\,m^{-2}}$ (Schnitzeler, 2010) is the variation in RM due to contribution from the intrinsic Faraday rotation of the extragalactic source, and $\sigma_{\rm err} = 10.1 \pm 0.4$ is the measurement error in RM. In this way we estimate the variation in Faraday depth of Sh2-27 to be $\sigma_{\rm H\,II} \approx 74 \pm 1\,{\rm rad\,m^{-2}}$. The degree of beam depolarization can be quantified by either the Burn (1966) depolarization law, or by the Tribble (1991) depolarization law if the depolarization (compared to the intrinsic polarisation fraction) is < 0.5:

$$\mathrm{DP}_{\rm Burn} = e^{-2\sigma^2\lambda^4} \tag{4.10}$$

$$\mathrm{DP}_{\rm Tribble} = \frac{1}{2\sqrt{2}\sqrt{N}\sigma\lambda^2} \tag{4.11}$$

where DP is the depolarization fraction (the ratio of observed to intrinsic PI), σ is the variation in Faraday depth, λ is the observed wavelength, and N is the number of independent, randomly varying areas within the beam. Across our band, the Burn depolarization factor is $< \exp(-1700)$ and the Tribble depolarization factor is $< 1/(130\sqrt{N})$ (< 0.008 for $N = 1$). In either case, the emission behind Sh2-27 is strongly beam depolarized in our survey. We find, however, a significant polarized signal towards Sh2-27. Since an H II region does not produce polarized emission itself we are able to proceed treating Sh2-27 as a 'depolarization wall' and we conclude that the polarized emission that we observe must arise between the Sun and Sh2-27.

Hill (2018) does note, however, that it is possible for polarization to make its way through a depolarizing volume, such as an H II region, using a semi-analytic mock observation matched to GMIMS-LBS. Their model included a lower-density H II region than Sh2-27. We ran a version of their model with a density and magnetic field which matches estimates for Sh2-27 (Harvey-Smith et al., 2011). Some polarized radiation does leak through at the Faraday depth of the H II region in the model, but the polarized intensity is $\lesssim 10\%$ of the background polarized intensity. In the model, there are components of the Faraday spectrum at Faraday depths comparable to what would be observed for background sources; we do not see components at the Faraday depths seen by Harvey-Smith et al. (2011), so the depolarization may be more wall-like than in the Hill (2018) model.

We identify the large depolarized feature that extends to the right from Sh2-27 as a depolarization canal. Depolarization canals are a common feature of many polarization maps. These canals can occur from a variety of physical scenarios, but most commonly occur through one of two mechanisms (Fletcher & Shukurov, 2006, 2007): either a strong gradient or discontinuity in Faraday depth across the sky, or depth depolarization along the LOS. Both of these mechanisms can produce depolarization which is the width of the telescope beam. In Figure 4.3(a) we show an image of the Faraday depth at the peak PI in the range $-3 < \phi < +3\,\mathrm{rad\,m^{-2}}$. We select this restricted range in order to find the peak around $0\,\mathrm{rad\,m^{-2}}$. The Faraday depth structure towards Sh2-27 is different to that along the feature. On Sh2-27 the peak ϕ is relatively smooth and constant ($\phi < 0$). In contrast, there is a clear discontinuity in ϕ along the canal, as well as a gradient towards Galactic North. We

confirm that these discontinuities are not artefacts of two peaks of similar heights by inspecting the first moment of the Faraday spectra in Figure 4.3(b). This map shows the same discontinuities and gradients as the peak ϕ map, which indicates that these are true features of the Faraday depth structure. Areas with a discontinuity in ϕ show depolarization on the order of a beamwidth, which leads us to the conclusion that the feature is a depolarization canal. We note that the canal is slightly wider than the beamwidth, but this is explained by a combination of a discontinuity and a gradient in ϕ. Both of these effects generate depolarization canals, and both appear in close proximity in the peak ϕ map. The depolarizing effects then blend into a wider canal. We conclude that this feature is distinct from Sh2-27 and we do not discuss it further.

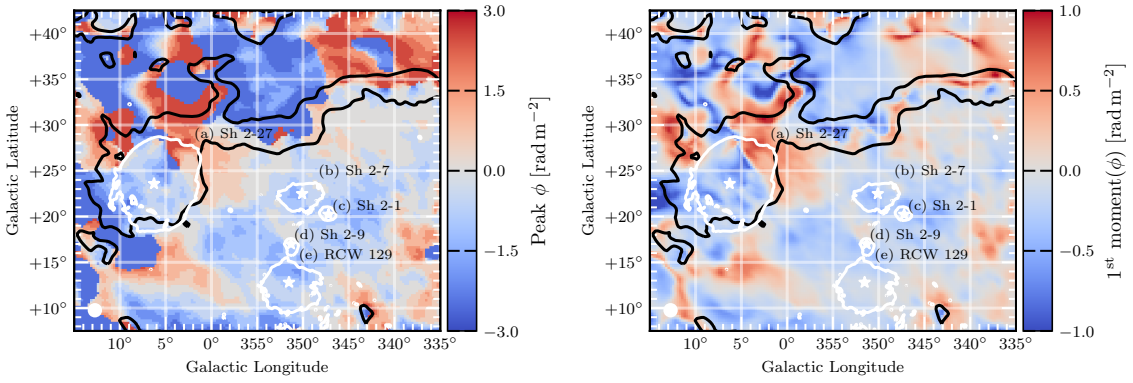

(a) (b)

Figure 4.3: (a): The Faraday depth at the peak PI in the region of Sh2-27 in the range $-3 < \phi < +3\,\mathrm{rad\,m^{-2}}$. (b): The first moment of the Faraday spectrum computed in the range $-3 < \phi < +3\,\mathrm{rad\,m^{-2}}$. White contours are H$\,\alpha$ intensity from Finkbeiner (2003) at 30 R. Black contours are of the peak PI (for all ϕ) at $0.3\,\mathrm{K\,RMSF^{-1}}$. We label the five visible H II regions, and their corresponding central stars (white stars), as in Figure 4.1. We show the beam as a white circle in the lower-left corner. The range $-3 < \phi < +3\,\mathrm{rad\,m^{-2}}$ is used to select only the peak around $0\,\mathrm{rad\,m^{-2}}$.

4.5.2 Faraday Spectra Towards Sh2-27

We find a consistent structure in the Faraday spectrum towards Sh2-27, shown in Figure 4.4. In the left-hand panel of Figure 4.4 we show azimuthal averages (through a full rotation) of the Faraday spectrum in polarized intensity as a function of radius on the sky from ζOph. For the region towards Sh2-27 we find a triple-peak structure, which is absent in the regions away from the H II region. In the middle panel of

Figure 4.4 we can see that each peak is well above our noise threshold and well fit by a single CLEAN component. For comparison, we show the RMSF for the same region. It is clear that the triple-peak structure is not generated by sidelobes in the RMSF. The polarized intensity also increases significantly away from Sh2-27, correlating with the loss of the triple-peak structure. As the foreground structure is unlikely to correlate precisely with the boundary of Sh2-27, we conclude that the foreground structure we probe towards Sh2-27 is overwhelmed by higher intensity background emission in directions away from the depolarization wall.

To identify the Faraday depth of the peaks on Sh2-27 we first apply the peak-finding algorithm from Duarte (2015) to find the Faraday-resolution-limited peaks in the azimuthally averaged spectra. We only search for peaks above our noise threshold of 60 mK. From this we find the triple-peak structure extends radially for 5.5° from ζOph, which is almost exactly the radius of Sh2-27 in H α. We fit three Gaussians to the triple-peak region excluding structures below our noise threshold and obtain the means of the three peaks weighted by the inverse variance from the radial profile, 1: $-7.4\pm0.4\,\mathrm{rad\,m^{-2}}$, 2: $-0.8\pm0.4\,\mathrm{rad\,m^{-2}}$, and 3: $+6.2\pm0.4\,\mathrm{rad\,m^{-2}}$.

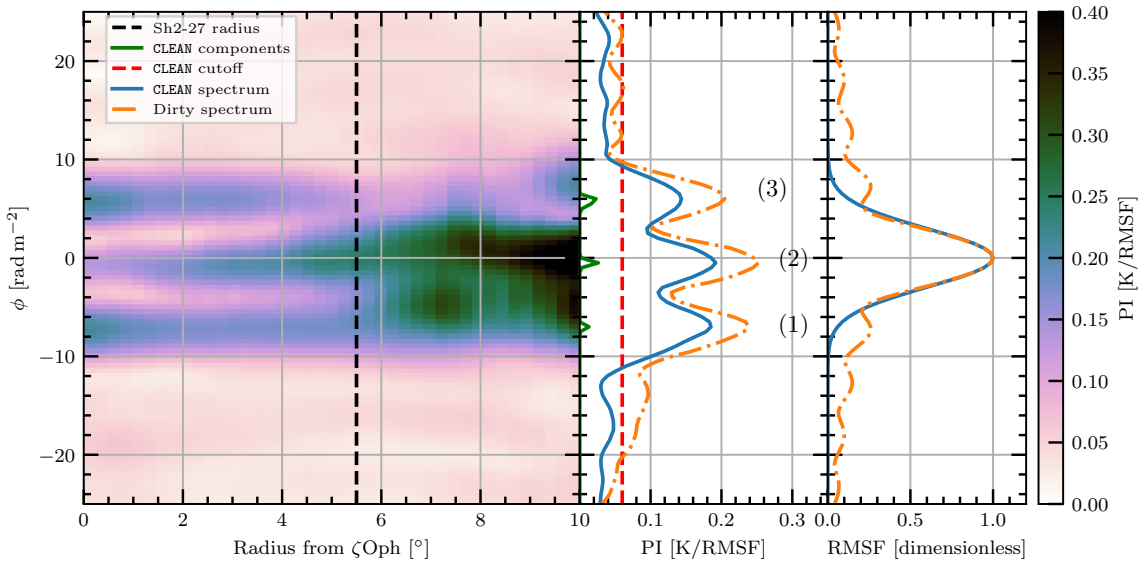

Figure 4.4: The Faraday depth structure towards Sh2-27. Left panel: Azimuthal averages of the Faraday spectrum as a function of radius from ζOph. Middle panel: Median CLEAN and dirty Faraday spectrum, and CLEAN components, on the Sh2-27 region (as defined by Harvey-Smith et al. (2011)). We also label the first, second, and third primary peaks. Right panel: Median dirty and CLEAN RMSF on the Sh2-27 region.

4.6 Analysis

When multiple peaks are present in a low-frequency Faraday spectrum two primary interpretations are possible: either the features are of separate origin, or the peaks arise from a Faraday thick medium which has been resolved out. We follow the method of Van Eck et al. (2017) (hereafter CVE17) for separating these scenarios. We estimate the distance to the front of Sh2-27 using the distance to ζOph. We use the parallax distance to this star from the *Gaia* DR2 survey (Gaia Collaboration et al., 2016, 2018), specifically the error-corrected distance estimates provided by Bailer-Jones (2015), 182^{+53}_{-33} pc. Taking the region to be a sphere centred on ζOph with an angular radius of 5.5° on the sky, we find the distance to the front of the region is 164^{+48}_{-30} pc.

4.6.1 Faraday Thin Models Towards Sh2-27

In this section we present a Faraday thin model of the foreground ISM towards Sh2-27, and show that it can accurately reproduce the observed Stokes Q and U spectra as a function of λ^2. We also consult additional data which can give information on the structure of the foreground column of ISM.

In general, the complex polarization of a Faraday thin component is given by:

$$\mathcal{P}(\lambda^2) = \exp[2i(\chi_0 + \phi_0\lambda^2)], \tag{4.12}$$

where χ_0 is the initial polarization angle of the emission and ϕ_0 is the Faraday depth of the component. We obtain the de-rotated χ_0 for peaks 1, 2, and 3 using:

$$\chi_0 = \chi_1 - \phi_0\lambda_0^2 \mod 180°, \tag{4.13}$$

where χ_1 is the polarization angle at the peak in the Faraday spectrum, and λ_0^2 is the de-rotated wavelength-squared as per Brentjens & de Bruyn (2005). We construct model spectra as the sum of three Faraday thin components using the Faraday depth of each peak, their corresponding initial angles, and amplitudes of 0.18 K. We show both the average Stokes Q, U, and PI λ spectrum on Sh2-27 and the Faraday thin model in Figure 4.5. We have not used any fitting routine, rather we have simply

constructed the model from the average values we infer from the Faraday spectrum.

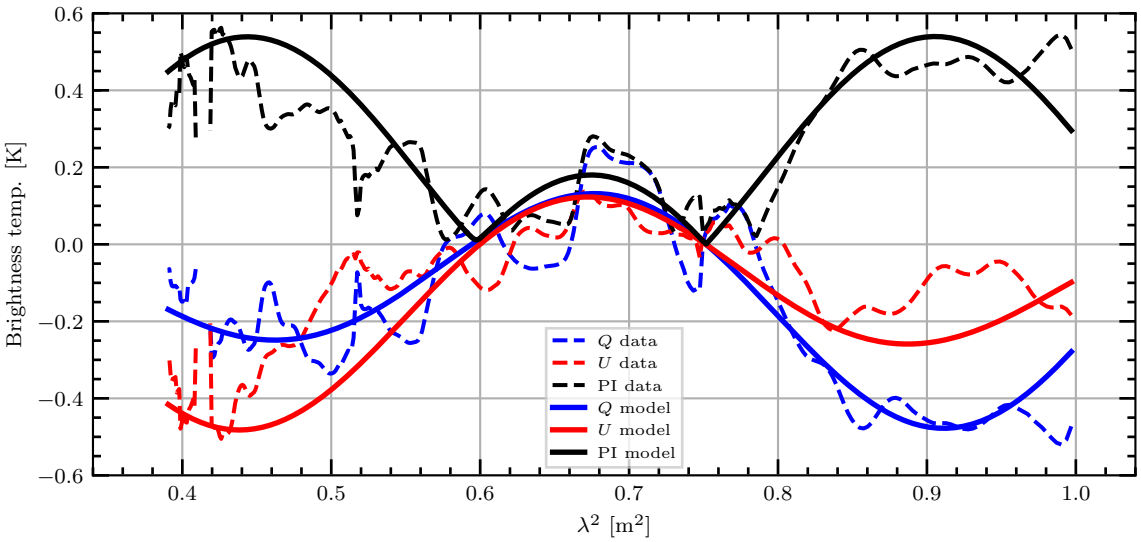

Figure 4.5: Faraday thin model spectra towards Sh2-27. Dashed lines: Average Stokes Q, U, and PI λ^2 spectra towards Sh-27 from GMIMS-LBS. Solid lines: Faraday thin model derived from the average Faraday spectrum.

There are two factors to consider as we construct a physical model of MIM along the LOS. We must consider where the polarized emission arises and determine to what degree the Faraday rotation occurs. We make this consideration under the constraint of the $\sim 160\,\mathrm{pc}$ path to the front of Sh2-27. Meaning that we are analysing small, localised structures, with a size scale much less than a kiloparsec. We will first consider the sources of Faraday rotation before considering the source of polarized emission. A Faraday thin model does not necessarily exclude mixed emission and rotation, but for a model to be considered Faraday thin in our context the Faraday thickness should should not exceed the $\phi_{\text{max-scale}}$ of our observations.

The most likely contributors in the ISM to Faraday rotation of low frequency polarized emission are the cold and warm neutral medium (CNM and WNM), the warm ionised medium (WIM), and the hot ionised medium (HIM). There are no large molecular clouds towards Sh2-27, as indicated by the absence of obscuration of the H$\,\alpha$ emission from the H II region. We can consider the amount of Faraday rotation each ISM phase is likely to contribute along the LOS, and quantify the path-length at which each phase will be resolved out of our observations. Here we take local electron densities of the various ISM phases from Ferrière (2001) and Heiles & Haverkorn (2012), and we assume a typical regular magnetic field value of $2\,\mu$G (Sun et al., 2008) with no reversals. CVE17 conducted a similar analysis in the LOFAR

Table 4.2: Faraday rotation properties for various ISM phases. Col.(1): The ISM phases. Col.(2): The local electron density of the ISM (Ferrière, 2001; Heiles & Haverkorn, 2012). Col.(3): The Faraday rotation per unit distance, assuming a $2\,\mu$G LOS magnetic field with no reversals. Col.(4) and (5): The depth along the LOS after which depth depolarization will filter out polarized emission for LOFAR and GMIMS, respectively.

Phase	n_e [$\mathrm{cm^{-3}}$]	Faraday rotation [$\mathrm{rad\,m^{-2}\,pc^{-1}}$]	Path length [pc]	
			LOFAR	GMIMS-LBS
CNM	0.016	0.026	42	310
WNM	0.0007	0.0011	1000	7300
WIM	0.25	0.41	2.7	20
WPIM	0.1	0.16	6.9	50
HIM	0.0034	0.006	200	1400

band, finding that only emissions produced in the WNM would not be resolved out. We summarise these results in Table 4.2, comparing the survey characteristics from GMIMS-LBS and LOFAR. Since the $\phi_{\text{max-scale}}$ of GMIMS-LBS is nearly eight times that of LOFAR, our survey is much less susceptible to resolving out Faraday thick structures. We therefore cannot construct a similar model to CVE17, where interpretation of the polarized emission was tied to the absence of depolarization in the WNM. Instead, the features that we observe must be explained by enhancements in the MIM along the LOS.

The different ISM phases along the LOS will each contribute differently to the Faraday rotation of synchrotron emission, due to their different magneto-ionic properties. The Local Bubble consists of a hot ionised medium (HIM), at $n_e = 0.005\,\mathrm{cm^{-3}}$ (Cordes & Lazio, 2002; Shelton, 2009), filling a volume around the Sun. Synchrotron emissions produced inside the Local Bubble should create a peak in the Faraday spectrum around $0\,\mathrm{rad\,m^{-2}}$, as emission produced close to the Sun should experience minimal Faraday rotation. Our peak 2 is consistent with $0\,\mathrm{rad\,m^{-2}}$ at 2σ. We therefore interpret peak 2 as emission that is produced within the Local Bubble. At 1σ of confidence, we observe $-0.8 \pm 0.4\mathrm{rad\,m^{-2}}$ of Faraday rotation through this volume.

Faraday rotation in the Local Bubble also affects the features which arise behind it; that is, we must subtract the $-0.8\,\mathrm{rad\,m^{-2}}$ contribution from peaks 1 and 3. Applying this moves peaks 1 and 3 to $-6.6 \pm 0.6\,\mathrm{rad\,m^{-2}}$ and $+7.1 \pm 0.6\,\mathrm{rad\,m^{-2}}$,

respectively. We can constrain what is producing these features by analysing how LOS components of the ISM are contributing to Faraday rotation. Taking our values from Table 4.2, assuming these phases are contributing $\sim 7\,\mathrm{rad\,m^{-2}}$ of Faraday rotation would require a path-length of about 270 pc, 6 kpc, 17 pc, 40 pc, and 1.2 kpc respectively.

Because of the short path-length (164^{+48}_{-30} pc) to the front of Sh2-27, the only possible candidates are the CNM, WIM, WPIM. Neutral gas is typically traced using H I observations. We inspect the H I emission in the region of Sh2-27 from HI4PI (HI4PI Collaboration et al., 2016b). Due to the proximity of Sh2-27 to the Sun, H I emissions produced in this region crowd around 0 km/s, making kinematic distances unreliable. We do find indications of H I self-absorption, however, in the H I spectra towards the H II region, which indicates the presence of cold atomic gas. We are therefore motivated to look to the STILISM project (Lallement et al., 2014; Capitanio et al., 2017; Lallement et al., 2018), which traces the CNM and provides the LOS distances to these neutral structures.

We show a series of slices through the STILISM cube in Figure 4.6. The Local Bubble appears as a void surrounding the Sun in these data. We find that the distance to edge of the Local Bubble is 80 pc in the direction of Sh2-27. Taking an electron density of $0.005\,\mathrm{cm^{-3}}$ we derive a magnetic field strength of $-2.5 \pm 1.2\,\mu$G in the Local Bubble, aligned away from the Sun.

The location of Sh2-27 correlates with a region of relatively lower dust content in STILISM, as expected around an H II region, compared to neutral clouds. Between the front of Sh2-27 and the edge of the Local Bubble two dust features appear. These regions occur at ~ 95 pc and ~ 135 pc and are each ~ 30 pc deep along the LOS. The distance error from the reddening inversion in this area is ~ 11 pc. We provide the spatial coverage of these clouds in the contours of Figure 4.7(a). The near cloud covers the entire region towards Sh2-27, whilst the far cloud only covers the lower-left portion of the region. Comparing the Faraday spectra between these areas we find that the triple-peak structure changes to a double-peak in the upper-right portion of the region, as shown in Figure 4.7(b). We see that there is neutral material in front of Sh2-27, and its location correlates with the Faraday spectra, so we can explain the Faraday properties of the foreground column without any WIM

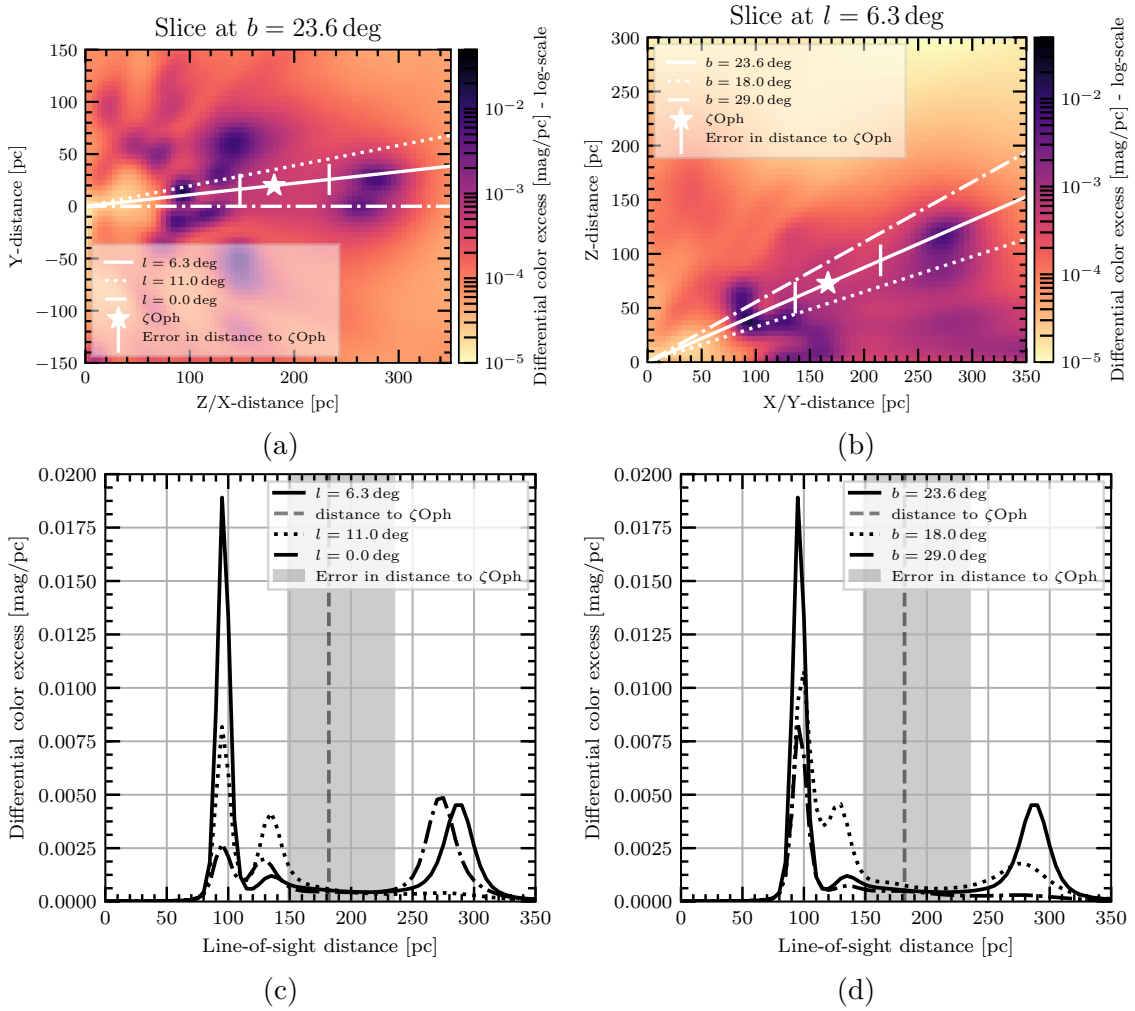

Figure 4.6: Three-dimensional dust structure towards Sh2-27 from STILISM (Lallement et al., 2014; Capitanio et al., 2017; Lallement et al., 2018). In all panels the solid line shows the LOS through the position of ζOph, and the dashed lines are LOS through the outer bounds of the H II regions. (a) Slice through data cube at a constant latitude. (b) Slice through data cube at a constant longitude. (c) and (d) show the LOS profiles for panels (a) and (b), respectively.

or WPIM along the line of sight. The magnetic fields need to be more intense, however, than the $\sim 2\,\mu$G we assumed previously.

In higher density regions of the ISM magnetic fields become compressed (Crutcher et al., 2010) and highly ordered, even in a relatively neutral medium (Clark et al., 2014; Kalberla et al., 2017; Gazol & Villagran, 2018; Tritsis et al., 2019). The dust features towards Sh2-27 are composed of CNM, and thus are a higher density region of neutral ISM. We can estimate the density in these clouds using a dust-to-gas ratio. Liszt (2014) find a ratio of H I column density (N(H I)) to dust reddening magnitude ($E(B-V)$) of $N(\mathrm{H\,I}) = 8.3 \times 10^{21}\,\mathrm{cm}^{-2}\,E(B-V)$ for for $|b| > 20°$ and

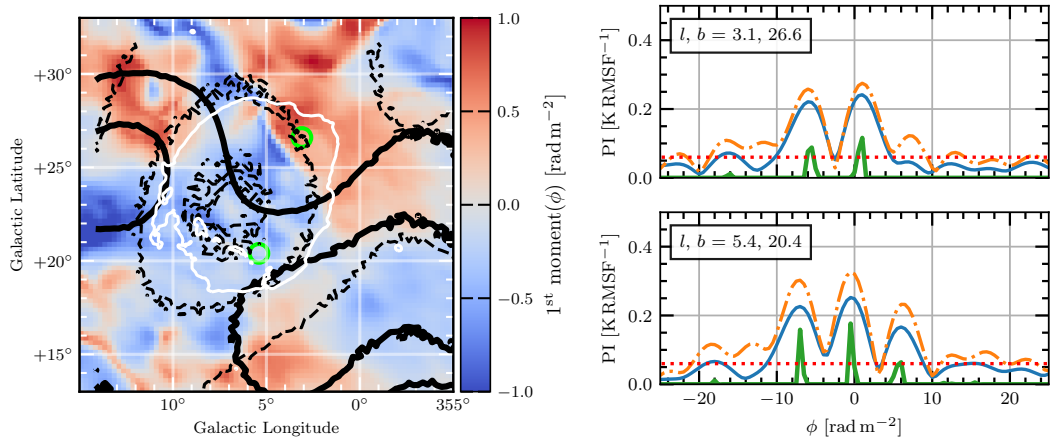

(a) (b)

Figure 4.7: (a): The first moment map of the Faraday spectrum (as in Figure 4.3(b)). White contours are H α intensity from Finkbeiner (2003) at 30 R. Black, dashed contours show STILISM dust reddening at 90 pc, corresponding to the near neutral cloud. Black, solid contours show STILISM dust reddening at 135 pc, corresponding to the far neutral cloud. Green circles show the positions for the Faraday spectra in the right-hand panel. (b): Faraday spectra for two lines-of-sight towards Sh2-27. The upper panel shows a LOS which intersects with only the near cloud. The lower panel shows a LOS which intersects both neutral clouds.

$E(B-V) \lesssim 0.1$ mag. This corresponds to a number density (n(H I)) to differential colour excess ratio of $\sim 2700\,\mathrm{cm^{-3}/(mag\,pc^{-1})}$. For the two foreground clouds, we find a total number density of $n_{\mathrm{tot}} \sim 50\,\mathrm{cm^{-3}}$ and $\sim 12\,\mathrm{cm^{-3}}$, which is consistent with typical values in the CNM (Ferrière, 2001). Increased electron density and magnetic fields in the dust features are evidently providing increased Faraday rotation over the more tenuous inter-cloud medium.

The observed triple-peaked Faraday spectrum can be reproduced from a simple model of the magneto-ionic structure towards Sh2-27. We summarise this model of the MIM towards Sh2-27 in Figure 4.8. In this model we first assume a constant synchrotron emissivity (ε) along the entire LOS towards Sh2-27. We interpret peaks 1 and 3 to be associated with the dust features. Such peaks would be produced if both clouds have stronger Faraday rotation, with LOS magnetic fields of opposite directions and with the cloud further from the Sun having stronger LOS magnetic field than the closer one. This must be the case to produce two peaks. If the clouds had similar strength LOS magnetic fields, emission produced behind both clouds would be Faraday rotated by the closer cloud to $\sim 0\,\mathrm{rad\,m^{-2}}$. Further, we are able to associate peak 3 with the far cloud from the change in the Faraday

spectrum on and off the cloud. This means that peak 1 arises from the near cloud. To summarise, assuming a uniform ε, the triple peak structure can be created from the far cloud with a Faraday depth of $+13.7 \pm 0.8\,\mathrm{rad\,m^{-2}}$, the near cloud with Faraday depth of $-6.6 \pm 0.6\,\mathrm{rad\,m^{-2}}$, and a peak near $0\,\mathrm{rad\,m^{-2}}$ from the Local Bubble. Emission produced in the warm inter-cloud regions is not depolarized, but undergoes an increased amount of Faraday rotation in the neutral dust clouds.

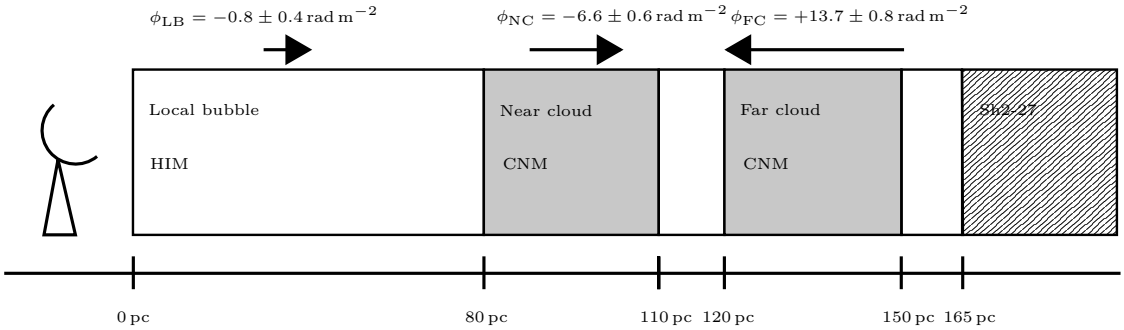

Figure 4.8: A cartoon of the magnetic field structure we observe along the LOS towards Sh2-27. We indicate the approximate distance to each feature along the bottom of the figure. We shade the two neutral clouds grey, indicating their increased density over other LOS components. The hatched region corresponds to the front of Sh2-27, behind which we receive no polarized emission. We give the values for the Faraday depths in each region. Arrows indicate the magnetic field direction in the Local Bubble and the two neutral clouds, as determined from our observations.

We confirm the viability of the model by constructing a simple 1D numerical simulation of the Faraday rotation produced by this model. Into this model we input LOS values for $B_\parallel$, n_e, and pseudo-ε, scaling the total emission to 1 flux unit. From this we obtain Stokes Q and U in the GMIMS-LBS band and perform Faraday tomography. We show the resulting Faraday spectra in Figure 4.9. In this evaluation of the simulation, we take $B_\parallel$ in the near and far cloud to be $-15\,\mu$G and $+30\,\mu$G, respectively, with the rest of the LOS having $2\,\mu$G. We find that the resulting Faraday spectrum is relatively insensitive to the sign of the intra-cloud and Local Bubble field directions. When we assume a uniform ε we obtain a triple-peak spectrum which is dominated by the component near $0\,\mathrm{rad\,m^{-2}}$, as shown in Figure 4.9(a). This is likely because this is over estimating the contribution of emission from the Local Bubble. More realistically, the magnetic fields in the HIM of the Local Bubble are likely to be weak (Hill et al., 2012, 2018), and therefore the ε in this region should be reduced relative to the rest of the LOS. In Figure 4.9(b) we show the result of setting the ε of the Local Bubble to be 10% of the remaining ε.

This produces three peaks of approximately equal height in the Faraday spectrum. It is possible that this same structure may arise from a more complicated LOS composition. In the absence of data to motivate such a model, this simulation demonstrates that our observed Faraday structure can be produced from a simple model.

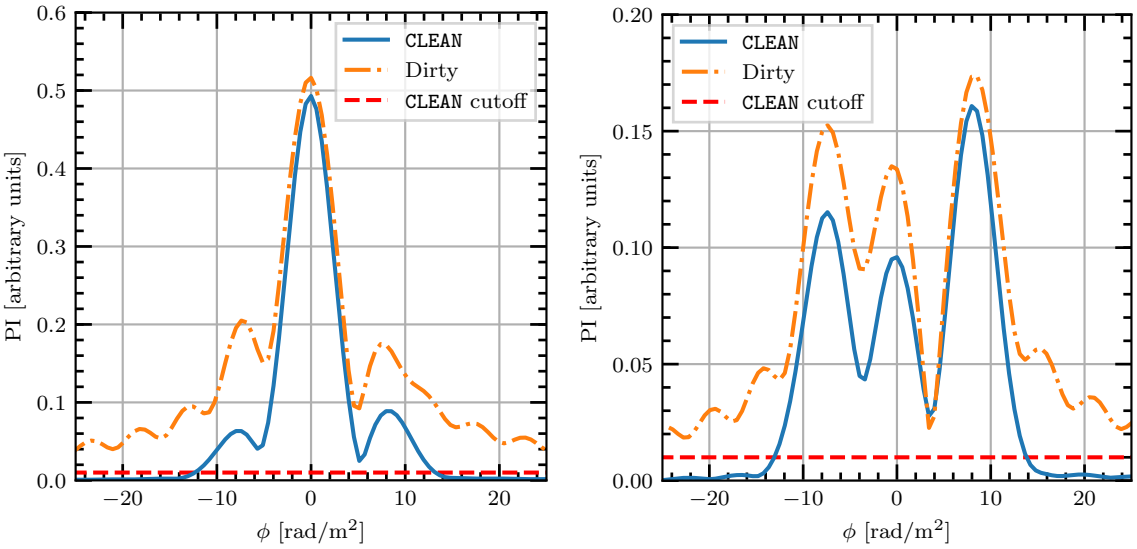

Figure 4.9: Simulated Faraday spectra of our Faraday thin model. The LOS distribution of the MIM is identical for each model, with only the emissivity changing. (a) Uniform emissivity along the entire LOS. (b) Emissivity in the Local Bubble reduced by 90%.

We can also determine how tenable this model is by calculating the polarization fraction. To do this we must also estimate the total synchrotron intensity towards Sh2-27. As Sh2-27 is a depolarization wall, we need to only consider the synchrotron emission from in front of the region. Roger et al. (1999) measured the total intensity towards a number of H II regions, including Sh2-27, at 22 MHz and estimated the synchrotron emissivity. They find $\varepsilon = 159\,\mathrm{K/pc}$ at 22 MHz, but they note that the emissivity towards Sh2-27 was very high relative to other H II regions, and that Sh2-27 might be not completely optically thick at 22 MHz. We investigate whether this is the case using values from the literature. The opacity (τ) of an H II region at a particular frequency (ν) is given by Mezger & Henderson (1967):

$$\tau = 3.28 \times 10^{-7} \left(\frac{T_e}{10^4}\right)^{-1.35} \left(\frac{\nu}{[\mathrm{GHz}]}\right)^{-2.1} \mathrm{EM}, \tag{4.14}$$

where $n_e \approx 2\,\mathrm{cm}^{-3}$ (Wood et al., 2005), $\mathrm{EM} = 240 \pm 26\,\mathrm{cm}^{-6}\,\mathrm{pc}$ (Celnik & Weiland, 1988) is the emission measure, and T_e is the electron temperature. Taking $T_e = 7000\,\mathrm{K}$ gives $\tau = 0.38$ at 22 MHz, meaning Sh2-27 is not optically thick. Using this opacity, we re-derive a foreground emissivity of $\varepsilon = 37^{+23}_{-15}\,\mathrm{K\,pc}^{-1}$. More recently, Su et al. (2018) calculated the synchrotron emissivity towards many H II regions at 76.2 MHz using the Murchison Widefield Array (MWA). They find an average value of $1 \pm 0.5\,\mathrm{K\,pc}^{-1}$ at 76.2 MHz. Taking a spectral index of $\beta = -2.5$ (where $I \propto \nu^{\beta}$), the emissivity at the GMIMS-LBS mid-band frequency of 390 MHz is $\varepsilon = 0.017 \pm 0.008\,\mathrm{K\,pc}^{-1}$. This value is also consistent with our recomputed value from Roger et al. (1999) assuming the same spectral index. Using the scaled emissivity from Su et al. (2018), we estimate the total brightness arising in front of Sh2-27 is $2.8^{+2.5}_{-1.6}\,\mathrm{K}$.

The use of depolarization walls is conceptually similar to using free-free absorption of Stokes I by H II regions. Similarly, we can determine the total received polarized emission towards Sh2-27. Using our Gaussian fit for the three Faraday thin components, we integrate the polarized intensity over the range of Faraday depths to determine the total polarized flux. From this we find a total polarized flux of $\sim 0.4\,\mathrm{K}$. Taking our previous estimate of the total intensity, this results in a polarization fraction of $12^{+16}_{-6}\,\%$. Given that spatial variation in Faraday depth will cause significant beam depolarization, this fraction is relatively high. This value further supports our finding that the magnetic fields causing the observed Faraday rotation towards Sh2-27 have a highly ordered component.

Finally, we estimate the magnetic field strengths in the neutral clouds. We have determined that the far cloud has a Faraday depth of $\sim +14\,\mathrm{rad\,m}^{-2}$ and the near cloud a Faraday depth of $\sim -7\,\mathrm{rad\,m}^{-2}$. From Equation 4.2 we also need to estimate n_e, and the path-length through each region (L). We find no pulsars between the Sun and Sh2-27 in ATNF Pulsar Catalogue (Manchester et al., 2005)[2], and since Sh2-27 is the dominant H α emission source in this direction it is not possible to constrain the n_e from these observations. As such, we present the LOS magnetic field strength as a function of the total number density (n_{tot}), the ionisation fraction (X_e), and L. We also estimate the strengths taking reasonable values from Ferrière

[2]Catalogue version: 1.59, Accessed 26$^{\mathrm{th}}$ of November 2018.

(2001) and our estimates above:

$$B_{\parallel,\mathrm{near}} \approx -15\,\mu\mathrm{G}\left(\frac{n_{\mathrm{tot}}}{20\,\mathrm{cm}^{-3}}\right)\left(\frac{X_e}{1\times10^{-3}}\right)\left(\frac{L}{30\,\mathrm{pc}}\right)$$
$$B_{\parallel,\mathrm{far}} \approx +30\,\mu\mathrm{G}\left(\frac{n_{\mathrm{tot}}}{20\,\mathrm{cm}^{-3}}\right)\left(\frac{X_e}{1\times10^{-3}}\right)\left(\frac{L}{30\,\mathrm{pc}}\right)$$

4.6.2 Faraday Thick Models Towards Sh2-27

We can also decide whether the Faraday structure towards Sh2-27 is Faraday thick using the CVE17 polarization flux method. After performing Faraday tomography, the PI spectra have units of K/RMSF. To obtain polarized flux, we must convert these units to K/(rad m^{-2}). This conversion factor of rad m^{-2}/RMSF is given by the integrated area (A) under the `CLEAN` Gaussian RMSF. For the region towards Sh2-27 in GMIMS-LBS this factor is 7.3 rad m^{-2}/RMSF. Note, that for LOFAR observations CVE17 obtained a conversion factor of near unity, whereas the factor for GMIMS-LBS is nearly an order of magnitude higher.

We can now model the depolarization of a Faraday thick medium in GMIMS-LBS. We model this as a 'Burn slab' (Burn, 1966), the simplest Faraday thick model. In Faraday depth space a Burn slab is a tophat function, which corresponds to the following complex polarization in λ^2:

$$\mathcal{P}(\lambda^2) = \exp[2i(\chi_0 + \phi_0\lambda^2)]\frac{\sin(\Delta\phi\lambda^2)}{\lambda^2}, \tag{4.15}$$

where ϕ_0 is the central Faraday depth of the slab, and $\Delta\phi$ is the width, or Faraday thickness, of the slab, and χ_0 again is the initial polarization angle. This model has the additional advantage of resolving out the least as a function of Faraday thickness; that is, other Faraday thick models will be filtered out more strongly. We model observations using GMIMS-LBS by evaluating this complex polarization using λ^2 values observed by GMIMS-LBS, taking the height of the slab to be 1 K, and then performing Faraday tomography on the resulting spectra. As the model is resolved out, the 'observed' Faraday spectrum is split into two peaks which also reduce in magnitude. We show this reduction as a function of Faraday thickness (matching Figure A.1. of Van Eck et al., 2017) in Figure 4.10. We note that this function is smooth compared to CVE17 because we have also applied `RM-CLEAN` to

our synthetic spectra (not doing so results in an oscillation due to interference between the sidelobes of the depolarized peaks). We find that if the Faraday thickness of the slab is greater than the FWHM of the RMSF, then the depolarization factor is about 11%. For a Faraday thickness less than that, the depolarization factor varies significantly, reaching a peak depolarization factor of about 21% at 2.4 rad m^{-2}.

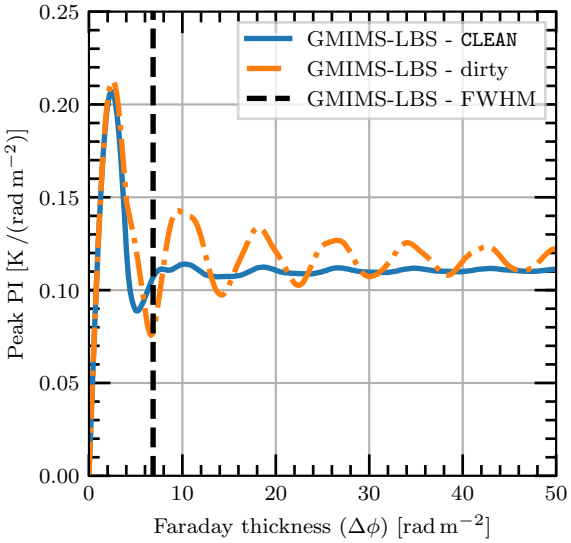

Figure 4.10: The depth depolarization of a Burn slab as a function of Faraday thickness, as observed by GMIMS-LBS. The peak PI is taken from a synthetic Faraday tomography observation of a Burn slab with a height 1 K and a variable thickness. Blue, dash-dotted: Depolarization from dirty spectra. Orange, solid: Depolarization from CLEAN spectra. Black, dashed: The FWHM of the RMSF.

There are three possible thick models that could apply to our observations (1): either peaks 1 and 2 are edges of a thick slab, (2): peaks 2 and 3 are edges of a slab, or (3): peaks 1 and 3 are the edges of the slab. In each case the third peak would be provided by a Faraday thin component. We will only consider cases (1) and (2), as case (3) will result in greater missing flux. In both cases we cannot know which peak represents the leading edge of a slab *a priori*. This condition, however, only sets the direction of the coherent magnetic field along the LOS, and does not affect the degree of missing flux. The Faraday thicknesses for models (1) and (2) are 6.6 ± 0.6 rad m^{-2}and 7.1 ± 0.6 rad m^{-2}, respectively. The heights of peaks 1, 2, and 3 are 0.185 ± 0.002 K/RMSF, 0.190 ± 0.005 K/RMSF, and 0.168 ± 0.006 K/RMSF, respectively. For simplicity, we can consider both of these cases together as a slab of thickness ~ 7 rad m^{-2}, and a depolarized peak of $\sim$ 0.18K/RMSF. Taking the conversion factor of 7.3 rad m^{-2}/RMSF gives the height of the depolarized peak

as $\sim 0.024\,\mathrm{K/(rad\,m^{-2})}$. A Faraday thickness of $\sim 7\,\mathrm{rad\,m^{-2}}$ will correspond to a depolarization factor of $\sim 11\%$, and therefore the height of the slab will be $\sim 0.23\,\mathrm{K/(rad\,m^{-2})}$. Integrating across the slab results in a polarized flux of $\sim 1.6\,\mathrm{K}$. From our estimate above, a Faraday thin component would provide about 0.1 K of flux.

For the ε we calculate above, the polarization fraction would therefore be $62^{+81}_{-29}\,\%$. For comparison, the maximum theoretical polarization fraction for synchrotron emission is 75% (Rybicki & Lightman, 1986), but this will only occur when the magnetic field generating the synchrotron emission is perfectly uniform. Such high values are highly unlikely to arise in the diffuse ISM.

We also evaluate the λ^2 spectra for each Burn slab model in a similar manner to the Faraday thin case. We show the resulting spectra in Section 4.9. None of these models recreate the average spectra well, especially in comparison to the thin model. From both this finding, and our analysis of the polarized flux from a Burn slab model, we conclude that a Faraday thick model is unlikely to apply here.

4.7 Discussion

Faraday tomography is a powerful method for probing the MIM of the Galactic ISM. Faraday depth, however, can vary in a non-monotonic fashion along the LOS and mapping structure in the Faraday dispersion function is therefore difficult. The use of depolarization to constrain distances to polarized features has been applied in many diffuse polarization surveys (e.g. Wolleben et al., 2010b; Hill et al., 2017). We have shown that at low frequencies this analysis can be extended. If a depolarization feature can be identified as a depolarization wall then any observed polarized emission can be constrained to the region along the LOS in front of the feature. In GMIMS-LBS we are sensitive to large angular scales, but our large beam also constrains us to this type of analysis only on large depolarization regions. Additionally, the current spatial density of extragalactic RMs (e.g. Taylor et al., 2009) is $\sim 1\,\mathrm{RM/deg^2}$, which also restricts the analysis of beam depolarization. Future polarized surveys, such as POSSUM (Gaensler et al., 2010) from the Australian SKA Pathfinder (ASKAP), aim to deliver $\sim 100\,\mathrm{RM/deg^2}$. With such data, the type of

analysis we present here can be extended to higher angular resolution with observations from aperture synthesis telescopes. Furthermore, distances to H II regions are being well constrained by the H II Region Discovery Surveys (HRDS, SHRDS Bania et al., 2010; Brown et al., 2017).

Understanding of the density-magnetic field relationship in the ISM is of great importance to many processes. Recent observations (e.g. Wolleben et al., 2010b; Clark et al., 2014; Kalberla et al., 2017; Tritsis et al., 2019) and numerical simulations (e.g. Gazol & Villagran, 2018) have shown that even in the diffuse ISM magnetic fields can be compressed and ordered. Our observations are highly compatible with this picture, and our model of the ISM towards Sh2-27 shows that magnetic fields have become ordered and magnified in nearby dust clouds. Crutcher et al. (2010) show that in densities associated with the CNM, magnetic fields are measured be on the order of 5μG, but can be as high as 10–20 μG. Wolleben et al. (2010b) use Faraday tomography to measure the magnetic field in large, nearby H I shell. They determine a LOS field strength of 20–34 μG. Clark et al. (2014) estimate a total magnetic field strength in the Riegel-Crutcher H I cloud of 10–50 μG, using a Chandrasekhar-Fermi-like method. McClure-Griffiths et al. (2006b) previously constrained that the total magnetic field in the Riegel-Crutcher cloud should be at least 30 μG. Tritsis et al. (2019) analyse a similar region in Ursa Major, finding a total magnetic field strength of 10–20 μG. Our magnetic field estimates are broadly consistent with these measurements. We note however, that each of these cases represents an atypical cloud, as compared with Crutcher et al. (2010) results for the same density. Further investigation of the clouds we find towards Sh2-27 is required to understand whether such a special case, such as compression within a shell wall, occurs here.

4.8 Summary and Conclusion

In this paper we have made use of the highly sensitive GMIMS-LBS observations to probe the magneto-ionic structure of the nearby ISM. We achieve this by identifying the nearby H II region Sh2-27 as a depolarization wall. The magneto-ionic properties of Sh2-27, as revealed by extragalactic RMs, prevent polarized emissions produced

behind the region at 300–480 MHz from propagating through it. We are then able to perform Faraday tomography on the observed polarized emission knowing that the structure we observe must originate between the Sun and the front of Sh2-27, a path length of only 160 pc.

We find a consistent triple-peaked structure in the Faraday spectrum in the region towards Sh2-27. We conclude that the structure is highly unlikely to arise from a resolved out Faraday thick source, but rather should be caused by magneto-ionic enhancements along the LOS. We draw this conclusion from both consideration of the polarized flux and by modelling Faraday thick and thin spectra. We find that only the thin model reproduces the observations well.

Using three-dimensional ISM maps we identify two neutral features in front of Sh2-27 as well as the ionised region of the Local Bubble. The Local Bubble extends for 80 pc in the direction of Sh2-27, and the two clouds lie in the remaining space in front of Sh2-27 and are each about 30 pc thick. Given the constraint on the LOS structure we also find that the observed Faraday structure cannot arise from a tenuous ionised region. Rather, the structure must arise from magneto-ionic enhancements. We are able to associate the three peaks in our Faraday spectrum with the two neutral clouds and the Local Bubble. We confirm the viability of this model using both a simple 1D simulation, and an analysis of the polarized flux. Following this, we find a Faraday depth in the local bubble of $-0.8 \pm 0.4 \mathrm{rad\,m^{-2}}$, meaning that magnetic field is aligned away from the Sun in this direction. Assuming that this Faraday rotation occurs uniformly throughout the Local Bubble, this Faraday depth corresponds to a LOS magnetic field strength of $-2.5 \pm 1.2\,\mu$G. In the near and far clouds we obtain Faraday depths $-6.6 \pm 0.6\,\mathrm{rad\,m^{-2}}$ and $+13.7 \pm 0.8\,\mathrm{rad\,m^{-2}}$, respectively. These Faraday depths correspond to LOS magnetic fields of opposite alignment in each cloud.

Here we have considered only a small region in the GMIMS-LBS. We chose this region as the morphological correlation between the polarization structure and the H II region Sh2-27 is immediately apparent. We have shown that interpretation of features in these data requires careful analysis and combination with extragalactic polarization observations and additional tracers of the ISM. We have shown that GMIMS observations are highly complementary to newly released survey data such

as *Gaia* and will be of great use for interpretation of results from the upcoming MWA and ASKAP surveys.

Acknowledgements

The authors wish to thank JinLin Han for his constructive input.

AT acknowledges the support of the Australian Government Research Training Program (RTP) Scholarship. N. M. M.-G. acknowledges the support of the Australian Research Council through grant FT150100024. C. F. acknowledges funding provided by the Australian Research Council (Discovery Project DP170100603 and Future Fellowship FT180100495), and the Australia-Germany Joint Research Cooperation Scheme (UA-DAAD).

The Parkes Radio Telescope is part of the Australia Telescope National Facility which is funded by the Commonwealth of Australia for operation as a national facility managed by CSIRO. This work has made use of data from the European Space Agency (ESA) mission *Gaia* (https://www.cosmos.esa.int/gaia), processed by the *Gaia* Data Processing and Analysis Consortium (DPAC, https://www.cosmos.esa.int/web/gaia/dpac/consortium). Funding for the DPAC has been provided by national institutions, in particular the institutions participating in the *Gaia* Multilateral Agreement. We further acknowledge high-performance computing resources provided by the Australian National Computational Infrastructure (grant ek9) in the framework of the National Computational Merit Allocation Scheme and the ANU Allocation Scheme. This research made use of Astropy,[3] a community-developed core Python package for Astronomy (Astropy Collaboration et al., 2013, 2018). This research made use of APLpy, an open-source plotting package for Python (Robitaille & Bressert, 2012). We have made use of the 'cubehelix' colour-scheme (Green, 2011).

[3]http://www.astropy.org

4.9 Appendix

Faraday Thick Spectra

We model Stokes Q and U, and PI as a function of λ^2 in the GMIMS-LBS band using Equation 4.15. Models 1.X, 2.X, 3.X refer to Faraday thick cases (1), (2), and (3) as described in Section 4.6.2. The 'X' value for each model refers to which χ_0 value is used for each slab. This is because there is a choice as to which χ_0 value to use from the two peaks which become the edges of the slab. We set the height of each Burn slab to be $0.25\,\mathrm{K/rad\,m^{-2}}$ to give a resolved height of about $0.18\,\mathrm{K/RMSF}$. In all cases, the fit to the original data is poor.

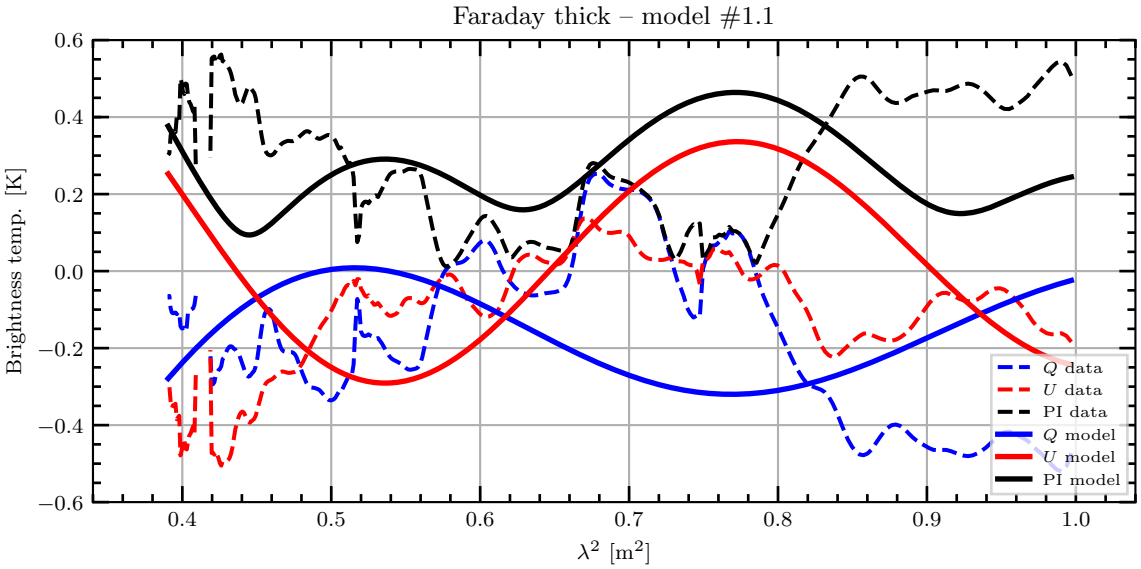

Figure 4.11: Faraday thick model spectra towards Sh2-27: A Burn slab spanning peaks 1 and 2, taking χ_0 from peak 1, and a Faraday thin component at peak 3. Dashed lines: Average Stokes Q, U, and PI λ^2 spectra towards Sh-27 from GMIMS-LBS. Solid lines: Faraday thick model derived from the average Faraday spectrum.

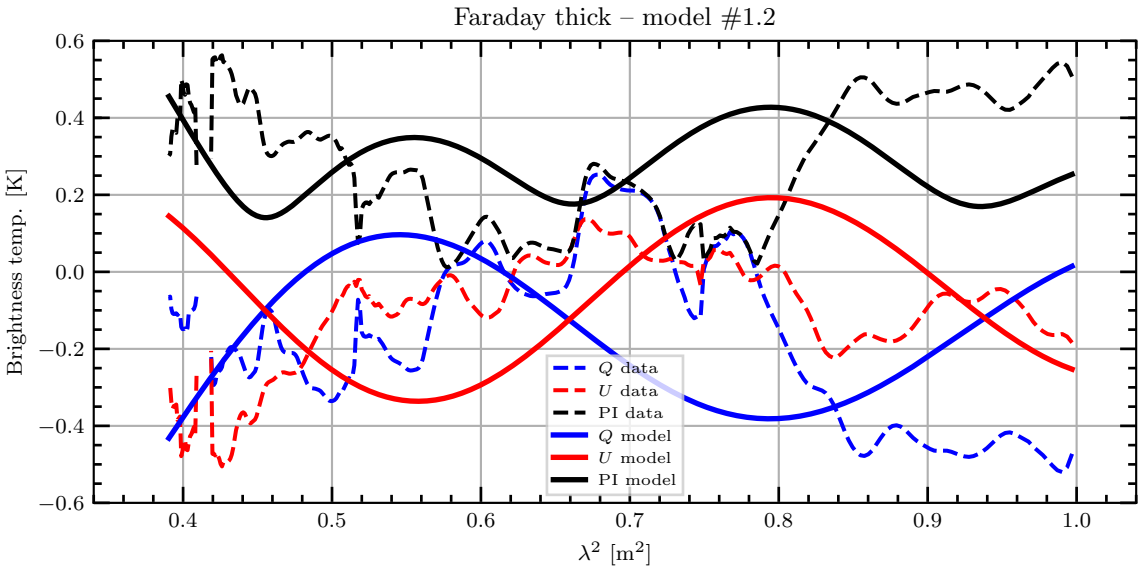

Figure 4.12: Faraday thick model spectra towards Sh2-27: A Burn slab spanning peaks 1 and 2, taking χ_0 from peak 2, and a Faraday thin component at peak 3. Dashed lines: Average Stokes Q, U, and PI λ^2 spectra towards Sh-27 from GMIMS-LBS. Solid lines: Faraday thick model derived from the average Faraday spectrum.

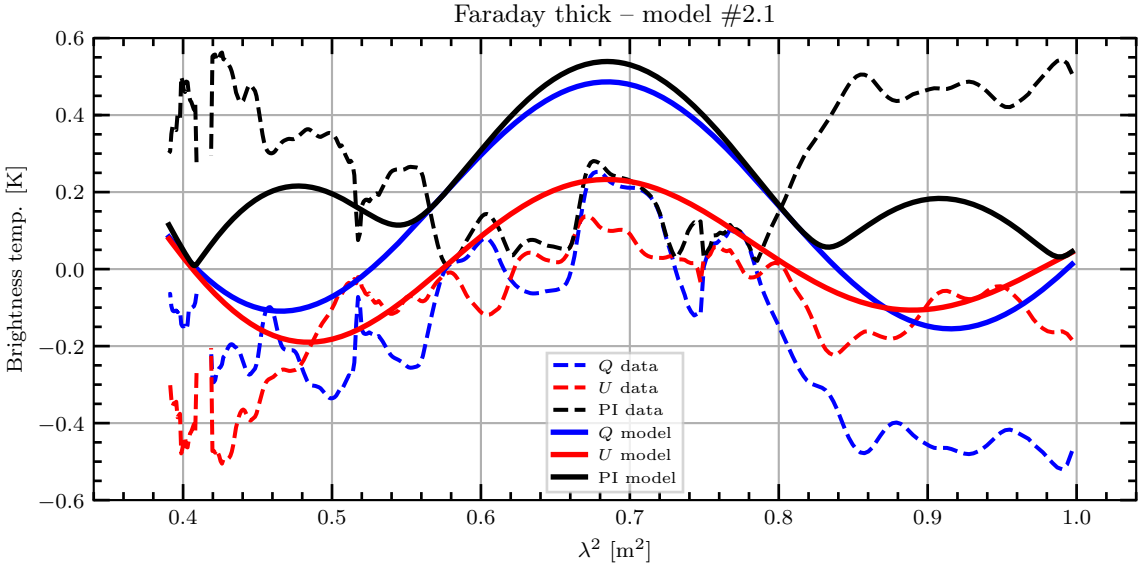

Figure 4.13: Faraday thick model spectra towards Sh2-27: A Burn slab spanning peaks 2 and 3, taking χ_0 from peak 3, and a Faraday thin component at peak 1. Dashed lines: Average Stokes Q, U, and PI λ^2 spectra towards Sh-27 from GMIMS-LBS. Solid lines: Faraday thick model derived from the average Faraday spectrum.

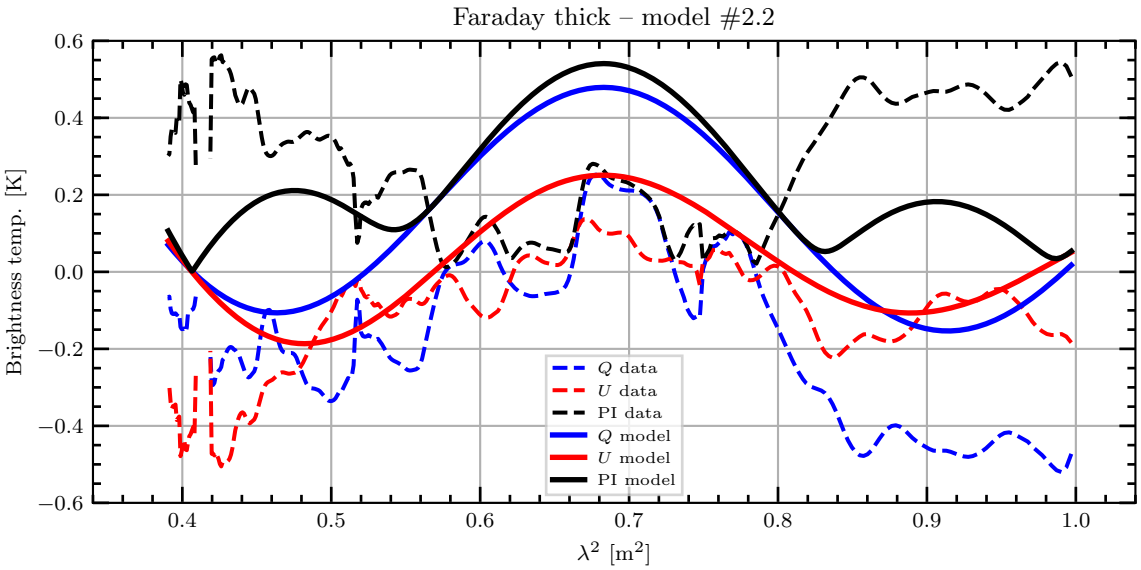

Figure 4.14: Faraday thick model spectra towards Sh2-27: A Burn slab spanning peaks 2 and 3, taking χ_0 from peak 2, and a Faraday thin component at peak 1. Dashed lines: Average Stokes Q, U, and PI λ^2 spectra towards Sh-27 from GMIMS-LBS. Solid lines: Faraday thick model derived from the average Faraday spectrum.

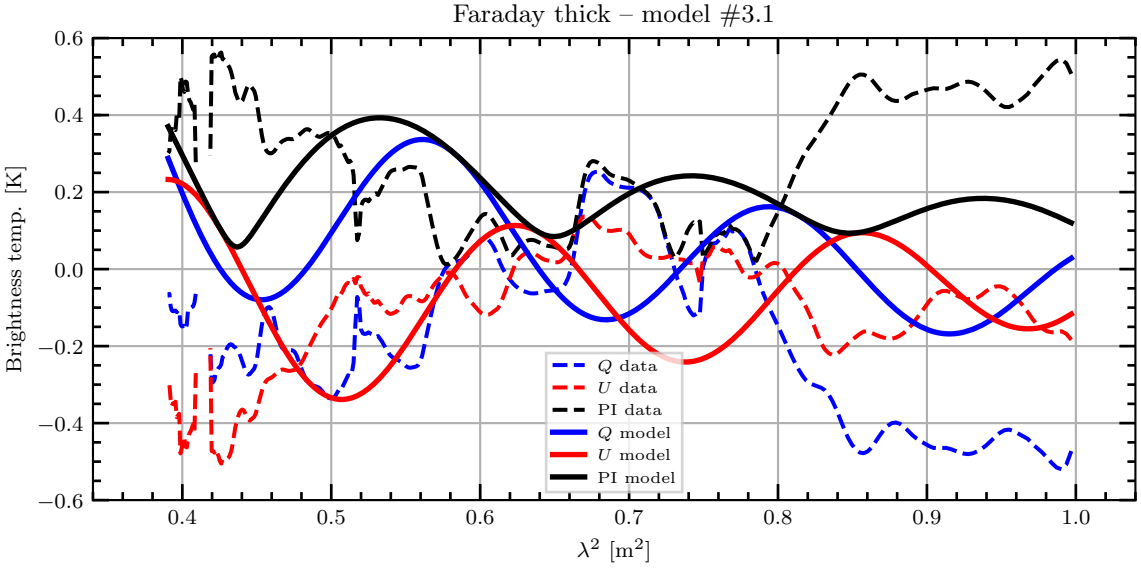

Figure 4.15: Faraday thick model spectra towards Sh2-27: A Burn slab spanning peaks 1 and 3, taking χ_0 from peak 3, and a Faraday thin component at peak 2. Dashed lines: Average Stokes Q, U, and PI λ^2 spectra towards Sh-27 from GMIMS-LBS. Solid lines: Faraday thick model derived from the average Faraday spectrum.

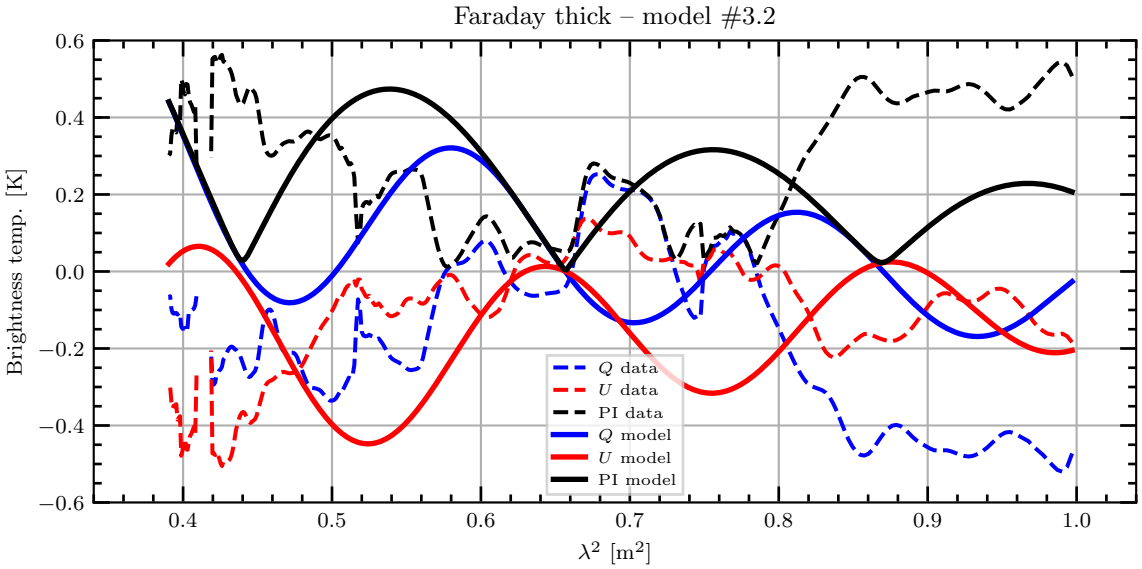

Figure 4.16: Faraday thick model spectra towards Sh2-27: A Burn slab spanning peaks 1 and 3, taking χ_0 from peak 1, and a Faraday thin component at peak 2. Dashed lines: Average Stokes Q, U, and PI λ^2 spectra towards Sh-27 from GMIMS-LBS. Solid lines: Faraday thick model derived from the average Faraday spectrum.

5

The first observational detection of a Faraday caustic

This chapter is in preparation for submission: **Thomson, Alec. J. M.**, GMIMS Consortium, et al. *"The brightest polarized region in the Southern sky at 400 MHz"*, 2019.

5.1 Abstract

The diffuse polarized radio sky contains many features that do not appear in total intensity. Additionally, it also drastically changes appearance at different wavelengths. This is due to the Faraday rotation effect which arises from the magneto-ionic medium of the Milky Way. We investigate the brightest region of the Southern polarized radio sky at 400 MHz, G150−50. This region is located at $l, b \sim (150, -50)^\circ$ and covers nearly $20\,\mathrm{deg}^2$ and is not present in L-band observations. Using the

Southern component of the Global Magneto-Ionic Medium Survey (GMIMS-LBS) we analyze both the spatial and spectral structure of this feature. To determine the origin of this feature we apply Faraday tomography and Stokes QU-fitting techniques. From both of these methods we find strong indications that G150−50 is a Faraday caustic, arising from a gradient in the line-of-sight component of the magnetic field. Using Faraday tomography we find a strong spike at a single Faraday depth with a tail towards negative Faraday depths. Using QU-fitting we find this structure corresponds to a Faraday caustic with a foreground rotating screen. This is the first observational detection of a Faraday caustic. It therefore indicates both a negative line-of-sight gradient of the Galactic magnetic field and that the field crosses $0\,\mu$G within $\sim 500\,$pc in this direction.

5.2 Introduction

At radio frequencies the polarized sky often bears little resemblance to its total intensity counterpart; despite the fact that the dominant emission mechanism, synchrotron radiation, can be highly polarized (up to $\sim 75\%$, Rybicki & Lightman, 1979). This discrepancy arises from the Faraday rotation in the magneto-ionic medium of the Galaxy, which modulates the polarized emission.

The interstellar medium (ISM) of Milky Way is a source of both polarized emission and Faraday rotation. The degree of Faraday rotation is therefore quantified by the Faraday depth (ϕ, Burn, 1966; Brentjens & de Bruyn, 2005):

$$\chi(\lambda^2) = \chi_0 + \lambda^2\phi, \tag{5.1}$$

where χ is the polarization angle at wavelength λ Faraday-rotated from an initial angle χ_0. The Faraday depth is defined by both the thermal electron density (n_e) and the line-of-sight (LOS) component of the magnetic field ($B_\parallel$):

$$\phi(d) \equiv 0.812 \int_d^0 n_e(r) B_\parallel(r) dr \left[\mathrm{rad\,m^{-2}}\right], \tag{5.2}$$

where d is the distance to the polarized source in pc, and n_e and $B_\parallel$ are measured in cm^{-3} and μG, respectively. Note that Faraday depth, while similar, is distinct

from the rotation measure (RM). RM is defined as the gradient of χ with λ^2:

$$\mathrm{RM} = \frac{d\chi(\lambda^2)}{d\lambda^2}. \tag{5.3}$$

RM only describes the Faraday rotation when the rotating and emitting volumes are not mixed.

Much progress has recently been made in the construction of polarization surveys that cover the entire sky. Early surveys, such as Brouw & Spoelstra (1976) and Mathewson & Milne (1965), were carefully processed but sparsely sampled both spatially and in frequency. More complete single-frequency maps have been produced at L-band (Wolleben et al., 2006; Testori et al., 2008), S-band (Carretti et al., 2019), and K-band (Page et al., 2007; Bennett et al., 2013). Together these data have revealed unique features on the radio polarized sky. In particular, three regions of bright Galactic polarized emission have been identified: the North Polar Spur (Hanbury Brown et al., 1960; Berkhuijsen et al., 1971), the Fan Region (Wilkinson & Smith, 1974; Spoelstra, 1984), and the Northern and Southern ridges of the Fermi Bubbles (Carretti et al., 2013). Due to the narrow frequency range of these surveys, however, using them to determine Faraday rotation is difficult.

The Global Magneto-Ionic Medium Survey (GMIMS, Wolleben et al., 2009, 2019, Wolleben et al. in prep.) will provide the necessary bandwidth to map Faraday rotation of diffuse emission across the entire sky. Recently, the low-frequency, Southern component (GMIMS-LBS, Wolleben et al., 2019) has been completed, which presents an entirely unique view of the polarized sky. This survey maps diffuse polarized emission from 300 to 480 MHz with 0.5 MHz channels. The low frequencies allow for high-precision Faraday tomography (e.g. Thomson et al., 2019), but the large beam does restrict the 'polarization horizon' (Uyaniker et al., 2003) to be within about 500 pc (Dickey et al., 2019). The high-band Northern component of GMIMS (GMIMS-HBN, Wolleben et al., 2010a, Wolleben et al. in prep.) has also been completed, and maps linearly polarized emission from 1.3 to 1.8 GHz. These data were used to investigate both the North Polar Spur (Sun et al., 2015) and the Fan Region (Hill et al., 2017), the brightest features in the Northern polarized sky. Despite the potential depolarization that likely effects GMIMS-LBS, there remain regions within these data with high polarized intensity.

When bright polarized emission is observed there are two broad explanatory models: 1) the polarized emissivity is enhanced towards that region on the sky, or 2) the magneto-ionic medium is aligned in such a way to maintain high polarization fraction (i.e. a lack of depolarization). The total synchrotron intensity (I) of a source with depth l is (Beck & Wielebinski, 2013):

$$I \propto N_0 B_\perp^{(1-\gamma)/2} L, \tag{5.4}$$

where N_0 is the density of cosmic-ray electrons per energy interval and $B_\perp$ is the magnetic field strength in the plane of the sky. Since the cosmic-rays themselves follow a power-law distribution with respect to their energy E, $N(E) = N_0 E^\gamma$, this formulation provides the familiar power-law spectrum in frequency (ν), $I \propto \nu^\alpha$, where $\alpha = (\gamma + 1)/2$. For a perfectly regular field in the plane of the sky, the intrinsic degree of polarization (p_0) is given by (Beck & Krause, 2005):

$$p_0 = \frac{3 - 3\alpha}{5 - 3\alpha}. \tag{5.5}$$

The measured polarized intensity can be reduced by either a turbulent field in the plane of the sky (e.g. Beck & Krause, 2005, Eq. 12) or by depolarization (Burn, 1966; Tribble, 1991; Sokoloff et al., 1999). In case (1), as described above, both the total and polarized intensity are increased together. Different depolarization scenarios can still apply here, but we note the models of depolarization all broadly predict higher polarization fraction at smaller λ^2. The alternative, case (2), may arise from many different physical scenarios. A particular case, however, has been predicted by Bell et al. (2011) as a 'Faraday caustic'.

A caustic arises when there is a gradient in $B_\parallel$ as a function of the LOS which causes the value of $B_\parallel$ to cross 0. In such a case, the polarization vectors 'pile up' at a single value of Faraday depth, thus providing a high degree of measured polarization in the absence of an increased polarized emissivity. The peak-ϕ value corresponds to the location along the LOS where $B_\parallel \to 0$. The observational confirmation of caustics has remained elusive, despite consideration in LOFAR observations (Van Eck et al., 2017, 2019). Bell et al. (2011) provide an observational condition to be

able to discriminate a Faraday caustic from a Faraday thin source:

$$\frac{\nu_{\rm max}}{\nu_{\rm min}} >\sim 1.5, \tag{5.6}$$

where $\nu_{\rm max}$ and $\nu_{\rm min}$ are the maximum and minimum frequencies observed, respectively. For GMIMS-LBS this factor is 1.6.

In this paper we present results from GMIMS-LBS towards the brightest polarized region in the survey. This region is roughly centred on $l, b \sim (150, -50)^\circ$ and covers nearly $20\,{\rm deg}^2$. Throughout we will refer to the region as G150−50. In Section 5.3 we briefly describe the GMIMS-LBS observations, and the complementary data we utilize. We discuss the morphology of G150−50 and how it relates to other ISM tracers in Section 5.4. In Section 5.5 we show the results of Faraday tomography towards this region. In Section 5.6 we apply QU-fitting techniques to the data. Finally, we discuss our results in Section 5.7 and provide our conclusions in Section 5.8.

5.3 Observations

5.3.1 GMIMS-LBS

GMIMS-LBS is described in-detail by Wolleben et al. (2019). The data from the survey are available in two forms: Stokes I, Q, and U cubes as function of frequency, and Faraday depth cubes resulting from Faraday tomography. The frequency cubes cover 300 to 480 MHz between declinations -90° and $+20^\circ$ with a minimum resolution of $81'$. For this analysis we have regridded both sets of data cubes into HEALPix[1] format with an $N_{\rm side}$ of 256 (pixel size of $\sim 13.7'$).

GMIMS is designed for the implementation of Faraday tomography, which is RM synthesis (Burn, 1966; Brentjens & de Bruyn, 2005; Heald et al., 2009) mapped across the sky. RM synthesis is a Fourier-transform-like process that maps the complex polarization (P) as a function of ϕ. For a given set of observations of

[1] http://healpix.sourceforge.net

Stokes I, Q, and U, the complex polarization is:

$$P = Q + iU. \tag{5.7}$$

Applying RM synthesis to such data provides the Faraday dispersion function (FDF(ϕ)). The absolute value ||FDF(ϕ)|| provides the polarized intensity ($L = \sqrt{Q^2 + U^2}$) as a function of Faraday depth. ||FDF(ϕ)|| is spectral in nature, and here we refer to it as the 'Faraday spectrum'. Due to the discrete nature of RM synthesis the Faraday spectrum is naturally convolved with the RM spread function (RMSF). The parameters of the Faraday spectrum are determined by the RMSF, which itself is determined by which values of λ^2 are observed. The resolution in Faraday depth ($\delta\phi$) is

$$\delta\phi \approx \frac{2\sqrt{3}}{\Delta\lambda^2}, \tag{5.8}$$

where $\Delta\lambda^2 = \lambda^2_{\rm max} - \lambda^2_{\rm min}$ and $\lambda^2_{\rm max}$ and $\lambda^2_{\rm min}$ are the maximum and minimum observed λ^2, respectively. The largest recoverable Faraday depth ($\phi_{\rm max}$) is:

$$\phi_{\rm max} \approx \frac{\sqrt{3}}{\delta\lambda^2}, \tag{5.9}$$

where $\delta\lambda^2$ is the size of each channel in wavelength-squared space. Finally, the maximum scale observable in Faraday depth space is:

$$\phi_{\text{max-scale}} \approx \frac{\pi}{\lambda^2_{\rm min}}. \tag{5.10}$$

For GMIMS-LBS these parameters are: $\delta\phi = 5.9\,\mathrm{rad\,m^{-2}}$, $\phi_{\rm max} = 1700\,\mathrm{rad\,m^{-2}}$, and $\phi_{\text{max-scale}} = 8.6\,\mathrm{rad\,m^{-2}}$. These values are allowed to vary slightly across the sky depending on which channels are blanked due to radio-frequency interference (RFI) mitigation. The Faraday spectra are deconvolved with `RM-CLEAN` (Heald et al., 2009), with a `CLEAN` cut-off of 60 mK, the RMS noise in GMIMS-LBS spectra.

5.3.2 Maps at 408 MHz

We obtain the all-sky map of total intensity at 408 MHz from Haslam et al. (1982), reprocessed by Remazeilles et al. (2015). These data, also observed with the Parkes

telescope in the South, match the GMIMS-LBS observations in spatial resolution and are considered to be the canonical tracer of total emission from synchrotron radiation without contamination from other sources. An in-depth discussion of the comparison between Haslam et al. (1982) and the GMIMS-LBS total intensity measurements is presented in Wolleben et al. (2019). We note that the GMIMS-LBS and the Haslam et al. (1982) map agree very well, with the only major difference being the sky minimum value, which is subtracted from the GMIMS-LBS data. For this reason, we use the Haslam et al. (1982) map to obtain the total intensity of the sky at 408 MHz.

Additionally, we use the survey of polarized intensity at 408 MHz from Mathewson & Milne (1965), which we grid onto a HEALPix map with an $N_{\rm side}$ of 64 (pixel size of $\sim 55.0'$). Despite being sparsely sampled, there are no other surveys that map diffuse polarization across the Southern sky at these frequencies. Here we use this map to confirm that the features observed in GMIMS-LBS are not artefacts from RFI or the data processing.

5.3.3 Maps at L-band

To complement the low-frequency maps, we also obtain all-sky maps at 21 cm. We use the total intensity map from Reich (1982); Reich & Reich (1986); Reich et al. (2001), observed with the Stockert 25 m and Villa Elisa 30 m telescopes. We also retrieve the polarization data from Wolleben et al. (2006). We regrid both maps into HEALPix format with an $N_{\rm side}$ of 256 and smooth them to a common resolution of $36'$.

5.4 Results

We show the all-sky map of polarized intensity at 408 MHz in Figure 5.1. Here we have averaged our data to match the Haslam et al. (1982) bandwidth. From this map we can see G150−50 is the brightest region on the sky at these frequencies. We note that what appears to be part of the North Polar Spur is present in both GMIMS-LBS and the Mathewson & Milne (1965) map, but G150−50 is at least 50% brighter in polarized intensity. We do not consider areas on the Galactic plane, nor

the regions of Centaurus A or Virgo A/M87, as these regions suffer from Stokes I leakage. The Stokes I emission towards G150−50 is relatively low, and should not suffer from leakage.

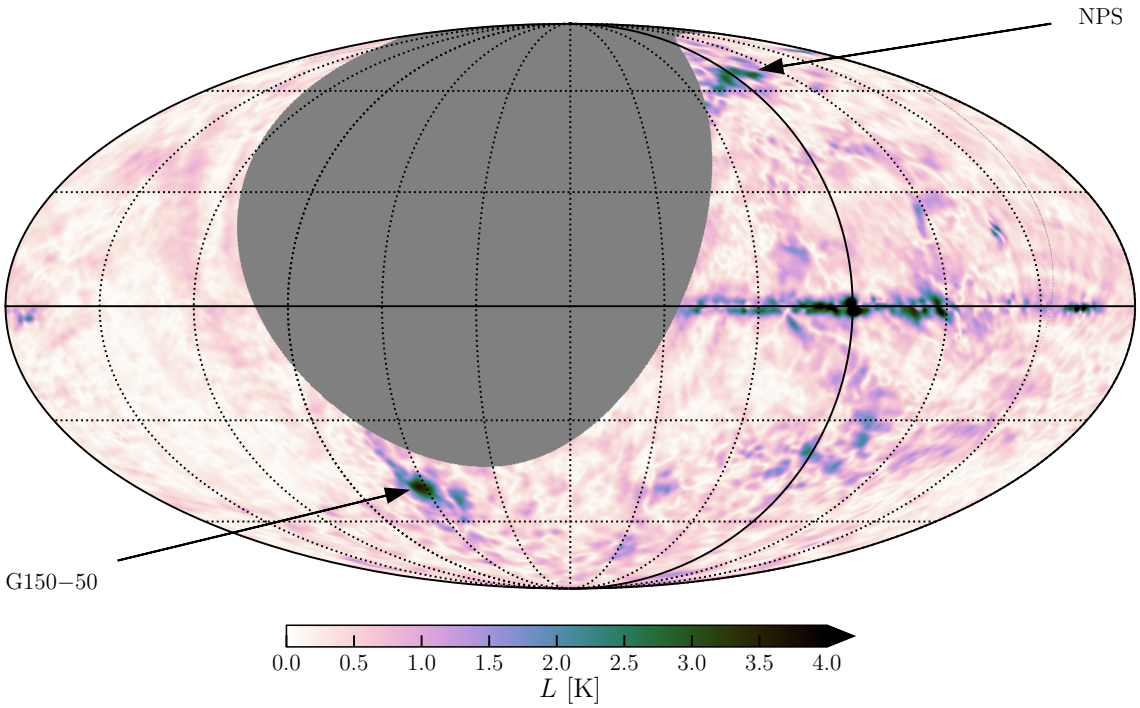

Figure 5.1: All-sky map of polarized intensity (L) from GMIMS-LBS at 408 MHz. We show this map using an Mollweide projection, centred on $l, b = (90, 0)°$. Here we average the GMIMS-LBS channels to match the bandwidth of Haslam et al. (1982). We highlight the locations of G150−50 and the North Polar Spur (NPS). We overlay graticules every 30° in longitude and latitude. Note that the Galactic plane, Centaurus A, and Virgo A/M87 suffer from Stokes I leakage.

In Figure 5.2 we zoom in on the G150−50 region. We see that this area is divided into two bright regions. We highlight these two sub-regions in Figure 5.2 with white circles, which are centred on $l, b \sim (151, -50)°$ (region 1) and $l, b \sim (139, -53)°$ (region 2), respectively. These same regions appear in the Mathewson & Milne (1965) map, which we show in blue contours. This correspondence further reassures us that G150−50 is not an artefact in GMIMS-LBS. We can be confident that this is a true feature of the polarized sky that ought to be investigated.

In Figure 5.3 we show the 408 MHz map using the Haslam et al. (1982) Stokes I data with contours of GMIMS-LBS polarized intensity overlaid. G150−50 appears to coincide with emission from radio Loop II (Large et al., 1962). This loop is described as a large circular feature on the sky, following a circle centred on $l, b \sim (100.0, -32.5)°$ with a radius of 45.5°, which we show in blue. In the Haslam et al.

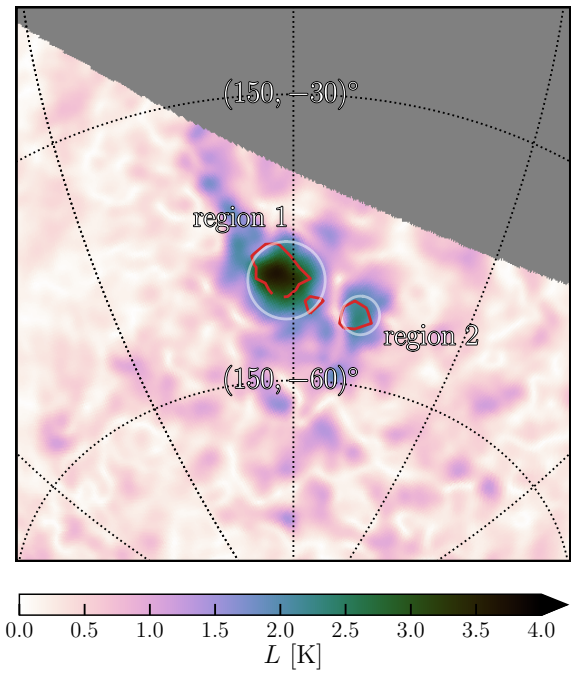

Figure 5.2: Map of polarized intensity (L) from GMIMS-LBS at 408 MHz focusing on G150−50. We show this map using an orthographic projection, centred on $l, b = (150, -50)°$. As per Figure 5.1, we average the GMIMS-LBS channels to match the bandwidth of Haslam et al. (1982). The red contour shows the polarized intensity from Mathewson & Milne (1965) at 3 K. In white circles we denote the two regions we refer to as 'region 1' (left) and 'region 2' (right). We overlay graticules every 30° in longitude and latitude.

(1982) map the loop is very diffuse, and appears to be reducing in intensity, from North to South, across the region of G150−50.

We also calculate the polarization fraction at 408 MHz using the Haslam et al. (1982) map. The polarization fraction in the two sub-regions is anomalously high, as we show in Figure 5.4. In this Figure we show the histogram of polarization fraction across the entire sky (as observed by GMIMS-LBS) and within the two sub-regions. Here we extract data towards these two regions from circular cut-outs, centred on the coordinates above, with radii of 4° and 2°, respectively. The median polarization fractions in regions 1 and 2 are 9.7% and 8.3%, meaning these regions have a higher fractional polarization than 99.9% and 99.8% of the observed sky, respectively.

5.5 Faraday Tomography

G150−50 does not appear in the Wolleben et al. (2006) map at 1.4 GHz, nor in GMIMS-HBN. To investigate this we utilize the spectral information provided by

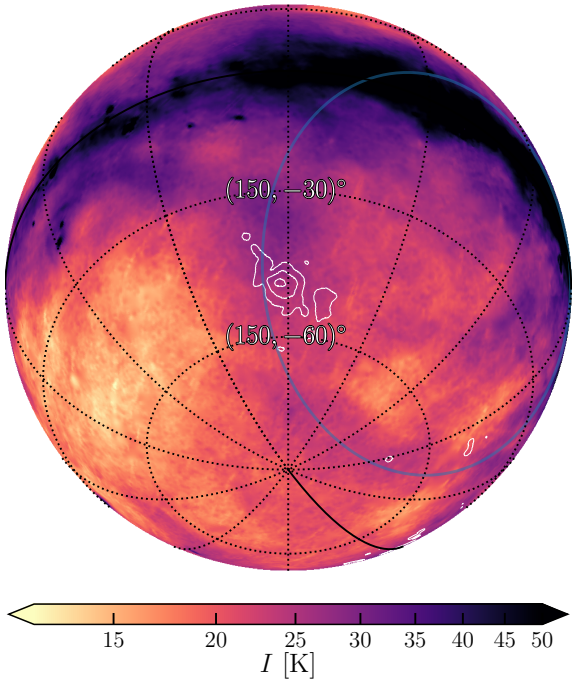

Figure 5.3: Map of total intensity at 408 MHz from Haslam et al. (1982), centred on $l, b = (150, -50)^\circ$ using an orthographic projection. Note that we use a logarithmic colour-scale. In white contours we show the polarized intensity at 408 MHz (as per Figure 5.2) at 1.5, 2.5, and 3.5K. In blue we draw the apparent location of radio Loop II (Large et al., 1962). We have selected a colour-scale such that the diffuse emission from Loop II is highlighted.

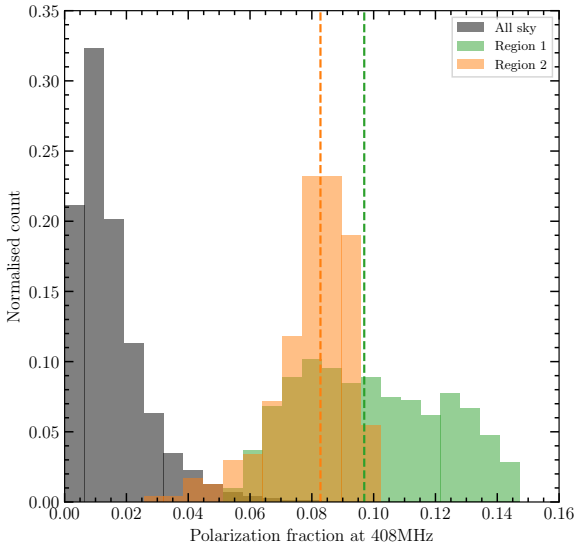

Figure 5.4: Histograms of polarization fraction (p_0) at 408 MHz, normalised such that the total area is unity. The polarization fraction is computed using the Remazeilles et al. (2015) map and the GMIMS-LBS channels which match these data. Grey: The entire sky as observed by GMIMS-LBS. Green: Region 1, a circular region centred on $l, b \sim (151, -50)^\circ$, with a radius of 4°. Orange: Region 2, a circular region centred on $l, b \sim (139, -53)^\circ$, with a radius of 2°. Dashed lines indicate the median value in each region.

GMIMS-LBS. From the morphological considerations alone, however, we can begin to draw some conclusions. G150−50 is unlikely to arise from a region of enhanced emissivity; in such a case we would expect to see a corresponding region of bright emission in total intensity. A caveat to this notion is that observed emission volumes in total and polarized intensity may be different. That is, there may be some polarized emission within the polarization horizon that only appears bright because there is very little background emission. That same emission would also be present in total intensity, but would be lost to confusion from background emission. We can dismiss this, however, as there is no corresponding bright polarized emission at higher frequencies, where the polarization horizon is much further away. This is compounded by the fact that depolarization models would predict higher polarization fraction at higher frequencies, whereas we observe the opposite. Such a scenario is highly suggestive of an alternative model.

G150−50 exhibits remarkable spectral structure. In Figure 5.5 we show the median linear polarization spectra over the area of sub-regions 1 and 2. For each region we fit a power-law model to the median Stokes I spectrum as a function of frequency, and we present the linear polarization spectra as a fraction of this model. Further, we perform some simple flagging for channels that were likely affected by RFI. We apply this by computing the difference in polarized intensity between each pair of adjacent frequency channels, and we discard channels that have an anomalously difference relative to their neighbouring channels. This method removes channels that are likely to be contaminated by RFI as the polarized intensity should be smooth as a function of frequency. The smoothly varying structure that remains in both of these regions, as a function of λ^2, is highly indicative of Faraday rotation. Additionally, the change in χ as function of λ^2 clearly demonstrates that a single RM cannot describe these spectra, as the gradient is not constant. Therefore we must apply more sophisticated analysis methods to these spectra.

The original data release of GMIMS-LBS provides Faraday spectra for $||\phi|| \leq 100\,\mathrm{rad\,m^{-2}}$. Dickey et al. (2019) showed that moment analysis is a powerful way to inspect the results of Faraday tomography. The 0^{th}, 1^{st}, 2^{nd}, and 3^{rd} moments of

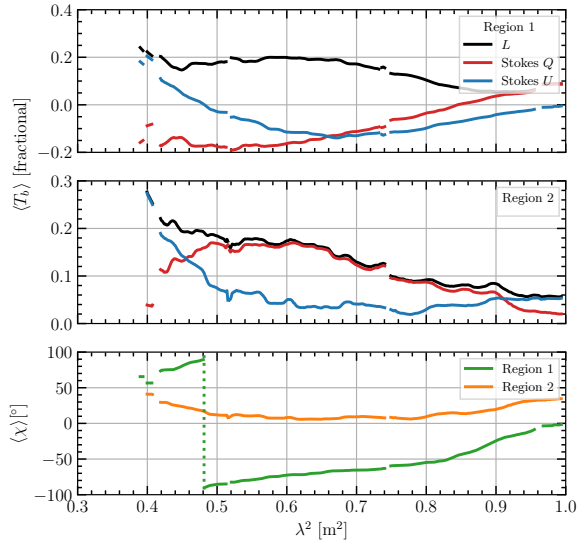

Figure 5.5: The median linear polarization in regions 1 and 2 as a function of λ^2. Here we present the linear polarization as a fraction of a power-law fit to the median Stokes I spectrum. Upper panel: Median Stokes Q, U, and polarized intensity (L) in region 1. Middle panel: Median Stokes Q, U, and polarized intensity (L) in region 2. Lower panel: Median polarization angle (χ) in both regions 1 (green) and 2 (orange).

Faraday spectra are defined as the integrated polarized intensity,

$$M_0 \equiv \sum_{i=1}^{n} L_i \Delta\phi, \tag{5.11}$$

the polarized intensity-weighted peak Faraday depth,

$$M_1 \equiv \frac{\sum_{i=1}^{n} L_i \phi_i}{\Delta\phi^{-1} M_0}, \tag{5.12}$$

the polarized intensity-weighted width of the peak,

$$M_2 \equiv \frac{\sum_{i=1}^{n} L_i \left(\phi_i - M_1\right)^2}{\Delta\phi^{-1} M_0} \tag{5.13}$$

and the polarized intensity-weighted skewness of the peak,

$$M_3 \equiv \frac{\sum_{i=1}^{n} L_i \left(\phi_i - M_1\right)^3}{\Delta\phi^{-1} M_0}, \tag{5.14}$$

respectively.

G150−50 does stand out in the original moment analysis of these data by Dickey et al. (2019) (e.g. in their Figure 5). Inspecting the Faraday depth spectra on

G150−50, we only find corresponding structure for $||\phi|| \leq 20\,\mathrm{rad\,m^{-2}}$. Here we compute the moments using this range in ϕ, capturing the primary Faraday depth structure we observe towards G150−50. We show the M_1 in Figure 5.6, masking using signal-to-noise ratio of 3 from M_0. From this we find that regions 1 and 2 are at Faraday depths of different sign, with a strong gradient between them. The separation of these regions is therefore caused by a depolarization canal (e.g. Fletcher & Shukurov, 2007), where ϕ changes sign within a single beamwidth. Inspecting the Faraday spectra of these regions reveals broad Faraday structure relative to the RMSF. This indicates that the Faraday spectra are either broadened or multi-component. Additionally, the broadening appears to be skewed towards negative ϕ across the entirety of G150−50. This is confirmed in the 3$^{\mathrm{rd}}$ moment map, which we show in Figure 5.7. Great care must be taken here, however, as the third moment is highly sensitive to noise and artefacts of `RM-CLEAN`.

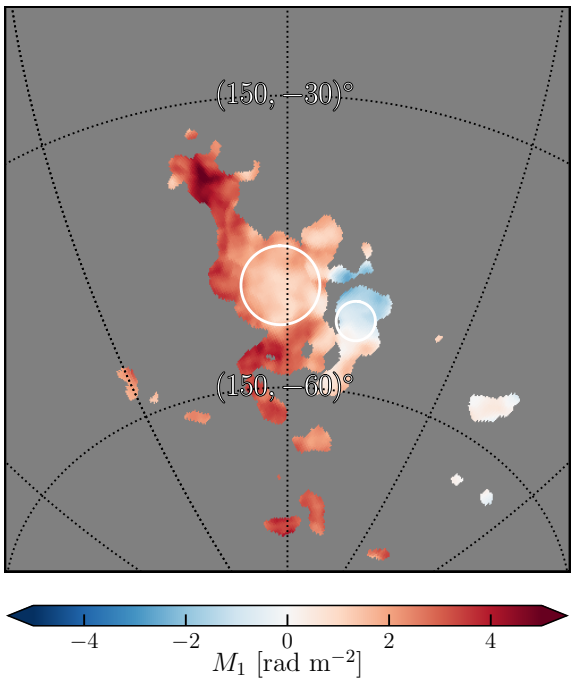

Figure 5.6: The first moment (M_1) of the Faraday spectra from GMIMS-LBS for $|\phi| \leq 20\,\mathrm{rad\,m^{-2}}$. We mask the data using signal-to-noise ratio of 3 from the zeroth moment. The first moment represents the intensity-weighted mean of the Faraday spectrum. Here find that regions 1 and 2 exhibit Faraday depths of opposite sign. We use the same projection as in Figure 5.2 and show regions 1 and 2 by white circles.

To minimize the potentially spurious effects of `RM-CLEAN` we perform RM-synthesis

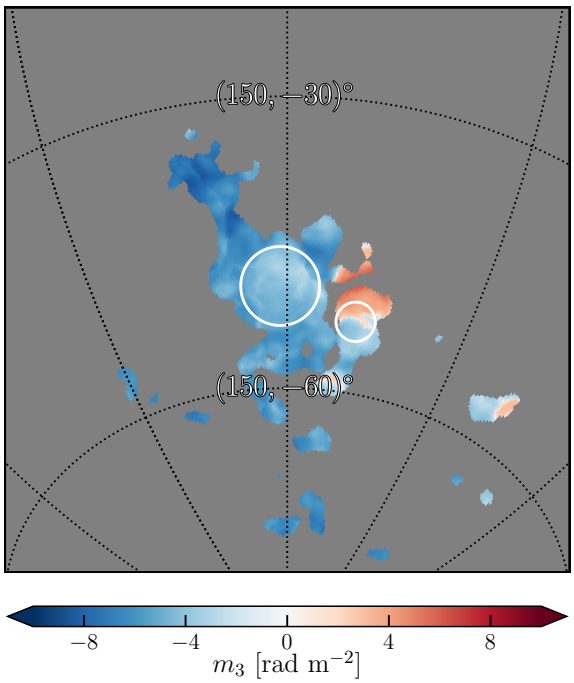

Figure 5.7: The cube root of the third moment $\left(m_3 = \sqrt[3]{M_3}\right)$ of the Faraday spectra from GMIMS-LBS for $|\phi| \leq 20\,\mathrm{rad\,m^{-2}}$. We use the same signal-to-noise mask as the map shown in Figure 5.6. This value quantifies the skewness of the Faraday spectrum, where positive values indicate a skew to positive Faraday depth and *vice versa*. We find that regions 1 and 2 mostly share a common, negative value of m_3, with a sharp sign-change boundary within region 2. Care should be taken in the interpretation of this value, however, as the `RM-CLEAN` algorithm, as well as noise, can introduce false or non-physical features in the Faraday spectrum.

on the median spectra we computed earlier using RM-TOOLS [2] (Purcell et al. in prep.). Here we have taken a number of steps beyond the original data release: we use the fractional spectra for RM-synthesis (rather than absolute Q and U), we have removed potential RFI artefacts, we stop `RM-CLEAN` at a higher cut-off of 180 mK, and we use much finer Faraday depth channels ($\Delta\phi = 0.01\,\mathrm{rad\,m^{-2}}$). We show the results of this in Figure 5.8.

Despite the additional measures we have applied, the asymmetric peak in Faraday depth remains, with `CLEAN` components cascading to more negative ϕ in both regions. This structure in Faraday depth is what is predicted by Bell et al. (2011) for a Faraday caustic: a strong peak in Faraday depth with an asymmetric tail. The direction of the tail corresponds the direction of the gradient in $B_\parallel$, with a tail towards negative ϕ indicating $dB_\parallel/dr < 0$, where r is the distance along the LOS.

It remains possible, however, that this structure is caused by multiple Faraday

[2] https://github.com/CIRADA-Tools/RM

depth components, which are blending in to a broader feature. On the scale of a beam-width, it would be quite likely to see different Faraday depth features blended together. For example, if there were a spatial gradient in ϕ on the plane of sky, or simply two adjacent features, a large beam would blend those two features together. The feature we observe, however, extends much further than the beam-width.

The spatially extended nature of G150−50 is indicative of a LOS feature. This includes a Faraday caustic, as already discussed, and multi-component or naturally Faraday depth-broadened features such as a Burn slab. We are unable to discriminate between these possibilities through RM synthesis alone; instead, we can look into QU-fitting techniques.

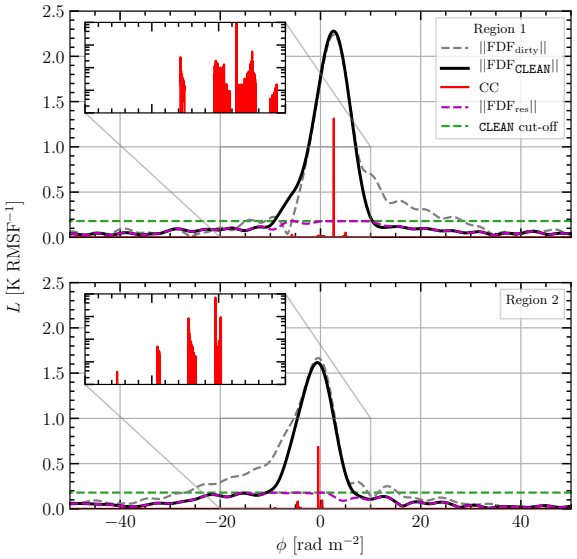

Figure 5.8: The Faraday spectra (||FDF||) in regions 1 (upper panel) and 2 (lower panel). For each region we show the Faraday spectra before ('dirty') and after ('CLEAN') the application RM-CLEAN in grey dashed and black solid lines, respectively. We also show the RM-CLEAN model components (CC), the RM-CLEAN intensity cut-off (CLEAN cut-off), and the residual ('res') Faraday spectrum after the application RM-CLEAN in red solid, green dashed, and purple dashed lines, respectively. In the inset panels we show the CC with a logarithmic scale. These inset panels spans ϕ from -20 to $+10\,\mathrm{rad\,m^{-2}}$ and L from 10^{-4} to $10^{0}\,\mathrm{K\,RMSF^{-1}}$.

5.6 QU-Fitting

QU-fitting is an alternative method of determining the cause of polarized spectral structure. Using this method, one specifies the functional form of a model to be fit to the data and a fitting routine is then applied to determine which model best

Table 5.1: A summary of the models we use in QU-fitting of the Faraday spectra. Column (1): The number we assign to each model. Column (2): A broad description of physical nature of each model. Column (3): The number of free parameters ($N_{\rm free}$) within each model. We provide the functional form definitions for each model in Appendix 5.9.1.1.

Model #	Description	$N_{\rm free}$
1	Faraday thin screen	3
2	Burn slab	3
3	Burn slab + foreground screen	4
4	Burn external dispersion	4
5	Internal dispersion	4
6	Internal dispersion + foreground screen	5
7	Tribble external dispersion	5
8	Two-component Faraday thin screen	6
9	Two-component w/ common Burn external dispersion	7
10	Two-component w/ separate Burn external dispersion	8
11	Caustic	3
12	Caustic + foreground screen	6

represents the data. This technique avoids some of the pitfalls of Faraday tomography, particularly with respect to `RM-CLEAN`, and allows for discrimination between different physical models. Additionally, these models can be extrapolated to other wavelengths. Naturally, the performance of QU-fitting depends on the selection of appropriate models. Here we utilise the QU-fitting routines of RM-TOOLS to both fit a number of models to the average spectra of regions 1 and 2, and compare their performance in representing the data. We describe these routines in detail in Appendix 5.9.1.

We analyze the results of QU-fitting for 12 models, including a Faraday caustic, which we summarize in Table 5.1. We further provide the details and description of each model in Appendix 5.9.1.1. The performance of QU-fitting can be inspected from three perspectives: the goodness-of-fit, the best-fitting parameters, and visual inspection of the best-fitting model. These details are provided in Appendix 5.9.2. In Table 5.2 we give a variety of goodness-of-fit values, such as the reduced χ^2 ($\chi^2_{\rm red}$), and in Table 5.3 we summarize the best-fitting values for the model parameters.

Considering both the best-fitting metrics and visual inspections of the models, models 1 – 7 do not represent the data well. The visual comparisons of these models to the data are given in Figures 5.10–5.16. Each of these models fail to capture both the general depolarization trend of the data in combination with the oscillation

that also appears. We therefore do not consider these models as being physically representative of the data, and we do not discuss them further.

On the best-fitting metrics alone the two-component models with external Faraday dispersion (models 9 and 10) appear to fit both sub-regions the best. This is including the metrics, such as the Bayesian information criterion (BIC), which take account of the number of free parameters of each model. Each of these models describes two emitting regions along the LOS affected by beam depolarization. In region 1, the more complex model 10 does not seem to capture any extra information over model 9. In region 2, however, model 9 appears to be preferenced over model 10. As we have previously discussed, depolarization models predict that the polarization fraction increases towards shorter wavelengths. In region 2, both models 4 and 5 predict an intrinsic polarization fraction of $\sim 99\%$, which is well above the maximum theoretical limit. In region 1, these models predict a more reasonable polarization fraction of $\sim 30\%$.

We have already established, however, that we do not see any significant polarization fraction at 21 cm in the region of G150-50. At L-band we find a polarization fraction of $2 \pm 0.7\%$ and $0.8 \pm 0.2\%$ for regions 1 and 2, respectively. In region 1, models 9 and 10 predict polarization fractions at 21 cm of 23% and 25%, respectively. In region 2 the two-component models predict 144% and 122%. Based on both the morphological evidence and degree of fractional polarization, we can reject these models.

The two-component Faraday thin screen model (model 8) also performs very well, with goodness-of-fit metrics that are on par with the caustic and foreground screen model (model 12). We are able to extrapolate this model to 21 cm, where it predicts more modest polarization fractions of 13% and 11% for regions 1 and 2, respectively. In comparison to the measured values, however, they are an order of magnitude too high. Again, we can reject this model as the predicted polarization fraction is far too high.

For both regions a Faraday caustic with a foreground screen (model 12) follows models 9 and 10 as the best-fitting model. A caustic alone (model 11) cannot reproduce the data well as it depolarizes with no oscillations along λ^2. For both models 11 and 12 we have the caveat that the model only holds for longer wavelengths

(see Appendix 5.9.1.1).

We note that all the models struggled to reproduce the region 2 observations. Of particular interest is the fact that, whilst models 9 and 10 appear to have the best goodness-of-fit metrics, visual inspection of the models is not nearly as convincing (see Figures 5.18 and 5.19). The models seem to be diverging strongly from the trend of the data, leading to the impossibly high polarization fractions at 21 cm. This highlights the importance of evaluating the results of QU-fitting using more than the goodness-of-fit metrics.

The best-fitting model that we cannot rule out is therefore a Faraday caustic with a foreground screen. From the best-fitting parameters, the primary spike in ϕ corresponding to the first moment is provided by the Faraday caustic term. For regions 1 and 2 these Faraday depths are $+3.119 \pm 0.007\,\mathrm{rad\,m^{-2}}$ and $-3.64 \pm 0.02\,\mathrm{rad\,m^{-2}}$, respectively. The foreground screens for each region have Faraday depths of $-2.68 \pm 0.003\,\mathrm{rad\,m^{-2}}$ and $-0.07 \pm 0.01\,\mathrm{rad\,m^{-2}}$, respectively. We show this model in comparison with the data in Figure 5.9. Here we compare the data and model in a number of forms, which highlights the performance of the model in different contexts. Namely, we compare Stokes Q and U vs. $\lambda 2$, L and χ vs. λ^2, and Stokes Q vs. U. We can see that the data are well reproduced by the model, with some deviations at the start and end of the GMIMS-LBS band. Inspecting the other models (e.g. Figures 5.17), we see this is a common feature. It may be possible that the data at the start and end of the band are affected by some RFI contamination. This band was carefully chosen to avoid the effects of RFI, however, so it is difficult to draw a definitive conclusion on this observation.

5.7 Discussion

Since their introduction by Bell et al. (2011) Faraday caustics have only been directly considered a handful of times. Their detection through processing techniques is discussed by Bell & Enßlin (2012) and Beck et al. (2012), and their appearance is found in simulated observations by Ideguchi et al. (2014). Faraday caustics have only received observational consideration in Van Eck et al. (2017, 2019). In these works, however, the observations were not able to exclude or confirm the presence of

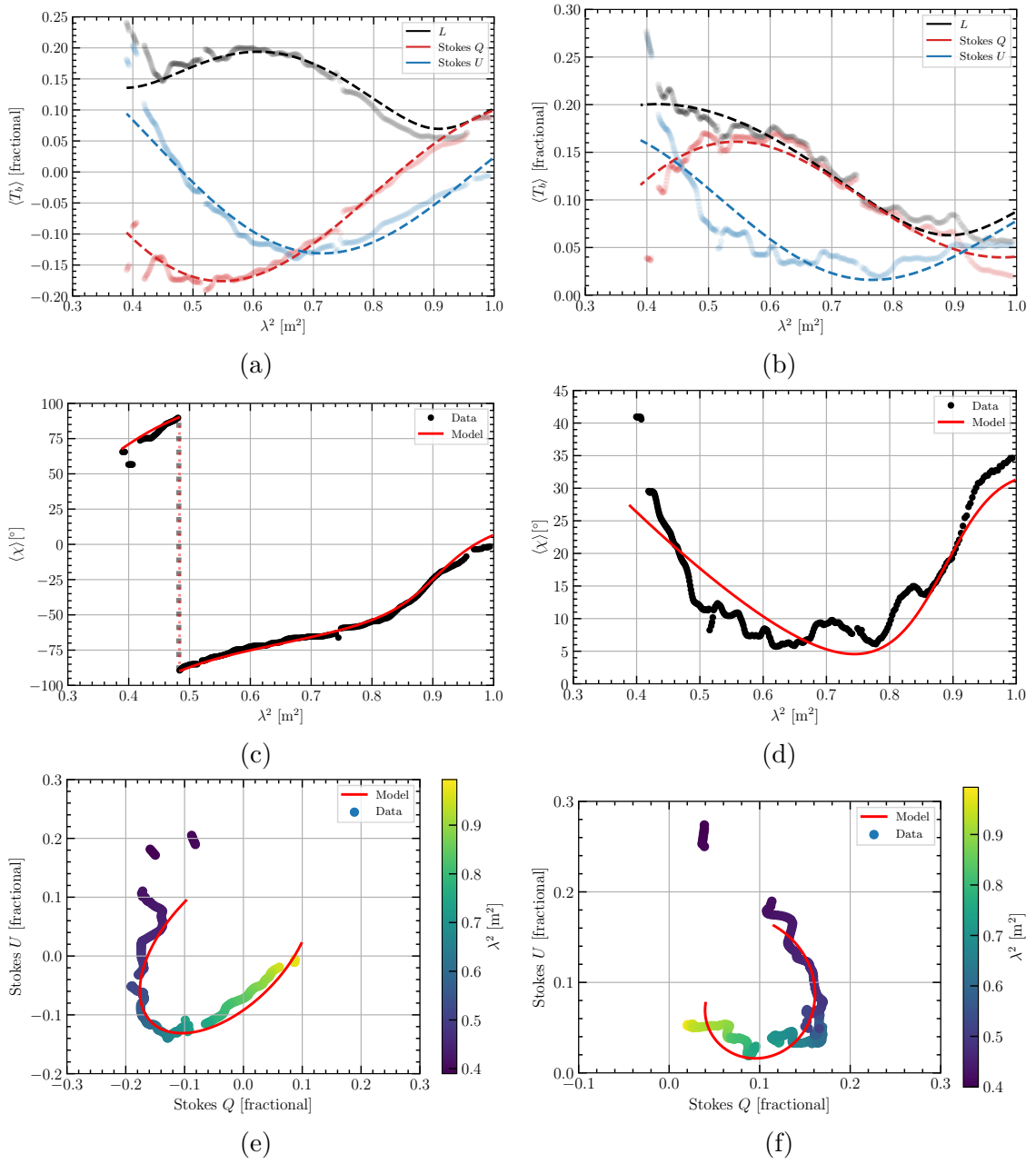

Figure 5.9: The Faraday caustic with a foreground screen model (model 12). Left column – Region 1, right column – Region 2. Top row – Stokes Q (red), Stokes U (blue), and polarized intensity (L, black) against λ^2. Here the dotted points are the average spectra as per Figure 5.5, and the dashed lines are the model values. Middle row – Polarization angle (χ) against λ^2. Here the data are shown in black points and model as a red line. Bottom row – Stokes Q against Stokes U. The data are the points coloured by λ^2 and again the model is shown in red.

Faraday caustics. As such, we consider this work to be the first strong observational indication of a Faraday caustic.

Our results for G150−50 require a foreground screen in addition to a background Faraday caustic. Further, the Faraday depths of the caustic component in each of the

two sub-regions we describe are substantially different. In both cases, however, the caustic indicates a negative gradient along the LOS in $B_{\parallel}$. This is a strong finding in regard to the nearby magneto-ionic medium. In addition to the gradient in $B_{\parallel}$, we also expect $B_{\parallel}$ to reach $0\,\mu$G within about 500 pc of the Sun in this direction.

From the polarization data alone, however, it is not possible to completely constrain the complete three-dimensional structure. This calls for further investigation of this region using additional ISM tracers. Such tracers would include H I (e.g. Thomson et al., 2018) and three-dimensional dust map (e.g. Van Eck et al., 2017; Thomson et al., 2019). We should note, however, that the prominence of this feature is due to the structure magnetic field. This will make finding a clear corresponding feature in the ISM difficult.

A clear follow-up to perform would be to utilize diffuse imaging from the Murchison Widefield Array (MWA). The GaLactic and Extragalactic All-sky Murchison Widefield Array (GLEAM) survey (Hurley-Walker et al., 2017b) covers the G150−50 region. The higher angular resolution would allow comparison with ISM tracers, such as H I. Additionally, the low frequencies would allow for very fine Faraday resolution, which would be very useful to compare with the GMIMS-LBS results. If the full GLEAM bandwidth could be utilized, that would provide a maximum-to-minimum frequency ratio of 3.2. As Bell et al. (2011) shows, high Faraday resolution in combination with a large bandwidth can unambiguously reveal a Faraday caustic, and can even reveal details of the turbulent magnetic field along the LOS.

Finally, the most natural extension of this work would be the incorporation of the complete GMIMS components. In particular, the mid-band surveys would allow us to test our model extrapolations and determine at what frequencies G150−50 no longer dominates the polarized sky. In preparation for such observations, we would require a Faraday caustic model that is free of its current constraints. Currently, we can only apply it to large values of λ^2 and it would therefore not hold for the high- and mid-band GMIMS components.

5.8 Conclusions

We have identified the brightest region in the Southern polarized sky at 400 MHz. Using observations from GMIMS-LBS we analyze both the morphology and spectral structure in polarization from 300 to 480 MHz. To support these observations we also analyse the 408 MHz maps from Haslam et al. (1982); Remazeilles et al. (2015) and Mathewson & Milne (1965), and L-band maps from Reich (1982); Reich & Reich (1986); Reich et al. (2001) and Wolleben et al. (2006).

The region, which we refer to as G150−50, is located at $l, b \sim (150, -50)^\circ$ and extends for nearly 20 deg^2. This same region appears in the Mathewson & Milne (1965) map, indicating that this a real feature of the sky and not an artefact in GMIMS-LBS. The region appears to be separated into two sub-regions centred on $l, b \sim (151, -50)^\circ$ and $l, b \sim (139, -53)^\circ$, respectively. At 408 MHz G150−50 is about 50% brighter than the North Polar Spur and exhibits polarization fractions of up to 15%. In total intensity there is no feature that resembles G150−50, but it does appear to align with part of radio Loop II. At 1.4 GHz Loop II does appear as a polarized feature, however, we find no indication of G150−50.

The polarized continuum spectra from GMIMS-LBS in each sub-region strongly indicate broad Faraday depth structure. From moment analysis of the Faraday depth cubes we find the two regions each have peak Faraday depths of opposite sign, but a skewness towards negative Faraday depths. We reprocess the Faraday spectra for each sub-region, finding broad Faraday depth structure with a tail towards negative Faraday depths. Such a structure in Faraday depth was predicted by Bell et al. (2011) to correspond to a Faraday caustic. These features are caused by a gradient in the LOS component of the Galactic magnetic field, and correspond to where $B_\parallel \rightarrow 0\,\mu$G. GMIMS-LBS is one of the first polarization surveys to meet the condition that $\nu_{\rm max}/\nu_{\rm min} > 1.5$, meaning that it can resolve the structure of a Faraday caustic in Faraday depth-space.

We apply Stokes QU-fitting analysis, testing 12 models which might cause Faraday spectra similar to a caustic. We find that the majority of best-fitting models predict a polarization fraction that is too high with respect to the measured values for each sub-region. The remaining best-fitting model that we cannot eliminate on

this basis is a Faraday caustic with a foreground Faraday-rotating screen.

These results are the first strong observational indications of a Faraday caustic. This observation indicates that the nearby Galactic magnetic field has a negative gradient along the LOS in this direction. Further confirmation of this finding can be made with the complete GMIMS survey, especially from the mid-band component. Those data would provide the large Faraday depth-scales in RM synthesis which are produced by Faraday caustics and would test our model-fitting results. High resolution follow-up with the MWA would allow investigation of how this region corresponds with other features the ISM, and provide high resolution in Faraday depth. Such observations may even produce information on the turbulent component of the nearby Galactic magnetic field.

Acknowledgements

We wish to thank both Michael Bell and Torsten Enßlin for their useful correspondence on this work. We also thank Emil Lenc for digitizing the Mathewson & Milne (1965) data.

AT acknowledges the support of the Australian Government Research Training Program (RTP) Scholarship.

The Parkes Radio Telescope is part of the Australia Telescope National Facility which is funded by the Australian Government for operation as a National Facility managed by CSIRO. The EBHIS data are based on observations performed with the 100-m telescope of the MPIfR at Effelsberg. EBHIS was funded by the Deutsche Forschungsgemeinschaft (DFG) under the grants KE757/7-1 to 7-3.

This research made use of Astropy,[3] a community-developed core Python package for Astronomy (Astropy Collaboration et al., 2013, 2018). We have made use of the 'cubehelix' colour-scheme (Green, 2011). Some of the results in this paper have been derived using the HEALPix (Górski et al., 2005) package.

[3]http://www.astropy.org

5.9 Appendix

5.9.1 QU-fitting procedure

5.9.1.1 Model functional forms

We obtain the model functional forms from Burn (1966), Tribble (1991), Sokoloff et al. (1999), Bell et al. (2011), and O'Sullivan et al. (2012). Here we describe both the physical interpretation of each model along with the function which describes the complex polarization as a function of λ^2.

Model 1 *Faraday thin screen:* Emission and Faraday rotation originate in separate volumes. The foreground rotating volume contains a uniform magnetic field and thermal electron density. The complex polarization is:

$$P = p_0 e^{\left[2i\left(\psi_0 + \phi_0 \lambda^2\right)\right]}. \tag{5.15}$$

Model 2 *Differential Faraday rotation/Burn slab:* The emitting volume additionally contains a uniform LOS B-field component which causes Faraday rotation through the volume. The complex polarization is:

$$P = p_0 \frac{\sin\left(\phi_0 \lambda^2\right)}{\phi_0 \lambda^2} e^{\left[2i\left(\psi_0 + \frac{1}{2}\phi_0 \lambda^2\right)\right]}. \tag{5.16}$$

Model 3 *Differential Faraday rotation/Burn slab with foreground screen:* The same as Model 2, but modulated by a foreground rotating screen. The complex polarization is:

$$P = p_0 \frac{\sin\left(\phi_0 \lambda^2\right)}{\phi_0 \lambda^2} e^{\left\{2i\left[\psi_0 + \left(\frac{1}{2}\phi_{0,1} + \phi_{0,2}\right)\lambda^2\right]\right\}}. \tag{5.17}$$

Model 4 *External Faraday dispersion (beam depolarization):* Emission and Faraday rotation originate in separate volumes. In this model, however, two scenarios are accounted for: either the foreground rotating volume contains a turbulent medium, comprised of multiple cells which fall within the telescope beam; or, the rotating volume contains a regular field which changes in strength or direction within the

beam. The complex polarization is:

$$P = p_0 e^{\left[2i\left(\psi_0+\phi_0\lambda^2\right)\right]} e^{\left(-2\sigma_\phi^2\lambda^4\right)}, \tag{5.18}$$

where σ_ϕ is the variation in Faraday depth.

Model 5 *Internal Faraday dispersion:* As in the Burn slab case, the emitting and rotating volumes are co-spatial. Here, however, the magnetic field has a turbulent component. The complex polarization is:

$$\begin{aligned} P &= p_0 e^{(2i\psi_0)} \left(\frac{1-e^{-S}}{S}\right), \\ S &= 2\sigma_\phi^2\lambda^4 - 2i\phi_0\lambda^2. \end{aligned} \tag{5.19}$$

Model 6 *Internal Faraday dispersion with a foreground screen:* The same as Model 5, but with a foreground rotating screen. The complex polarization is:

$$\begin{aligned} P &= p_0 e^{\left(2i\psi_0+\phi_{0,2}\lambda^2\right)} \left(\frac{1-e^{-S}}{S}\right), \\ S &= 2\sigma_\phi^2\lambda^4 - 2i\phi_{0,1}\lambda^2. \end{aligned} \tag{5.20}$$

Model 7 *External Tribble Faraday dispersion:* This model describes the same physical scenario as Model 4, but with the correction of Tribble (1991). This case holds for long wavelengths, and an intrinsic polarization fraction of $p_0 \leq 0.5$. The complex polarization is:

$$P = p_0 e^{\left[2i\left(\psi_0+\phi_0\lambda^2\right)\right]} \frac{1}{2\sqrt{2N_{\text{cell}}}\sigma_\phi\lambda^2}. \tag{5.21}$$

Model 8 *Two Faraday thin screens:* The same physical scenario as Model 1, but with two separate emitting volumes and two rotating volumes along the LOS. The complex polarization is:

$$P = p_{0,1} e^{\left[2i\left(\psi_{0,1}+\phi_{0,1}\lambda^2\right)\right]} + p_{0,2} e^{\left[2i\left(\psi_{0,2}+\phi_{0,2}\lambda^2\right)\right]}. \tag{5.22}$$

Model 9 *Two components with common external Faraday dispersion:* The same conditions as Model 4, but with two separate emitting regions with a common

rotating volume. The complex polarization is:

$$P = \left(p_{0,1} e^{\left[2i\left(\psi_{0,1}+\phi_{0,1}\lambda^2\right)\right]} + p_{0,2} e^{\left[2i\left(\psi_{0,2}+\phi_{0,2}\lambda^2\right)\right]}\right) e^{\left(-2\sigma_\phi^2\lambda^4\right)}. \tag{5.23}$$

Model 10 *Two components with separate external Faraday dispersion:* The same conditions as Model 4, but with two separate emitting regions and rotating volumes. The complex polarization is:

$$\begin{aligned} P = {} & p_{0,1} e^{\left[2i\left(\psi_{0,1}+\phi_{0,1}\lambda^2\right)\right]} e^{\left(-2\sigma_{\phi,1}^2\lambda^4\right)} \\ & + p_{0,2} e^{\left[2i\left(\psi_{0,2}+\phi_{0,2}\lambda^2\right)\right]} e^{\left(-2\sigma_{\phi,2}^2\lambda^4\right)}. \end{aligned} \tag{5.24}$$

Model 11 *Faraday caustic:* As derived by Bell et al. (2011), a caustic will occur when the LOS component of the magnetic field crosses 0 μG. In their derivation Bell et al. (2011) assumed a flat spectrum where $\alpha = -1$. For GMIMS-LBS (Wolleben et al., 2019) the brightness temperature spectral index, β, was consistent with -2.8. Since $\alpha = \beta + 2$ this corresponds to $\alpha \sim -0.8$, which we consider not to be a significant deviation. Bell et al. (2011) also note that this model is divergent as λ becomes small. In their full formulation, the D term acts against this divergence. In our case, however, we are simply fitting D as a parameter. Therefore we consider this formulation suitable only for longer wavelengths. The complex polarization is:

$$P = \left[\Re(D) + i\Im(D)\right] e^{\left(2i\phi_0\lambda^2\right)} \frac{(-1-i)\sqrt{\pi}}{2\sqrt{\lambda^2}}, \tag{5.25}$$

where $D = \Re(D) + i\Im(D)$ is a complex number defined in Bell et al. (2011) Eqn. 13. This quantity contains information of both the initial polarization angle, and the gradient in $B_\parallel$.

Model 12 *Faraday caustic with a foreground screen:* The same as Model 11, but modulated by a foreground rotating screen. The complex polarization is:

$$\begin{aligned} P = {} & \left[\Re(D) + i\Im(D)\right] e^{\left(2i\phi_{0,1}\lambda^2\right)} \frac{(-1-i)\sqrt{\pi}}{2\sqrt{\lambda^2}} \\ & + p_0 e^{\left[2i\left(\psi_{0,2}+\phi_{0,2}\lambda^2\right)\right]}. \end{aligned} \tag{5.26}$$

5.9.1.2 Best-fitting routine

The QU-fitting of RM-TOOLS utilizes the MultiNest algorithm (Feroz & Hobson, 2008; Feroz et al., 2009, 2019), implemented as PYMULTINEST (Buchner et al., 2014). The details of this algorithm and its implementation are in the aforementioned references, however, we will provide a brief overview as it pertains to this work.

MultiNest uses a Bayesian approach to model fitting. In such an approach, we want to obtain the posterior probability (P) of a set of model parameters (θ). This can also be thought of as the probability (p) of the model parameters, given the data (d) and the model ($\mathcal{M}$). Using Bayes' theorem, the posterior can be evaluated as:

$$P(\theta) = p(\theta|d, \mathcal{M}) = \frac{p(d|\theta, \mathcal{M})p(\theta|\mathcal{M})}{p(d|\mathcal{M})} = \frac{\mathcal{L}(\theta)\mathcal{P}(\theta)}{\mathcal{E}(\theta)}, \tag{5.27}$$

where $\mathcal{L}(\theta)$ is the likelihood, or the probability of the data given the parameters and the model:

$$\mathcal{L}(\theta) = p(d|\theta, \mathcal{M}), \tag{5.28}$$

$\mathcal{P}(\theta)$ is the prior, or the probability of the parameters and the model:

$$\mathcal{P}(\theta) = p(\theta, \mathcal{M}), \tag{5.29}$$

and $\mathcal{E}(\theta)$ is the evidence, or the probability of the data given the model. Further, since this is a model selection problem, the evidence is taken to be the factor which normalizes the posterior over the entire model-space ($\Omega_{\mathcal{M}}$):

$$\mathcal{E}(\theta) = p(d|\mathcal{M}) \equiv \int_{\Omega_{\mathcal{M}}} \mathcal{L}(\theta)\mathcal{P}(\theta)d\theta. \tag{5.30}$$

In RM-TOOLS, the log-likelihood is evaluated as:

$$\ln(\mathcal{L}) = -N_{\rm data} \ln(2\pi) - 2\left[\sum_{i=1}^{N_{\rm data}} \ln(\sigma_{QU,i})\right] - \frac{\chi^2_Q}{2} - \frac{\chi^2_U}{2}, \tag{5.31}$$

where $N_{\rm data}$ is the number of data points, $\sigma_{QU,i}$ is the error on each data point, and χ^2_Q and χ^2_U is the χ^2 for the Stokes Q and U data, respectively.

We provide the data, error estimates, and priors for each parameter to PYMULTINEST, which returns the prior distribution for each model parameters, and

the likelihood of each model, which allows for a number of goodness-of-fit quantities to be evaluated. We note that for all of the following quantities, a factor of 10 is typically considered a 'significant' difference. Typically, one could consider the reduced-χ^2 ($\chi^2_{\rm red}$) to determine goodness-of-fit:

$$\chi^2_{\rm red} = \frac{\chi^2}{\rm DoF}, \tag{5.32}$$

where DoF is the number of degrees-of-freedom:

$$\rm DoF = N_{data} - N_{free} - 1, \tag{5.33}$$

where $N_{\rm free}$ is the number of free parameters and χ^2 is:

$$\chi^2 = \sum_{i=1}^{N_{\rm data}} \left[\left(\frac{Q_{{\rm data},i} - Q_{{\rm model},i}}{\sigma_{QU,i}} \right)^2 + \left(\frac{U_{{\rm data},i} - U_{{\rm model},i}}{\sigma_{QU,i}} \right)^2 \right]. \tag{5.34}$$

This evaluation is blind, however, to the number of model parameters. Instead one could consider the Bayesian information criterion (BIC):

$$\rm BIC = \ln\left(N_{data}\right) N_{free} - 2\ln\left(\hat{\mathcal{L}}\right), \tag{5.35}$$

which has a 'penalty' term for the number of free parameters. Similarly, we can also look at the Akaike information criterion (AIC):

$$\rm AIC = 2N_{free} - 2\ln\left(\hat{\mathcal{L}}\right), \tag{5.36}$$

which has a weaker penalty term than the BIC, and the AICc:

$$\rm AICc = AIC + \frac{2N_{free}^2 + 2N_{free}}{N_{data} - N_{free} - 1}, \tag{5.37}$$

which corrects the AIC for small sample sizes.

5.9.2 Results of QU-fitting

Table 5.2: A summary of the best-fitting metrics for each model we use in QU-fitting of the Faraday spectra. Col. (1): The number of degrees of freedom (see Equation 5.33). Col. (2): The χ^2 of the model (see Equation 5.34). Col. (3): The reduced χ^2 of the model (see Equation 5.32). Col. (4): The Akaike information criterion (see Equation 5.36. Col. (5): The corrected Akaike information criterion (see Equation 5.37). Col. (6): The Bayesian information criterion (see Equation 5.35). Col. (7): The log-Bayesian-evidence, or the log-probability of the data given the model (see Equation 5.30). Col. (8): The error in the log-Bayesian-evidence, as determined by MultiNest. Note that the values of BIC, AIC, and AICc should be taken as relative, with the absolute value applying specifically to the model-fitting process at hand. These metrics can also take on negative values, implying less information is lost relative to a positive value. In other words, one should preference the information criterion which sits furthest down the number line.

Model #	DoF	χ^2	$\chi^2_{\rm red}$	AIC	AICc	BIC	$\ln(\mathcal{E})$	$\sigma[\ln(\mathcal{E})]$
Region 1								
1	654	7.91×10^4	121	7.36×10^4	7.36×10^4	7.36×10^4	-3.68×10^4	0.16
2	654	6.71×10^4	103	6.16×10^4	6.16×10^4	6.16×10^4	-3.08×10^4	0.15
3	653	3.24×10^4	49.7	2.69×10^4	2.69×10^4	2.69×10^4	-1.35×10^4	0.18
4	653	3.48×10^4	53.2	2.92×10^4	2.92×10^4	2.93×10^4	-1.46×10^4	0.17
5	653	6.71×10^4	103	6.16×10^4	6.16×10^4	6.16×10^4	-3.08×10^4	0.19
6	652	2.68×10^4	49.6	2.68×10^4	2.68×10^4	2.68×10^4	-1.38×10^4	0.20
7	652	4.51×10^4	69.1	3.90×10^4	3.89×10^4	3.90×10^4	-1.95×10^4	0.17
8	651	2.2×10^4	33.8	1.65×10^4	1.65×10^4	1.65×10^4	-7.39×10^3	0.21
9	650	5.45×10^3	8.38	-1.32×10^3	-1.33×10^3	-1.29×10^3	614	0.22
10	649	3.56×10^3	5.49	-1.96×10^3	-1.98×10^3	-1.93×10^3	927	0.24
11	654	5.42×10^4	82.9	4.87×10^4	4.87×10^4	4.87×10^4	-2.44×10^4	0.19
12	651	1.15×10^4	17.7	6×10^3	5.99×10^3	6.03×10^3	-3.05×10^3	0.24
Region 2								
1	658	5.44×10^4	82.6	4.96×10^4	4.96×10^4	4.96×10^4	-2.48×10^4	0.16
2	658	2.89×10^4	44.0	2.36×10^4	2.36×10^4	2.36×10^4	-1.18×10^4	0.15
3	657	2.12×10^4	32.3	1.60×10^4	1.60×10^4	1.60×10^4	-8.02×10^3	0.17
4	657	2.23×10^4	33.9	1.71×10^4	1.71×10^4	1.71×10^4	-8.59×10^3	0.17
5	657	1.55×10^4	23.6	1.02×10^4	1.02×10^4	1.03×10^4	-5.15×10^3	0.18
6	656	1.55×10^4	23.6	1.02×10^4	1.02×10^4	1.03×10^4	-5.16×10^3	0.20
7	656	2.85×10^4	43.4	2.33×10^4	2.33×10^4	2.34×10^4	-1.17×10^4	0.17
8	655	9.86×10^3	15	4.57×10^3	4.56×10^3	4.6×10^3	-2.32×10^3	0.20
9	654	1.46×10^4	22.4	-905	-919	-874	409	0.22
10	653	6.14×10^3	9.41	881	865	917	-509	0.27
11	658	3.79×10^4	57.7	3.3×10^4	3.3×10^4	3.3×10^4	-1.65×10^4	0.18
12	655	1.11×10^4	17.0	5.92×10^3	5.91×10^3	5.94×10^3	-3.01×10^3	0.23

Table 5.3: A summary of the resulting physical parameters from QU-fitting of the Faraday spectra. The values produced here are the median from the parameters' probability distribution functions, and the error ranges correspond to $\pm 1\sigma$. Each of these parameters are defined in Section 5.9.1.1 (Equations 5.15–5.26). The parameters p_0, ϕ_0, and ψ_0 are the intrinsic polarization fraction, Faraday depth, and polarization angle of the fitted component, respectively. The σ_ϕ parameter quantifies the Faraday dispersion of the component. Subscripts '1' and '2' refer to the first and second fitted components. For single-component models, the latter term is omitted. The parameter D applies to Faraday caustic models, and is defined in Section 5.9.1.1 and Equation 5.25. The N_{cell} term applies to the Tribble external dispersion model, and describes the number of turbulent cells inside the telescope beam (see Section 5.9.1.1 and Equation 5.21).

Model #	$p_{0,1}$	$\phi_{0,1}$	$\psi_{0,1}$	$\sigma_{\phi,1}$	$p_{0,2}$	$\phi_{0,2}$	$\psi_{0,2}$	$\sigma_{\phi,2}$	D	N_{cell}
Region 1										–
1	0.1355 ± 0.0002	2.67 ± 0.005	11.9 ± 0.2	–	–	–	–	–	–	–
2	0.2943 ± 0.0007	2.977 ± 0.003	56.61 ± 0.08	–	–	–	–	–	–	–
3	0.2583 ± 0.0007	-2.594 ± 0.01	15.1 ± 0.2	–	–	3.87 ± 0.01	–	–	–	–
4	0.2715 ± 0.0009	2.607 ± 0.006	14.2 ± 0.2	0.847 ± 0.002	–	–	–	–	–	–
5	0.2943 ± 0.0007	2.977 ± 0.003	51.6 ± 0.08	0.002 ± 0.002	–	–	–	–	–	–
6	0.2601 ± 0.0007	-2.571 ± 0.007	16.3 ± 0.3	0.233 ± 0.02	–	3.816 ± 0.01	–	–	–	–
7	0.4 ± 0.1	2.658 ± 0.005	12.4 ± 0.2	0.07 ± 0.04	–	–	–	–	–	500 ± 300
8	0.1244 ± 0.0003	3.423 ± 0.008	167.2 ± 0.3	–	0.0637 ± 0.0003	-0.86 ± 0.02	128.3 ± 0.9	–	–	–
9	0.309 ± 0.004	2.77 ± 0.02	185.7 ± 0.9	–	0.088 ± 0.002	-4.37 ± 0.08	-78 ± 3	0.914 ± 0.003	–	–
10	0.293 ± 0.001	2.776 ± 0.007	7.1 ± 0.3	0.873 ± 0.003	0.057 ± 0.001	-4.45 ± 0.02	100.0 ± 0.9	0.59 ± 0.02	–	–
11	–	2.658 ± 0.005	–	–	–	–	–	–	$-0.0849 \pm 0.0003 + i(0.0313 \pm 0.0006)$	–
12	–	3.119 ± 0.007	–	–	0.0498 ± 0.0003	-2.68 ± 0.03	25 ± 1	–	$-0.0519 \pm 0.0007 + i(0.0742 \pm 0.0005)$	–
Region 2										
1	0.1264 ± 0.0003	-0.148 ± 0.008	19.8 ± 0.3	–	–	–	–	–	–	
2	0.292 ± 0.001	-3.046 ± 0.007	64.04 ± 0.1	–	–	–	–	–	–	–
3	0.271 ± 0.001	2.84 ± 0.01	36.19 ± 0.3	–	–	-2.05 ± 0.03	–	–	–	–
4	0.299 ± 0.001	-0.580 ± 0.009	34.3 ± 0.3	0.969 ± 0.003	–	–	–	–	–	
5	0.3467 ± 0.001	-2.90 ± 0.01	56.01 ± 0.2	0.896 ± 0.006	–	–	–	–	–	–
6	0.3483 ± 0.002	-2.90 ± 0.01	56.5 ± 0.4	0.904 ± 0.008	–	-0.02 ± 0.01	–	–	–	–
7	0.38 ± 0.1	-0.401 ± 0.007	28.9 ± 0.2	0.07 ± 0.04	–	–	–	–	–	500 ± 300
8	0.132 ± 0.002	-0.35 ± 0.04	35 ± 2	–	0.072 ± 0.002	-3.37 ± 0.07	99 ± 3	–	–	
9	0.993 ± 0.006	0.05 ± 0.04	24 ± 1	1.422 ± 0.002	0.569 ± 0.005	2.74 ± 0.06	40 ± 2	–	–	
10	0.998 ± 0.002	4.295 ± 0.02	153.7 ± 0.5	2.2150 ± 0.0008	0.4659 ± 0.0006	0.050 ± 0.002	10.14 ± 0.08	1.114 ± 0.001	–	
11	–	-0.273 ± 0.007	–	–	–	–	–	–	$-0.0845 \pm 0.0002 + i(-0.0055 \pm 0.0008)$	
12	–	-3.64 ± 0.02	–	–	0.1196 ± 0.0004	-0.07 ± 0.01	23.1 ± 0.6	–	$0.0423 \pm 0.0003 + i(0.006 \pm 0.001)$	

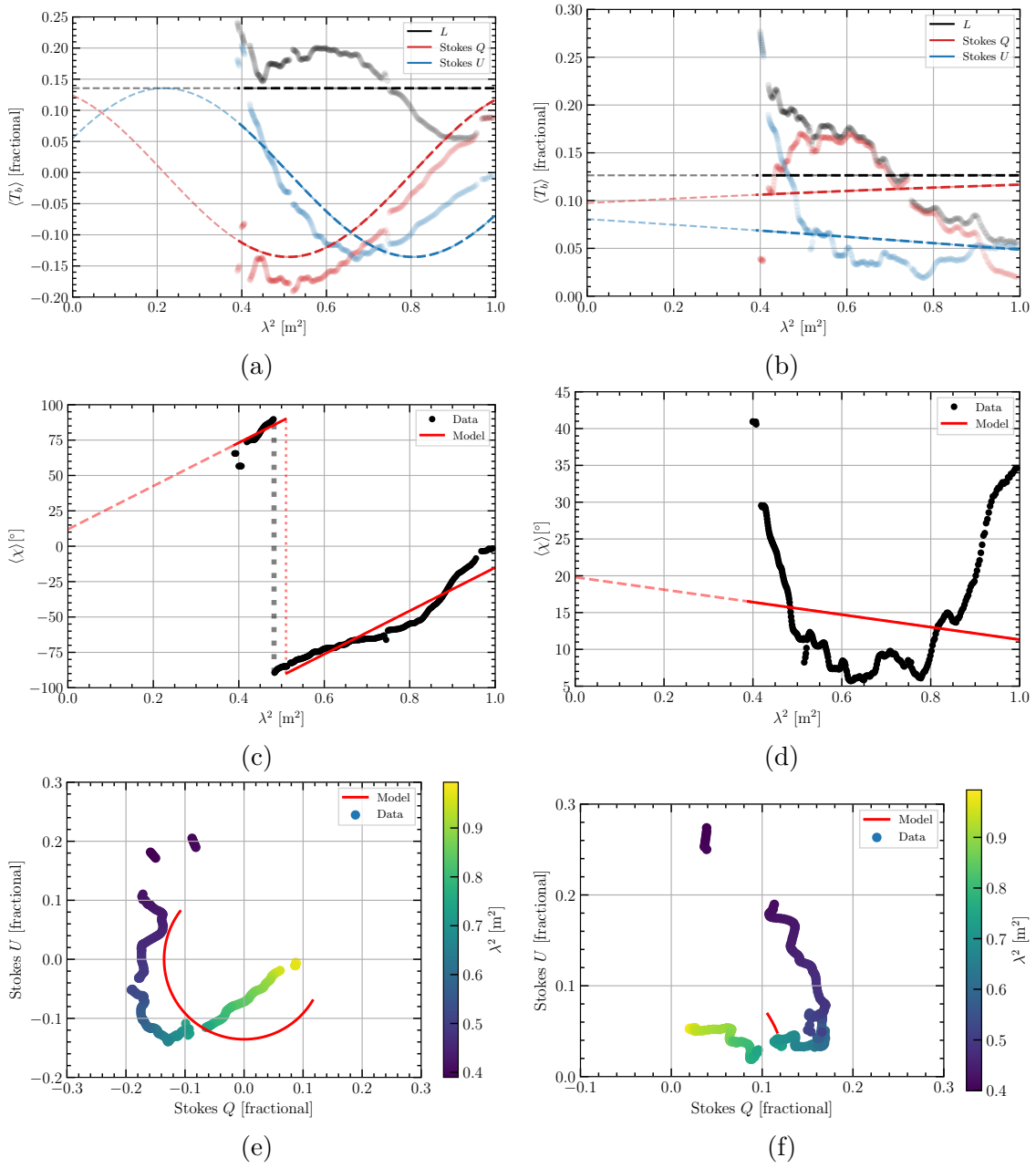

Figure 5.10: Faraday thin screen model (model 1). Left column – Region 1, right column – Region 2. Top row – Stokes Q (red), Stokes U (blue), and polarized intensity (L, black) against λ^2. Here the dotted points are the average spectra as per Figure 5.5, and the dashed lines are the model values. Middle row – Polarization angle (χ) against λ^2. Here the data are shown in black points and model as a red line. Bottom row – Stokes Q against Stokes U. The data are the points coloured by λ^2 and again the model is shown in red.

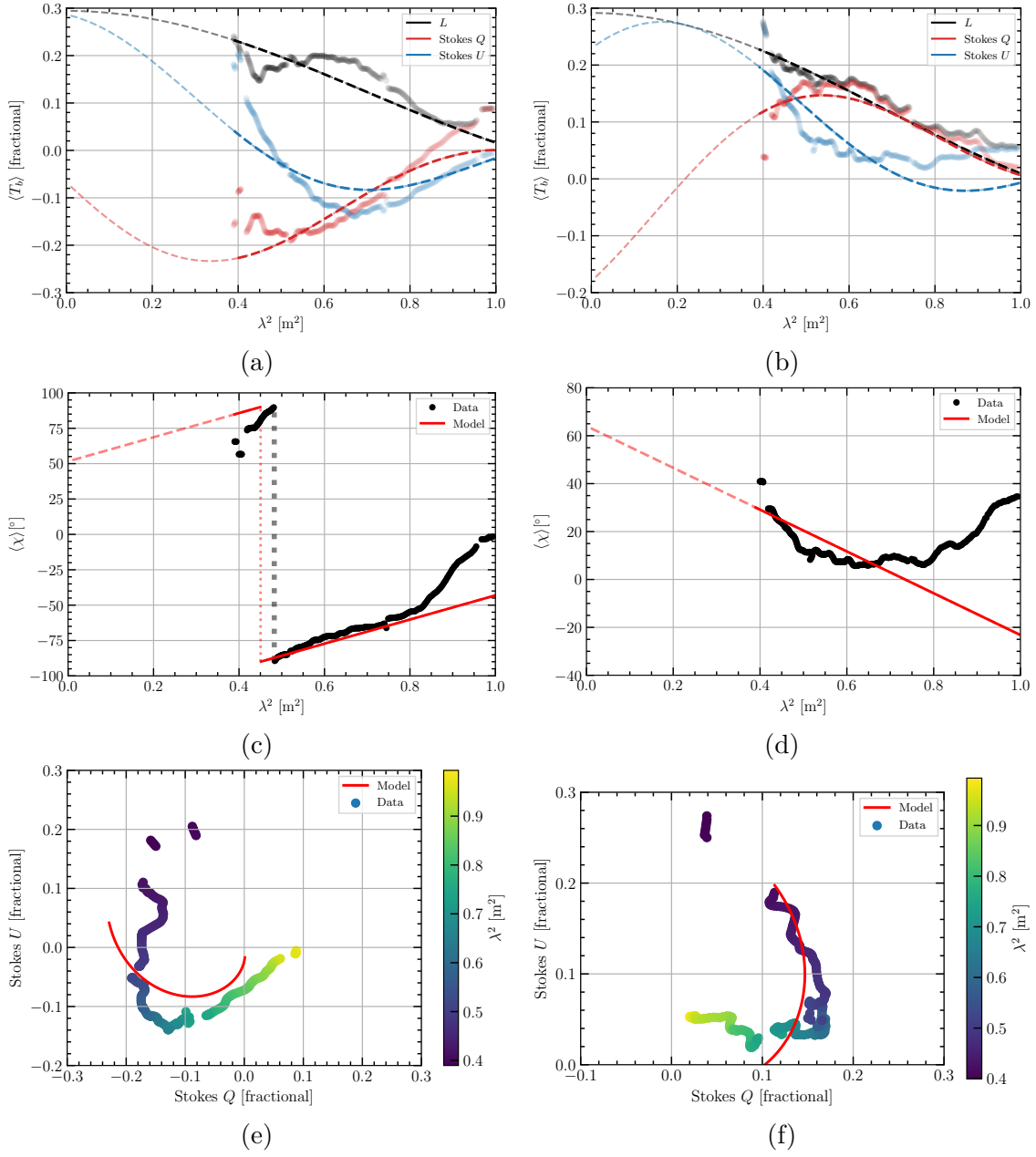

Figure 5.11: The Burn slab model (model 2). Left column – Region 1, right column – Region 2. Top row – Stokes Q (red), Stokes U (blue), and polarized intensity (L, black) against λ^2. Here the dotted points are the average spectra as per Figure 5.5, and the dashed lines are the model values. Middle row – Polarization angle (χ) against λ^2. Here the data are shown in black points and model as a red line. Bottom row – Stokes Q against Stokes U. The data are the points coloured by λ^2 and again the model is shown in red.

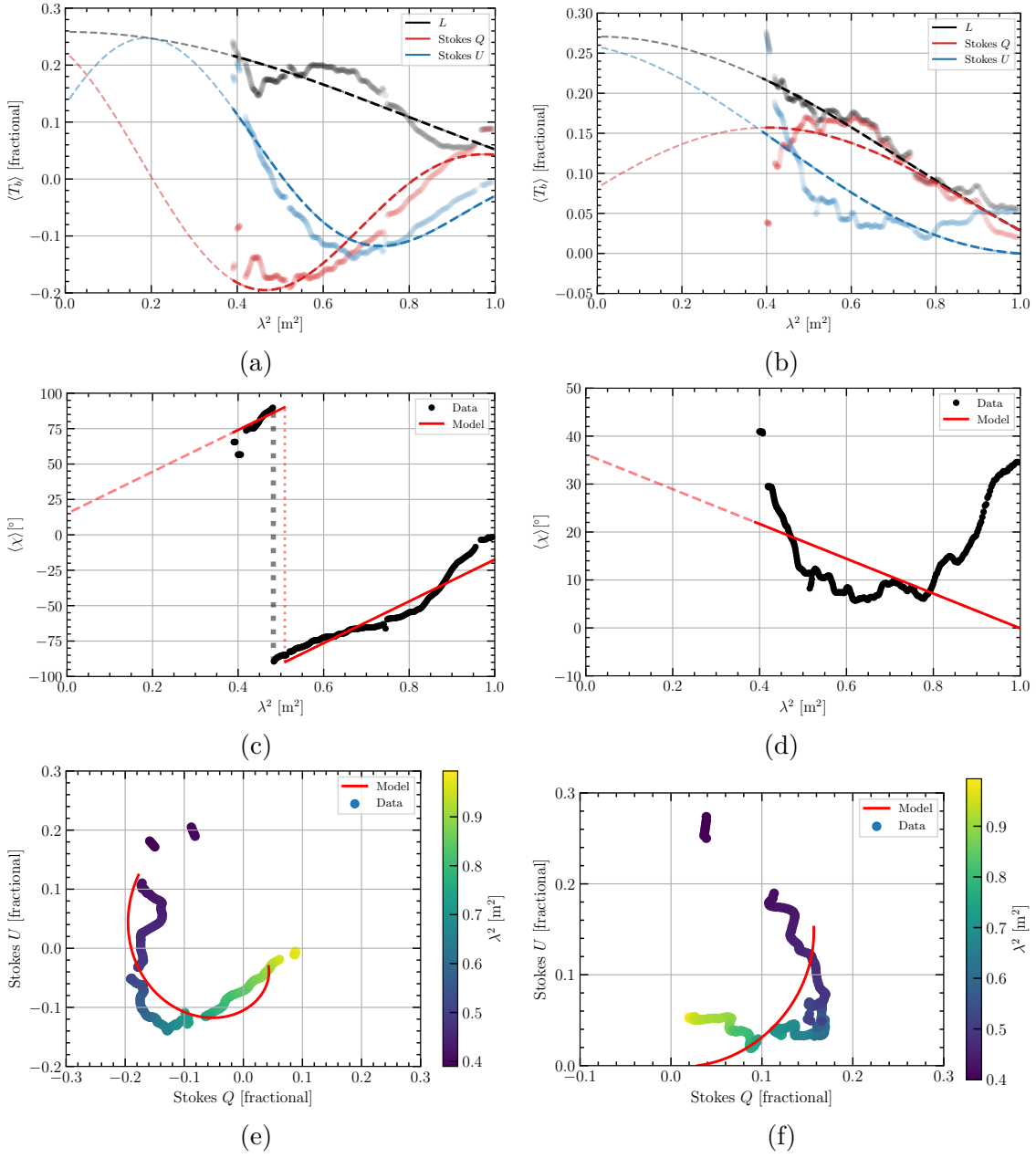

Figure 5.12: The Burn slab model with a foreground screen (model 3). Left column – Region 1, right column – Region 2. Top row – Stokes Q (red), Stokes U (blue), and polarized intensity (L, black) against λ^2. Here the dotted points are the average spectra as per Figure 5.5, and the dashed lines are the model values. Middle row – Polarization angle (χ) against λ^2. Here the data are shown in black points and model as a red line. Bottom row – Stokes Q against Stokes U. The data are the points coloured by λ^2 and again the model is shown in red.

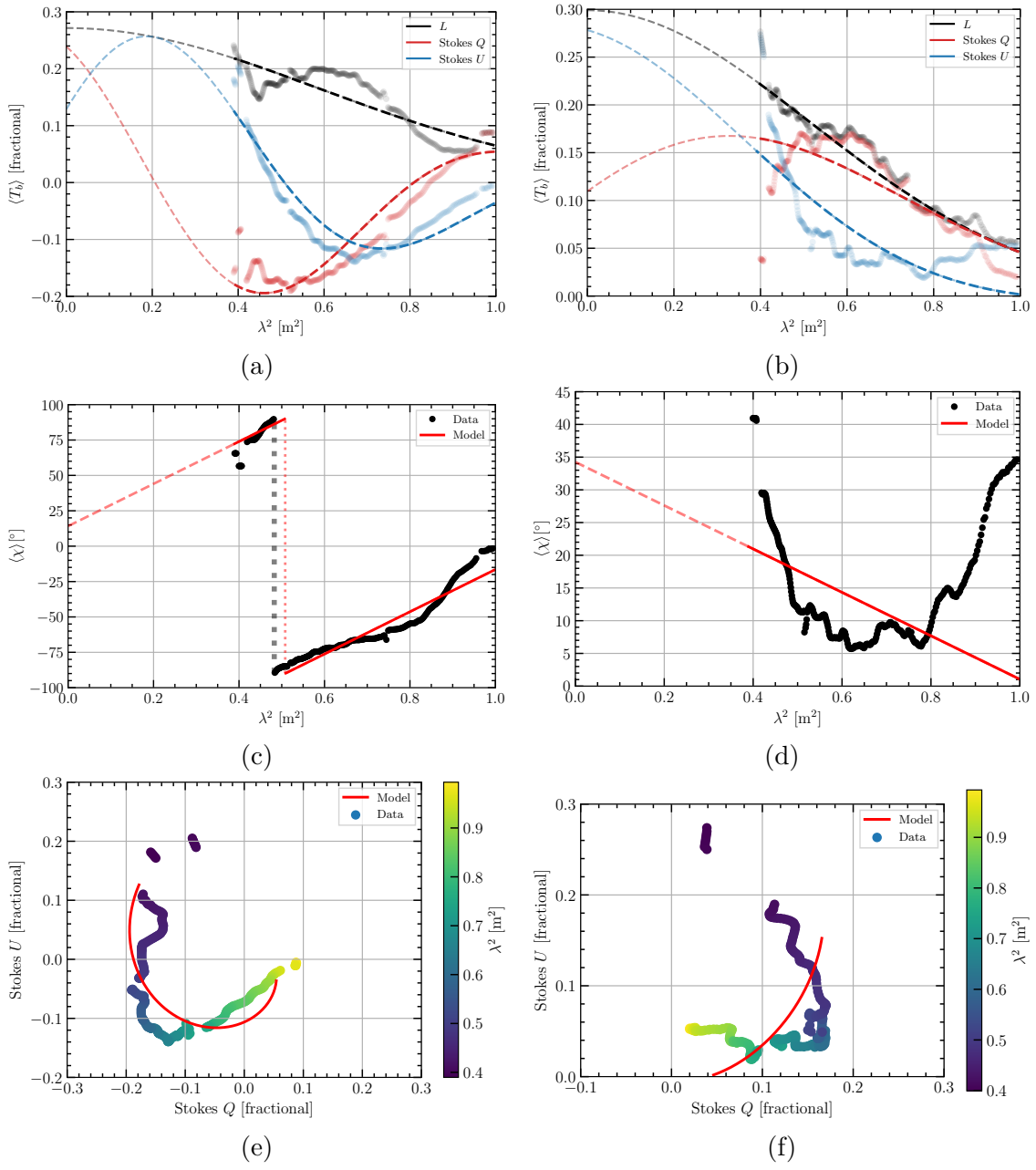

Figure 5.13: The external Faraday dispersion model (model 4). Left column – Region 1, right column – Region 2. Top row – Stokes Q (red), Stokes U (blue), and polarized intensity (L, black) against λ^2. Here the dotted points are the average spectra as per Figure 5.5, and the dashed lines are the model values. Middle row – Polarization angle (χ) against λ^2. Here the data are shown in black points and model as a red line. Bottom row – Stokes Q against Stokes U. The data are the points coloured by λ^2 and again the model is shown in red.

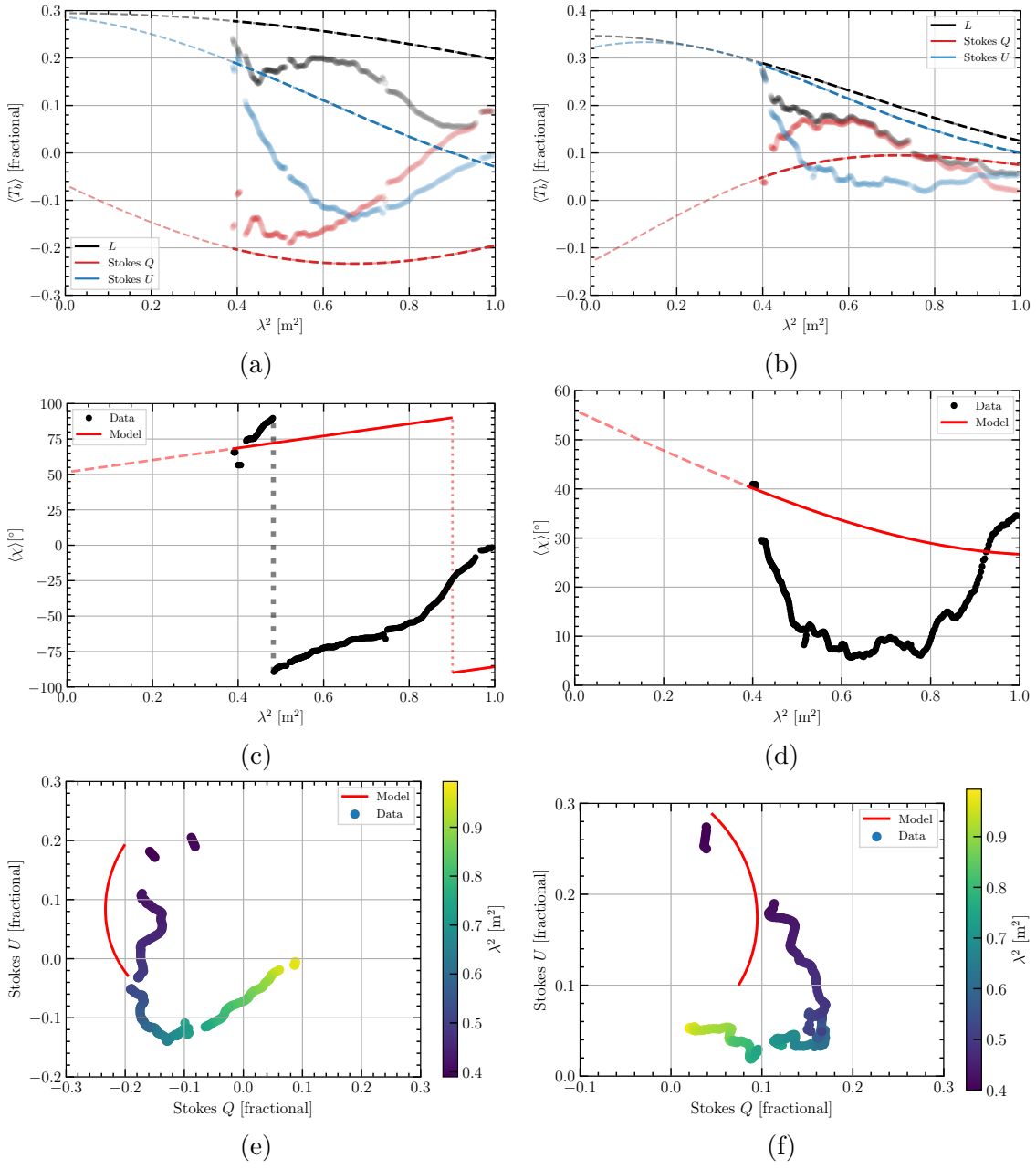

Figure 5.14: The internal Faraday dispersion model (model 5). Left column – Region 1, right column – Region 2. Top row – Stokes Q (red), Stokes U (blue), and polarized intensity (L, black) against λ^2. Here the dotted points are the average spectra as per Figure 5.5, and the dashed lines are the model values. Middle row – Polarization angle (χ) against λ^2. Here the data are shown in black points and model as a red line. Bottom row – Stokes Q against Stokes U. The data are the points coloured by λ^2 and again the model is shown in red.

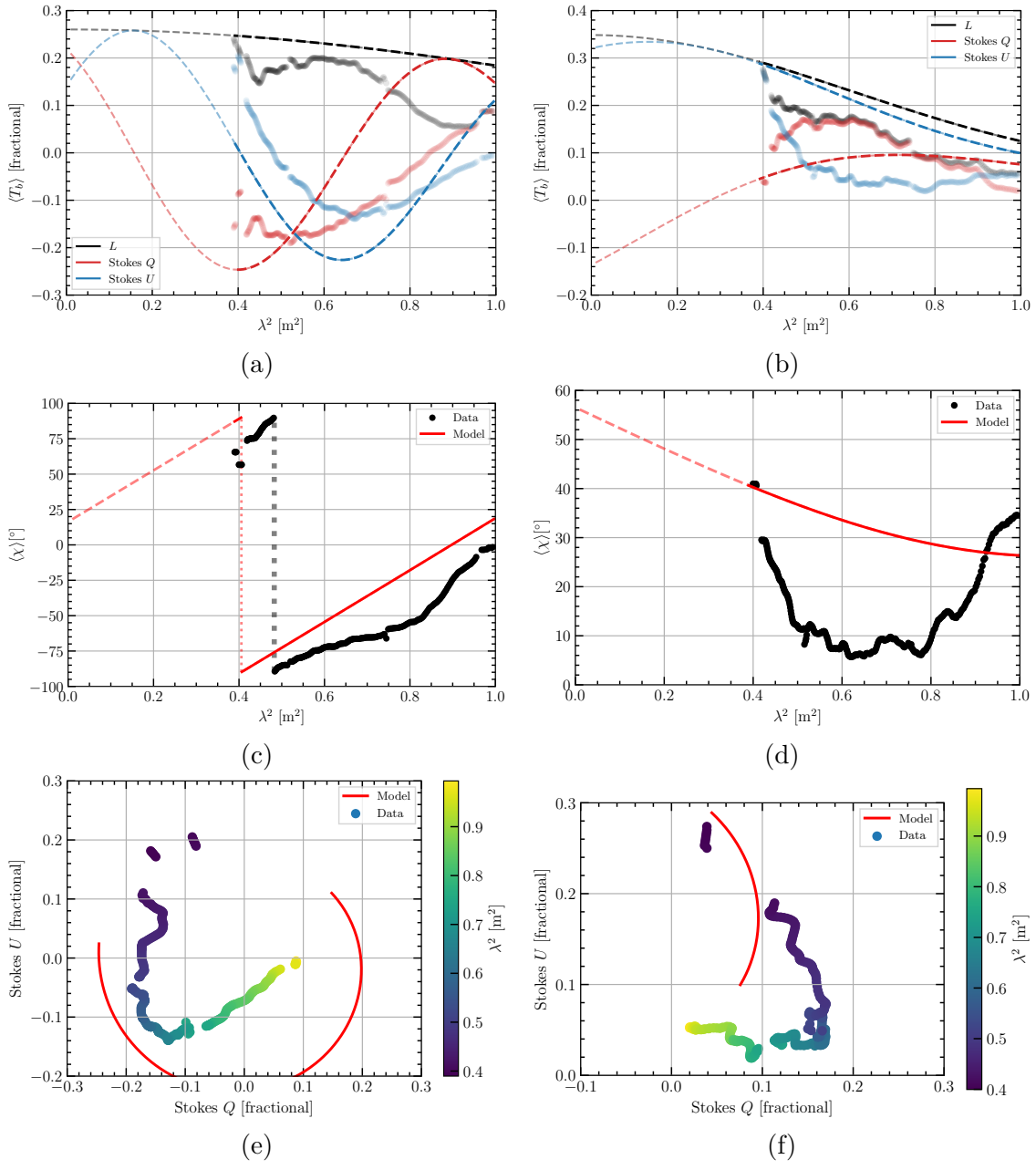

Figure 5.15: The internal Faraday dispersion model with a foreground screen (model 6). Left column – Region 1, right column – Region 2. Top row – Stokes Q (red), Stokes U (blue), and polarized intensity (L, black) against λ^2. Here the dotted points are the average spectra as per Figure 5.5, and the dashed lines are the model values. Middle row – Polarization angle (χ) against λ^2. Here the data are shown in black points and model as a red line. Bottom row – Stokes Q against Stokes U. The data are the points coloured by λ^2 and again the model is shown in red.

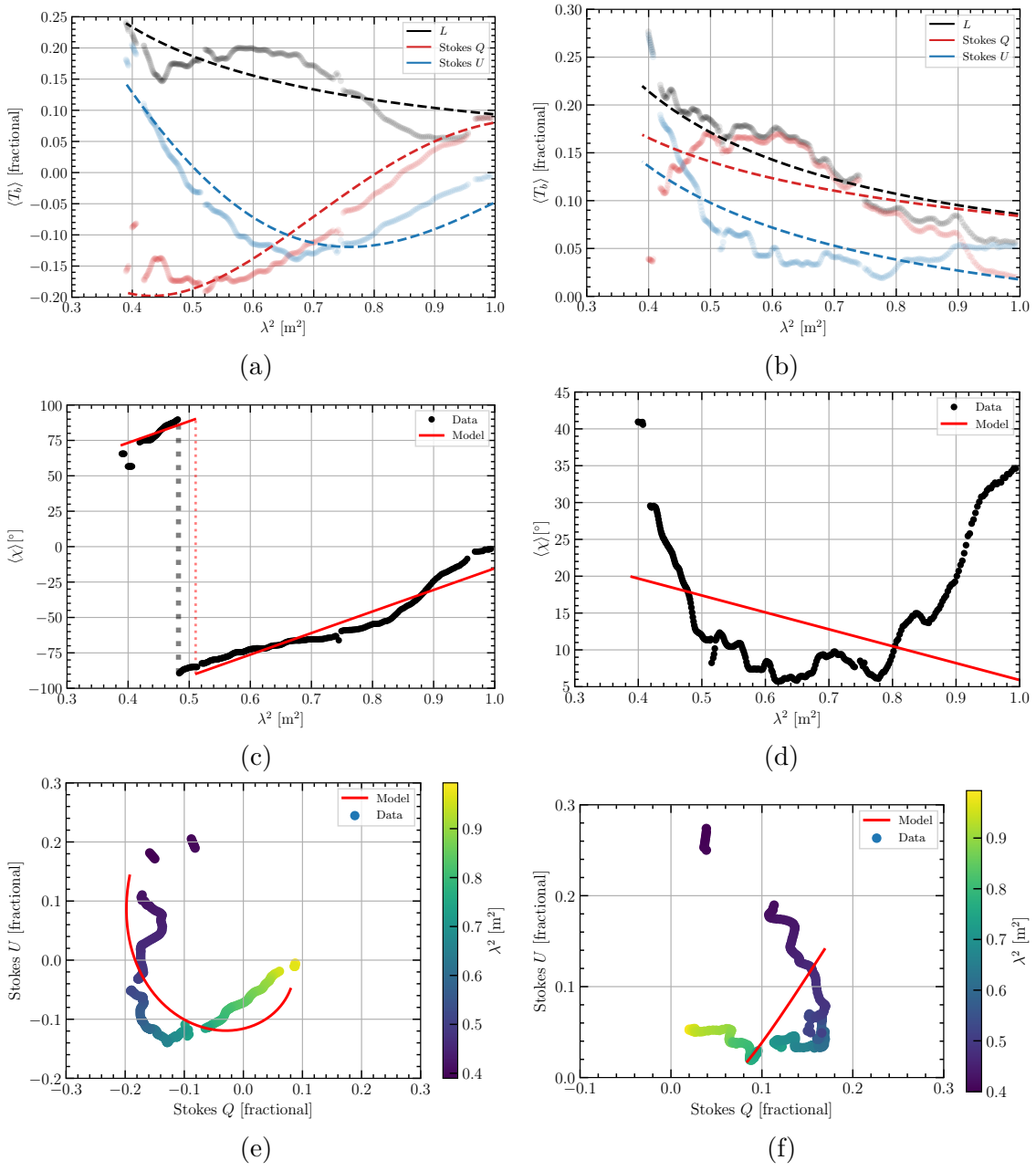

Figure 5.16: The Tribble (1991) external Faraday dispersion model (model 7). Left column – Region 1, right column – Region 2. Top row – Stokes Q (red), Stokes U (blue), and polarized intensity (L, black) against λ^2. Here the dotted points are the average spectra as per Figure 5.5, and the dashed lines are the model values. Middle row – Polarization angle (χ) against λ^2. Here the data are shown in black points and model as a red line. Bottom row – Stokes Q against Stokes U. The data are the points coloured by λ^2 and again the model is shown in red.

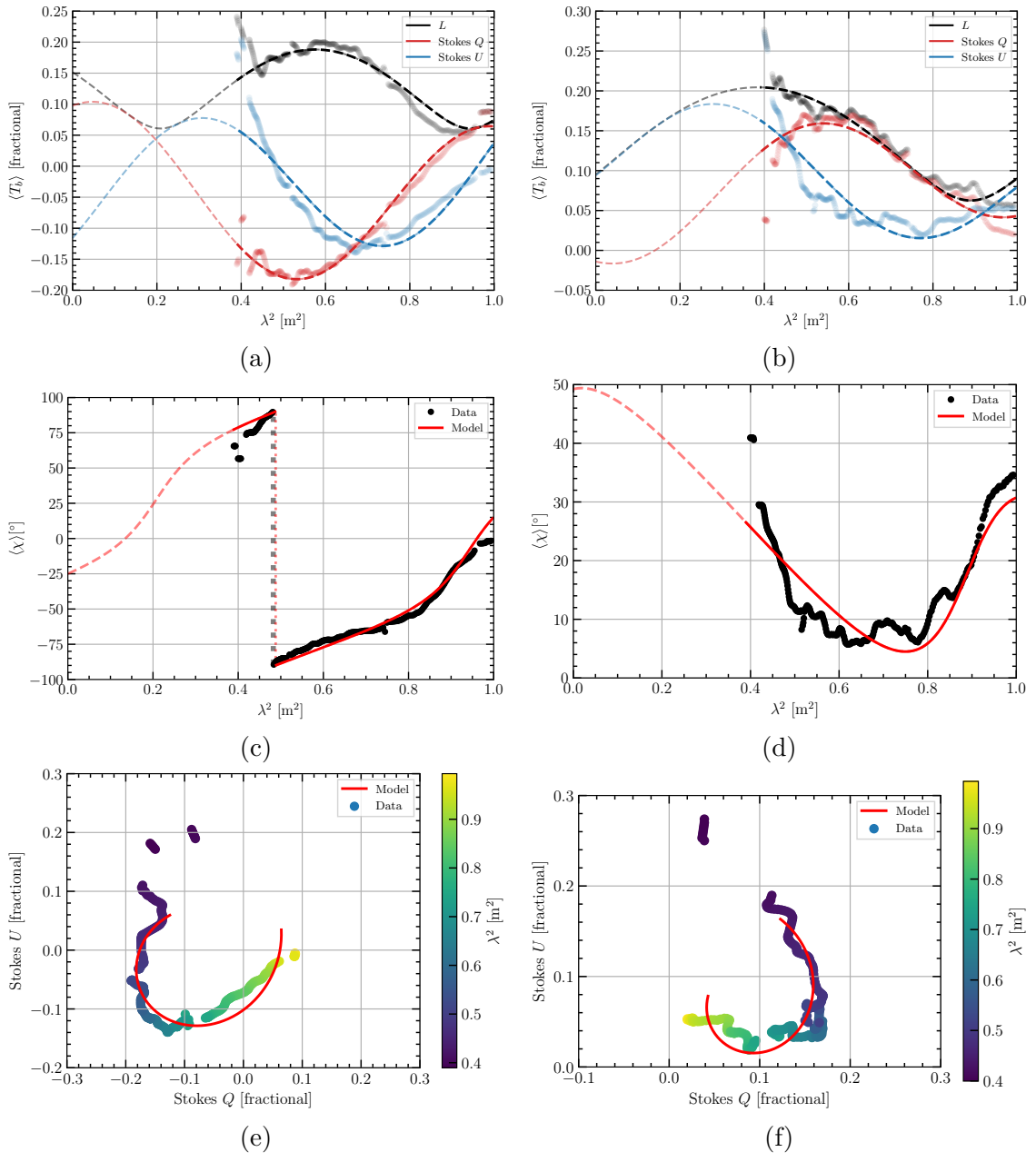

Figure 5.17: The two-component Faraday thin screen (model 8). Left column – Region 1, right column – Region 2. Top row – Stokes Q (red), Stokes U (blue), and polarized intensity (L, black) against λ^2. Here the dotted points are the average spectra as per Figure 5.5, and the dashed lines are the model values. Middle row – Polarization angle (χ) against λ^2. Here the data are shown in black points and model as a red line. Bottom row – Stokes Q against Stokes U. The data are the points coloured by λ^2 and again the model is shown in red.

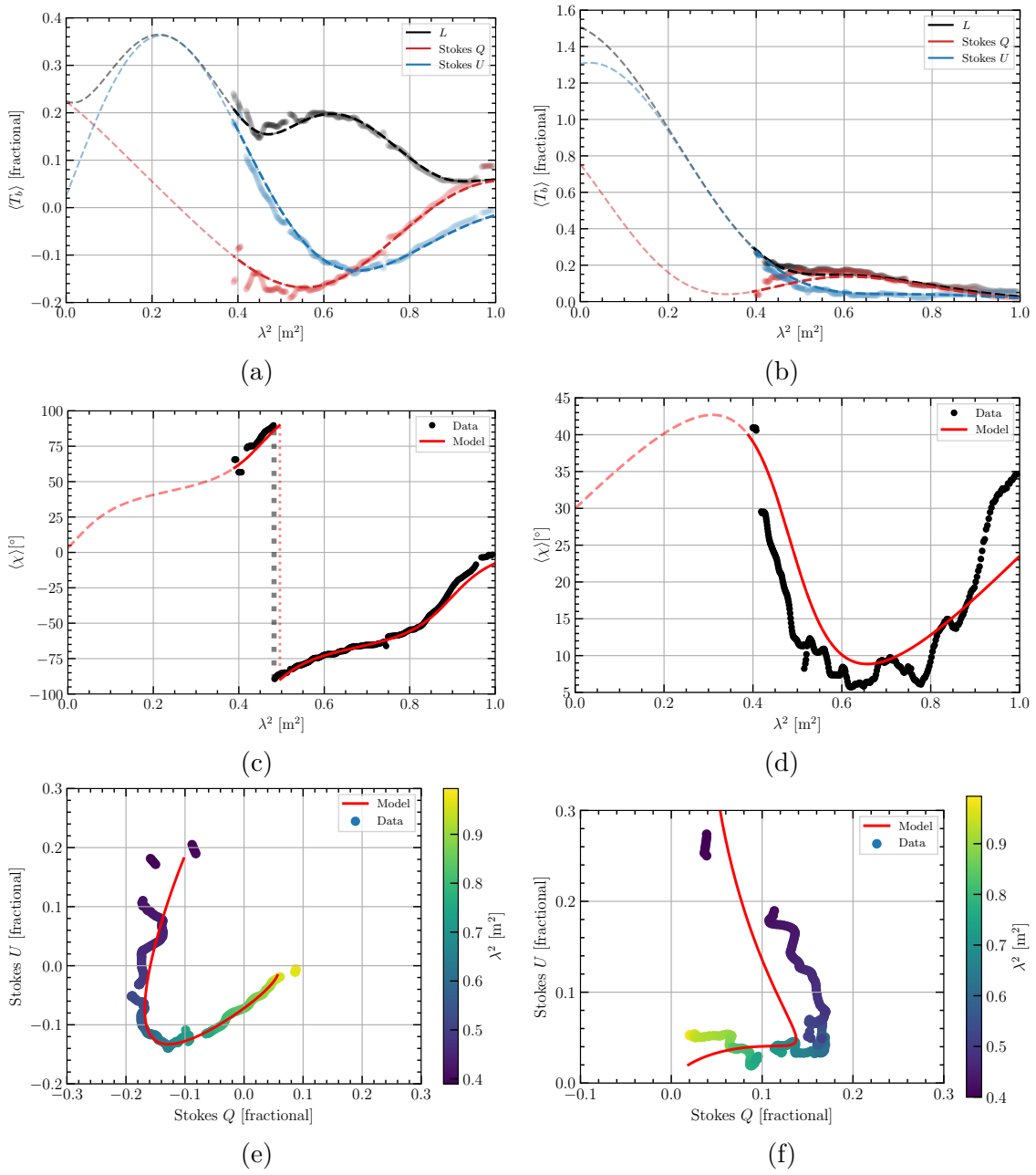

Figure 5.18: The two-component model with common Burn external dispersion (model 9). Left column – Region 1, right column – Region 2. Top row – Stokes Q (red), Stokes U (blue), and polarized intensity (L, black) against λ^2. Here the dotted points are the average spectra as per Figure 5.5, and the dashed lines are the model values. Middle row – Polarization angle (χ) against λ^2. Here the data are shown in black points and model as a red line. Bottom row – Stokes Q against Stokes U. The data are the points coloured by λ^2 and again the model is shown in red.

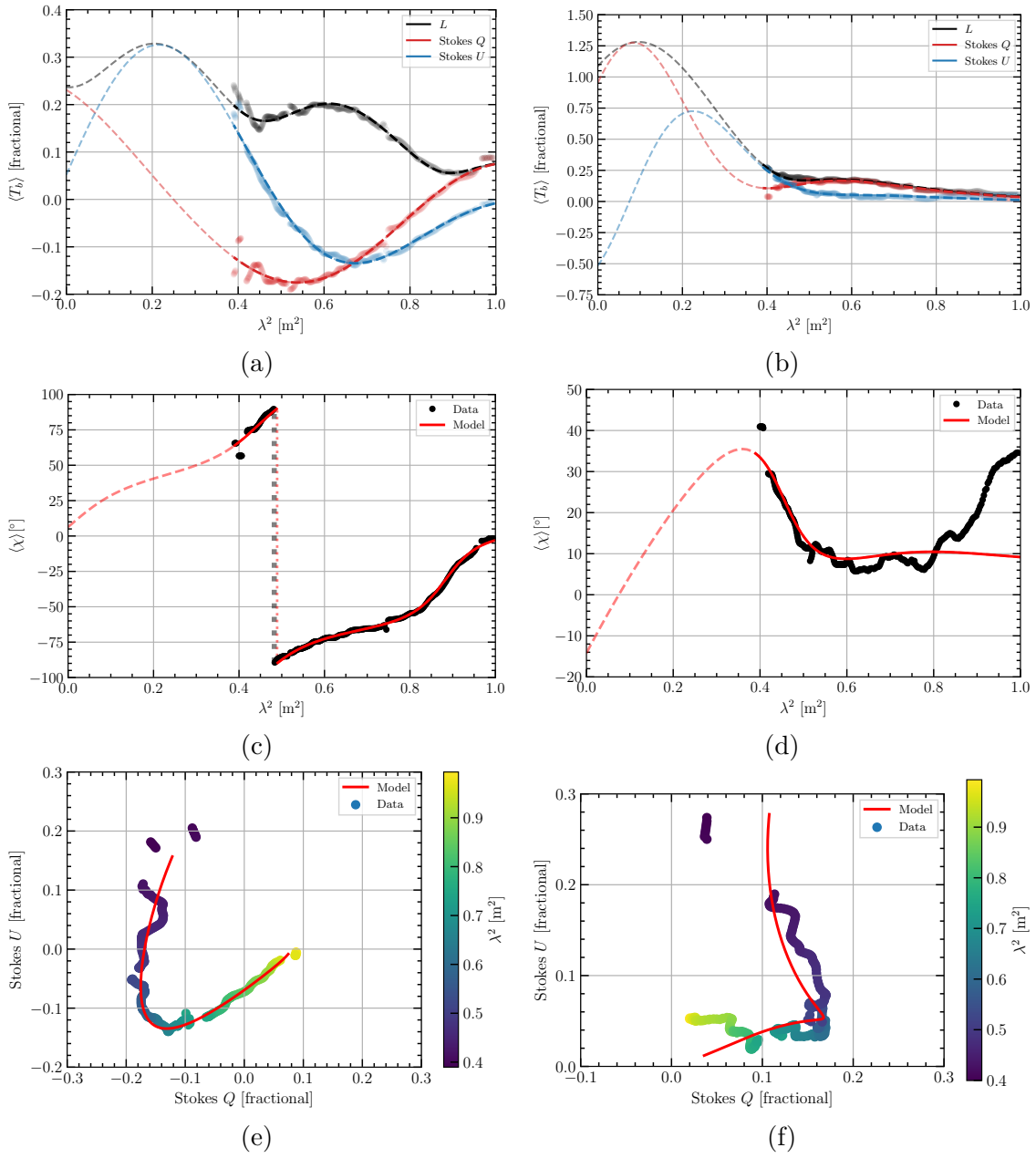

Figure 5.19: The two-component model with separate Burn external dispersion (model 10). Left column – Region 1, right column – Region 2. Top row – Stokes Q (red), Stokes U (blue), and polarized intensity (L, black) against λ^2. Here the dotted points are the average spectra as per Figure 5.5, and the dashed lines are the model values. Middle row – Polarization angle (χ) against λ^2. Here the data are shown in black points and model as a red line. Bottom row – Stokes Q against Stokes U. The data are the points coloured by λ^2 and again the model is shown in red.

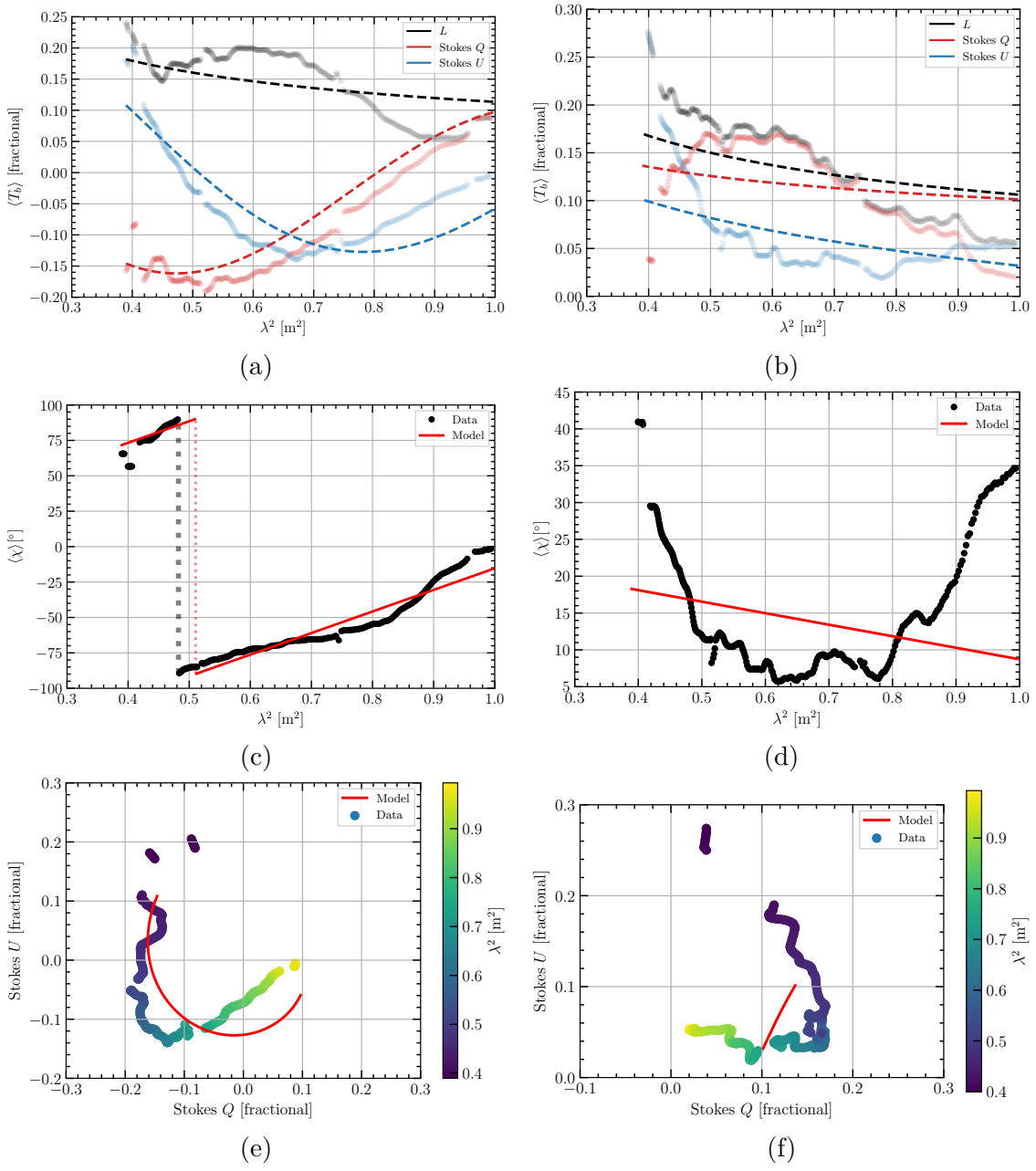

Figure 5.20: The Faraday caustic model (model 11). Left column – Region 1, right column – Region 2. Top row – Stokes Q (red), Stokes U (blue), and polarized intensity (L, black) against λ^2. Here the dotted points are the average spectra as per Figure 5.5, and the dashed lines are the model values. Middle row – Polarization angle (χ) against λ^2. Here the data are shown in black points and model as a red line. Bottom row – Stokes Q against Stokes U. The data are the points coloured by λ^2 and again the model is shown in red.

6

Conclusion

6.1 Summary of thesis

Magnetic fields fill the interstellar medium of the Milky Way Galaxy. These fields are lit up by cosmic ray electrons spiralling around these fields at relativistic speeds, producing synchrotron radiation. This emission is diffuse, and produces large extended features on the sky. As this highly linearly polarized emission propagates through the magneto-ionic medium of the Galaxy, it is perturbed by the Faraday rotation effect. In this thesis I have used the latest single-dish all-sky polarization surveys to study the magnetic fields of the Milky Way. Through combining tracers of the other components of the Galactic interstellar medium, I have begun to unravel the complex fabric of the Galactic magneto-ionic medium.

In Chapter 2, I present my work on the Southern low-frequency component of the Global Magneto-Ionic Medium Survey (GMIMS-LBS), published in Wolleben

et al. (2019). We analyzed the quality of the total intensity spectrum from GMIMS-LBS, which informed us on the calibration of both the Stokes I and polarization data. We found that our observations at 408 MHz correspond very well to the Haslam et al. (1982) survey. These surveys were both observed with the Parkes 64 m Telescope, but calibrated independently. We therefore found our calibration method was successful. Looking at our Stokes I spectrum across the GMIMS-LBS band, we showed that the spectral index derived from observations were consistent with the expected value of $\beta \approx -2.8$. From both of these analyses we conclude our intensity measurements, both total and polarized, are accurate within a factor of $\sim 10\%$.

We also applied Faraday tomography to the GMIMS-LBS data for use in investigating the Galactic magneto-ionic medium. We produced a cube of polarized intensity against Faraday depth (ϕ) across the entire Southern sky, covering the range $-100 \leq \phi \leq +100\,\mathrm{rad\,m^{-2}}$ in steps of $0.5\,\mathrm{rad\,m^{-2}}$. For each pixel we accounted for the effects of missing channels in the RM synthesis process, producing a unique RM spread function (RMSF) for each pixel on the sky. We deconvolved each pixel using this RMSF down to the RMS noise of the survey. The resulting spectra contained many interesting features, including broad, narrow, and mutli-peaked Faraday spectra. I analyzed a number of these spectra in later chapters.

In Chapter 3 (Thomson et al., 2018), I analyzed the magnetic fields of a giant Galactic supershell, GSH 006−15+7. In the all-sky polarization maps at 2.3 GHz from the S-band Polarization All Sky Survey (S-PASS), we found the signature of this supershell. This signature corresponds to the magneto-ionic medium of the shell causing Faraday rotation. We modelled the Faraday rotation through GSH 006−15+7, using Wilkinson Microwave Anisotropy Probe (WMAP) K-band observations to estimate the background polarized synchrotron emission. To determine the magnetic field strength, we combined our modelled Faraday depth with the all-sky H$\,\alpha$ data from the Wisconsin H-Alpha Mapper Sky Survey (WHAM-SS). From these data we estimated the thermal electron density in the supershell, which allowed us to separate out the magnetic field component of the Faraday depth. We found a line-of-sight magnetic field structure which appears to wrap around the shell, which is expected for a shell blown into an ambient field primarily aligned in the plane

of the sky. The magnetic field strength we derived, $\sim 2\,\mu$G, is dynamically weak but comparable to similar large objects in the Galactic ISM. Despite these weak fields, they produced a significant signature on the polarized sky. This highlights both the power of diffuse polarization for mapping Galactic magnetic fields, and the consideration they must be given for mapping background polarized sources. For example, studies of the polarized cosmic microwave background (CMB), or hydrogen intensity mapping experiments, must take into account the foreground polarized emission and Faraday rotation effects. Diffuse polarization is proving to be one of the best tracers of large-scale polarization features.

The correlation of H I and polarization as tracers of the ISM has been a surprising result. We would normally expect to see Faraday rotation in regions of highly ionized gas, such the WIM. Magnetic features have been found to arise in the CNM (e.g. McClure-Griffiths et al., 2006b; Clark et al., 2014), but the H I in this supershell is part of the WNM. Here we may be seeing the WPIM, as described by Heiles & Haverkorn (2012), where Faraday rotation should be the best tracer. By unravelling the ISM into its constituent components, we can also evaluate those components in relative isolation. In this work, this unravelling process allowed me to evaluate how this Galactic super-structure has influenced magnetic fields on kilo-parsec scales.

I revisited the results of GMIMS-LBS in Chapter 4 (Thomson et al., 2019). Here we found that the nearby H II region, Sharpless 2-27 (Sh2-27), produces a depolarization feature in GMIMS-LBS. Despite this, however, we still found polarized emission towards this region. Using point source rotation measures from Taylor et al. (2009), we determined that Sh2-27 is a depolarization wall in GMIMS-LBS. A depolarization wall depolarizes all polarized emission produced behind it. The emission we detected towards Sh2-27 must therefore be produced in the foreground. In the Faraday spectra towards Sh2-27 we find a triple-peaked structure, which arises somewhere in the ~ 165 pc foreground column towards Sh2-27. Using 3D dust maps from STructuring by Inversion the Local Interstellar Medium (STILISM, Lallement et al., 2014; Capitanio et al., 2017; Lallement et al., 2018) we showed that the peaks in the Faraday spectra are correlated with two foreground neutral clouds. We modelled the triple-peaked Faraday depth structure as being produced by diffuse emission along the entire line of sight with magnetic fields of opposite alignment in each neutral

cloud. Our modelling also showed that the polarized emissivity in the hot cavity of the Local Bubble is likely reduced relative to the rest of the foreground column. From this modelling, we estimated magnetic field strengths of ~ -2.5, ~ -15, and $\sim +30\,\mu$G in the Local Bubble and the near and far neutral clouds, respectively. The magnetic fields in these clouds are atypically strong for the generic cold neutral medium, and might be associated with a compressed shell wall or similar feature.

Faraday tomography, by its very name, carries the promise of mapping the magneto-ionic medium in three dimensions. With large-scale projects such as GMIMS, we now have the data capable of realising this promise. What remains challenging, however, is converting the Faraday depth axis of our data into the line-of-sight axis through the Milky Way. We are now finding this conversion process is possible by combining Faraday and ISM tomography together. Here I have found a powerful tool we can use to untangle the magneto-ionic medium: depolarization walls. These 'walls' can give us the critical distance information which we need to map out diffuse polarization observations in the Galaxy.

Finally in Chapter 5 (Thomson et al., in prep.), we investigated the brightest polarized region in GMIMS-LBS, G150−50. Our analysis of this region showed that it arises from a feature known as a 'Faraday caustic'. Bell et al. (2011) predicted that a caustic will occur when the line-of-sight magnetic field has a gradient causing it to cross $0\,\mu$G. A Faraday caustic appears as a strong spike in the Faraday spectrum with a tail towards either positive or negative Faraday depths, corresponding to a positive or negative gradient in the magnetic field, respectively. Additionally, the strong spike in Faraday depth will occur even in the absence of enhanced polarized emissivity. GMIMS-LBS, with a minimum to maximum frequency ratio of 1.6, is one of the first polarization surveys capable of discriminating a Faraday caustic from a Faraday screen. We inspected total intensity images at 408 MHz and 1.4 GHz, and polarization images at 1.4 GHz, and found no corresponding feature in any of those observations. We did find that G150−50 appears in the 408 MHz survey of Mathewson & Milne (1965), assuring us that this is a real feature on the sky. We analyzed the Faraday spectra towards G150−50, finding that an asymmetric tail appears, as predicted for a Faraday caustic. We further investigated the polarization spectra using QU-fitting techniques. From 12 possible models, we found that the

best-fitting model that was consistent with all observations was a Faraday caustic with a foreground screen. We conclude that as a Faraday caustic, G150−50 should be a followed up with both the full GMIMS observations and by high-resolution instrument such as the Murchison Widefield Array (MWA).

The magneto-ionic medium of the Milky Way is a unique component of the Milky Way's ISM. The features that form there are often unique, and simply cannot be found in tracers of the ISM other than radio polarization. Faraday caustics are prime example of such a feature that is unique to the magneto-ionic medium and radio polarization. In order to determine the origin of the bright object I found in GMIMS-LBS I had to utilize the full power of the survey and draw upon additional polarization and total intensity maps. Using both Faraday tomography and QU-fitting techniques together has revealed the strengths of each technique when trying to understand the potentially tangled and enigmatic magneto-ionic medium. Faraday tomography can capture complex information and present it to us in a very readable manner; a caustic will appear as a strong spike in the Faraday spectrum, with an asymmetric tail. QU-fitting then enables us to drill-down onto the physical origins of the observed spectrum. Modelling allows us to quantify how likely particular physical models are given our data and uncertainties. As I continue my work to investigate the complex tapestry that is the Galactic magneto-ionic medium, I will look to applying both of these methods to the exciting new observations that are now becoming available to us.

6.2 Future work

The work I have presented in this thesis opens up a number of avenues for further investigation. The magneto-ionic medium is complex as it is vast, and there remain many unanswered scientific questions. We find ourselves, however, in an area of rapid observational progress. As stated by Carretti et al. (2019), we are in the 'golden age' of all-sky single-dish surveys. The complete GMIMS will be an enormously powerful tool by itself, and it will also be complemented by high-frequency surveys such as S-PASS and the C-Band All-Sky Survey (C-BASS). Further, we are in the midst of the lead up to the Square Kilometre Array (SKA). The precursors to the

SKA, such as ASKAP, MeerKAT, and the MWA, are now starting to produce their first scientific results. These incredible new surveys and instruments will allow us to probe the Galactic magneto-ionic medium with unprecedented detail, and I hope to apply the methods I have developed here to the next generation of polarization observations.

6.2.1 Depolarization walls in the Milky Way

In Chapter 4 (Thomson et al., 2018), I showed that we can use 'depolarization walls' to constrain distances in diffuse polarization observations. Depolarisation walls are akin to localised polarization horizons (Uyaniker et al., 2003), and are thus strongly frequency and beam-size dependant. We made use of low-frequency (300-480 MHz), single-dish data from GMIMS-LBS in combination with point-source RMs from Taylor et al. (2009). The combination of the large GMIMS-LBS beam with the sparse RM grid from Taylor et al. (2009) constrained us to use only the largest, nearby H II regions as a depolarisation walls. New observations from SKA precursors will allow this technique to be applied throughout the sky.

The Polarisation Sky Survey of the Universe's Magnetism (POSSUM) (Gaensler et al., 2010) project on the Australian Square Kilometre Array Pathfinder (ASKAP), together with the Very Large Array Sky Survey (VLASS), will provide the new state-of-the-art all-sky survey of extragalactic rotation measures. These surveys will produce a broadband catalogue with a source density two orders of magnitude higher than the NRAO VLA Sky Survey (Taylor et al., 2009).

In addition, low-frequency surveys are under way using the Murchison Widefield Array (MWA) and the Low-Frequency Array (LOFAR). Low frequency polarised observations are much more sensitive to Faraday rotation effects. As such, they are able to provide very fine Faraday tomography measurements of the nearby MIM (e.g. Lenc et al., 2016; Van Eck et al., 2017). These observatories are currently carrying out all-sky polarization surveys in the form of the GaLactic and Extragalactic All-Sky MWA-eXtended (GLEAM-X, Hurley-Walker et al., 2017b,a) and the LOFAR Two-metre Sky Survey (LoTSS, Shimwell et al., 2017).

Combining these high and low frequencies surveys together will allow us to construct a three-dimensional map of magnetic field structure in the nearby Milky Way

in areas that have not previously been studied. First, depolarizing H II regions should be identified in the diffuse low-frequency surveys. The locations and distances to Galactic H II regions is being greatly improved by the H II Region Discovery Surveys (HRDS and SHRDS, Bania et al., 2010; Brown et al., 2019), and the *Gaia* mission (Gaia Collaboration et al., 2016, 2018). The dense RM grids from VLASS and POSSUM will then allow us to identify which depolarizing H II regions are acting as depolarization walls. Using Faraday tomography techniques, as shown in Thomson et al. (2018), we will be able to reconstruct the three-dimensional magnetic field structure in unprecedented detail across huge areas of the sky.

6.2.2 Follow-up of G150−50

In Chapter 5 (Thomson et al., in prep.), I found that the polarization feature G150−50 is a Faraday caustic. These features offer a unique opportunity to study the Galactic magneto-ionic medium. Bell et al. (2011) showed that caustics map even weakly polarized emission to a small range of Faraday depths, thereby producing a strong spike in the Faraday spectrum. This strong spike can, in effect, illuminate small-scale features as well as a large-scale gradients and zero-points in the magnetic field. Bell et al. (2011) derive that in the presence of a turbulent field, in combination with a caustic, the main caustic feature will split into sub-features in the Faraday spectrum. These sub-caustics probe the turbulent features of the magneto-ionic medium.

To find these features we require a survey with high Faraday depth resolution. Such a survey should measure diffuse polarization, at low radio-frequencies, with a minimum to maximum frequency ratio of at least 1.5. The GaLactic and Extragalactic All-Sky MWA Survey (Wayth et al., 2015) is a survey which meets such a requirement, and has already observed the G150−50 region. If the full GLEAM band can be utilized, this survey is capable of providing a Faraday resolution of $\sim 0.2\,\mathrm{rad\,m^{-2}}$, with a Faraday maximum scale of $\sim 1.9\,\mathrm{rad\,m^{-2}}$, and a frequency ratio of 3.2. By targeting the diffuse observations from this survey, and similar surveys, we might finally unlock a new probe of the turbulent magneto-ionic medium using Faraday caustics like G150−50.

6.2.3 Compilation of full GMIMS

In Chapter 3, I showed the power that can be gained by combining complementary all-sky surveys. In Chapters 4 and 5, I demonstrated how we can use broadband polarization surveys to perform Faraday tomography. The Global Magneto-Ionic Medium Survey (GMIMS, Wolleben et al., 2009) has been designed with Faraday tomography at its heart, measuring diffuse polarization across the entire sky from 300 MHz to 1.8 GHz. The overall survey has been broken into 6 components across multiple instruments. In Chapter 2, I present my contribution to the low-band Southern GMIMS (Wolleben et al., 2019). The high-band Northern component (GMIMS-HBN, Wolleben et al., 2010a, Wolleben et al., in prep.) has also been completed, and the high-band Southern component (a.k.a. the Southern Twenty-centimeter All-sky Polarization Survey, STAPS, Haverkorn, 2015) has been observed and is currently being reduced. So far, these surveys have been analyzed independently (Wolleben et al., 2010b; Hill et al., 2017; Dickey et al., 2019; Thomson et al., 2019, Thomson et al., in prep.). We now have the opportunity to begin combining these surveys, and complementary surveys, together.

Processing the information that these broadband surveys provide is a significant technical challenge. In Chapter 2, I show how we applied RM synthesis and `RM-CLEAN` to GMIMS-LBS. This technique is computationally very efficient, but depends on near-contiguous frequency coverage. In Chapter 5, I also applied QU-fitting techniques, which can potentially bridge large frequency gaps. Model fitting is computationally intensive, however. This is a particular problem for diffuse all-sky polarization surveys, which would require fitting millions of spectra for each pixel on the sky.

If we wish to apply RM synthesis techniques whilst combining the current surveys, we must pay particular attention to the `RM-CLEAN` process. A frequency large gap will produce a complicated RMSF which is sensitive to narrow and broad Faraday depth structures simultaneously. `RM-CLEAN`, which is based on fitting δ-functions, may struggle to correctly deconvolve such data. Instead we should look to improving the `RM-CLEAN` algorithms, taking lessons from aperture synthesis. In particular, the multi-scale (Cornwell, 2008) `CLEAN` algorithms (e.g. Akiyama et al., 2018) and maximum likelihood techniques (e.g. Bell et al., 2013). The combined

GMIMS components will be an ideal testing-ground for these algorithms.

If instead we wish to utilize QU-fitting with the combined GMIMS, there are a number of problems we must contend with. First, model fitting algorithms require accurate uncertainty estimations of the data. In many areas of GMIMS-LBS, for example, there remain scanning and RFI artefacts. We must quantify where we believe the data represents the true sky and where artefacts remain with uncertainty estimations. Second, as I showed in Chapter 5, we must select reasonable models to be fitted to the observed spectra. So far, this decision has been at the discretion of the observer. It is simply not feasible, however, for a single person to evaluate every spectra of an all-sky survey. This calls for some form of an automated approach. I would envision that such an approach could be informed by the results of RM synthesis. Additionally, we would also expect the sky to vary smoothly, and therefore adjacent pixels should not be entirely independent. Finally, we must not discount the computational cost of QU-fitting techniques. Computational power does thankfully improve year-over-year. In addition, the use of an informed model-fitting technique, as I have described, should cut down on the amount of computational time required.

By solving the technical challenges I have outlined here, we will be able to yield an enormous amount of information on the Galactic magneto-ionic medium. By successfully combining the GMIMS components we will be able to realise the full potential of diffuse polarization observations; performing Faraday tomography with high Faraday-depth precision and sensitivity to broad Faraday depth features.

6.3 Final remarks

The field of radio polarimetry is rapidly growing. We have many new exciting surveys underway, which will provide us with copious broadband, all-sky spectro-polarimetric data. This includes both high-resolution surveys of extra-galactic point-sources, which probe the entire Galaxy, and diffuse polarization surveys, which enable Faraday tomography. Additionally, new analysis tools are also being developed to help yield the maximum amount of information possible from these polarization surveys. The techniques include the Faraday tomographic and model-fitting techniques I have used, as well as gradient analysis methods such as Gaensler et al.

(2011) or Lazarian & Yuen (2018) and (Zhang et al., 2019). All together, it is a very exciting time to be working in this field.

In this thesis I have shown how we can use diffuse all-sky polarization surveys to unravel to complex Galactic magneto-ionic medium. It is my hope that the methods and results I have shown here can be utilized as new surveys and analysis tools come online. Consistently, my investigations have shown that we need to consider all components of the Galactic interstellar medium together. It is only under this holistic framework that we can obtain impactful results. Parallel to the progress in radio polarimetry, there is also significant work being done on other ISM tracers. These results will be equally important in revealing the complete picture of the Galactic ISM. Many mysteries still remain, however, in the complex tapestry of the Galactic magneto-ionic medium. As such, I look forward with excitement to continuing my work, trying to understand the magneto-ionic properties of our home Galaxy.

Bibliography

Ackermann M., et al., 2014, ApJ, 793, 64

Akiyama K., Akahori T., Miyashita Y., Ideguchi S., Yamaguchi R., Ikeda S., Takahashi K., 2018, arXiv e-prints, p. arXiv:1811.10610

Astropy Collaboration et al., 2013, A&A, 558, A33

Astropy Collaboration et al., 2018, AJ, 156, 123

Bailer-Jones C. A. L., 2015, PASP, 127, 994

Bania T. M., Anderson L. D., Balser D. S., Rood R. T., 2010, ApJ, 718, L106

Beck R., 2007, A&A, 470, 539

Beck R., 2015, A&A Rev., 24, 4

Beck R., Krause M., 2005, Astronomische Nachrichten, 326, 414

Beck R., Wielebinski R., 2013, Magnetic Fields in Galaxies. p. 641, doi:10.1007/978-94-007-5612-0_13

Beck R., Frick P., Stepanov R., Sokoloff D., 2012, A&A, 543, A113

Bell M. R., Enßlin T. A., 2012, A&A, 540, A80

Bell M. R., Junklewitz H., Enßlin T. A., 2011, A&A, 535, A85

Bell M. R., Oppermann N., Crai A., Enßlin T. A., 2013, A&A, 551, L7

Bennett C. L., et al., 2013, ApJS, 208, 20

Berkhuijsen E. M., Haslam C. G. T., Salter C. J., 1971, Astronomy and Astrophysics, Vol. 14, p. 252 - 262, 14, 252

Boumis P., Dickinson C., Meaburn J., Goudis C. D., Christopoulou P. E., López J. A., Bryce M., Redman M. P., 2001, MNRAS, 320, 61

Brandenburg A., Subramanian K., 2005, Phys. Rep., 417, 1

Brentjens M. A., de Bruyn A. G., 2005, A&A, 441, 1217

Brouw W. N., Spoelstra T. A. T., 1976, A&AS, 26, 129

Brown C., et al., 2017, AJ, 154, 23

Brown S., et al., 2019, MNRAS, 483, 964

Buchner J., et al., 2014, A&A, 564, A125

Burbidge G. R., 1956, ApJ, 124, 416

Burn B. J., 1966, MNRAS, 133, 67

Calabretta M. R., Staveley-Smith L., Barnes D. G., 2014, PASA, 31, e007

Capitanio L., Lallement R., Vergely J. L., Elyajouri M., Monreal-Ibero A., 2017, A&A, 606, A65

Carretti E., et al., 2013, Nature, 493, 66

Carretti E., et al., 2019, MNRAS, 489, 2330

Celnik W. E., Weiland H., 1988, A&A, 192, 316

Chandrasekhar S., Fermi E., 1953, ApJ, 118, 113

Clark S. E., Peek J. E. G., Putman M. E., 2014, ApJ, 789, 82

Cohen A. S., Lane W. M., Cotton W. D., Kassim N. E., Lazio T. J. W., Perley R. A., Condon J. J., Erickson W. C., 2007, AJ, 134, 1245

Condon J. J., Cotton W. D., Greisen E. W., Yin Q. F., Perley R. A., Taylor G. B., Broderick J. J., 1998, AJ, 115, 1693

Cooper B. F. C., Price R. M., 1962, Nature, 195, 1084

Cordes J. M., Lazio T. J. W., 2002

Cornwell T. J., 2008, IEEE Journal of Selected Topics in Signal Processing, 2, 793

Costain C. H., 1960, MNRAS, 120, 248

Crutcher R. M., Wandelt B., Heiles C., Falgarone E., Troland T. H., 2010, ApJ, 725, 466

Davis Leverett J., Greenstein J. L., 1951, ApJ, 114, 206

Dennison B., Simonetti J. H., Topasna G. A., 1998, Publications of the Astronomical Society of Australia, 15, 147

Dickey J. M., Lockman F. J., 1990, ARA&A, 28, 215

Dickey J. M., et al., 2019, ApJ, 871, 106

Duarte M., 2015, Notes on Scientific Computing for Biomechanics and Motor Control, `https://github.com/demotu/BMC`

Duncan A. R., Haynes R. F., Jones K. L., Stewart R. T., 1997, MNRAS, 291, 279

Ehlerová S., Palouš J., 2005, A&A, 437, 101

Ehlerová S., Palouš J., 2013, A&A, 550, A23

Federrath C., 2015, MNRAS, 450, 4035

Federrath C., 2016, Journal of Plasma Physics, 82, 535820601

Federrath C., Klessen R. S., 2012, ApJ, 761, 156

Federrath C., Schrön M., Banerjee R., Klessen R. S., 2014, ApJ, 790, 128

Feroz F., Hobson M. P., 2008, MNRAS, 384, 449

Feroz F., Hobson M. P., Bridges M., 2009, MNRAS, 398, 1601

Feroz F., Hobson M. P., Cameron E., Pettitt A. N., 2019, The Open Journal of Astrophysics, 2, 10

Ferrière K. M., 2001, Reviews of Modern Physics, 73, 1031

Ferriere K. M., Mac Low M.-M., Zweibel E. G., 1991, ApJ, 375, 239

Finkbeiner D. P., 2003, ApJS, 146, 407

Fletcher A., Shukurov A., 2006, MNRAS, 371, L21

Fletcher A., Shukurov A., 2007, in Miville-Deschênes M. A., Boulanger F., eds, EAS Publications Series Vol. 23, EAS Publications Series. pp 109–128 (arXiv:astro-ph/0602536), doi:10.1051/eas:2007008

Gaensler B. M., Dickey J. M., McClure-Griffiths N. M., Green A. J., Wieringa M. H., Haynes R. F., 2001, ApJ, 549, 959

Gaensler B. M., Beck R., Feretti L., 2004, New A Rev., 48, 1003

Gaensler B. M., Madsen G. J., Chatterjee S., Mao S. A., 2008, PASA, 25, 184

Gaensler B. M., Landecker T. L., Taylor A. R., POSSUM Collaboration 2010, in American Astronomical Society Meeting Abstracts #215. p. 470.13

Gaensler B. M., et al., 2011, Nature, 478, 214

Gaia Collaboration et al., 2016, A&A, 595, A1

Gaia Collaboration et al., 2018, A&A, 616, A1

Gao X. Y., et al., 2010, A&A, 515, A64

Gao X. Y., Reich W., Reich P., Han J. L., Kothes R., 2015, A&A, 578, A24

Gaustad J. E., McCullough P. R., Rosing W., Van Buren D., 2001, PASP, 113, 1326

Gazol A., Villagran M. A., 2018, MNRAS, 478, 146

Górski K. M., Hivon E., Banday A. J., Wand elt B. D., Hansen F. K., Reinecke M., Bartelmann M., 2005, ApJ, 622, 759

Green D. A., 2011, Bulletin of the Astronomical Society of India, 39, 289

Green D. A., 2014, Bull. Astr. Soc. India, 42, 47

Green G. M., et al., 2015, ApJ, 810, 25

Green G. M., et al., 2018, MNRAS, 478, 651

Green G. M., Schlafly E., Zucker C., Speagle J. S., Finkbeiner D., 2019, ApJ, 887, 93

HI4PI Collaboration et al., 2016a, A&A, 594, A116

HI4PI Collaboration et al., 2016b, A&A, 594, A116

Haffner L. M., Reynolds R. J., Tufte S. L., 1998, ApJ, 501, L83

Haffner L. M., Reynolds R. J., Tufte S. L., Madsen G. J., Jaehnig K. P., Percival J. W., 2003, ApJS, 149, 405

Haffner L. M., et al., 2010, in Kothes R., Landecker T. L., Willis A. G., eds, Astronomical Society of the Pacific Conference Series Vol. 438, The Dynamic Interstellar Medium: A Celebration of the Canadian Galactic Plane Survey. p. 388 (arXiv:1008.0612)

Han J. L., 2017, ARA&A, 55, 111

Hanbury Brown R., Davies R. D., Hazard C., 1960, The Observatory, 80, 191

Harvey-Smith L., Madsen G. J., Gaensler B. M., 2011, ApJ, 736, 83

Harwit M., 2006, Astrophysical Concepts, doi:10.1007/978-0-387-33228-4.

Haslam C. G. T., Quigley M. J. S., Salter C. J., 1970, MNRAS, 147, 405

Haslam C. G. T., Klein U., Salter C. J., Stoffel H., Wilson W. E., Cleary M. N., Cooke D. J., Thomasson P., 1981, A&A, 100, 209

Haslam C. G. T., Salter C. J., Stoffel H., Wilson W. E., 1982, A&AS, 47, 1

Haverkorn M., 2015, in Lazarian A., de Gouveia Dal Pino E. M., Melioli C., eds, Astrophysics and Space Science Library Vol. 407, Magnetic Fields in Diffuse Media. p. 483 (arXiv:1406.0283), doi:10.1007/978-3-662-44625-6_17

Haverkorn M., Katgert P., de Bruyn A. G., 2004, A&A, 427, 549

Heald G., Braun R., Edmonds R., 2009, A&A, 503, 409

Heiles C., 1979, ApJ, 229, 533

Heiles C., 1984, ApJS, 55, 585

Heiles C., Haverkorn M., 2012, Space Sci. Rev., 166, 293

Heiles C., Troland T. H., 2003, ApJ, 586, 1067

Heiles C., Haffner L. M., Reynolds R. J., 1999, New Perspectives on the Interstellar Medium, 168, 211

Heyer M., Dame T. M., 2015, ARA&A, 53, 583

Hill A., 2018, Galaxies, 6, 129

Hill A. S., Joung M. R., Mac Low M.-M., Benjamin R. A., Haffner L. M., Klingenberg C., Waagan K., 2012, ApJ, 750, 104

Hill A. S., et al., 2017, MNRAS, 467, 4631

Hill A. S., Mac Low M.-M., Gatto A., Ibáñez-Mejía J. C., 2018, ApJ, 862, 55

Högbom J. A., 1974, Astronomy and Astrophysics Supplement, 15, 417

Hu E. M., 1981, ApJ, 248, 119

Hurley-Walker N., Seymour N., Staveley-Smith L., Johnston-Hollitt M., Kapinska A., McKinley B., 2017a, GaLactic and Extragalactic All-Sky MWA-eXtended (GLEAM-X) survey: Pilot observations, MWA Proposal id.2017A-1

Hurley-Walker N., et al., 2017b, MNRAS, 464, 1146

Iacobelli M., et al., 2014, A&A, 566, A5

Ideguchi S., Tashiro Y., Akahori T., Takahashi K., Ryu D., 2014, ApJ, 792, 51

Jansky K. G., 1933, Nature, 132, 66

Jelić V., et al., 2015, A&A, 583, A137

Jo Y.-S., Min K.-W., Seon K.-I., Edelstein J., Han W., 2011, ApJ, 738, 91

Jo Y.-S., Min K.-W., Seon K.-I., 2015, ApJ, 807, 68

Kaczmarek J. F., Purcell C. R., Gaensler B. M., McClure-Griffiths N. M., Stevens J., 2017, MNRAS, 467, 1776

Kalberla P. M. W., Haud U., 2015, A&A, 578, A78

Kalberla P. M. W., Haud U., 2018, A&A, 619, A58

Kalberla P. M. W., Kerp J., 2009, ARA&A, 47, 27

Kalberla P. M. W., Dedes L., Kerp J., Haud U., 2007, A&A, 469, 511

Kalberla P., McClure-Griffiths N. M., Kerp J., 2009, in Panoramic Radio Astronomy: Wide-field 1-2 GHz Research on Galaxy Evolution. p. 26 (arXiv:0910.5910)

Kalberla P. M. W., et al., 2010, A&A, 521, A17

Kalberla P. M. W., Kerp J., Haud U., Haverkorn M., 2017, A&A, 607, A15

Kerp J., Winkel B., Ben Bekhti N., Flöer L., Kalberla P. M. W., 2011, Astronomische Nachrichten, 332, 637

Koo B.-C., Heiles C., Reach W. T., 1992, ApJ, 390, 108

Kraus J. D., 1966, Radio astronomy

Lallement R., Vergely J. L., Valette B., Puspitarini L., Eyer L., Casagrande L., 2014, A&A, 561, A91

Lallement R., et al., 2018, A&A, 616, A132

Landecker T. L., 1969, PhD thesis

Landecker T. L., 2012, Space Sci. Rev., 166, 263

Large M. I., Quigley M. J. S., Haslam C. G. T., 1962, MNRAS, 124, 405

Lazarian A., Yuen K. H., 2018, ApJ, 865, 59

Lenc E., et al., 2016, ApJ, 830, 38

Liszt H., 2014, ApJ, 780, 10

Ma Y. K., Mao S. A., Stil J., Basu A., West J., Heiles C., Hill A. S., Betti S. K., 2019, MNRAS, 487, 3454

Maciejewski W., Murphy E. M., Lockman F. J., Savage B. D., 1996, ApJ, 469, 238

Manchester R. N., Hobbs G. B., Teoh A., Hobbs M., 2005, AJ, 129, 1993

Mathewson D. S., Milne D. K., 1965, Australian Journal of Physics, 18, 635

McClure-Griffiths N. M., Dickey J. M., Gaensler B. M., Green A. J., Haynes R. F., Wieringa M. H., 2000, AJ, 119, 2828

McClure-Griffiths N. M., Dickey J. M., Gaensler B. M., Green A. J., 2001, ApJ, 562, 424

McClure-Griffiths N. M., Dickey J. M., Gaensler B. M., Green A. J., 2002, ApJ, 578, 176

McClure-Griffiths N. M., Dickey J. M., Gaensler B. M., Green A. J., Haverkorn M., Strasser S., 2005, ApJS, 158, 178

McClure-Griffiths N. M., Ford A., Pisano D. J., Gibson B. K., Staveley-Smith L., Calabretta M. R., Dedes L., Kalberla P. M. W., 2006a, ApJ, 638, 196

McClure-Griffiths N. M., Dickey J. M., Gaensler B. M., Green A. J., Haverkorn M., 2006b, ApJ, 652, 1339

McClure-Griffiths N. M., et al., 2009, ApJS, 181, 398

McClure-Griffiths N. M., Madsen G. J., Gaensler B. M., McConnell D., Schnitzeler D. H. F. M., 2010, ApJ, 725, 275

McKee C. F., Ostriker J. P., 1977, ApJ, 218, 148

Mezger P. G., Henderson A. P., 1967, ApJ, 147, 471

Moss V. A., McClure-Griffiths N. M., Braun R., Hill A. S., Madsen G. J., 2012, MNRAS, 421, 3159

Neuhäuser R., Forbrich J., 2008, The Corona Australis Star Forming Region. p. 735

Nord M. E., Henning P. A., Rand R. J., Lazio T. J. W., Kassim N. E., 2006, AJ, 132, 242

Norman C. A., Ikeuchi S., 1989, ApJ, 345, 372

Ntormousi E., Dawson J. R., Hennebelle P., Fierlinger K., 2017, A&A, 599, A94

O'Sullivan S. P., et al., 2012, MNRAS, 421, 3300

Offner S. S. R., Clark P. C., Hennebelle P., Bastian N., Bate M. R., Hopkins P. F., Moraux E., Whitworth A. P., 2014, in Beuther H., Klessen R. S., Dullemond C. P., Henning T., eds, Protostars and Planets VI. p. 53 (arXiv:1312.5326), doi:10.2458/azu_uapress_9780816531240-ch003

Oppermann N., et al., 2012, A&A, 542, A93

Oppermann N., et al., 2015, A&A, 575, A118

Padoan P., Nordlund Å., 2011, ApJ, 730, 40

Page L., et al., 2007, ApJS, 170, 335

Peek J. E. G., et al., 2011, ApJS, 194, 20

Peek J. E. G., et al., 2018, ApJS, 234, 2

Pidopryhora Y., Lockman F. J., Shields J. C., 2007, ApJ, 656, 928

Planck Collaboration et al., 2018a, arXiv e-prints, p. arXiv:1801.04945

Planck Collaboration et al., 2018b, arXiv e-prints, p. arXiv:1807.06205

Planck Collaboration et al., 2018c, arXiv e-prints, p. arXiv:1807.06208

Planck Collaboration et al., 2018d, arXiv e-prints, p. arXiv:1807.06212

Purcell C. R., et al., 2015, ApJ, 804, 22

Reber G., 1944, ApJ, 100, 279

Reber G., Greenstein J. L., 1947, The Observatory, 67, 15

Reich W., 1982, A&AS, 48, 219

Reich P., Reich W., 1986, A&AS, 63, 205

Reich P., Testori J. C., Reich W., 2001, A&A, 376, 861

Remazeilles M., Dickinson C., Banday A. J., Bigot-Sazy M. A., Ghosh T., 2015, MNRAS, 451, 4311

Reynolds R. J., Tufte S. L., Haffner L. M., Jaehnig K., Percival J. W., 1998, PASA, 15, 14

Robitaille T., Bressert E., 2012, Astrophysics Source Code Library, p. ascl:1208.017

Robitaille J. F., et al., 2017, MNRAS, 468, 2957

Robitaille J. F., Scaife A. M. M., Carretti E., Haverkorn M., Crocker R. M., Kesteven M. J., Poppi S., Staveley-Smith L., 2018, A&A, 617, A101

Roger R. S., Costain C. H., Landecker T. L., Swerdlyk C. M., 1999, A&AS, 137, 7

Rybicki G. B., Lightman A. P., 1979, Radiative processes in astrophysics

Rybicki G. B., Lightman A. P., 1986, Radiative Processes in Astrophysics, doi:https://doi.org/10.1002/9783527618170.

Savage B. D., Wakker B. P., 2009, ApJ, 702, 1472

Schlegel D. J., Finkbeiner D. P., Davis M., 1998, ApJ, 500, 525

Schnitzeler D. H. F. M., 2010, MNRAS, 409, L99

Schnitzeler D. H. F. M., Carretti E., Wieringa M. H., Gaensler B. M., Haverkorn M., Poppi S., 2019, MNRAS, 485, 1293

Shelton R. L., 2009, Space Sci. Rev., 143, 231

Shimwell T. W., et al., 2017, A&A, 598, A104

Shull J. M., Jones J. R., Danforth C. W., Collins J. A., 2009, ApJ, 699, 754

Sironi G., 1974, MNRAS, 166, 345

Slavin J. D., Cox D. P., 1992, ApJ, 392, 131

Sokoloff D. D., Bykov A. A., Shukurov A., Berkhuijsen E. M., Beck R., Poezd A. D., 1999, MNRAS, 303, 207

Spoelstra T. A. T., 1984, A&A, 135, 238

Stil J. M., et al., 2006, AJ, 132, 1158

Stil J., Wityk N., Ouyed R., Taylor A. R., 2009, ApJ, 701, 330

Su M., Slatyer T. R., Finkbeiner D. P., 2010, ApJ, 724, 1044

Su H., et al., 2018, MNRAS, 479, 4041

Suad L. A., Caiafa C. F., Arnal E. M., Cichowolski S., 2014, A&A, 564, A116

Sun X. H., Han J. L., Reich W., Reich P., Shi W. B., Wielebinski R., Fürst E., 2007, A&A, 463, 993

Sun X. H., Reich W., Waelkens A., Enßlin T. A., 2008, A&A, 477, 573

Sun X. H., Reich W., Han J. L., Reich P., Wielebinski R., Wang C., Müller P., 2011, A&A, 527, A74

Sun X. H., et al., 2015, ApJ, 811, 40

Taylor A. R., et al., 2003, AJ, 125, 3145

Taylor A. R., Stil J. M., Sunstrum C., 2009, ApJ, 702, 1230

Testori J. C., Reich P., Reich W., 2008, A&A, 484, 733

Thomson A. J. M., et al., 2018, MNRAS, 479, 5620

Thomson A. J. M., et al., 2019, MNRAS, 487, 4751

Tomisaka K., 1990, ApJ, 361, L5

Tomisaka K., 1998, MNRAS, 298, 797

Tribble P. C., 1991, MNRAS, 250, 726

Tritsis A., Federrath C., Pavlidou V., 2019, ApJ, 873, 38

Turtle A. J., Pugh J. F., Kenderdine S., Pauliny-Toth I. I. K., 1962, MNRAS, 124, 297

Uyaniker B., Fürst E., Reich W., Reich P., Wielebinski R., 1999, A&AS, 138, 31

Uyaniker B., Landecker T. L., Gray A. D., Kothes R., 2003, ApJ, 585, 785

Valls-Gabaud D., 1998, PASA, 15, 111

Van Eck C. L., et al., 2017, A&A, 597, A98

Van Eck C. L., et al., 2019, A&A, 623, A71

Vergely J. L., Valette B., Lallement R., Raimond S., 2010, A&A, 518, A31

Wardle J. F. C., Sramek R. A., 1974, ApJ, 189, 399

Wayth R. B., et al., 2015, PASA, 32, e025

Webster A. S., 1974, MNRAS, 166, 355

Wilkinson A., Smith F. G., 1974, MNRAS, 167, 593

Wolfire M. G., Hollenbach D., McKee C. F., Tielens A. G. G. M., Bakes E. L. O., 1995, ApJ, 443, 152

Wolfire M. G., McKee C. F., Hollenbach D., Tielens A. G. G. M., 2003, ApJ, 587, 278

Wolleben M., Reich W., 2004, A&A, 427, 537

Wolleben M., Landecker T. L., Reich W., Wielebinski R., 2006, A&A, 448, 411

Wolleben M., et al., 2009, in Strassmeier K. G., Kosovichev A. G., Beckman J. E., eds, IAU Symposium Vol. 259, Cosmic Magnetic Fields: From Planets, to Stars and Galaxies. pp 89–90 (arXiv:0812.2450), doi:10.1017/S1743921309030117

Wolleben M., Landecker T. L., Hovey G. J., Messing R., Davison O. S., House N. L., Somaratne K. H. M. S., Tashev I., 2010a, AJ, 139, 1681

Wolleben M., et al., 2010b, ApJ, 724, L48

Wolleben M., et al., 2019, AJ, 158, 44

Wood K., Haffner L. M., Reynolds R. J., Mathis J. S., Madsen G., 2005, ApJ, 633, 295

Zhang J.-F., Lazarian A., Ho K. W., Yuen K. H., Yang B., Hu Y., 2019, MNRAS, 486, 4813

Zheng H., et al., 2017, MNRAS, 464, 3486

de Avillez M. A., Breitschwerdt D., 2005, A&A, 436, 585

van Leeuwen F., 2007, A&A, 474, 653